Optical Confinement in the Nanocoax:

Author: Yitzi M. Calm

Persistent link: http://hdl.handle.net/2345/bc-ir:108652

This work is posted on eScholarship@BC,
Boston College University Libraries.

Boston College Electronic Thesis or Dissertation, 2019

Copyright is held by the author. This work is licensed under a Creative Commons Attribution 4.0 International License (http://creativecommons.org/licenses/by/4.0).

Optical Confinement in the Nanocoax

Yitzi M. Calm

A dissertation

submitted to the faculty of

the department of physics

in partial fulfillment

of the requirements for the degree of

Doctor of Philosophy

Boston College
Morrissey College of Arts and Sciences
Graduate School

August 2019

© Copyright 2019 Yitzi M. Calm

Optical Confinement in the Nanocoax

Yitzi M. Calm

Advisor: Michael J. Naughton, Ph.D.

The nanoscale coaxial cable (nanocoax) has demonstrated sub-diffraction-limited optical confinement in the visible and the near infrared, with the theoretical potential for confinement to scales *arbitrarily smaller* than the free space wavelength.

In the first part of this thesis, I define in clear terms what the diffraction limit is. The conventional resolution formulae used by many are generally only valid in the paraxial limit. I performed a parametric numerical study, employing techniques of Fourier optics, to resolve precisely what that limit should be for nonparaxial (*i.e.* wide angle) focusing of scalar spherical waves. I also present some novel analytical formulae born out of Debye's approximation which explain the trends found in the numeric study. *These new functional forms* remain accurate under wide angle focusing and could materially improve the performance, for example, in high intensity focused ultrasound surgery by further concentrating the power distributed within the point spread function to suppress the side lobes. I also comment of some possible connections to the focusing of electromagnetic waves.

In the second part of this thesis I report on a novel fabrication process which yields optically addressable, sub-micron scale, and high aspect ratio metal-insulator-metal nanocoaxes made by atomic layer deposition of Pt and Al_2O_3. I discuss the observation of optical transmission via the fundamental, TEM-like mode by excitation with a radially polarized optical vortex beam. Also, Laguerre-Gauss beams are shown to overlap well with

cylindrical waveguide modes in the nanocoax. My experimental results are based on interrogation with a polarimetric imager and a near-field scanning optical microscope. Various optical apparatus I built during my studies are also reviewed. Numerical simulations were used with uniaxial symmetry to explore 3D adiabatic taper geometries much larger than the wavelength.

Finally, I draw some conclusions by assessing the optical performance of the fabricated nanocoaxial structures, and by giving some insights into future directions of investigation.

Table of Contents

Table of Contents ..... **iv**

Acknowledgements ..... **vii**

List of Figures ..... **ix**

List of Tables ..... **xii**

1 Introduction **1**

1.1 Problem statement 1

1.2 Motivation 1

1.3 Application areas 3

1.4 Organization of this thesis 4

2 Wide Angle Effects in Scalar Focusing **5**

2.1 Motivation 6

2.2 Theoretical foundation 8

2.2.1 Wave mechanics in cylindrical coordinates 8

2.2.2 Cardinal directions 9

2.2.3 Angular spectrum method 10

2.3 Statement of the focusing problem 12

2.3.1 Analytic solutions 14

2.3.1.1 Debye's approximation 14

2.3.1.2 Paraxial limit 15

2.3.2 Numeric solutions 17

2.4 Parametric study of nonparaxial focusing 18

2.4.1 Numerical methods 18

2.4.2 Characteristics of a nonparaxial PSF 20

2.4.3 Results 23

2.4.4 Discussion 29

2.4.4.1 Transverse resolution 29

2.4.4.2 Longitudinal resolution 35
2.5 Conclusions 36
2.6 Perfect focusing for ultrasound imaging 37
3 Optical Toolset 38
3.1 Tightly focused laser beams 38
3.1.1 Experimental framework – high magnification imaging 38
3.1.2 Theoretical framework – paraxial Laguerre-Gaussian beams 39
3.1.2.1 Scalar beams 39
3.1.2.2 Electromagnetic beams 45
3.1.3 Vortex generation 56
3.1.4 Coincident dual microscopes 58
3.2 Polarimetric imaging 59
3.2.1 Encoded rotation mount 60
3.2.2 Brewster's window calibration 61
3.2.3 Orbit shift correction 64
3.2.4 HSV color composition 66
3.3 Near-Field scanning optical microscopy 70
3.4 Plasmonics 71
4 Nanocoaxial Waveguides 78
4.1 Elements of waveguide theory 78
4.1.1 PEC/Al_2O_3 coaxial waveguide modes 81
4.1.2 Overlap between PEC nanocoax modes and LG beams 90
4.1.3 Real-metal/Al_2O_3 coaxial waveguide modes 93
4.2 Fabrication 96
4.2.1 Review of prior work 96
4.2.1.1 Top-down approaches 97
4.2.1.2 Bottom-up approaches 105
4.2.2 Horizontal nanocoax fabrication schemes 108
4.2.2.1 By metal oxidation 109
4.2.2.2 Cast from a solution of Ag/SiO_2 nanowires 114

4.2.2.3 By atomic layer deposition 117
4.2.3 Vertical nanocoax fabrication 126
4.2.3.1 Nanohole array patterning by Bosch deep reactive ion etching 128
4.2.3.2 Conformal MIM coating by ALD 134
4.2.3.3 Excavation and electroplating 138
4.2.3.4 Wafer bonding and back-side thinning 141
4.3 Optical interrogation 147
4.3.1 Polarimetric imaging 148
4.3.2 NSOM 151
4.4 2D axisymmetric simulation 153
4.5 Conclusions 162
5 Conclusions and Outlook 164
5.1 3D NCOM: Template-stripped pyramid 166
5.2 2D NCOM: fanned-out Ag NW 167
5.3 Revisiting Klopfenstein's taper 168
5.4 Proposed taper fabrication scheme 169
References 171

Acknowledgements

Silvia, you are a constant source of inspiration for me, a beacon that lights my way. When the stars aligned and our paths crossed, my fate was sealed in an instant.

Mom, I would have nothing without your unconditional love and unconquerable spirit. I could never live up to the example you've set, although I still look up to it every day. Momo, Reena, and Taly: you guys are on my mind always, a driving force in my life. It took a village to raise me, and there are many people back home to whom I owe thanks, I'm sorry I cannot mention everyone. Wayne and Sherri, thank you. To all my friends back home, thank you. Stefania, I could never possibly repay your generosity. Your sacrifice is a lesson about the importance of family. Julian crește într-o persoană frumoasă, o reflectare a ta.

To my lab-mates at BC, thank you for everything you have taught me, for your patience, and for the community we established inside the fish bowl. Being around high performing individuals such as yourselves raises the bar. In particular, a 6:00 am Snicker's bar. I would also like to thank Paul Dee, Rich Pijar, and Svet Simidjyiski for teaching me how to build real, working things. Steve, your breadth of knowledge, career of experience, and eagerness to teach me the elements of microfabrication have molded me. I really appreciate our time together. Brent, it was a pleasure to work with you as well.

I would also like to thank all of the BC staff and facilities personnel who made this possible and who taught me a great deal about the infrastructural, administrative, and human aspects to conducting research. John O'Grady, Keil Smith, Paul Madden, Bob Klaus, Sile Powers, Scott Bortolotto, Nancy Chevry, and Jane Carter: all of you made an impact on this work. Walter Carberry, in particular, I'd like to thank you for all of the crazy requests, the friendly advice, and the rides in the morning.

I have been fortunate to work with my brilliant and hardworking people beyond the BC Dept. of Physics: my prior academic advisors have really made their Mark on me, perhaps more than they realize. Dan Pajerowski, Elisabeth Knowles, Marcus Peprah, Ozgur Yavuzcetin, Stefan Dickert, Qijun Xiao and Huajie Ke, thank you all for taking me under your wing. To Mike Madden and John Cummings, those were the most important 6 months of my career so far; I had never learned so much so quickly.

I had many helpful conversations with Michael Burns, each one would open my eyes to some new piece of technology or field of research. Watching Dr. Burns solve technical problems taught me to think critically. Hearing Dr. Burns' perspectives on the relationship between commercial and academic development has influenced my own sentiments and partly inspired my own career pathway.

I would also like to thank my committee: Prof.'s Burch and Graf thank you for your guidance over the years, and for the many metaphorical cups of sugar. Prof. Kempa, I had many enlightening conversations in your office, and will always remember the kind words of advice you've shared with me over the years. Finally, I would like to thank my advisor, Mike Naughton. Mike opened a window of opportunity for me at a moment of uncertainty in my career. It inspired a profound sense of loyalty in me. This research topic was totally new for me when I started, and if it wasn't for your repeated moments of trust in me, for your wise guidance, and for your scrupulous review of our results, I never could have made it through. Thank you.

For Julian

List of Figures

Figure 2.1: Cylindrical coordinates defined. 9

Figure 2.2: Graphical statement of the focusing problem. 13

Figure 2.3: Airy's PSF. 17

Figure 2.4: Numeric steps in the angular spectrum method. 19

Figure 2.5: Visual comparison of paraxial *vs*. nonparaxial PSF's. 20

Figure 2.6: Characteristics of a nonparaxial PSF. 21

Figure 2.7: Higher-resolution rendering of a nonparaxial PSF. 22

Figure 2.8: Parametric study part 1, varying α 24

Figure 2.9: Nonparaxial resolution limits. 27

Figure 2.10: Parametric study part 2, varying n. 28

Figure 2.11: Transverse spectral width for nonparaxial focusing. 32

Figure 3.1: Tightly focused laser spots in a high magnification imaging system. 39

Figure 3.2: Paraxial laser beam parameters. 41

Figure 3.3: Two low-order LG modes, a Gaussian and a right-handed donut. 43

Figure 3.4: Time evolution of a donut beam. 45

Figure 3.5: Electric field components of a paraxial, $\hat{x}$-polarized Gaussian beam. 52

Figure 3.6: Electric field components of a paraxial, $\hat{\rho}$-polarized donut beam. 56

Figure 3.7: Picture of the donut module. 57

Figure 3.8: Tightly focused vortex and polarimetric imaging schematic. 58

Figure 3.9: Encoded, motorized rotation mount. 60

Figure 3.10: Brewster's reference for absolute AOLP. 63

Figure 3.11: Image-shift correction in a division of time polarimeter. 65

Figure 3.12: Polarimetric imaging - HSV color fusion. 67

Figure 3.13: Near-field scanning optical microscope. 70

Figure 3.14: Optical constants for Ag, Al, Au, and Cu. 73

Figure 3.15: SP dispersion on a planar metal/Al_2O_3 interface. 74

Figure 4.1: First two coaxial modes, TEM and TE_{11} 79

Figure 4.2: TEM mode of a PEC/Al_2O_3 coax. 83

Figure 4.3: TE_{11} mode of a PEC/Al_2O_3 coax. 88

Figure 4.4: Matching LG_p^l beams to PEC coax modes. 91

Figure 4.5: Summarizing the effects of metallic loss on nanocoaxial waveguides. 94

Figure 4.6: Molding μm-scale coaxial structures with molten metal. 100

Figure 4.7: Fabricating out-of-plane, μm-scale coaxes. 103

Figure 4.8: In-plane μm-scale coaxes requiring multi-layer patterning. 105

Figure 4.9: Ag nanowires as 1D plasmonic waveguides. 108

Figure 4.10: Oxidized metal nanocoax fabrication. 111

Figure 4.11: Anodized coax, electrochemical setup. 113

Figure 4.12: Nanocoaxial waveguides from single crystal Ag NWs. 116

Figure 4.13: Horizontal Pt/Al_2O_3 nanocoaxes on suspended Si_3N_4 beams. 119

Figure 4.14: Optical constants of ALD Pt and Al_2O_3 123

Figure 4.15: Adhesive bonding and optical access to the horizontal ALD nanocoax. .. 126

Figure 4.16: Fabrication of vertical nanocoaxes by ALD: overview. 128

Figure 4.17: Oxide growth details 133

Figure 4.18: Conformal ALD into high AR nanoholes. 137

Figure 4.19: Ni-for-Si substitution by excavation and electroplating. 139

Figure 4.20: Optical constants of Ni and Si. 140

Figure 4.21: Adhesive wafer bonding. 142

Figure 4.22: Optical constants for SU-8 and sodalime glass. 143

Figure 4.23: Backside thinning of Si bonded to glass. 145

Figure 4.24: Back-side thinned nanocoaxes. 147

Figure 4.25: Donut transmission through nanocoaxes, polarimetric imaging. 149

Figure 4.26: NSOM scan of donut transmission by a heptamer of nanocoaxes. 151

Figure 4.27: Finite element model definition. 153

Figure 4.28: 2D-Axisymmetric simulation: overview. 156

Figure 4.29: Fabry-Perot tuning of the finite element modeled taper. 159

Figure 4.30: Focal shift tuning for a finite-port input beam. 161

Figure 5.1: Optical confinement in the nanocoax. 164

Figure 5.2: Ridgeline detection. 165

Figure 5.3: 3D NCOM from FIB-milled, template-stripped Ag on epoxy pyramids. ... 167

Figure 5.4: 2D NCOM by corralling Ag NW. 168

Figure 5.5: Proposed taper coaxial fabrication scheme. 170

List of Tables

Table 2.1: Logarithmic approach of Debye's transverse resolution. 26

Table 2.2: Moments of Debye's power spectral density. 31

Table 2.3: Comparison of paraxial *vs*. nonparaxial resolution criteria. 36

Table 4.1: LG_p^l beam to coaxial waveguide mode overlap: large coaxial diameters. 92

Table 4.2: LG_p^l beam to coaxial waveguide mode overlap: small coaxial diameters. ... 93

Table 4.3: Confinement and loss in real metal/Al_2O_3 nanocoaxes. 96

Table 4.4: Vertical nanocoax by ALD, fabrication topologies. 134

Table 4.5: Si abrasion rates for Al_2O_3 lapping films. 144

1 INTRODUCTION

1.1 Problem statement

The ability to confine light into small spaces has driven many revolutionary advances in technology. However free-space light, being an electromagnetic wave, cannot be made substantially smaller than its wavelength λ. This is called the diffraction limit [1]. In broad terms, the problem statement for this thesis is to make nanostructures which confine light to smaller scales than the diffraction limit would otherwise allow.

1.2 Motivation

Any imaging system which can beat the diffraction limit is called super-resolving. Super-resolution imaging has revolutionized many fields of science and engineering. To give some contemporary context, I point to Moore's law which says that the number of transistors on an integrated circuit doubles every two years. This progress is largely driven by technical advances that yield ever finer lithographic resolution. There is a lesser known corollary to Moore's law called Rock's law, which says the cost of fabricating those integrated circuits also grows exponentially, doubling every four years. This growth is in no small part driven by the R&D costs of developing those new nanolithography processes, part of which is the super-resolving imaging tool itself. In 2018 the revenues generated by companies which make those lithographic imaging tools exceeded $14 billion. The point is that even within the niched context of developing new lithography tools for the semiconductor industry, and furthermore even only considering the types of tools which are used by high volume manufacturers within that industry, even in that narrow setting

there is still an enormous economic driver. But the impact of super-resolution imaging systems reaches far beyond that limited context, one need look no further than the sea-change it brought to the life sciences. In a broader sense, the utility of super-resolution imaging systems to the world could hardly be overstated.

There are a wide variety of super-resolution techniques used to beat the diffraction limit. This work uses an already well-established technique, which is to confine light in a metal-insulator-metal (MIM) waveguide [2], which substantially reduces the scope of the above problem statement. I have made specifically MIM nanostructures. This MIM approach is motivated by a simple phenomenon: that the fundamental mode of any multiconductor waveguide can be made *arbitrarily smaller* than λ, provided that the metal and insulator constituents behave materially as their names suggest. This is because multi-conductor waveguides always have at least one TEM-like fundamental mode [3], where TEM means transverse electromagnetic. One could say this phenomenon is a topologically robust feature: two or more conductors can sustain DC excitations, for example in the form of an electrostatic separation of charge, or in the form of magnetostatic supply and return currents. Such bipolar DC excitations are not possible on any single-conductor system, they instead decay as transients. For finite frequencies above DC, therefore also with a finite λ, the waveguide behavior of the fundamental TEM-like mode is described by the *quasistatic* limit. But for higher-order modes, the wave can only propagate for sufficiently short λ, a phenomenon known as cut-off. All higher order modes above the fundamental are subject to cutoff.

The motivation for this work is also furnished by the *scale invariance* of electromagnetism. While waveguides are most typically used to channel RF energy

$(f < 100\ \text{GHz})$, where f is the frequency, they function in essentially the same manner when channeling optical energy, even for photon energies up to the ultraviolet $(f < 800\ \text{THz})$. However, in order to operate a waveguide at 1000 times faster frequencies, roughly speaking, it must be minified by a corresponding factor of 1000. Applying the lessons learned from conventional RF waveguide engineering into the optical domain requires modern fabrication procedures to make nano-sized structures. There are, of course, important detailed differences between waveguide behaviors in these two frequency ranges, as will be discussed later in this thesis. But their essential operation is not different. And from a historical perspective, many of the limitations overcome in optical MIM waveguide research have been due to innovative fabrication and excitation schemes which simply have no analog in the RF domain. Among the common RF waveguide topologies, only the coaxial cable [4] totally encloses the insulating space, thus eliminating fringe/stray fields. Early theoretical predictions [5] and experimental observations [6]–[9] have demonstrated transmission at visible frequencies through sub-μm coaxial MIM structures.

1.3 Application areas

The nanocoax has numerous photonics applications, including color filters [10], [11], optical tweezers [12], negative index metamaterials [13], fiber-terminating lenses [14], [15], super-resolution imaging [16], scanning Raman probes [17], and lasers [18], [19], to name a few. And while the action of a metal in this context can be mimicked by an all dielectric photonic crystal [20], it is important to note that there are caveats attached to

this mimicked behavior, and for the most general set of physical conditions only a true MIM waveguide can facilitate these phenomena.

1.4 Organization of this thesis

Since the aim of this work is to confine light to sub-diffraction-limited scales, this dissertation starts in Chapter 2 by defining in clear terms what is meant precisely by "the" diffraction limit, particularly how the lesser-known effects of wide angle focusing can be understood as a departure from their better-known paraxial counterparts. In Chapter 3, I describe some of the experimental apparatus and methods I used to probe a microscopic device under test. Chapters 2 and 3 lend themselves mostly to the first half of the title for this work, "Optical Confinement …". In Chapter 4 I address the second half of the title, "… in the Nanocoax". There I describe the theoretical foundations of and the experimental progress I have made towards super-resolved nanoconfinement in the nanocoax, and using the foundations established in the earlier Chapters.

2 WIDE ANGLE EFFECTS IN SCALAR FOCUSING

The overall aim of this work is to "beat the diffraction limit". So, having a clearly defined limit is the first logical step. Recent advances in optical microscopy have enabled imaging with spatial resolution beyond the diffraction limit. This limit is sometimes taken as one of several different criteria according to different conventions, including Rayleigh's $0.61\lambda/\mathrm{NA}$, Abbe's $0.5\lambda/\mathrm{NA}$, and Sparrow's $0.47\lambda/\mathrm{NA}$. This Chapter retells our published result [1], where we perform a parametric study, numerically integrating the scalar Kirchhoff diffraction integrals, and we propose *new functional forms* for the resolution limits derived from scalar focusing. The new expressions remain accurate under wide angle focusing, up to $90°$.

In Section 2.1 I provide the motivation for this Chapter and give the familiar paraxial formulae. In Section 2.2 I discuss some mathematical preliminaries to be used throughout this thesis and describe a computational approach for evaluating and analyzing non-paraxial point spread functions. In Section 2.3 I define the focusing problem and summarize some known solutions. In Section 2.4 I quantify the effects of strong focusing by reporting the results of a parametric study, this section accounts for most of my original contribution to the field. And in Section 2.5 I summarize with some key takeaways which elude to similar trends in electromagnetic focusing, and I describe some potential application of the scalar results discussed in this Chapter. Our results could materially impact the design of high intensity focused ultrasound systems and can be used as a qualitative guideline for the design of a particular type of planar optical element: the flat lens metasurface.

2.1 Motivation

The role of diffraction in imaging systems has been studied since the days of Airy [21], Abbe [22], [23], and Rayleigh [24]. Textbook theory [25]–[29] says that conventional optical microscopes cannot resolve spatial features finer than approximately half the wavelength of light, $\lambda/2$. Pushing beyond the diffraction limit, near-field techniques based on scanning probe and plasmonic technologies collect information present *only* in evanescent waves [30], [31]. Far-field techniques based on fluorescence microscopy [32], [33] beat the diffraction limit with *a priori* information about the positions of fluorescent molecules (or about their concentration). Far-field super-resolution has even been demonstrated for non-fluorescent specimens, for example by using a super-oscillatory lens [34]. With this context, the motivation for the present work is to reexamine the textbook resolution limits of a conventional optical microscope:

$$d_x = \chi \frac{\lambda}{\mathrm{NA}} \tag{2.01}$$

$$d_z = \zeta \frac{\lambda n}{\mathrm{NA}^2} \tag{2.02}$$

d_x and d_z are, respectively, the minimum transverse and longitudinal separations between two "barely resolved" point sources, α is the half angle subtended by the objective lens, n is the refractive index of the immersion medium, and $\mathrm{NA} = n \sin\alpha$ is the numerical aperture. The numerical factors χ and ζ take on different values with different definitions of "barely resolved". For example, $\chi \approx 0.61$ according Rayleigh, $\chi = 1/2$ according to Abbe, and $\chi \approx 0.47$ according to Sparrow (see page 474 of [25]); some sources [35] use $\zeta = 2$, while others [36] use $\zeta = 1.4$. Although the different numerical

values stem from important conceptual differences, we present them here succinctly in order to highlight the common , carried by NA^{-1} and NA^{-2}.

There is an expansive body of work on the theory, computation, and experiments within the focal region, including textbooks [37] as well as volumes of journal articles that deal exclusively with the electromagnetic [38] and scalar [39] aspects of focusing. In broad terms, scalar and electromagnetic theory give the same result to within 5% for angles up to $\alpha \sim 50°$. For example, figure 8 of [40] shows less than a 1% difference for $\alpha < 30°$. For strong focusing (*i.e.* 'wide angle', $\alpha > 50°$), polarization effects become increasingly important, see in particular figures 7 and 8 of [41].

While those polarization effects certainly cannot be ignored for optical confinement, the scope of this work was restricted intentionally to scalar theory. As such, our results have limited *quantitative* applicability to high-NA optical microscopy, where objective lens angles can approach $\alpha \sim 70°$. For a detailed discussion of polarization effects, we refer the interested reader to the works cited in [38], Chapters 3 and 4 of [29], or Chapters 15 and 16 of [37]. However, scalar theory is often used as a *qualitative* guideline in the design of new optical elements [42], [43], and furthermore our scalar results can be applied quantitatively to the focusing of waves other than light, for example in high intensity focused ultrasound [44]. With our numerical results we quantify the effects of wide angle focusing in a way that has not been previously reported, and our novel analytic formulae retain an accurate α-dependence (within scalar theory) beyond the paraxial limit.

2.2 Theoretical foundation

For the entirety of this thesis, I will consider monochromatic wave propagation and follow the physics convention for the $\pm$ signs in the complex exponentials, and I will only consider physical systems which bear separable solutions. A harmonic scalar wave u is

$$u = u(\mathbf{r},t) = u(\mathbf{r})\left(Fe^{-i\omega t} + Be^{+i\omega t}\right) \tag{2.03}$$

where $\omega = 2\pi f > 0$ is the frequency, and the coefficients F and B describe waves propagating "forward" and "backward" in time, respectively. Without any loss of generality, one can set $F = 1$ and $B = 0$, so that, going forward in this thesis, "a harmonic time dependence" means explicitly

$$u(\mathbf{r},t) = u(\mathbf{r})e^{-i\omega t}. \tag{2.04}$$

2.2.1 Wave mechanics in cylindrical coordinates

I will also only consider physical systems with axial symmetry, and therefore will work in cylindrical coordinates $\mathbf{r} = (\rho,\phi,z)$, as depicted in Figure 2.1. Because of the continuous rotational symmetry, all wave equation solutions have following angular dependence:

$$u(\mathbf{r}) = u(\rho,z)\left(Re^{-il\phi} + Le^{+il\phi}\right) \qquad l = 0, 1, 2,\ldots \tag{2.05}$$

The positive integer l gives the angular order of the solution, and the coefficients R and L describe a harmonic wave which circulates in a clockwise or counter-clockwise fashion about the z-axis, respectively. For a wave which propagates forward along the $+\hat{z}$ direction, these coefficients also correspond to a right- and left-handed helicity, respectively.

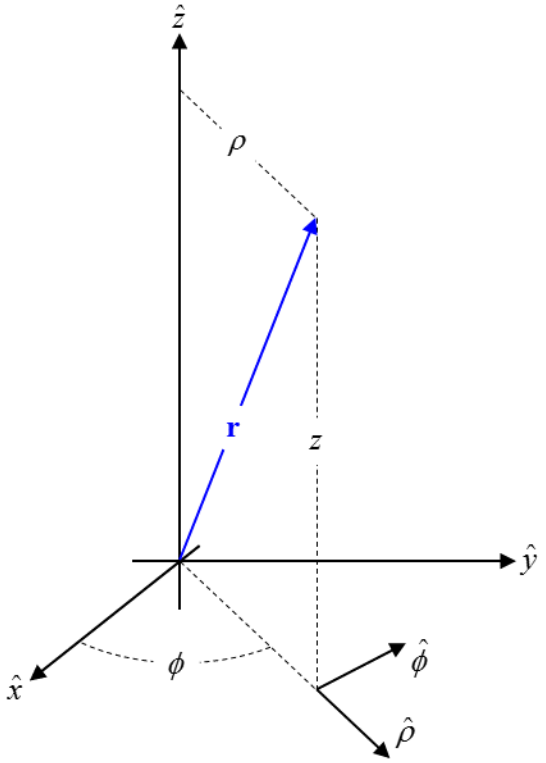

Figure 2.1: Cylindrical coordinates defined.

2.2.2 Cardinal directions

Figure 2.1 shows that the unit vectors in Cartesian and cylindrical coordinates are related by rotation about $\hat{z}$.

$$\begin{bmatrix} \hat{\rho} \\ \hat{\phi} \\ \hat{z} \end{bmatrix} = \mathbf{R} \begin{bmatrix} \hat{x} \\ \hat{y} \\ \hat{z} \end{bmatrix} \tag{2.06}$$

$$\mathbf{R} = \begin{bmatrix} \cos\phi & \sin\phi & 0 \\ -\sin\phi & \cos\phi & 0 \\ 0 & 0 & 1 \end{bmatrix} \qquad \mathbf{R}^{-1} = \begin{bmatrix} \cos\phi & -\sin\phi & 0 \\ \sin\phi & \cos\phi & 0 \\ 0 & 0 & 1 \end{bmatrix} \tag{2.07}$$

As will become clear in Sections 0 and 0, these unit vectors can be used to establish some physically meaningful cardinal directions. The "natural ways" of pointing at something in a rectilinear coordinate system are left, right, front, back, up, and down. But in a circular

coordinate system, these are somewhat foreign concepts. Perhaps a more "natural way" to point at something would involve a clockwise (CW) or counterclockwise (CCW) rotation, much like a navigational heading. Cylindrical waves swirl in exactly that rotational fashion. In the context of polarization optics, see Chapter 3, the cardinal directions are used as Jones vectors. The most common way of writing the right- and left-handed unit vectors is

$$\hat{R} = \frac{1}{\sqrt{2}}\left(\hat{x} - i\hat{y}\right) \tag{2.08}$$

$$\hat{L} = \frac{1}{\sqrt{2}}\left(\hat{x} + i\hat{y}\right) \tag{2.09}$$

But with Equations (2.06) and (2.07) in mind, these should be cast into polar coordinates

$$\hat{R} = \frac{e^{-i\phi}}{\sqrt{2}}\left(\hat{\rho} - i\hat{\phi}\right) \tag{2.10}$$

$$\hat{L} = \frac{e^{+i\phi}}{\sqrt{2}}\left(\hat{\rho} + i\hat{\phi}\right) \tag{2.11}$$

Note that these directions have an intrinsic ϕ-dependence, tantamount to setting $l = 1$ in Equation (2.05).

2.2.3 Angular spectrum method

The angular spectrum method is technique for modeling wave propagation through homogeneous media, wherein one uses Fourier analysis to decompose a wave $u(\mathbf{r})$ into its spatial frequency spectrum $U(\mathbf{k})$. The mathematical details of this technique can be found elsewhere [27], but the necessary parts are summarized in this section. For physical systems with rectilinear (*i.e.* Cartesian) symmetry, it is natural to expand in a basis of sines and cosines. For systems with axial symmetry, such as in this thesis, the natural basis are

cylindrical waves, where the radial dependence comes from Bessel's functions. In cylindrical coordinates, one generally uses the Hankel transform, as given by Equations (2-22) and (2-23) in [27]. In this Chapter I will only consider wave solutions of the lowest angular order (*i.e.* without angular variation), so I set $l = 0$ and $R = L = 1/2$ in Equation (2.05). The Hankel transform is then reduced to the Fourier-Bessel transform (FBT)

$$U\left(k_\rho\right) = \int_0^\infty d\rho \left\{ \rho \mathrm{J}_0\left(k_\rho \rho\right) u\left(\rho\right) \right\}, \tag{2.12}$$

and the inverse transform (iFBT)

$$u\left(\rho\right) = \int_0^\infty dk_\rho \left\{ k_\rho \mathrm{J}_0\left(k_\rho \rho\right) U\left(k_\rho\right) \right\}. \tag{2.13}$$

k_ρ is the radial component of the wavevector $\mathbf{k}$

$$\mathbf{k} = k_z \hat{z} + k_\rho \hat{\rho}, \tag{2.14}$$

and $\mathrm{J}_l\left(x\right)$ is a Bessel function of the first kind, order l. The action of the angular spectrum method is to propagate the wave from an input surface, say the plane $z = 0$, to an output surface, say some plane $z > 0$, with the wave fields in the two surfaces being connected by a transfer function. While in direct-space this connection is a convolution, in reciprocal-space the connection is a simple multiplication, so propagating the wave can be carried out by evaluating the sequence of transforms

$$u\left(\rho, z\right) = \mathrm{iFBT}\left[\exp\left(ik_z z\right) \mathrm{FBT}\left[u\left(\rho, 0\right) \right] \right], \tag{2.15}$$

where $\exp\left(ik_z z\right)$ is the transfer function connecting two $z = \text{const}$ planes.

As indicated in Equations (2.01) and (2.02), I consider a homogenous, isotropic, lossless medium with refractive index n, so that the wavelength in that medium is λ/n. For far-field waves, the magnitude of $\mathbf{k}$ is fixed,

$$|\mathbf{k}| = nk = \frac{2\pi n}{\lambda}, \tag{2.16}$$

where k is the vacuum wavenumber. One uses Equations (2.14) and (2.16) to find k_z,

$$k_z = \sqrt{(nk)^2 - k_\rho^2}\,. \tag{2.17}$$

From Equation (2.17), one can see a sort of threshold which separates the near-field from the far-field. If the input wave u contains rapid spatial variations on length scales shorter than λ/n (*e.g.* at the abrupt truncation by a hard edge), then the resulting spectral components U with spatial frequencies k_ρ larger than nk are propagated by a purely imaginary k_z. Those rapid variations are thus evanescent, trapped in the near-field. Propagating waves must satisfy Equation (2.16).

2.3 Statement of the focusing problem

Consider an infinitely thin, aplanatic flat lens which transforms monochromatic, axial, plane waves into converging spherical waves, truncated abruptly by a circular aperture, as shown in Figure 2.2. The truncated waves are commonly referred to as 'spherical caps' due to their resulting shape. Using Kirchhoff's approximation [45] for the aperture boundary condition, the spherical caps emerge from the lens (at the $z = 0$ plane) with a wave function u of the form:

$$u_{sphere} = u_{sphere}(\rho)$$
$$= \sqrt{I_{plane}}\, f \exp(inkf) \frac{\exp(-inkr)}{r} \text{tophat}\left(\frac{\rho}{a}\right) \tag{2.18}$$

$$r = \sqrt{\rho^2 + f^2} \tag{2.19}$$

$$\text{tophat}(x) = \begin{cases} 1 & 0 \le x < 1 \\ 0 & 1 \le x \end{cases} \tag{2.20}$$

where a is the aperture radius, f is the focal length, I_{plane} is the input plane wave intensity, $\rho = \sqrt{x^2 + y^2}$ is the radial distance in cylindrical coordinates (in this case at the $z = 0$ plane), and r is the distance from the focal point to a point within the aperture. At the origin, where the output spherical cap has the same amplitude and phase as the input plane wave, the flat lens has a transmission coefficient of unity.

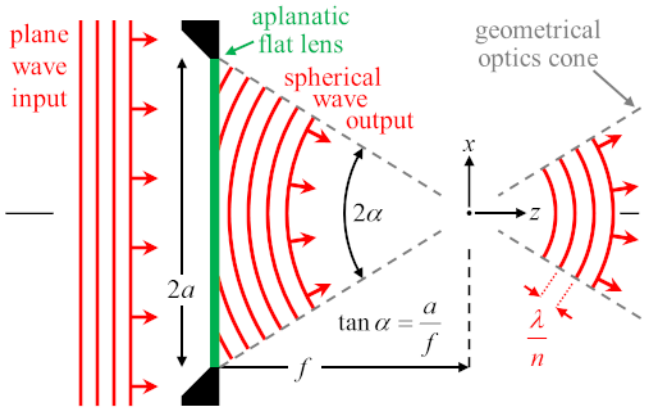

Figure 2.2: Graphical statement of the focusing problem. Taken with permission from the authors of [1]. The aplanatic flat lens, given a plane wave input, transmits converging spherical wave output. Truncated abruptly by the lens' aperture, the spherical waves are referred to as "caps". As the caps propagate through the focus, they flip their curvature from converging to diverging. Also drawn, for reference, is the geometrical optics cone, which is the solid angle subtended by the lens aperture.

It is known that Equations (2.01) and (2.02) are valid only under paraxial $\left(\sin\alpha \approx \alpha\right)$, large N_F focusing, where N_F is the Fresnel number:

$$N_F = \frac{a^2 n}{f\lambda}. \tag{2.21}$$

2.3.1 Analytic solutions

For axial points, given by $\rho = 0$, the diffraction integrals can be evaluated exactly [46]–[50], and from the exact solution there are two important observations: first, the z-position of peak intensity is shifted toward the lens, $z_{peak} < f$; and second, the intensity distribution generally does not have inversion symmetry about any $z = \text{const}$ plane. The focal shift [51]–[55] is a robust feature for any coherent, converging wave [56], and inversion symmetry emerges for lenses with sufficiently large N_F [57]. For off-axis points, given by $\rho > 0$, the diffraction integrals cannot be evaluated exactly. Analytically approximate solutions [58]–[60] typically employ the Debye approximation [28], [37].

2.3.1.1 Debye's approximation

A detailed mathematical overview of Debye's approximation can be found elsewhere [37], specifically Chapter 12. I summarize here as follows: Debye's approximation only considers the waves which propagate within the geometrical optics cone subtended by the lens. This contrasts with Kirchhoff's approximation, which considers waves diffracted in all directions, including outside of that cone. It is natural to wonder how the lens could produce a wave outside of that cone. The answer lies in the "boundary diffracted waves" [61] (BDW). These BDW are scattered in all directions, due to the diffraction at the hard edge along the rim of the lens aperture. The basic idea behind Debye theory is that for a

sufficiently large lens, where the size of the lens is quantified by N_F, that these BDW form a negligible component of the focal field in proportion to those transmitted by the interior clear aperture of the lens, far away from the rim. One of the key differences in the physics between Debye's add Kirchhoff's formulations is whether to include the contribution from BDW.

2.3.1.2 Paraxial limit

Combining the paraxial limit with Debye's approximation is the scope of Fraunhofer diffraction, which yields the seminal result of Airy [21]. In the focal plane, this is

$$\left(z = f\right) \quad \rightarrow \quad u_{Airy} = -2i\sqrt{I_{peak}}\,\mathrm{jinc}\left(\mathrm{NA}\,k\rho\right), \tag{2.22}$$

and for points along the z-axis

$$\left(\rho = 0\right) \quad \rightarrow \quad u_{Airy} = -i\sqrt{I_{peak}}\exp\left(i\pi\frac{z-f}{\Delta z}\frac{4-\alpha^2}{\alpha^2}\right)\mathrm{sinc}\left(\pi\frac{z-f}{\Delta z}\right). \tag{2.23}$$

I_{peak} is the peak intensity,

$$I_{peak} = \left(\frac{\mathrm{NA}ka}{2}\right)^2 I_{plane}, \tag{2.24}$$

Δz is the paraxial depth of focus,

$$\Delta z = \pi\frac{4n}{\mathrm{NA}^2 k} = 2\frac{\lambda n}{\mathrm{NA}^2}, \tag{2.25}$$

and the functions jinc and sinc are given by

$$\mathrm{jinc}\left(\rho\right) = \frac{\mathrm{J}_1\left(\rho\right)}{\rho} \qquad \mathrm{sinc}\left(z\right) = \frac{\sin z}{z}. \tag{2.26}$$

The wave's intensity distribution is the square modulus of the amplitude. For the system sketched in Figure 2.2, the focal intensity distribution is equivalently called the point spread function (PSF),

$$\mathrm{PSF} = I = |u|^2 . \tag{2.27}$$

Equations (2.22) and (2.23) then give a longitudinal line-cut and a transverse slice through Airy's PSF. These are plotted for reference in Figure 2.3.

It is from Equation (2.22) that the Rayleigh criterion is derived, $\chi \approx 0.61$ in Equation (2.01), such that $\mathrm{J}_1(2\pi\chi) = 0$. Similarly, $\zeta = 2$ in Equation (2.02) comes from Equations (2.23) and (2.25), such that $\sin(\pi\zeta/2) = 0$. Note that tophat $\leftrightarrow$ jinc form an FBT pair, and due to the symmetry of swapping $k_\rho \leftrightarrow \rho$ in the FBT, that the forward and inverse transform yield the same result, for example

$$\mathrm{FBT}[\mathrm{tophat}] = \mathrm{i}\,\mathrm{FBT}[\mathrm{tophat}] = \mathrm{jinc}, \tag{2.28}$$

or *vice versa*. This means Airy's spectrum (at the focal plane) is

$$U_{Airy} = \frac{-2i\sqrt{I_{peak}}}{(\mathrm{NA}\,k)^2}\,\mathrm{tophat}\left(\frac{k_\rho}{\mathrm{NA}\,k}\right). \tag{2.29}$$

Along a similar vein, the 1D Cartesian "rectangle" function forms the Fourier pair, rect $\leftrightarrow$ sinc, however the Fourier transform (in a basis of sines and cosines) does not have the same "swapping" symmetry in $k_x \leftrightarrow x$ as the FBT mentioned above. In the context of this thesis, tophat is ever only supplied "radial" arguments, so that it is generally defined over a 2D domain. So unlike rect(), which is a *linear* step function, tophat() is a *circular* step function, and hence the name: it looks much like flat-crowned hat for men traditionally worn with 19th century western formal dress.

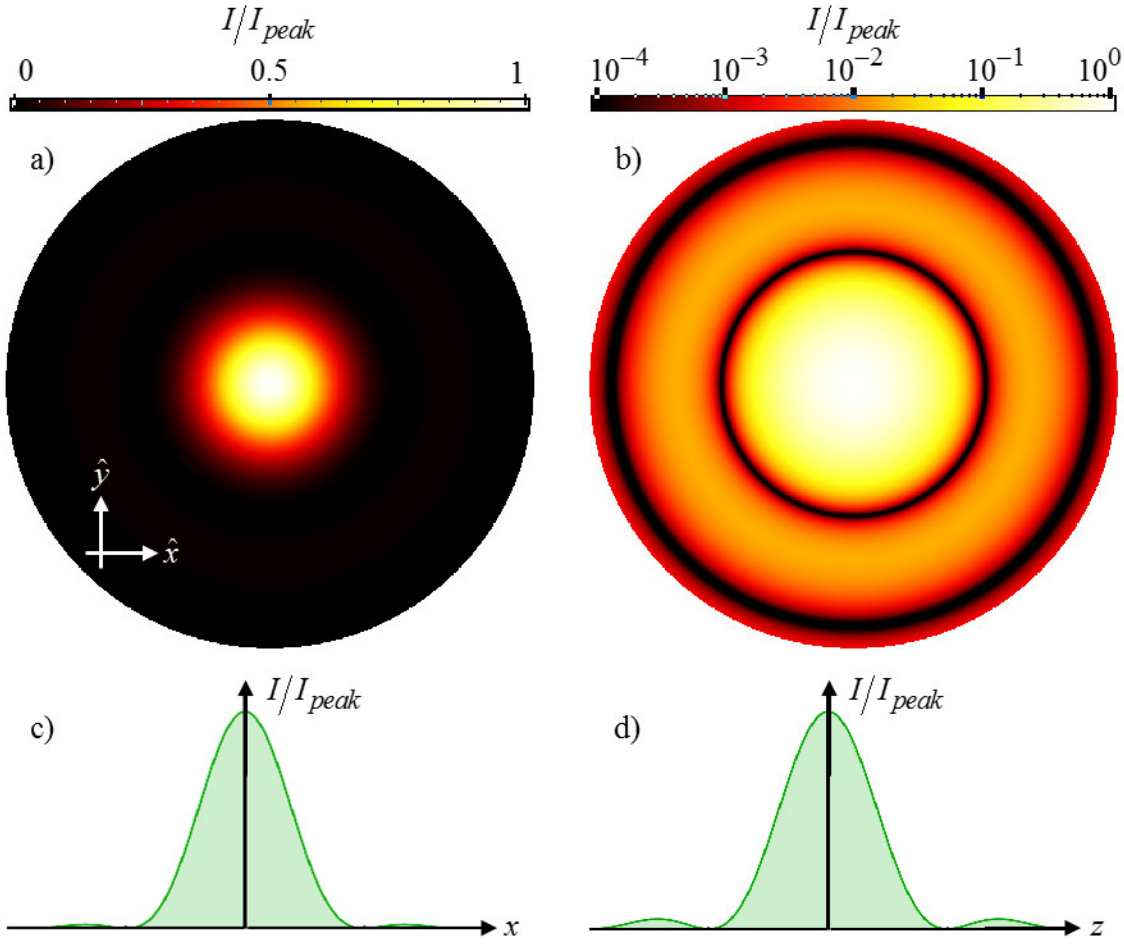

Figure 2.3: Airy's PSF. Transverse slices at the focal plane $(z = f)$ colored (a) linearly and (b) logarithmically. The first dark ring occurs at $\rho \approx 0.61\lambda/\mathrm{NA}$. Line cuts through the focus along the (c) x- and (d) z-axes show the characteristic $\mathrm{jinc}^2(x)$ and $\mathrm{sinc}^2(z)$ dependences.

2.3.2 Numeric solutions

For numerically approximate solutions, the wave at the input plane, $u_{sphere}(\rho)$, is sampled discretely. To compute the wave function in the focal region, one commonly employs the discrete Fourier transform (DFT), wherein the computation is done by either the summation of a discrete summand or by a matrix multiplication. A noncomprehensive selection of DFT implementations can be found in [62]–[65]. In this thesis, I employ direct

numeric integration (DNI), in which the computation is done by numerically integrating a continuous integrand (which is sampled recursively). Although a DFT is generally orders of magnitude faster than a DNI [62], one must take extra care when employing DFT to avoid aliasing [66] and to mitigate errors [67] and artifacts [68] which result from the discrete sampling and tiling.

2.4 Parametric study of nonparaxial focusing

A lens is uniquely specified by three parameters f, a, and n, which are indicated in Figure 2.2, we vary these parameters and numerically integrate both Kirchhoff's and Debye's diffraction integrals to illuminate the trends of nonparaxial focusing.

2.4.1 Numerical methods

All numerical computation is performed using the built-in functionality of commercially available software (Mathematica and MATLAB) running on personal computers. To save time on lengthy calculations, we network several computers together for parallel computation on a grid environment. In total, we have access to 64 processing cores at nominally 3 GHz and 400 GB of local RAM. A sketch of the numeric steps in our computational process are shown in Figure 2.4. In Figure 2.4-a) the input wave u_{sphere} is truncated abruptly by the lens aperture radius, a. Figure 2.4-b) Shows the input spectrum $U\left(k_\rho\right)$. Due to the infinitely sharp edge at the aperture boundary, U contains spatial frequencies larger than what far-field waves could possibly support, nk. Note that in the limit $N_F \to \infty$ (*i.e.* Debye theory), the maximal spatial frequency is NAk, not nk. The spectrum U is computed by FBT over a discrete series of k_ρ-values, sampled densely

enough that aliasing is of no concern. Figure 2.4-c) Shows the action of the free space transfer function (see Equation (2.15)), propagating the wave from the input plane $(z=0)$ to some output plane $(z>0)$. For sufficiently large z, the free space transfer function attenuates the spectral components with spatial frequency larger than nk. A continuous output spectrum is rendered by interpolation (gray curve). Figure 2.4-d) The output wave u is computed over a discrete series of ρ-values by taking the iFBT of the spectrum shown in Figure 2.4-c). Keeping track of the lens parameters, one of the features accounted for by our parametric study is the position of the first transverse zero. For reference, the value $0.61\lambda/\mathrm{NA}$ is shown in Figure 2.4-d). The discrete output wave is also interpolated for further analysis (gray curve).

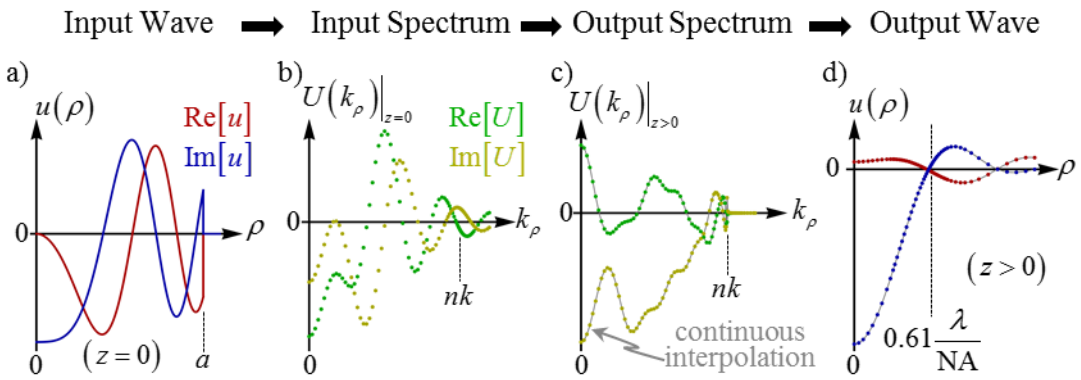

Figure 2.4: Numeric steps in the angular spectrum method. We use Kirchhoff's approximation. (a) The input wave u_{sphere} and (b) input spectrum $U\left(k_\rho\right)$. (c) The output spectrum is obtained by the action of the free-space transfer function. (d) The output wave is computed by iFBT.

2.4.2 Characteristics of a nonparaxial PSF

Figure 2.5 shows a side-by-side, qualitative comparison of PSF's for paraxial and non-paraxial focusing. It illustrates that as the lens angle widens, the side-lobes get proportionately brighter, power is redistributed from the central spot into rings.

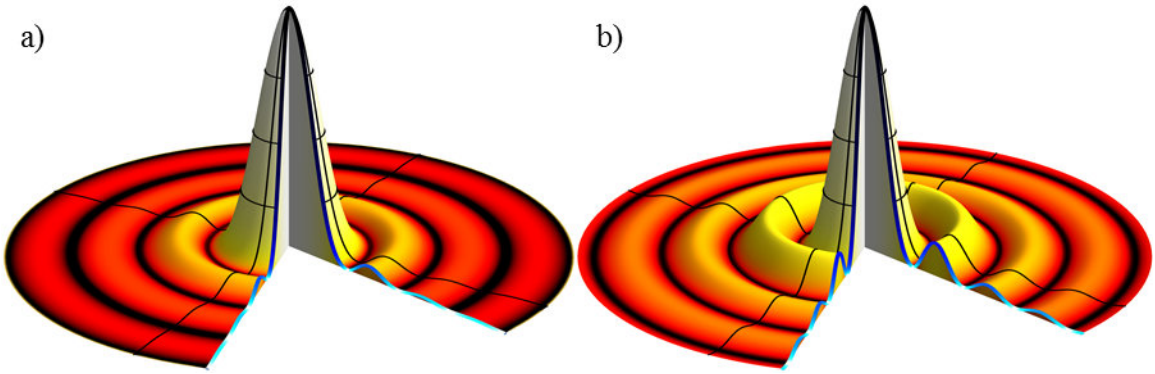

Figure 2.5: Visual comparison of paraxial *vs*. nonparaxial PSF's. (a) Paraxial and (b) Nonparaxial PSF's have some key qualitative differences. Surface plots of a transverse slice in the $z = f$ focal plane, with logarithmic color-scaling and linear surface heights, show how power is redistributed for large focusing angles α.

For a more concrete example, consider a lens with $f = a = 75\lambda$ (so that $\alpha = 45°$) and $n = 1$ (in air). The output wave, plotted in Figure 2.6, has been normalized against its peak amplitude, u_{peak}, and has been computed on a mesh of points within the dashed green boundary. Plotting the PSF on a logarithmic scale in Figure 2.6-b) clearly displays the structure outside of the geometrical optics cone, and isophotes (contours of constant intensity) are drawn at each decade in order to reveal the asymmetry in Kirchhoff's result.

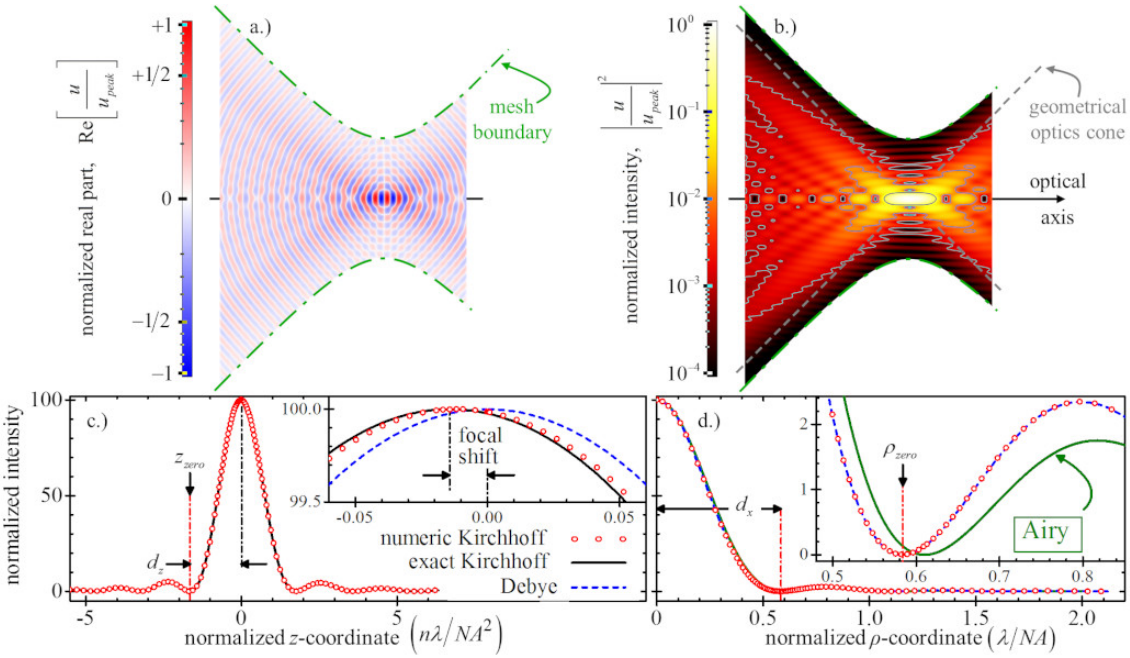

Figure 2.6: Characteristics of a nonparaxial PSF. Taken with permission from the authors of [1]. (a) A plot of $\mathrm{Re}[u]$ shows the wavefronts. (b) A plot of I shows the PSF. (c) Longitudinal and (d) transverse cuts of the PSF are plotted on a 100x scale, and with coordinates normalized using equations (1) or (2). The insets show magnified views of the peak and of the first transverse zero. The numeric result (red circles) are plotted at a reduced density of points for clarity.

A higher resolution version of Figure 2.6-b) (but omitting the geometrical optics cone and using thinner linewidths on the contours) is shown in Figure 2.7. The purpose of showing a high-resolution rendering of the PSF in Figure 2.7 is to highlight the asymmetry in Kirchhoff's result, which owes itself to BDW. Debye's approximation does not include BDW. Note: the lens in Figure 2.7 is positioned vertically above the top part of the figure, with waves propagating in an overall "downward" direction through the PSF. This is rotated 90° clockwise *w.r.t.* Figure 2.6-b), where the lens is on the left-hand side and waves propagate in an overall "rightward" direction. The underlying data are the same, only the resolution and orientation of the rastered image are different. This asymmetry is especially

clear for the isophotes drawn at $10^{-2} I_{peak}$. Note how the 4 pockets on the bottom part of the figure are broken off into 4 separate "islands" of intensity, however the corresponding features on the top part of the figure are merged-in as part of largest contour. There is also a single island on the top part of the figure which is not included within the range of the bottom part.

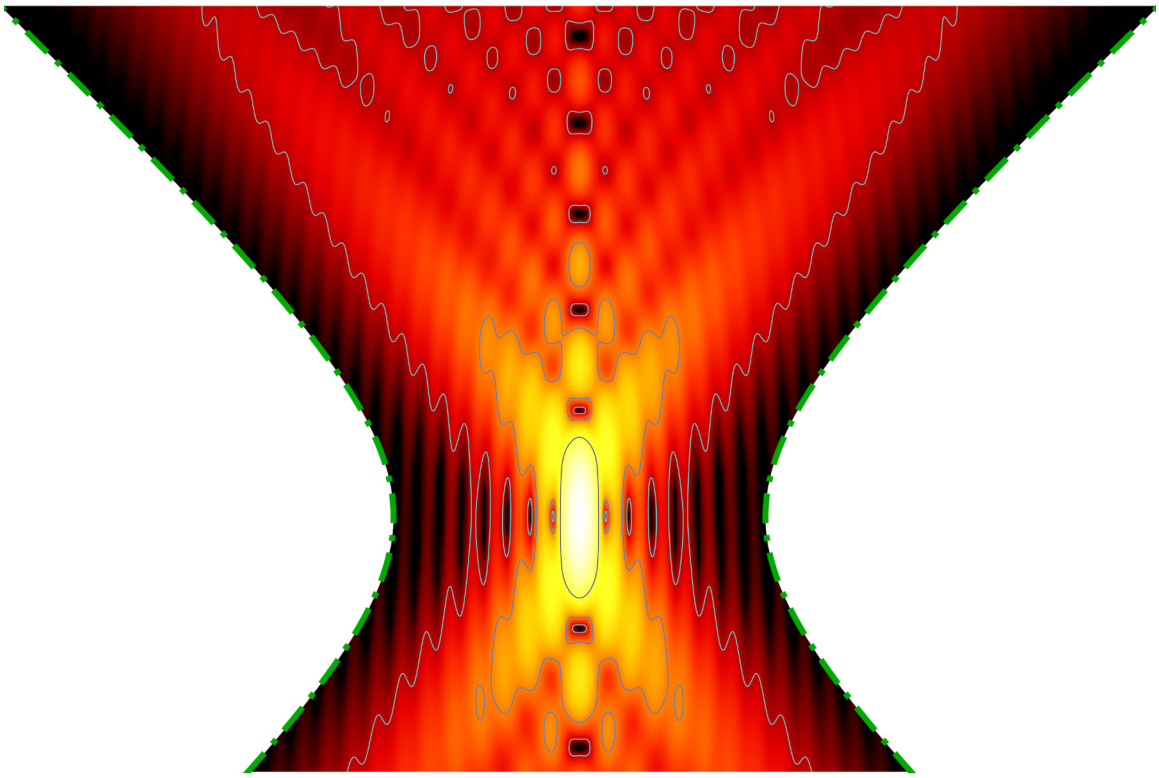

Figure 2.7: Higher-resolution rendering of a nonparaxial PSF. This is an alternate version of Figure 2.6-b), rendered at high resolution specifically to highlight the asymmetry in Kirchhoff's result.

From the nonparaxial PSF, we define the transverse and the longitudinal resolution criteria by the positions of the first zeros in the respective directions ($d_x = \rho_{zero}$ and $d_z = z_{peak} - z_{zero}$). Note that there are many different conventions for how to define the width of the PSF [25]. Also note that since Kirchhoff's result is asymmetric, we always

take the first axial zero towards the lens, which is in the same direction of the focal shift (*i.e.* $-\hat{z}$). We follow the choice of Rayleigh (using the position of the first zero), which is addressed further in Section 2.4.4. For the lens shown in Figure 2.6, where $\alpha = 45°$, and in the parlance of Equations (2.01) and (2.02), we find $\chi \approx 0.58$ and $\zeta \approx 1.65$ (as opposed to the paraxial values $\chi \approx 0.61$ and $\zeta = 2$). We also compute the encircled energy (integrated intensity) in the central spot of the PSF (that is, integrating out to only the first dark ring) at the focal plane $\left(z = z_{peak}\right)$, as a fraction of the total encircled energy at the aperture, E_{spot}/E_{total} . For Airy's PSF, where $\alpha \to 0$, the encircled energy is $E_{spot} = 83.8\%$, but at $\alpha = 45°$ the energy is reduced to $E_{spot} = 77.8\%$. In the inset of Figure 2.6-d) one sees that the side lobes are proportionately brighter at $\alpha = 45°$ than in the paraxial case, as already illustrated qualitatively in Figure 2.5. Thus we recognize two general characteristics of a nonparaxial PSF: first, the central spot is generally 'tighter' than in the paraxial case (smaller χ and ζ); second, energy is redistributed outward from the central spot and into the side lobes.

2.4.3 Results

The general characteristics of nonparaxial PSFs mentioned above have been identified previously, for example see figures 12.7 and 12.11 of [37]. The novel aspect of our work is that we identify *a trend*, tracking these features as we vary the three parameters which uniquely specify a lens $\left(f, a, n\right)$. The criteria $d = d\left(\alpha, n\right)$ in Equations (2.01) and (2.02) are valid only in the paraxial limit, and for nonparaxial focusing they are inaccurate even in their functional form (*i.e.* independent of the choice in χ and ζ). In our numeric study, we analyze the PSFs for ~2,500 sets of unique lens parameters.

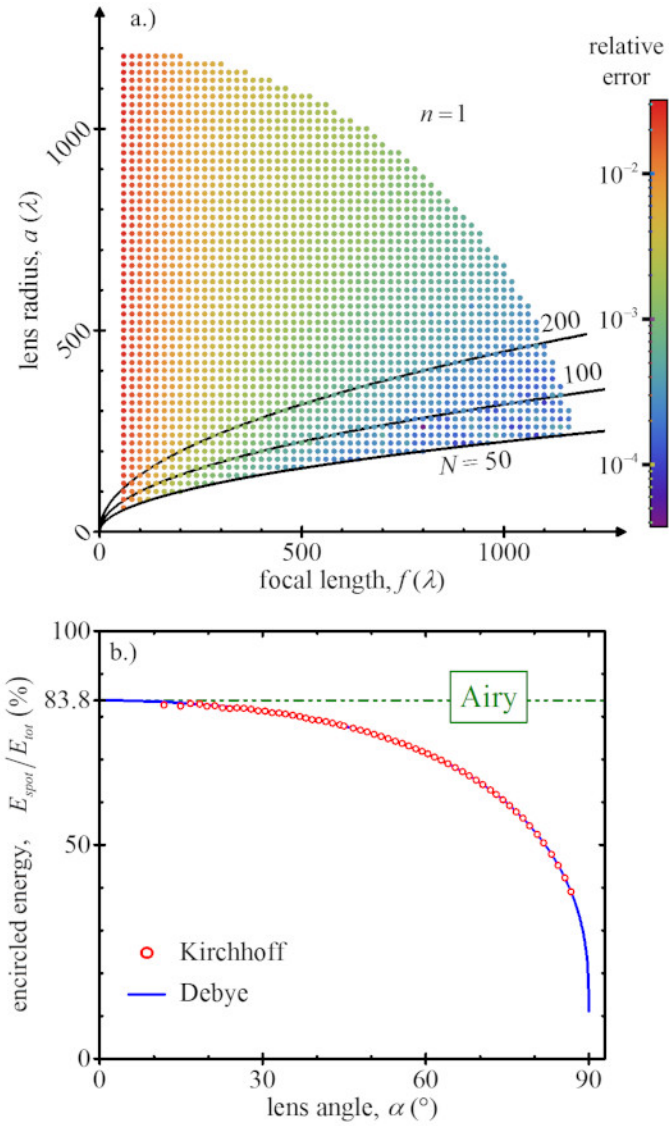

Figure 2.8: Parametric study part 1, varying α. Taken with permission from the authors of [1]. (a) We fix $n=1$ and choose points in the fa-plane. The black curves show different Fresnel numbers, N_F. The relative error is computed by comparing our numerically approximate result against an analytically exact formula. b.) The energy contained in the central spot is plotted *vs.* α, and is expressed as a percentage of the input energy at the aperture. The numeric data in b.) are shown at reduced density for clarity.

The parameters (f, a, n) form a 3D space, and Figure 2.8-a) shows that in the first part of our two-part parametric study, we keep $n = 1$ constant and choose points in the 2D fa-plane. In this plane, α is the clockwise polar angle, just like ϕ in the Cartesian xy-plane drawn in Figure 2.1. For each lens, we compute longitudinal and transverse line-cuts in the PSF, and a relative error is calculated by comparing the longitudinal cut from the numeric result against the analytically exact solution [46]–[50]. Among all of the results, the median relative error is on the order of parts per thousand $\left(10^{-3}\right)$, and we find that this error, which aggregates from the multiple numeric steps of our computational process (including but not limited to those sketched in Figure 2.4), generally can be controlled with a tradeoff in computational time. In Figure 2.8-b) one can see that as $\alpha \to 90°$ and energy gets redistributed outward to the side lobes, the fraction of energy remaining in the central spot falls precipitously to 0.

Two general traits emerge from the ensemble results of our parametric study: first, in the transverse cut of the PSF (at the focal plane), we find good agreement between the direct numeric integration of Kirchhoff's and Debye's theories, as expected [69]–[72] since we have intentionally restricted our study to lenses with $N_F > 50$; second, if we plot some characteristic of the nonparaxial PSF vs. α and take the limit $\alpha \to 0$, then we always recover the result of Airy's PSF, no matter what the characteristic.

Further results from our parametric study are shown in Figure 2.9, where we plot d_x and d_z vs. α. Although the vertical axis in Figure 2.9-a) has been normalized against λ/NA, the data still have a clear, monotonic trend in α. The numeric data (red dots, at reduced density for clarity) are compared against Debye's approximation (blue solid line).

It is therefore evident that Equation (2.01) for d_x has an inaccurate functional form, specifically that NA^{-1} does not give an accurate α-dependence. We observe a similar trend in d_z which is shown in Figure 2.9-b). We show our analytic results (yellow, dashed lines), Equations (2.39) and (2.40), and the black curves (circle, square, and diamond) are from numerical analysis of the exact solution at different Fresnel numbers. The apparent spread in the numerical result in Figure 2.9-b) is not due to the error of our computational process, but rather due to the fact that the 2D fa-plane illustrated in Figure 2.8-a) covers a range of Fresnel numbers. Consistent with the findings of [57]–[60], we observe that Kirchhoff's theory and Debye's approximation agree for sufficiently large N_F. Quite interestingly, the trend in the "constant" χ, shown in Figure 2.9-a), is from Airy's limit $(\chi \approx 0.61)$ down to Abbe's criterion $(\chi = 1/2)$ as α varies from 0 to $90°$, and our numerical results indicate that χ logarithmically approaches $1/2$ as α logarithmically approaches $90°$, as summarized in Table 2.1. Considering that Airy's and Abbe's criteria originate from very different theoretical considerations (Airy's PSF *vs*. Abbe's sine condition), it's especially interesting that there is *any* connection at all.

lens angle $\alpha\,(°)$	**transverse resolution** $\chi_{Debye}\,(\mathbf{dim'less})$
89.9	0.5002653…
89.99	0.5000265…
89.999	0.5000027…
89.9999	0.5000003…

Table 2.1: Logarithmic approach of Debye's transverse resolution. Debye's integrals are evaluated numerically for α logarithmically approaching $90°$, tabulating the position of the first transverse zero in accord with Equation (2.01).

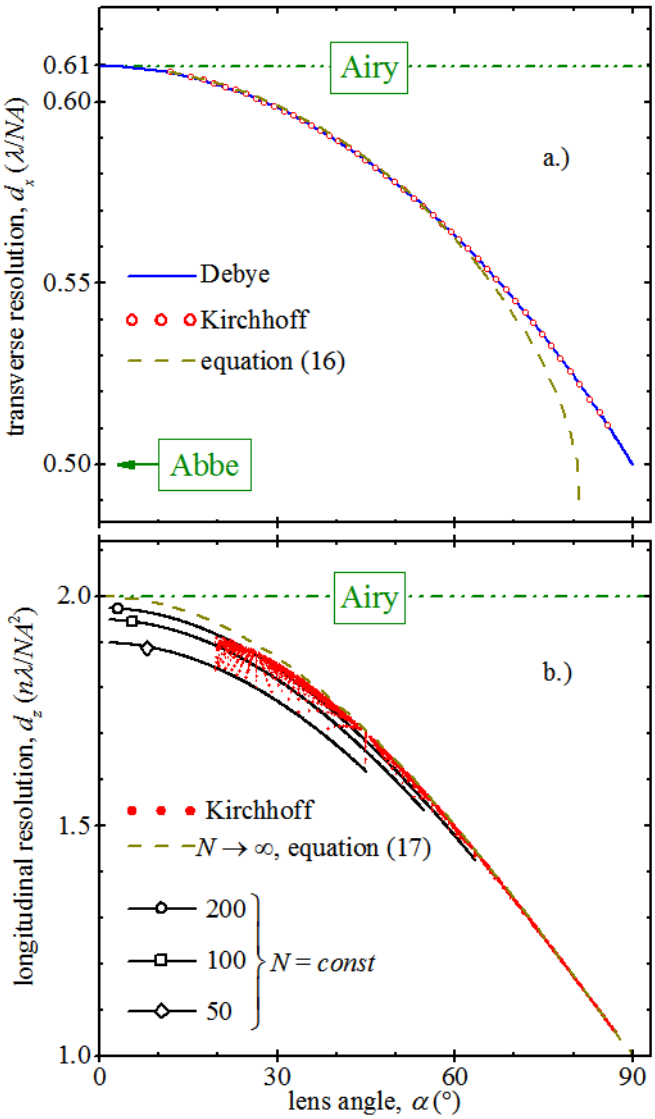

Figure 2.9: Nonparaxial resolution limits. Taken with permission from the authors of [1]. (a) Plotting the normalized transverse resolution d_x vs. α reveals a monotonic trend. (b) There is a similar trend in the longitudinal resolution d_z. Note that the numbering in Figure 2.9, equations (16) and (17), does not point to entries in this thesis, but the corresponding entries in [1].

In the second part of our two-part parametric study, we kept $\alpha = \text{const}$ by choosing several points in the 2D fa-plane illustrated in Figure 2.8-a) and varying n from 1 to 2 while fixing

both f and $\mathbb{d}$. In summary, we observe that Equations (2.01) and (2.02) indeed have the correct dependence on $\mathbb{n}$. For example, plotting the normalized d_x and d_z *vs.* $\mathbb{n}$ yields flat lines, independent of $\mathbb{n}$ and α, meaning that the accurate n-dependence is n^{-1}. Plots of d_x *vs.* $\mathbb{n}$ for a few values of α are shown in Figure 2.10. Taken together, parts 1 and 2 of our parametric study indicate unambiguously that the resolution criteria are accurately expressed as:

$$d_j(\alpha,n)=\frac{\lambda}{n}F_j(\alpha)\cdot \tag{2.30}$$

where $F_j(\alpha)$ is some function of α, and j is either x or z.

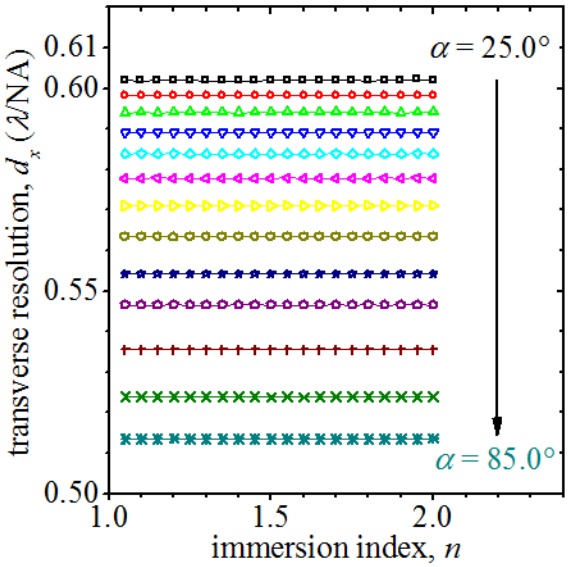

Figure 2.10: Parametric study part 2, varying n. A similar plot is obtained for d_z *vs.* $\mathbb{n}$, flat lines which are independent of both $\mathbb{n}$ and α. This means unambiguously that n^{-1} is the correct n-dependence.

2.4.4 Discussion

It makes intuitive sense that that the d_j in Equation (2.30) carry an n^{-1} dependence; after all, λ/n is the wavelength and therefore the only possible choice of length scale for oscillations in $u(\mathbf{r})$. This is essentially the same reasoning which motivates Equation (2.16). To find the correct α -dependence, we perform spectral analysis.

2.4.4.1 Transverse resolution

Starting with the transverse resolution, d_x, and following the same approach used in [73], [74], the natural choice for $F_x(\alpha)$ is to take the inverse of the spectral width, $(\Delta k_x)^{-1}$. Using Debye's approximation (see Ch. 12 of [37]), one can write down an expression for the spectrum at the focal plane $z = f$

$$U_{Debye} = \frac{-i\sqrt{I_{peak}}}{1-\cos\alpha} \frac{\text{tophat}\left(\dfrac{k_\rho}{\text{NA}\,k}\right)}{nk\sqrt{(nk)^2 - k_\rho^2}}. \tag{2.31}$$

Equation (2.31) is naturally compared against its paraxially limiting form, Airy's spectrum, which is given in Equation (2.29). To find Δk_x, one must normalize the square modulus of a spectrum $|U|^2$ (*i.e.* the power spectral density) against the total power, thus rendering a probability density function in reciprocal space. From Plancherel's theorem, the total power must be $P = \pi a^2 I_{plane}$. This theorem was already used to derive Equation (2.24), which relates I_{peak} to I_{plane} (*i.e.* the paraxial intensity enhancement). It must be noted

that Equation (2.24) is valid only for Airy's spectrum, *i.e.* in the paraxial limit. For Debye's spectrum, one must integrate

$$P_{Debye} = \frac{2\pi I_{peak}}{\left(nk\left(1-\cos\alpha\right)\right)^2}\int_0^{\sin\alpha} d\beta \frac{\beta}{1-\beta^2}, \tag{2.32}$$

using the integration variable $\beta = k_\rho / nk$. The integral in Equation (2.32) evaluates to $\ln\left(\sec\alpha\right)$. Debye's intensity enhancement, which is the non-paraxial, large N_F limit for Equation (2.24), is therefore:

$$I_{peak} = \frac{\left(nka\left(1-\cos\alpha\right)\right)^2}{\ln\left(\sec\alpha\right)} I_{plane}, \tag{2.33}$$

Note that expanding Equation (2.33) as a Taylor series about $\alpha = 0$

$$I_{peak} = \left(nka\right)^2\left(\frac{\sin^2\alpha}{2} - \frac{\sin^4\alpha}{6} + \cdots\right) I_{plane}, \tag{2.34}$$

recovers to leading order Equation (2.24). Equation (2.24) is (and more generally all of the characteristics from Airy's PSF) therefore the paraxial-limiting form of Equation (2.33) (and more generally the corresponding characteristics from Debye's PSF).

To find the spread in momentum, one must compute moments of the probability density function associated with the power spectral density *via* $\Delta k_\rho = \sqrt{\left\langle k_\rho^2 \right\rangle - \left\langle k_\rho \right\rangle^2}$. For Debye's spectrum, Equation (2.31), one must evaluate integrals of the form:

$$\left\langle k_\rho^m \right\rangle = \frac{\left(nk\right)^m}{\ln\left(\sec\alpha\right)}\int_0^{\sin\alpha} d\beta \frac{\beta^{m+1}}{1-\beta^2}, \tag{2.35}$$

where the positive integer m is the order of the moment in the probability distribution, and the integration variable β has the same definition as in Equation (2.32). Indeed one

can inspect Equations (2.32) and (2.35) to see how the total power normalizes the zeroth moment of the probability distribution function to unity. Isolating the α-dependence from Equation (2.35),

$$G_m(\alpha) \equiv \frac{1}{\ln(\sec\alpha)} \int_0^{\sin\alpha} d\beta \frac{\beta^{m+1}}{1-\beta^2}, \tag{2.36}$$

one can tabulate the first few moments of the probability density function associated with Debye's power spectral density; these are given in Table 2.2.

moment order m	**evaluated integral** $G_m(\alpha)$
0	1
1	$\frac{\tanh^{-1}(\sin\alpha)-\sin\alpha}{\ln(\sec\alpha)}$
2	$1-\frac{\sin^2\alpha}{2\ln(\sec\alpha)}$

Table 2.2: Moments of Debye's power spectral density. As described in Section 2.4.4.1, the moments of the probability density function associated with Debye's power spectral density are used to the α-dependence for a transverse resolution criterion similar to Equation (2.01), but valid for non-paraxial focusing. The integral $G_m(\alpha)$ is defined in Equation (2.36).

Next, noting that k_ρ is the radial component of the momentum and examining Figure 2.1 and see $k_\rho = \sqrt{k_x^2 + k_y^2}$, where k_x and k_y are the Cartesian components of the momentum. Interestingly, this is true even in spite of the fact k_ρ sets the length scale for oscillation in the non-periodic Bessel functions, however k_x and k_y set the length scale for periodic oscillations in sines and cosines. Furthermore, as stated in Section 2.2.3, since we seek

solutions to the focusing problem only of the lowest angular order $l=0$, one uses $k_x = k_y$ and notes $\langle k_x \rangle = \langle k_y \rangle = 0$ to write $\Delta k_x = \left(k_\rho\right)_{RMS} / \sqrt{2}$, where "RMS" means keeping only the $m=2$ moment in Δk_ρ, given by the last row in Table 2.2. Finally, one obtains:

$$\Delta k_x = \frac{nk}{2}\sqrt{2+\frac{\sin^2\alpha}{\ln(\cos\alpha)}}. \tag{2.37}$$

To the best of our knowledge, Equation (2.37) has not been previously published. A qualitatively similar expression for Δk_x was obtained using a ray optics approach [73], [74], and both expressions are compared against our numerical result in Figure 2.11.

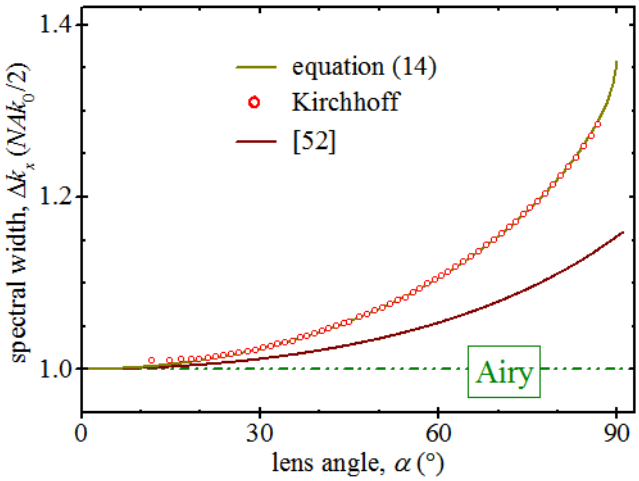

Figure 2.11: Transverse spectral width for nonparaxial focusing. Taken with permission from the authors of [1]. The spectral width Δk_x is plotted *vs*. lens angle α, and normalized against Airy's (paraxial) result, $\mathrm{NA}\,k/2$, which is obtained from Equation (2.29). Our numerical results (red circles), shown at reduced density for clarity, agree well with Equation (2.37) (solid yellow line). A similar result was obtained by [73] (solid maroon line). Note that the numbering in Figure 2.11, equation (14) and reference [52], does not point to entries in this thesis, but the corresponding entries in [1].

It is interesting to note the limits of the radical on the right-hand side of Equation (2.37): at $\alpha \to 90°$ one gets $\sqrt{2}$; and at $\alpha \to 0$ one recovers the result of Airy, $\mathrm{NA}\, k/2$, which can be deduced from Equation (2.29). The latter limit to Equation (2.37) can be seen by expanding in powers of $\sin\alpha$ about $\alpha = 0$, and keeping only the leading order term:

$$\Delta k_x = \frac{nk}{2}\left(\sin\alpha + \frac{\sin^3\alpha}{12} + \cdots\right). \tag{2.38}$$

The radical on the right-hand side of Equation (2.37) can be used to get a *phenomenological* α-dependence for d_x, in the mold of Equation (2.30). However, in order to maintain accuracy when comparing to our numerical result, (*i.e.* the position of the first transverse zero in the PSF at the focal plane, $z = f$ for Debye's result and $z = z_{peak}$ for Kirchhoff's), we include two dimensionless *empirical* parameters in $F_x(\alpha)$, namely χ_0 and b:

$$F_x(\alpha) = \chi_0 b\left(2 + \frac{\sin^2(b\alpha)}{\ln(\cos(b\alpha))}\right)^{-1/2}. \tag{2.39}$$

Fixing $\chi_0 = 0.61$, we find a good fit to our numerical results for $\alpha < 60°$ with $b = 1.11$, which is shown as a dark yellow, dashed curve in Figure 2.9-a).

Regarding the parameters χ_0 and b, we make two comments. The first comment, as pointed out in Section 2.1, is there are several alternative definitions [25] for the transverse width Δx of the PSF. For example, we have used the RMS k_ρ-value to compute Δk_x, but in general the RMS ρ-value of the PSF *cannot* be computed; even for Airy's $\mathrm{jinc}^2(\rho)$, the variance $\langle \rho^2 \rangle$ diverges. For nonparaxial focusing, this divergence only diverges more

rapidly with increasing α. Indeed rendering a probability density function from Airy's PSF using Equations (2.22) and (2.24), one finds that all higher-order moments with $m \geq 2$ diverge. So we have followed the convention of Rayleigh and chosen the positions of the first zeros: ρ_{zero} and z_{zero}. But we could have chosen the half-widths at half maximum, followed Sparrow's criterion, or several different positions instead; the different choices are just different conventions, and we find that the general trends of nonparaxial focusing are insensitive to the convention choice. With a different choice, the trends could equally well be described by a different set of values for χ_0 and b. In all cases, Equation (2.37) can be used to obtain a phenomenological α-dependence.

The second comment: independent of which convention is used to define Δx, the space-bandwidth (SW) product $\Delta x \Delta k_x$ is generally not independent of α. This peculiar feature of u_{sphere} is not present in all types of focused waves. For example, in the focusing of Gaussian beams, as long as the beam waist w at the input plane is much smaller than the lens radius a (*i.e.* an underfilled aperture), the SW-product is always equal to $1/2$, as shown in [75]. In that work, the authors' parametric study showed that the focusing of u_{sphere} and of a Gaussian beam can be thought of as two limiting cases of the truncation ratio w/a (*i.e.* the degree of filling). When juxtaposing results from Kirchhoff's and Debye's formulation, something which is not present in the Debye result, and which can result only from the inclusion of "boundary diffracted waves" (BDW) from the hard edge at the rim of the lens aperture. It is tempting to point to BDW [61] as the culprit responsible for there being an α-dependent SW product. After all, within Kirchhoff's formulation, the

authors of [75] clearly showed that several of the features of a focused u_{sphere} emerge when increasing w/a for a focused Gaussian beam. Surely, it must be the presence of hard-edge diffraction at the rim which is responsible for this difference, no? However, it is also important to realize that an α-dependent SW product also emerges even only within Debye's approximation, which totally neglects the contribution from BDW. BDW therefore could not possibly be the culprit. The main point here is that an α-dependent SW product means that taking $(\Delta k_x)^{-1}$ does not account for the full α-dependence in Δx, and thus we introduce the parameter b to compensate for this.

2.4.4.2 Longitudinal resolution

Next, for the longitudinal resolution d_z, we examine equations 12.21 (a)-(d) of [37] and note that within Debye's approximation, for points along the optical axis, the first zero in the PSF always satisfies:

$$d_z = \frac{\lambda}{n}\frac{1}{1-\cos\alpha}. \tag{2.40}$$

As before, this can be expanded in powers of $\sin\alpha$ to recover the paraxial limit:

$$d_z = \frac{\lambda}{n}\frac{1}{\frac{\sin^2\alpha}{2}+\frac{\sin^4\alpha}{8}+\cdots}. \tag{2.41}$$

Equation (2.40) is plotted alongside the numerical results in Figure 2.9-b), and a nearly identical formula has been reported [73], [74] using a ray-optics approach. In Figure 2.9-b), we also plot a family of curves which result from numerical analysis of the exact solution at different Fresnel numbers ($N_F = 50$, 100, and 200).

2.5 Conclusions

In practice, the resolution limits predicted by our nonparaxial formulae, Equations (2.39) and (2.40) differ by nominally 10 - 30% from the limits predicted by the paraxial formulae, Equations (2.01) and (2.02). Consider an $\mathrm{NA} = 1.4$ oil-immersion objective with $n = 1.52$ at $\lambda = 0.532$ μm, the paraxial and nonparaxial results are tabulated in Table 2.3.

resolution criterion	**paraxial**		**nonparaxial**	
	Equation	**result (μm)**	**Equation**	**result (μm)**
transverse, d_x	(2.01)	0.232	(2.39)	0.208
longitudinal, d_z	(2.02)	0.825	(2.40)	0.573

Table 2.3: Comparison of paraxial *vs*. nonparaxial resolution criteria. $\mathrm{NA} = 1.4$, $n = 1.52$, and $\lambda = 0.532$ μm were used, meaning $\alpha = 67.0°$ and $\lambda/n = 0.350$ μm .

The wide-angle features of a PSF have also been explained in the context of scaling the coefficients χ and ζ in Equations (2.01) (2.02) [76], or by introducing appropriate optical coordinates [77]. Alternatively, one can compose a nonparaxial PSF from a superposition of prolate spheroidal wave functions [78]; these are eigenfunctions of a finite-bandwidth Fourier transform, and therefore the natural choice for the focusing problem [79]. These explanations are rich with mathematical rigor and quite accurate, however our novel, closed-form expressions offer accessible alternative means of understanding a nonparaxial PSF.

As discussed in Section 2.1, scalar and electromagnetic focusing give quantitatively "the same result to within 1%" for $\alpha < 30°$ [40], which is further beyond merely the paraxial limit. $\sin\alpha \approx \alpha$ holds to within 1% only up to roughly 15°. And there is even reasonable agreement, within 5%, between scalar and electromagnetic results for $\alpha < 50°$

. In those cases, one observes that the nonparaxial characteristics identified in section 2.4.2 (as well as focal shift from Kirchhoff's approximation) are present in both scalar and electromagnetic diffraction, for another example see Figure 1-c) of [80], and therefore we consider the two diffraction theories qualitatively similar in this regard.

2.6 Perfect focusing for ultrasound imaging

The lens studied here and sketched in Figure 2.2 follows the *aplanatic* transformation rule, converting input plane waves into output spherical waves. It would be interesting to repeat this parametric study using a flat lens which obeys a different transformation rule, such as

$$u_{perfect} = u_{sphere} \frac{1 + inkr}{1 + inkf}, \tag{2.42}$$

where $u_{perfect}$ is Stamnes' so-called "perfect" wave [37], and the distance r is defined in Equation (2.19). and to apply the focusing of perfect waves to high-intensity focused ultrasound [44]. Such an application could materially improve the imaging contrast (specifically, by preserving Airy's 83.8% energy concentration). For electromagnetic focusing, Stamnes' perfect wave could be used as a design goal for a new class of metasurface, the flat lens [81], [82].

3 OPTICAL TOOLSET

This Chapter is divided into sections as follows: In Section 3.1 I describe a theoretical framework which builds up to the electromagnetic focusing of Laguerre Gaussian laser beams. Section 3.2 describes some experimental apparatus and image processing methods I used for to make a polarimetric imager. Section 3.3 briefly describes the experimental apparatus I used to record sub-diffraction limited optical micrographs. Finally, Section 3.4 describes the plasmonic responses of various metals at optical frequencies.

3.1 Tightly focused laser beams

Tightly focused laser beams with nearly diffraction-limited spot sizes are a very useful, indeed sometimes necessary, tools for exciting nanophotonic structures. Nanostructures can do the rest of the confinement, but careful optical design with conventional far-field optics can get you almost all the way there.

3.1.1 Experimental framework – high magnification imaging

Figure 3.1 shows a schematic of a confocal microscope. A pinhole aperture is positioned in image plane that is conjugated to an image sensor. Illuminating this pinhole with a light source forms a near diffraction limited spot on the sample.

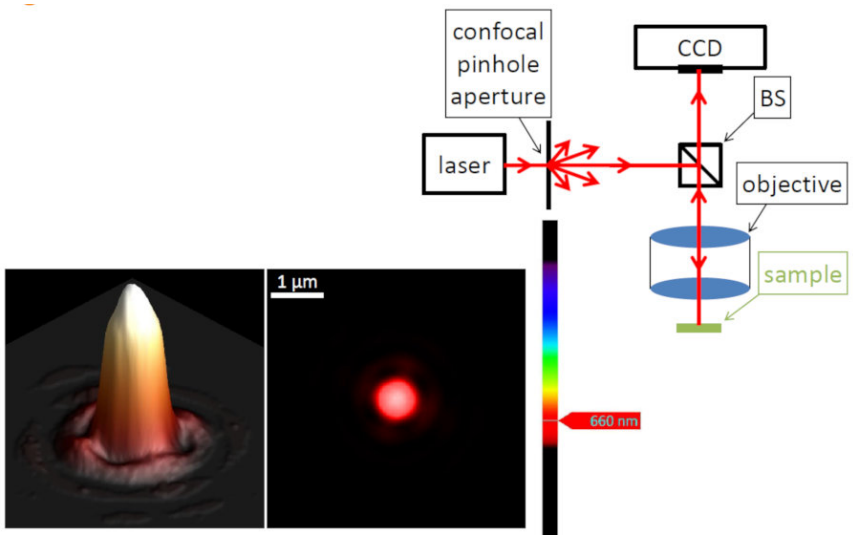

Figure 3.1: Tightly focused laser spots in a high magnification imaging system. A confocal microscope illuminates a sample with a near diffraction limited spot.

3.1.2 Theoretical framework – paraxial Laguerre-Gaussian beams

Next, I will summarize some textbook beam solutions to the wave equation, valid in the *paraxial limit*. For a thorough overview of beam solutions to the paraxial wave equation, Chapter 3 of [26], Chapter 3 of [29], or Chapter 16 [83] are all very good references on the subject. I will not rederive any of those textbook results, instead just recall some of the elements which are most essential to this thesis.

3.1.2.1 Scalar beams

Time-harmonic (*i.e.* stationary) waves, as in Equation (2.04), are solutions to the Helmholtz equation. Within the context of Section 2.3 (*i.e.* for the focusing problem sketched in Figure 2.2), the paraxial approximation means equivalently a small angle approximation, $\sin\alpha \approx \alpha$. For this Chapter, "small angle" means that the wavefronts within the beam propagate *basically* along the $+\hat{z}$ direction, so that, in air,

$$u \propto e^{ikz} \tag{3.01}$$

accounts for the primary spatial dependence of the wave. Unlike Equation (2.14), which allowed for an arbitrary balance between the longitudinal and transverse components of a wavevector $\mathbf{k}$ (see Equation (2.14)), in the paraxial approximation $\mathbf{k}$ is *principally oriented* along $+\hat{z}$, hence in Equation (3.01) the longitudinal component of $\mathbf{k}$ has the "full strength" of $|\mathbf{k}|$. Although the total, complex spatial variations in $u = u(\mathbf{r})$ are such that propagating waves must still satisfy Equations (2.16) and (2.17). With the dominant spatial dependence given by Equation (3.01), one separates the Laplacian into the transverse and longitudinal parts, see for example Equation 16.6 of [83], and substitutes $\partial^2 u / \partial z^2 \to +2ik\,\partial u/\partial z$ for the longitudinal part, rendering a paraxially-approximate version of the Helmholtz equation. Laguerre-Gaussian (LG) modes are eigenfunctions of the paraxial Laplacian, written in cylindrical coordinates (see Figure 2.1), and form a complete orthonormal set. The spatial dependence of the LG modes along the transverse dimensions ρ and ϕ are indexed by the positive integers p and l, respectively, so LG modes are labeled using an LG_p^l notation. The angular dependence, allowing for solutions which circulate in both a CW and a CCW sense, was given in Equations (2.05).

The family of LG laser beams has sparked a recent explosion in optical sciences [84]. The fundamentally new thing about them is their ability to carry optical orbital angular momentum (OAM) [85], [86]. Indeed the early works proved this point by observing the rotational motion of dielectric particles trapped within the beam [87]. Imbuing light with OAM accesses a degree of freedom which has enabled entirely new means of communication [88], [89], cryptography [90], computing [91], and, notably,

super-resolution imaging [92], [93] and photolithography [94] to name a few. For this thesis, I need not the whole family of LG modes, but only two low-order LG beams, namely:

$$\left.\begin{matrix} l=0 \\ p=0 \end{matrix}\right\} \rightarrow \text{"Gaussian"} \qquad \left.\begin{matrix} l=1 \\ p=0 \end{matrix}\right\} \rightarrow \text{"donut"} \tag{3.02}$$

Figure 3.2, adapted from [95], illustrates the conventional beam parameters,

$$\theta_{\text{beam}} = \frac{w_0}{z_0} = \frac{2}{kw_0} = \frac{\lambda}{\pi w_0}, \tag{3.03}$$

where θ_{beam} is the beam divergence angle, w_0 is the beam waist at focus, and z_0 is the Rayleigh range. In the paraxial limit, $\sin\theta_{\text{beam}} \approx \theta_{\text{beam}}$. And while the analogy is not exact, one can think of w_0 and z_0 in Equation (3.03) as analogous to d_x and d_z in Equations (2.39) and (2.40), which are, respectively, the diffraction-limited transverse and longitudinal resolutions for focused, scalar spherical waves. z_0 and d_z may be more commonly referred to as a "depth of focus".

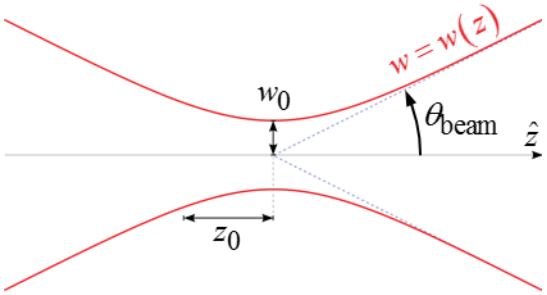

Figure 3.2: Paraxial laser beam parameters. Adapted from [95].

The paraxial beam in Figure 3.2 can be constructed from the following pieces:

$$w = w_0\sqrt{1+\left(\frac{z}{z_0}\right)^2} \tag{3.04}$$

$$R_c = z\left(1+\left(\frac{z_0}{z}\right)^2\right) \tag{3.05}$$

$$\Psi = e^{i\tan^{-1}(z/z_0)} \tag{3.06}$$

$$\mathrm{PRX} = e^{-(\rho/w)^2} e^{-ik\left(z-\rho^2/2R_c\right)}. \tag{3.07}$$

where $w = w(z)$ is the beam waist, $R_c = R_c(z)$ is the wavefront curvature, $\Psi = \Psi(z)$ is a unit Guoy phase, and $\mathrm{PRX} = \mathrm{PRX}(\rho, z)$ is the paraxial beam envelope. The Gaussian beam referred to by Equation (3.02) is then

$$g = g(\rho, z) = \sqrt{\frac{2}{\pi}}\frac{w_0}{w}\mathrm{PRX}\,\Psi\,. \tag{3.08}$$

Incorporating the angular dependence in Equation (2.05), the donut beam referred to by Equation (3.02) is

$$d = d(\rho, \phi, z) = \frac{\sqrt{2}\rho}{w} g\Psi\left(Re^{-i\phi} + Le^{+i\phi}\right). \tag{3.09}$$

Note that the $l = 1$ donut in Equation (3.09) (or any $l \neq 0$ LG mode) can have a helicity, depending on the values of the coefficients R and L. For example, a right- and left-handed donut are obtained by setting

$$\left.\begin{matrix} R=1 \\ L=0 \end{matrix}\right\} \rightarrow d_R \qquad \left.\begin{matrix} R=0 \\ L=1 \end{matrix}\right\} \rightarrow d_L \tag{3.10}$$

respectively. The Gaussian beam, Equation (3.08), and a right-handed donut, Equations (3.09) and (3.10), are plotted in Figure 3.3 for a beam with

$\mathrm{NA}_{\mathrm{beam}} = 0.31 \approx \theta_{\mathrm{beam}} = 18.1°$, which is basically the upper limit where $\sin\theta_{\mathrm{beam}} \approx \theta_{\mathrm{beam}}$ is worse than *ca*. 1%.

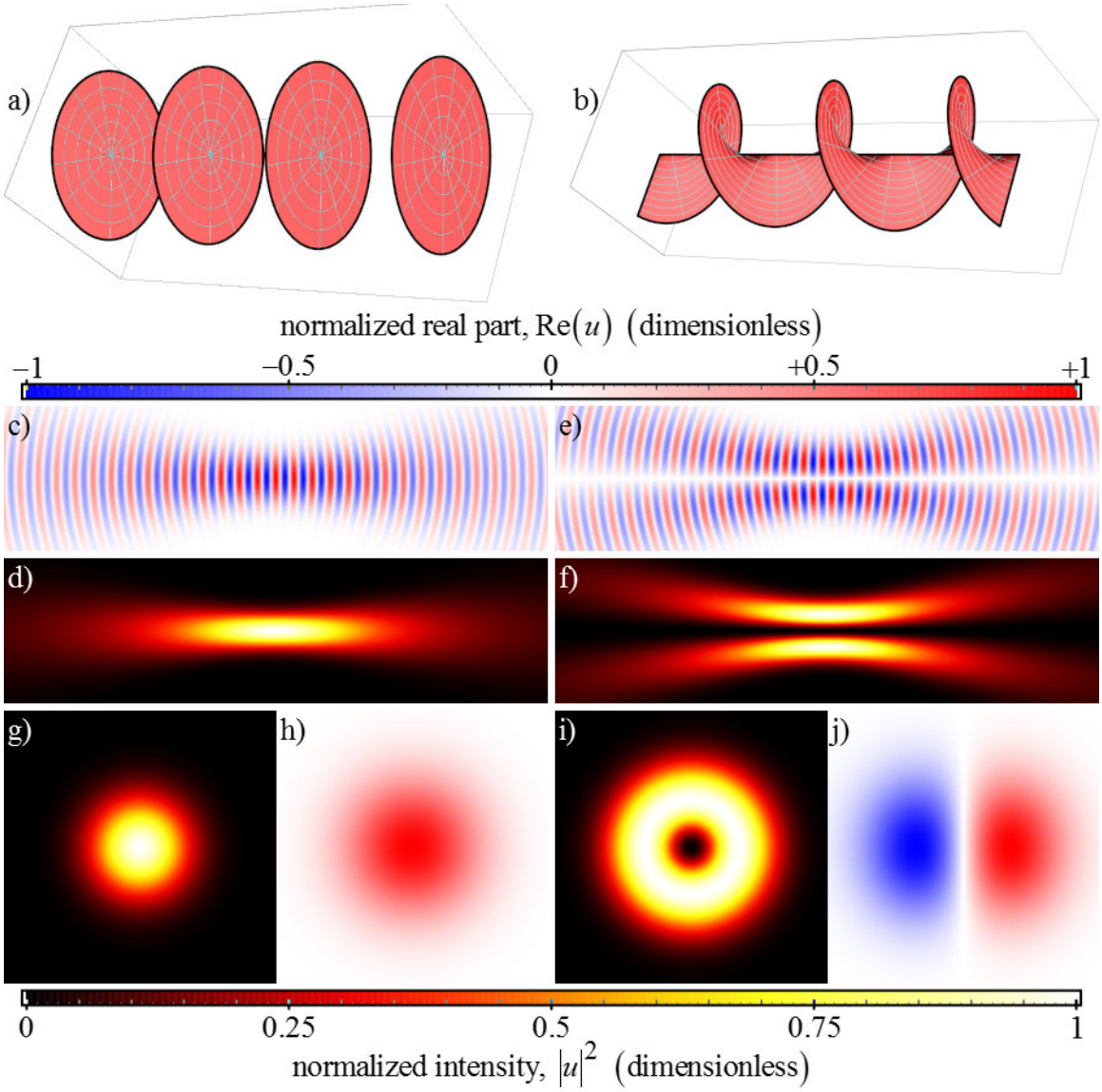

Figure 3.3: Two low-order LG modes, a Gaussian and a right-handed donut. (a-b) Show wavefronts in g and d_R with $\theta_{\mathrm{beam}} = 18.1°$. The beams g and d_R can be sliced longitudinally (c-f) in the zx-plane, or transversely (g-j) in the $(z = 0)$ xy-plane.

Figure 3.3-a) and Figure 3.3-b) show plots of the wavefronts in g and d_R, respectively. Note that any wavefront, by definition, is a surface of constant phase. So, these plots were rendered by finding the surface(s) in $u(\mathbf{r})$ where $\mathrm{Arg}(u) = 0°$. For clarity, only points very close to the optical axis, where $\rho << w_0$ are shown, so that the effects of PRX can be safely ignored. The Gaussian beam has planar wavefronts, while the wavefronts in the right-handed donut beam form a right-handed helix, the same type of twist as the thread on a single-start, right-handed machine screw. Figure 3.3-c) and Figure 3.3-d) show plots of the Gaussian beam in the zx-plane, in accord with the color scales above and below. Figure 3.3-e) and Figure 3.3-f) show the same plots but for the right-handed donut. Note that for points along the optical axis, where $\rho = 0$, the donut has a null, $d_R = 0$. There is also a sign change for any pair of points diametrically opposed about the axis, as dictated by Equation (2.05).

Figure 3.3-g) and Figure 3.3-h) show plots of g in the focal $(z = 0)$ xy-plane, with Figure 3.3-i) and Figure 3.3-j) showing the corresponding plots for d_R. In these plots, the $+\hat{z}$ direction points out of the page. With the assumed harmonic time dependence, the waves are propagating out towards you. For clarity, I also plot in Figure 3.4 the time-evolution of a right-handed, harmonic donut beam at a few snapshots in time during the first quarter cycle. When viewed from this perspective, with a line of sight pointing along $-\hat{z}$ (as in these figures), the red and blue lobes circulate in a CCW fashion. This is consistent with the right-handed helicity of d_R shown in Figure 3.3-b).

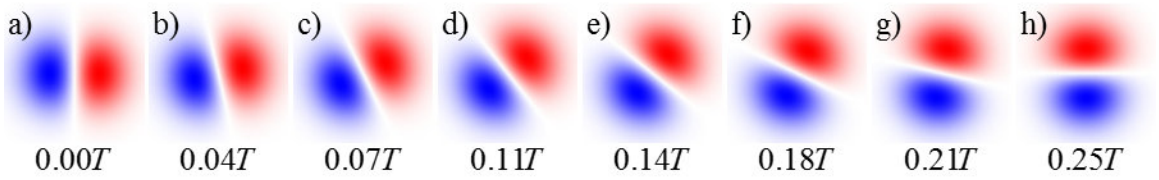

Figure 3.4: Time evolution of a donut beam. (a-h) Snapshots of $\mathrm{Re}\left(d_R\right)$ in the $\left(z=0\right)$ *xy*-plane at a sequence of different instants in time. T is the period of oscillation. The red-white-blue color-coding is the same as in Figure 3.3.

3.1.2.2 Electromagnetic beams

In addition to OAM, light also carries spin angular momentum (SAM). The earliest experimental observation of optical SAM [96] confirmed what many understand intuitively, that SAM is manifest, under those experimental conditions, in the light's polarization state. Polarization effects are a set of phenomena which cannot be accounted for using the scalar formalism of Section 3.1.2.1 and of Chapter 2. Furthermore, many of the useful applications of LG beams exploit their *vortex* polarization states [97], where superpositions of differently polarized LG beams can give rise to compounded polarization textures that are simply not obtainable in plane waves. While it may be intuitive to separate light's total angular momentum (JAM) into its spin and orbital parts SAM and OAM, respectively, this is not always physically possible (see for example Chapter 2 of [98]). For focused beams in particular, the two parts are inextricably linked, with the degree of spin-orbit coupling in a paraxial LG beam varying in proportion to θ_{beam} [99], [100].

For an isotropic, homogenous, local, linear, non-magnetic medium in the absence of any charge or current other than due to the polarized and conductive responses of the charge-neutral medium itself (*i.e.* no "free" or "unbound" sources of field), and assuming the explicit harmonic time dependence in Equation (2.04), Maxwell's equations are

$$\nabla \times \mathbf{E} = i\omega\mu_0 \mathbf{H} \tag{3.11}$$

$$\nabla \times \mathbf{H} = -i\omega\varepsilon_0 \varepsilon \mathbf{E} \tag{3.12}$$

$$\nabla \cdot \mathbf{E} = 0 \tag{3.13}$$

$$\nabla \cdot \mathbf{H} = 0\,, \tag{3.14}$$

For the electric and magnetic fields, $\mathbf{E}$ and $\mathbf{H}$. Constrained within the above list of caveats, the frequency-dependent, complex, scalar relative permittivity in Equation (3.12)

$$\varepsilon = \varepsilon(\omega) = \varepsilon_1 + i\varepsilon_2 \tag{3.15}$$

totally encodes the medium's electromagnetic response. The material response could equivalently be cast into a complex refractive index

$$N = \sqrt{\varepsilon} = n + i\kappa \tag{3.16}$$

with the real and imaginary parts related by

$$\varepsilon_1 = n^2 - \kappa^2 \qquad \varepsilon_2 = 2n\kappa \tag{3.17}$$

$$n = \sqrt{\frac{|\varepsilon| + \varepsilon_1}{2}} \qquad \kappa = \sqrt{\frac{|\varepsilon| - \varepsilon_1}{2}}\,. \tag{3.18}$$

In SI units, where for example the permittivity of free space is $\varepsilon_0 = 8.85\ \mathrm{aF/\mu m}$, the quantity $\varepsilon_0\omega$ has dimensions $[\varepsilon_0\omega] = (\Omega \cdot \mu\mathrm{m})^{-1}$, the same as electrical conductivity. As it happens, within the caveats listed above, there is a constitutive relation which allows one to alternatively encode a material's response totally in terms of the frequency dependent conductivity

$$\begin{aligned}\sigma &= \sigma(\omega) \\ &= \sigma_1 + i\sigma_2 \\ &= i\omega\varepsilon_0(\varepsilon - \varepsilon_1)\end{aligned} \quad . \tag{3.19}$$

It is a matter of preference which among Equations (3.15), (3.16), or (3.19) to use in describing the material response; they are mathematically interchangeable, at least within those constraints. In light of Equation (3.16), one might see the curl Equations (3.11) and (3.12) could perhaps be more clearly construed in terms of the factor $\varepsilon/c^2 = (N/c)^2$, where the vacuum speed of light is $c \approx 300\ \mu\text{m/ps}$, and c/n is the phase velocity in the medium. By taking the curl of the curl, and with the assumed harmonic time dependence, one can use Maxwell's Equations (3.11) through (3.14) to make the vector Helmholtz equation (*i.e.* a stationary wave equation) for the electric and magnetic fields, $\mathbf{E}$ and $\mathbf{H}$

$$\left(\nabla^2 + \left(N\frac{\omega}{c}\right)^2\right)\mathbf{F} = 0\,, \tag{3.20}$$

where $\mathbf{F}$ is either $\mathbf{E}$ or $\mathbf{H}$, and ∇^2 is the Laplace operator. The complex wavenumber $|\mathbf{k}| = N\omega/c$ accounts for both oscillatory and decaying (or growing) behavior of the wave as it propagates, depending on the medium's refractive index and absorption coefficient (or gain).

There is no closed-form vector beam solution to Maxwell's equations. The most accurate way to model focal fields is by numerically solving diffraction integrals, for example a vectorial version of the scalar Debye theory covered in Section 2.3.1.1. These vectorial integrals are presented in a very accessible manner in Chapter 3 of [29], or several other standard texts on the subject. Accessible as they are, however, they are also numeric solutions, as in Section 2.4.1. This means they are evaluated only on a point-by-point basis.

In some scenarios, this can become computationally burdensome. It would be easiest, especially for the finite-element modeling discussed in Section 4.4, to use analytic (closed-form), approximate formulae. One can find comprehensive juxtapositions of the various analytically approximate formulae for focused electromagnetic beams against the numeric results [101].

The standard prescription is to "vectorize" the scalar result, constructing a purely transverse electromagnetic (TEM) beam by setting the transverse components of the fields $\mathbf{F}_\perp = F_\rho \hat{\rho} + F_\phi \hat{\phi}$, equal to independent scalar LG modes. While this is a useful starting point, it produces a vector beam which does not solve Maxwell's equations, to any degree of approximation. Beams with a finite waist $w(z)$ cannot be TEM, as such hypothetical fields would fail to satisfy the divergence conditions, Equations (3.13) and (3.14). Only plane waves (of infinite extent) can be TEM. For such hypothetical beams to be physical, even in vacuum, one must invoke fictitious charges and currents in order to source and sink the fields [102]. This violation becomes increasingly worse as the azimuthal order l increases [103], as it would also for an increasing radial order p. Therefore, a focused electromagnetic beam *necessarily* has a finite longitudinal component in at least one of the $\mathbf{F}$ [104]. One approach, called the Lax expansion [105], can account for the F_z by starting with the standard "TEM prescription" and perturbatively expanding the field components in powers of the small divergence angle, θ_{beam} [106]. Another straightforward approach [107], which I employ below, is to start with the "TEM prescription" and find the F_z by subjecting the $\mathbf{F}_\perp$ to paraxially-approximate forms of Maxwell's equations [108]. This amounts, for my purposes, to finding a paraxially approximate form of $\nabla \cdot \mathbf{F}$, and since all

components of **F** have the assumed dominant spatial dependence given by Equation (3.01), this ultimately amounts to substituting (again, in air where $N=1$)

$$\nabla \cdot \mathbf{F} \approx \nabla_{\perp} \cdot \mathbf{F} + ikF_z \,, \tag{3.21}$$

so that

$$F_z \approx \frac{i}{k}\left(\frac{1}{\rho}\frac{\partial}{\partial \rho}\left(\rho F_\rho\right) + \frac{1}{\rho}\frac{\partial F_\phi}{\partial \phi}\right) \tag{3.22}$$

could approximately account for the divergence violation of the prescribed TEM beam.

The two vector beams used in this thesis are a linearly polarized Gaussian, and a radially polarized donut. The standard "TEM prescription" uses Jones vectors, already introduced in Section 2.2.2, and reviewed in most standard optics textbooks, for example see Table 8.5 of [25]. Looking at Equations (2.10) and (2.11), one can make a generalized circular polarization Jones vector from

$$\hat{S} = \frac{e^{i\sigma_z \phi}}{\sqrt{2}}\left(\hat{\rho} + i\sigma_z \hat{\phi}\right). \tag{3.23}$$

where choosing σ_z from either -1 or $+1$ selects between a right- and left-hand circular polarization, $\hat{R}$ and $\hat{L}$ respectively. As it turns out [99], for a TEM plane wave with polarization $\hat{S}$, σ_z is the SAM carried by the light. And similarly, for an LG beam with angular order l, the beam carries an l-worth of OAM; l is often referred to as the beam's "topological charge", as in Equation (1.95) of [109].

Denoting the **E**-field in a circularly polarized Gaussian beam with the notation $\mathbf{E}_{g\sigma}$, the prescribed transverse parts are

$$\left(\mathbf{E}_{g\sigma}\right)_{\perp} = E_0 g \hat{S} \,. \tag{3.24}$$

The scalar beam g is from Equation (3.08), and E_0 is a unit of electric field strength, say $E_0 = 1$ V/μm. Interestingly, even though g is an LG mode with $l = 0$, the Gaussian beam in Equation (3.24) picks up a ϕ-dependence through $\hat{S}$. Divergent as they are, it is instructive to see that any prescribed TEM LG beam with circular polarization has an overall ϕ-dependence given by $\exp\left(i\left(l+\sigma_z\right)\phi\right)$. Noting that

$$\frac{\partial}{\partial\rho}(\rho g) = g\left(1-\theta_{\text{beam}}\Psi\frac{k\rho^2}{w}\right), \tag{3.25}$$

and using Equations (3.22), (3.24), and (3.25), one can find $\hat{z}\cdot\mathbf{E}_{g\sigma}$. Putting it all together,

$$\mathbf{E}_{g\sigma} = E_0\frac{ge^{i\sigma_z\phi}}{\sqrt{2}}\left(\hat{\rho}+i\sigma_z\hat{\phi}-i\theta_{\text{beam}}\Psi\frac{\rho}{w}\hat{z}\right). \tag{3.26}$$

It is interesting to see that E_z, in addition to being simply proportional to θ_{beam}, also has an extra ρ-dependence and Guoy phase. This makes E_z functionally the same as d in Equation (3.09). It is as if operating ∇ on g promotes it to the next highest LG order. This is exactly the spin-orbit coupling mentioned previously [99], [100]. For a well-collimated beam (*i.e.* unfocused), where $\theta_{\text{beam}} \to 0$, E_z vanishes and the beam becomes increasingly TEM. For example, affordable HeNe lasers have beam divergence typically smaller than $\theta_{\text{beam}} = 0.04°$. In that case, and to the same approximation that $0.04°$ can be rounded to zero, the JAM is exclusively due to SAM (*i.e.* the value of σ_z). However when the beam is focused, the twist imparted onto E_z with increasing θ_{beam} appears as the OAM of a promoted LG mode. So, the JAM of a focused beam is partly OAM and partly SAM, even if the collimated beam has exclusively a SAM.

A linearly polarized Gaussian (say, along $\hat{x}$) can be made from the superposition of right- and left-circular polarizations

$$\begin{aligned}\mathbf{E}_{\hat{x}\text{-Gaussian}} &= \frac{1}{\sqrt{2}}\left(\mathbf{E}_{g\hat{R}} + \mathbf{E}_{g\hat{L}}\right) \\ &= E_0 g\left(\hat{x} - i\theta_{\text{beam}}\Psi\frac{x}{w}\hat{z}\right)\end{aligned}. \tag{3.27}$$

I used Equation (2.06) in order to express the linearly polarized Gaussian in its "natural" Cartesian basis. Equation (3.27) has been derived previously, see Equations (5.2), (5.25) and (5.26) of [110], although that result was obtained using a different theoretical approach, instead starting with a prescribed vector potential $\mathbf{A}$. Plotted in Figure 3.5 are the field components of $\mathbf{E}_{\hat{x}\text{-Gaussian}}$ for $\theta_{\text{beam}} = 18.1°$. Figure 3.5-a), -b), -c), and -d) show energy densities, proportional to E^2, for the total field $|E_x|^2 + |E_y|^2 + |E_z|^2$, and for each of the separate components $|E_x|^2$, $|E_y|^2$, and $|E_z|^2$, respectively. These should be contrasted against the scalar result, shown in Figure 3.3-g). Figure 3.5-a) and -b) look nearly identical because virtually all of $\mathbf{E}_{\hat{x}\text{-Gaussian}}$ is channeled into E_x. However, Figure 3.5-c) shows that $E_y = 0$ everywhere. One drawback of using Equation (3.22) is that it totally fails to account for cross-polarization effects, which also ultimately stem from satisfying the divergence-free constraint. Numeric integration of the diffraction integrals [101], theoretical analysis [111], and experiments [112] all show that a focused, $\hat{x}$-polarized beam would result in some finite E_y. In this regard, the shortcomings of Equation (3.27) are readily seen. I should emphasize Equation (3.27) is an approximate formula. Figure 3.5-d) shows that $|E_z|^2$, colored for clarity on a different color-scale from the rest, is only

a minor component of $\mathbf{E}_{\hat{x}\text{-Gaussian}}$, though still present. Figure 3.5-e) and -f) show plots of $\mathrm{Re}(\mathbf{E})$ as line-cuts along the x-axis, where $y = z = 0$, and at two different snapshots in time, at the cycle start and a quarter cycle later, respectively. The fields E_x (red) and E_z (blue) oscillate out of phase, as dictated by the factor of i in Equation (3.27), and E_y (green) is zero at all times.

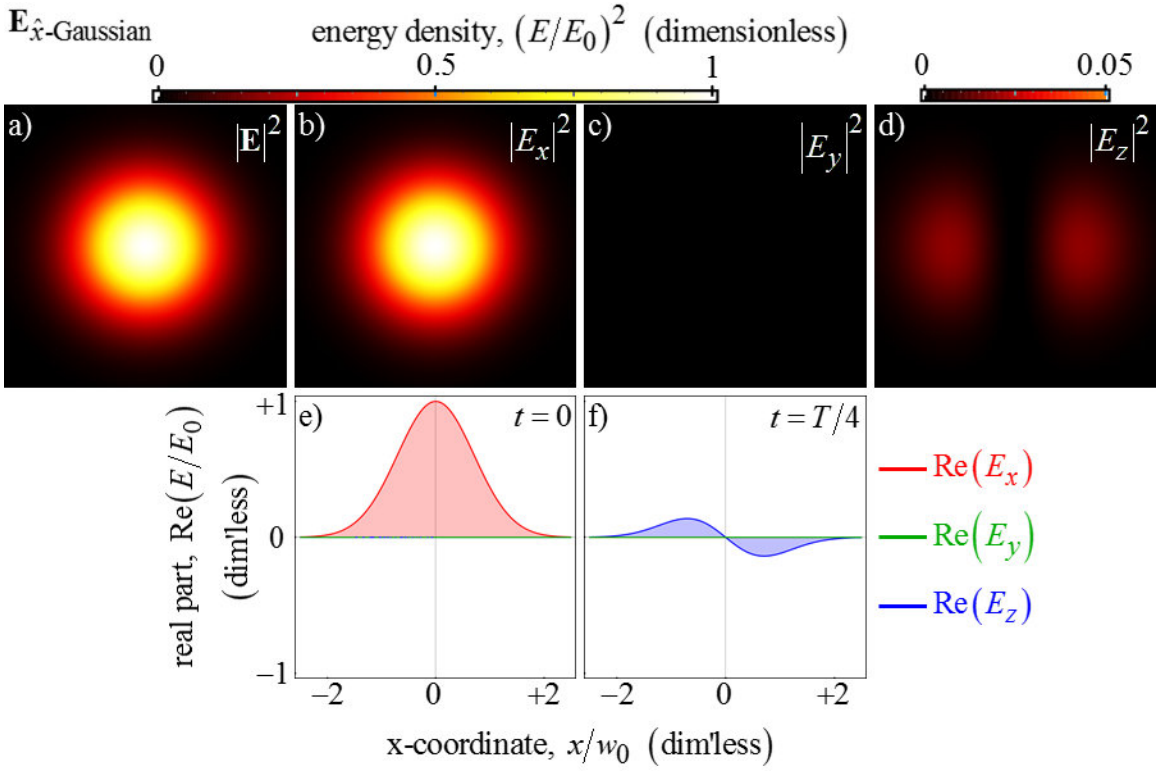

Figure 3.5: Electric field components of a paraxial, $\hat{x}$-polarized Gaussian beam. (a-d) Show energy densities, proportional to $|E|^2$, with (a) showing the total energy density, and (b-d) showing each of the x-, y-, and z-channels separately. (e-f) Are plots of $\mathrm{Re}(\mathbf{E})$ at two instants in time t and along the x-axis, where $y = z = 0$, with $t = 0$ and $t = T/4$ shown in (e) and (f), respectively, and where T is the period.

Next, I will follow the same set of steps to find a formula for a radially polarized donut. The radial polarization state is considered a *vortex* state. If one restricts themselves to prescribing only polarizations which are realizable in plane waves (*e.g.* circular polarization), then a radially polarized beam can be made only from a linear combination of differently polarized LG beams. It is not correct to say that vortex beams *need* to be made of multiple beams *per se*; after all any linear combination of solutions to Equation (3.20) is itself a valid solution. There is nothing *wrong* with prescribing a radial polarization from the get-go, those vortex directions are perfectly valid for a cylindrically symmetric beam, they should even be considered the "natural" cardinal directions. However, there are simply no "radially" nor "azimuthally" polarized plane waves, as those polarization states require a singularity. Since plane waves are more intuitively understood and more often encountered in nature, the term "vortex" applies.

For the circularly polarized Gaussian, where $l = 0$ in Equation (3.24), any arbitrary polarization state can be made from a basis of two polarization states, $\sigma_z = \pm 1$, which are diametrically-opposed points on the Bloch sphere. But for an $l = 1$ donut, as in Equation (3.09), there would be four combinations of (l, σ_z). These combinations are discussed in [97]. The radially polarized donut is composed of LG beams with opposite orbital and spin helicities,

$$\left(\mathbf{E}_{\hat{\rho}\text{-donut}}\right)_{\perp} = \frac{1}{\sqrt{2}}\left(\mathbf{E}_{d_L \hat{R}} + \mathbf{E}_{d_R \hat{L}}\right). \tag{3.28}$$

Because of these opposite helicities, the overall ϕ-dependence cancels. Much like Equation (3.25), one can use the relation

$$\frac{\partial}{\partial\rho}(\rho d) = d\left(2 - \theta_{\text{beam}}\Psi\frac{k\rho^2}{w}\right), \tag{3.29}$$

and compile the electric field of a radially polarized donut

$$\mathbf{E}_{\hat{\rho}\text{-donut}} = E_0 d\left(\hat{\rho} - i\theta_{\text{beam}}\left(\Psi\frac{\rho}{w} - \frac{w_0}{\rho}\right)\hat{z}\right). \tag{3.30}$$

As was the case for $\mathbf{E}_{\hat{x}\text{-Gaussian}}$ in Equation (3.27), the longitudinal component of E_z has a different LG order from the transverse components. In this case, the two terms in $\hat{z}\cdot\mathbf{E}_{\hat{\rho}\text{-donut}}$ would increment and decrement the overall exponent of ρ, effectively raising and lowering the LG order l, respectively. The first term in E_z, with promoted LG order, also has an additional Guoy phase. It has, in fact, identically the same spatial dependence as an $l = 2$ mode. Equation (3.30) has been derived previously, for example see Equations (3) and (7) in [113]. The field components of $\mathbf{E}_{\hat{\rho}\text{-donut}}$ are plotted in Figure 3.6, again for $\theta_{\text{beam}} = 18.1°$. Figure 3.6 is a companion of Figure 3.5. There are a few features worth mention. First, the color scale at the top of Figure 3.6 is the same for all of panels (a-d). This is different from Figure 3.5, where E_z was small enough to warrant a separate color scale for clarity. Apparently, E_z is in proportion *much stronger* in a radially polarized donut than in a linearly polarized Gaussian (or any polarization state of a Gaussian). One way to understand this is that the null at the beam center causes a more egregious divergence violation in the prescribed TEM beam. This is readily apparent in comparing Figure 3.6-f) against Figure 3.5-f); at this θ_{beam}, E_z is nearly as strong as the $\mathbf{E}_\perp$ for the radially polarized donut. This raises the second point, Figure 3.6-a) shows that the null isn't indeed a null. There is finite field strength, due exclusively to E_z, along the optical axis.

One way to think of this is that any LG beam with $l \neq 0$ gets "flung out" away from the optical axis as it orbits around it, much as a centrifugal force would have it. Only the set of LG beams with $l = 0$ could have a finite field strength on the axis, just as in the second ("demoted") term for E_z in Equation (3.30). So Figure 3.6-a) ought to be compared against Figure 3.3-i), which, being a scalar beam, could not possibly account for this effect. The third point is that Figure 3.6-e) and -f) would seem to indicate that $E_y = 0$ for all instants in time, as was the case for $\mathbf{E}_{\hat{x}\text{-Gaussian}}$, but this is not generally the case for $\mathbf{E}_{\hat{\rho}\text{-donut}}$. It is only because I took an $\hat{x}$-line-cut, where $y = z = 0$, to plot the fields. Clearly, as indicated in Figure 3.6-c), this would not be the case had I taken any line-cut which departs the $y = 0$ plane. Forth, and finally, is that Figure 3.6-b) and -c) together are indicative of the radial polarization state. In those panels, the lobes of high energy density are oriented along the same direction as their respective polarization components of $\mathbf{E}$, x and y. Figure 3.6-b) and -c) in plotting $|E|^2$, contain no information about phase. While there is no explicit ϕ-dependence in Equation (3.30), it is worth noting, for example see Equations (2.06) and (2.07), that when projecting $\hat{\rho}$ onto $\hat{x}$ and $\hat{y}$, one incurs a $\cos\phi$ or $\sin\phi$ dependence. This means diametrically opposed points have an $\exp(i\pi)$ phase difference. The lobes are of opposite sign, as indicated by the zero-crossing of E_x in Figure 3.6-e).

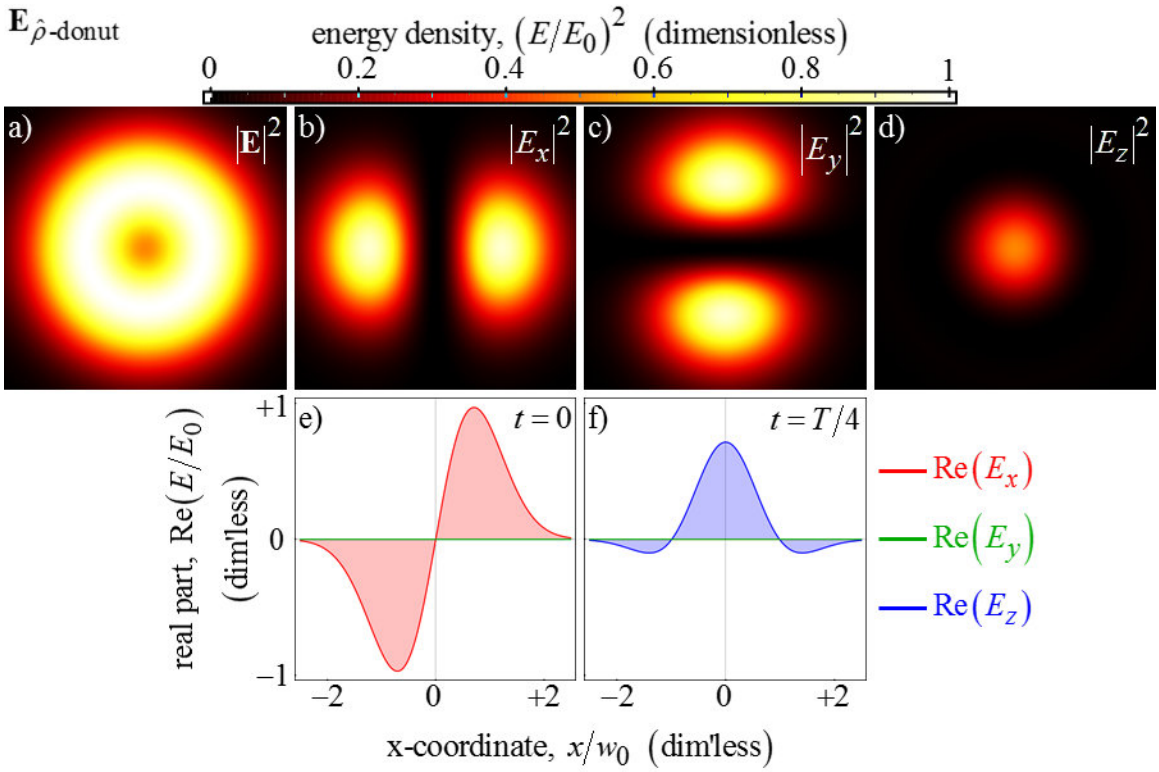

Figure 3.6: Electric field components of a paraxial, $\hat{\rho}$-polarized donut beam. These are companion plots to Figure 3.5, see the caption there for a detailed explanation. The same color scale is used for panels (a-d).

3.1.3 Vortex generation

To excite the fundamental, TEM-like mode of the nanocoax [114], I used a radially-polarized donut beam (*i.e.* an optical "vortex") at $\lambda = 980$ nm. This beam was generated with the apparatus pictured in Figure 3.7 and diagramed in the bottom half of Figure 3.8. The vortex generation apparatus was packaged into a module, and the collimated beam was coupled into a confocal pair of inverted and upright microscopes, aligned for collinearity and with a sample positioned at their common focus. One key component lies at the heart of the vortex generation module: a commercially available liquid crystal waveplate [115].

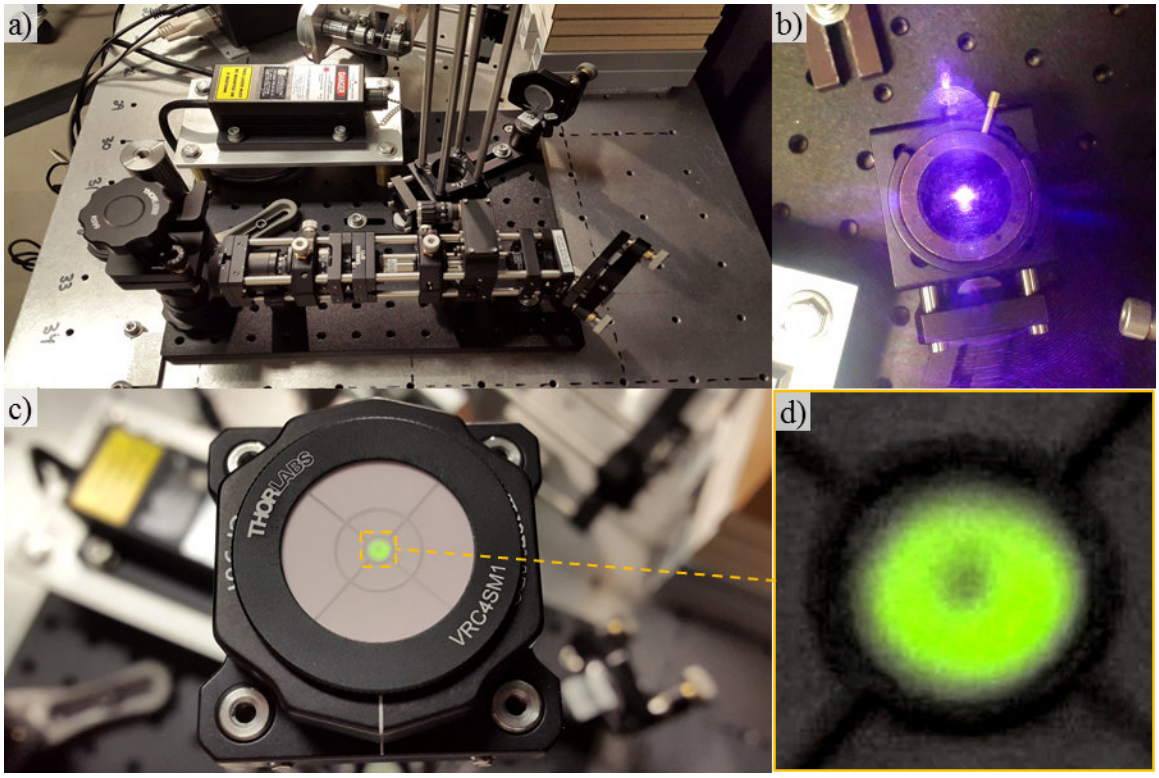

Figure 3.7: Picture of the donut module. This module is diagramed in **Figure 3.8**. The letter-paper sized optical breadboard (black) slides under the inverted microscope in the NSOM cabinet.

A periscope, shown on the left in Figure 3.7, is used to keep the form factor to a minimum, with a beam height of 20 mm from the breadboard. Also pictured here is a temporary 12” vertical cage used to steer the collimated beam as parallel to the zenith as possible and was achieved using a pair of cage plates which register a quick-release alignment phosphor by magnetic retention of ball-bearings into roller-bearing detents. When the alignment cage is removed, the module’s exit aperture is only 40 mm from the surface of the breadboard, well within the space constraints of the inverted microscope in the NSOM cabinet.

3.1.4 Coincident dual microscopes

The pair of coincident upright and inverted microscopes, as well as the polarimetric imager discussed in Section 3.2, are drawn in Figure 3.8. The results obtained by these apparatus are discussed later in Section 4.3.1. In this section I describe these apparatus in some more detail.

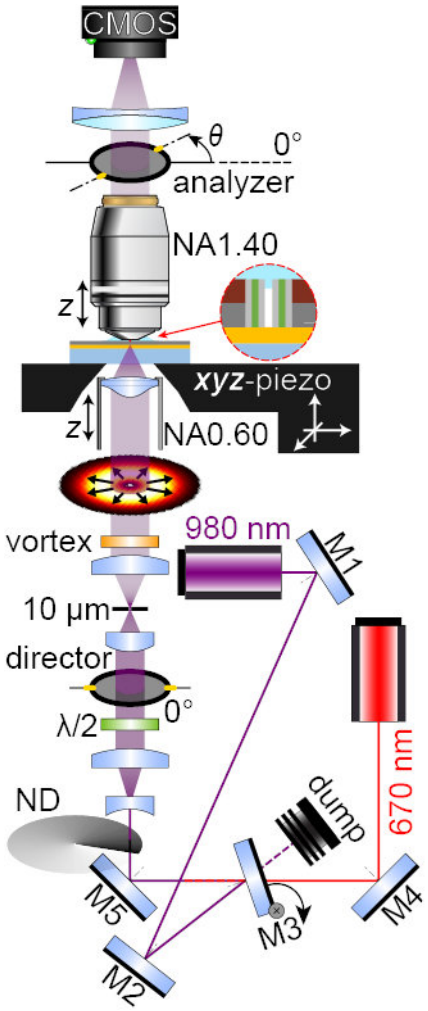

Figure 3.8: Tightly focused vortex and polarimetric imaging schematic. The vortex is generated by the apparatus at the bottom of this figure, everything below the inverted microscope. That vortex generation is packaged into a module pictured Figure 3.7. The encoded rotation mount of Section 3.2.1 is represented by the analyzer in this figure.

On the substrate's backside, the inverted microscope focused the beam through 0.5 mm of glass at NA0.64. The backside objective is an aspheric singlet lens, so there are no forms of imaging correction typically present in most compound objective lenses. The resolving power of that inverted microscope could be improved by using an objective lens with a correction collar for focusing through a thick, glass substrate. I intentionally underfilled the asphere's clear aperture, $\mathrm{CA} \sim 3.6$ mm, to avoid clipping/truncating the collimated beam with waist $2w \sim 1.5$ mm. So the beam does not, nor in best practice should not, access the full NA of the backside objective and is instead focused at a lower $\mathrm{NA}_{\mathrm{beam}} = 0.31$ than the objective's marginal ray. This corresponds to a beam divergence angle $\theta_{\mathrm{beam}} = 18.1°$, which was used throughout Section 3.1.2.

Light transmitted by the sample is collected on the topside by the upright microscope with high-NA objective, either an oil-immersion NA1.40 or a dry NA0.95. In the tube space of the upright microscope, I placed a rotating analyzer, mounted into apparatus described in Section 3.2.1, and acquired an image using a complementary metal oxide semiconductor (CMOS) sensor at a series of angles θ, registered absolutely to within 0.1° of the sensor's x-axis.

3.2 Polarimetric imaging

The apparatus described here is a "division of time, incomplete polarimeter" [116], such that, with only a rotating analyzer, one can measure only the degree of linear polarization (the strength of I_1 in Equation (3.33)), but cannot resolve the circular polarization content (some fraction of I_0 in Equation (3.33)). While a complete Mueller polarimeter would

resolve the full Stokes parameters, for the purposes of this work, an incomplete polarimetric measurement is enough.

3.2.1 Encoded rotation mount

The division of time polarimeter is made from two pieces: a motorized, encoded rotation mount, and a camera. The rotation mount was assembled from several off-the-shelf and stock parts, with a few components machined in house, as shown in Figure 3.9-a).

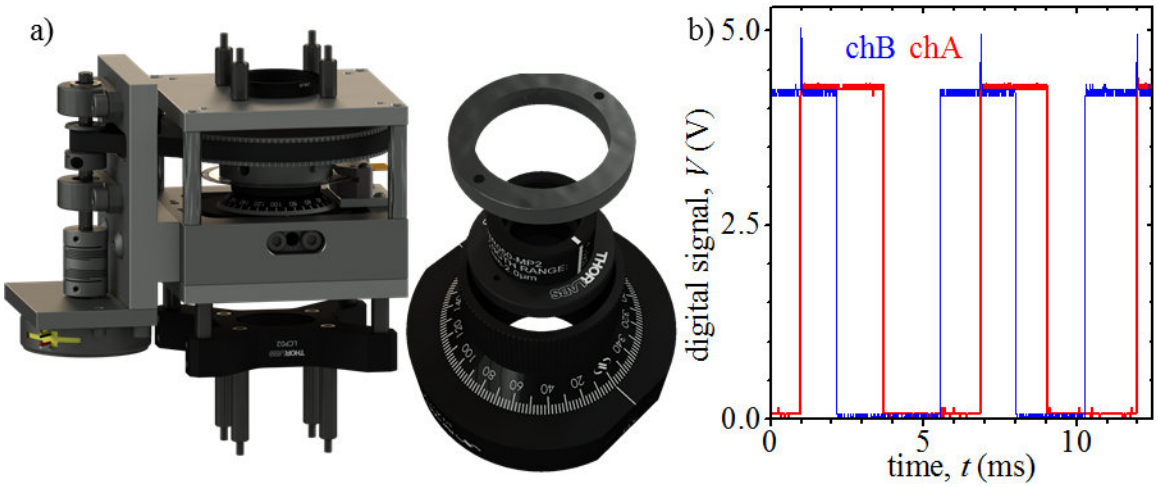

Figure 3.9: Encoded, motorized rotation mount. (a) 3D ray traces rendered from the CAD model. The assembly is made from *ca*. 30 individual, mostly stock parts. (b) An oscilloscope trace from the encoder's quadrature A and B channels while rotating at *ca*. 5 RPM.

A 100 steps per revolution stepping motor drove a Newport RM25A rotation mount through an MXL pulley system with a 120:18 gearing ratio. Fastened onto the barrel of the RM25A was a 2500 counts per revolution (CPR) code-disk, read out optically into quadrature channels A and B, as shown in Figure 3.9-b). By encoding the angular position of the load (not the drive shaft), the closed-loop position feedback was immune to backlash and torsional windup in the drive train as well as any missed steps by the motor. This

motion control was implemented with an Arduino Uno microcontroller, which was programmed using interrupt service requests (ISRs) attached to the encoder Ch.'s A, B, and Z (index), so that program execution was paused in order to ensure no counts were missed. The ISRs were triggered on any edge (rising or falling) in either Ch.'s A or B, so that the 2500 CPR code-disk was read out into 10,000 incremental counts. So, the encoded rotation mount has an angular resolution of 0.036°, and is essentially agnostic to the source of mechanical drive (*e.g.* when denied motor power and rotating manually by hand). The microcontroller is programmed as a state machine with various motion control and system states and communicates with an associated LabVIEW driver by sending and receiving messages over a USB. This LabVIEW driver was employed by a higher-level virtual instrument (VI) which synchronized the rotational action of the polarizer with acquisition from a USB camera (Thorlabs DCC1545M), and in the end acquired still images transmitted through an analyzer fixed at different angles.

3.2.2 Brewster's window calibration

With a relative measurement of the angle of linear polarization (AOLP, φ in Equation (3.33)), one cannot distinguish between vortex donut beams in the orthogonal radial and azimuthal polarization states [97]. To make an absolute AOLP measurement, it is necessary to have a polarization reference with an AOLP that is known *w.r.t.* a mechanical datum plane. This reference was generated by cutting a straight edge into a flat piece of glass, which was tilted to reflect at the Brewster's angle, θ_B:

$$\theta_B = \tan^{-1}\left(n_{glass}\right) \approx 56.7° . \tag{3.31}$$

Figure 3.10-a) shows how that tilt angle was produced by supporting the glass plate on three points of contact. The two points where the straight edge touches the two optical cage rails assure the glass is tilted by rotation about the cage's mechanical x-axis. A third point of contact on a backing cage plate sets the tilt angle. A pair of centered-drilled cage plates, shown in red, define some range of angles which can be reflected to the camera. The setup pictured in Figure 3.10 had an acceptance cone with marginal rays at about ±1.2° *w.r.t.* the optical axis. With careful adjustment of the reflector's angle (*i.e.* by adjusting the space between the backing plate and the aft center-drilled plate), one can set the received angle of reflection to θ_B, within the angular aperture of that acceptance cone. By using a randomly polarized incandescent source, shown in Figure 3.10-b), the reflected AOLP is aligned with the cage's mechanical x-axis to within the mechanical precision of the following items: the straightness of the edge; the flatness of the reflective surface; and the centering of the drilled thru-holes. In practice, the last item bears the largest impact on precision of the polarization reference angle.

Figure 3.10-c) shows an image of the fore thru-hole cage plate, with scribe marks made parallel to its edges. How closely the scribe marks intercept the countersunk, Ø1.6 mm thru hole along a diameter indicates the accuracy of the centering, which is about ±50 μm. This image allows one to reference the camera sensor's xy-grid of pixels against the mechanical x-axis of the cage. Figure 3.10-d) shows a polarization trace, measuring the light reflected by the glass plate through the pair of thru-holes and onto the camera. The angular measurements in Figure 3.10-c) and -d) allow one to register the polarizer's transmissive axis absolutely *w.r.t.* the camera sensor's xy-grid, at a precision of ±0.1°.

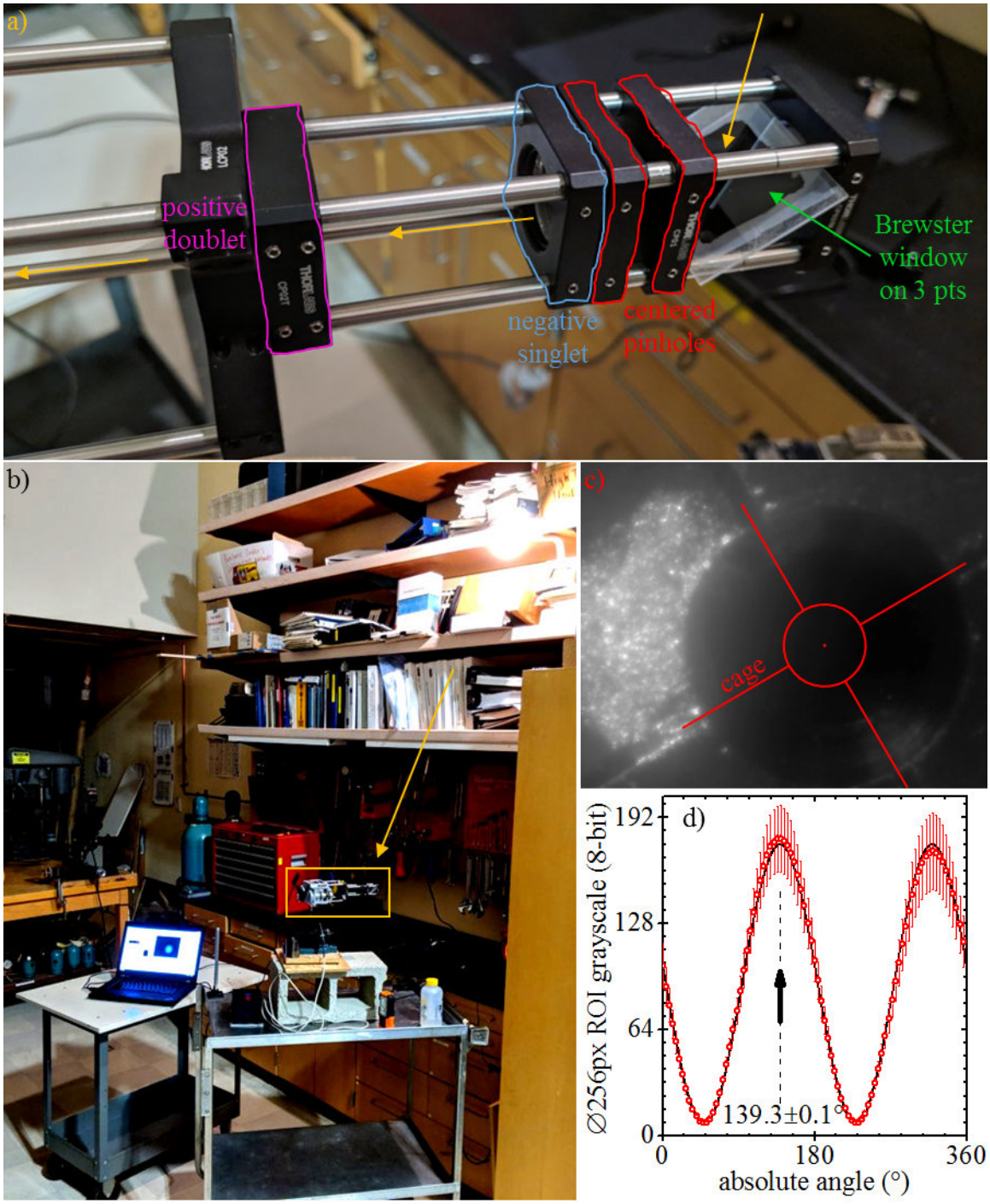

Figure 3.10: Brewster's reference for absolute AOLP. (a) Light from an incandescent bulb (b) is reflected to the camera. (c) Center-drilled thru holes are used as mechanical fiducials, with a red reticle superimposed on scribe marks. (d) The polarizer's transmissive axis can be registered against the camera sensor's x-axis to within 0.1°.

3.2.3 Orbit shift correction

For a division of time polarimeter, any aparallelism in the analyzer's surfaces will cause the image formed on the camera's sensor to shift as the analyzer rotates. This shift, which is a highly repeatable, systematic effect, was measured and corrected for. For example, highlighted with a blue circle in Figure 3.11-a) is a piece of debris on a resolution target. The blue points plotted in Figure 3.11-b) show how the debris' centroid *xy*-position (in pixels) tracks an ellipsoid as the analyzer is rotated through one revolution. These points are used to find the red curve of best fit, which is a shifted, rotated ellipse,

$$\left(\frac{(x-x_c)\cos\alpha+(y-y_c)\sin\alpha}{a}\right)^2+\left(\frac{(x-x_c)\sin\alpha-(y-y_c)\cos\alpha}{b}\right)^2=1, \qquad (3.32)$$

where (x,y) are points (in pixels) along the red curve, (x_c,y_c) is the center of the ellipse, a and b are the semi-major and semi-minor axes, and α is the angle of rotation. The best-fit values of those five parameters are determined by regression. A sixth parameter, the angle β, (which is fixed, not part of the regressive fit) is required in order to register the index position of the code-disk onto the red ellipse.

A sequence of stills from the first roughly ¼ revolution are shown in Figure 3.11-c) through -j). For each still, a pair of two images (top and bottom) is shown. On the top, the blue crescent is used as a guide for the eye to show how the image of the debris shifts around on the image sensor as the analyzer rotates, while the bottom image is after correcting for this shift using Equation (3.32). Note that due to the polarizing nature of the inverted microscope's beam splitter, the illumination brightness varies with analyzer angle and the debris does not have the same contrast in all the stills. To determine the debris' centroid positions, the stills were all equalized by background subtraction and histogram

transforms, thereby mitigating the effect of polarized illumination. Note how the shift correction, typically about 15 pixels in magnitude, leaves some of the border region filled with blank pixels (colored black). The red reticle indicates the centroid position, which is determined by the grayscale-weighted center of mass in those equalized images. Note that in the shift-corrected images, the red reticles are all very close to the image centers, indicating the sub-pixel accuracy of this correction.

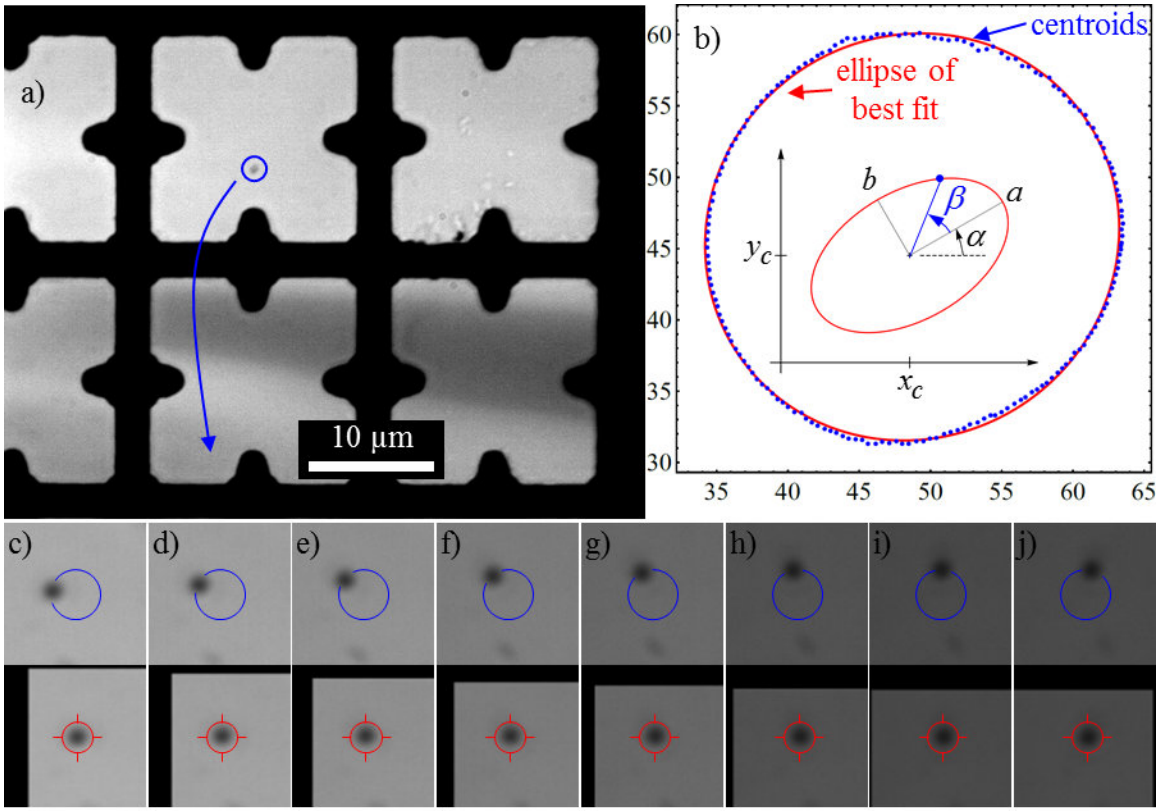

Figure 3.11: Image-shift correction in a division of time polarimeter. (a) A piece of debris on a resolution target is tracked as the analyzer rotates. (b) An ellipse of best fit is used to correct for the image shift. (c-j) Several stills of the raw (top) and corrected (bottom) images are shown, through the first roughly ¼ revolution. The centering of the red reticle indicates the level of accuracy in this correction.

3.2.4 HSV color composition

Figure 3.12 shows the polarimetric imaging of a tightly focused vortex beam, where the "bare" beam has been focused through the glass substrate only (*i.e.* no coaxial apertures). The top surface of the glass substrate was positioned by an *xyz*-piezo stage at the common focus of the dual microscope system sketched in Figure 3.8. Figure 3.12-a) shows an image of the "bare" beam acquired without any analyzer. There is no polarimetric information in Figure 3.12-a).

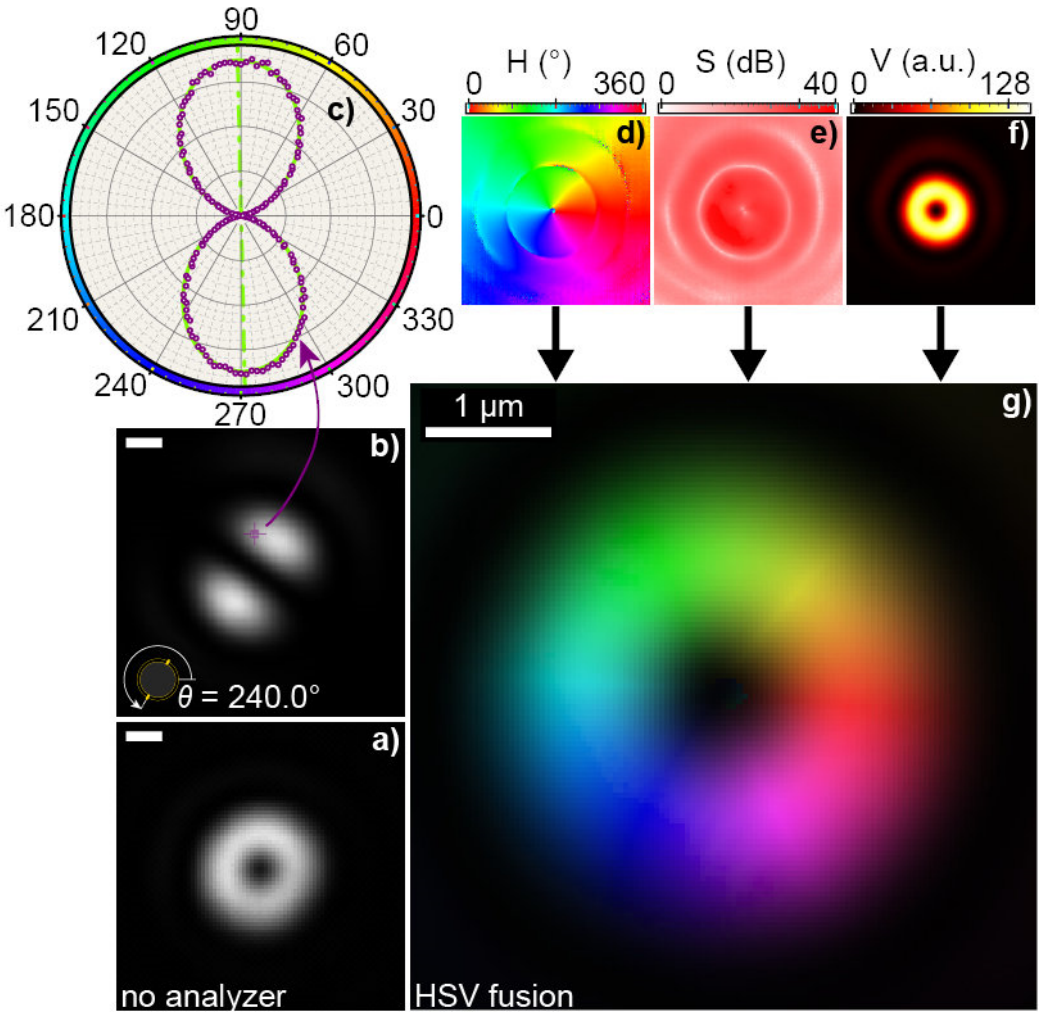

Figure 3.12: Polarimetric imaging - HSV color fusion. (a) Donut beam imaged without an analyzer and (b) with an analyzer at 240.0°. (c) Polarization trace from a pixel outlined with a purple reticle in (b). (d-f) Polarization information is used to raster three color channels which are combined (g) into a 24-bit color fusion image. Scale bars: 1 µm.

Figure 3.12-b) shows an image of the beam filtered through an analyzer oriented at 240.0° *w.r.t.* the CMOS x-axis, picking off two lobes with polarization parallel to the analyzer's transmissive axis. Note that if the analyzer position was not known absolutely, then Figure 3.12-a) and -b) alone could only indicate that the beam is in either the radial or in the azimuthal polarization state. They could, at least, rule out vortices with aligned spin and

orbital helicities [97], but not more. With the absolute θ known, however, Figure 3.12-a) and -b) already indicate the beam is likely radially polarized. But to decipher more clearly, instead of acquiring a single image, a series of images is acquired over a set of θ.

The accumulated images form layers of a stack, and at each pixel in the stack I sampled the grayscale intensities with a 5×5 Gaussian kernel. For example, the purple reticle in Figure 3.12-b) points to a single pixel. I sampled that pixel's intensity (and some nearest neighboring pixels) from each of a 180 images and plotted that intensity as purple circles in polar coordinates on Figure 3.12-c). There is nothing special about the purple-marked pixel, it is a result typical of any pixel in the "bare" beam images. Note that the purple-marked pixel, which is due North of the vortex beam's topological singularity is brightest when the analyzer points North (or South). This is indicative of a radial polarization. The sampled grayscale intensities I can be fit to Malus' law

$$I = I_0 + I_1 \cos^2\left(\theta - \varphi\right). \tag{3.33}$$

Here I_0 is the non-plane polarized intensity, I_1 is the plane polarized intensity, and φ is the AOLP. From the three fitting parameters, I_0, I_1, and φ, I raster three channels of polarimetric information, shown in Figure 3.12-d) through -f), and I combine them into a 24-bit color fusion image shown in Figure 3.12-g) by mapping them into a cylindrical color space [117], [118]. I used the standard mappings for hue and value,

$$\mathrm{H} = \varphi, \tag{3.34}$$

$$\mathrm{V} = \frac{I_0 + I_1}{2}, \tag{3.35}$$

but I plotted the saturation using a log-scale and color-coded using a cube root:

$$S = \sqrt[3]{10\log_{10}\left(\frac{I_0 + I_1}{I_0}\right)}. \tag{3.36}$$

I used this non-linear color-coding to reveal more easily [119] the AOLP. Even though Equation (3.33) is periodic every 180°, in the fitting regression routine I allowed φ up to 360° by seeding the fit with the polar angle ϕ (see Figure 2.1) that the pixel makes *w.r.t.* the topological singularity. For example, for the purple-marked pixel in Figure 3.12-b), I would seed the regressive fit with $\varphi \sim 90°$ (not 270°) (or, I guess, not any other angle). The HSV-fusion image therefore encodes polarization information colorimetrically [120]–[122]. The fit curve, drawn in green underneath the sampled grayscale intensities, is colored green in accord with the angular hue scale. To the best of my knowledge, this work is the first to apply a full three-channel HSV-fusion method to the polarimetric imaging of a cylindrical vortex beam, although several other works [123], [124] have used a similar two-channel approach. In concert with the color scales above, Figure 3.12-g) indicates unambiguously the "bare" beam is radially polarized.

While the incomplete imaging polarimeter here cannot resolve the difference, for example between random- and circular-polarization, there is no need for the purposes of this work to make that distinction. Figure 3.12-e) (the S-channel) and Equation (3.36) show that the beam is predominantly linearly polarized, with an extinction ratio of 20 dB being typical. Note that the apparatus could be modified into a Stokes/Muller imaging polarimeter by adding a waveplate into the tube-space of the upright microscope drawn in Figure 3.8. A full Stokes image, bearing one additional piece of information at each pixel, could be color-fused using the alpha channel of a 32-bit image. In Section 4.3.1 this

apparatus is used to observe the transmission of the donut beam by nanocoaxial waveguides.

3.3 Near-Field scanning optical microscopy

I used a MultiView 4000 (Nanonics Inc.) near-field scanning optical microscope (NSOM) to probe the near field intensity of samples in various nanophotonics experiments. Figure 3.13 shows a schematic of an NSOM. It is nearly the same optical setup as presented in Figure 3.8, with one major difference: the objective lens on the upright microscope needs a long working distance (LWD), at least 15 mm, in order to accommodate a quart tuning fork (QTF) based fiber optic NSOM probe. An SEM image of the Ø250 nm metallized aperture probe is shown in Figure 3.13-a).

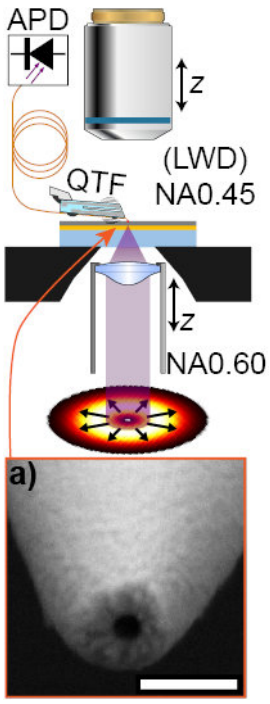

Figure 3.13: Near-field scanning optical microscope. (above) Schematic of the optical setup. Also drawn, as an example, is backside illumination by a radially polarized optical vortex. The inset (a) shows SEM image of the Ø250 nm apertured fiber probe. Scale bar: 1 µm.

In most cases, the space gained by using an LWD objective, comes at a sacrifice in optical performance. There are specialized LWD objectives which can mitigate this trade-off. But very often one must sacrifice on the numerical aperture; this apparatus is equipped with a NA0.45 LWD objective and the ramifications of this sacrifice are resolved more clearly in Section 4.3.2. Some experimental NSOM data are shown in Figure 4.26.

3.4 Plasmonics

A plasmon is a density wave in a gas of free charges [125]. Metals can be described as a gas of free electrons, which collide with their environment (*i.e.* the Drude model) [126]. For the purposes of optical confinement [127], a surface plasmon (SP) is the wave of charge density and accompanying electromagnetic fields which are trapped against the surface of a metal, right at the interface it shares with an adjacent insulator. So, an SP is bound to an MI interface. By coupling light into the motion of free charges in the metal, the wave slows down significantly compared to light moving through just the insulator alone, thereby "shrinking" the wavelength of the light trapped against the surface. SP waves are a resonant material response; for any given material they are excited much more prominently at some free space wavelengths than at others, and different materials respond with different strengths. So plasmonics are a resonant means of optical confinement. This resonance stems from the bulk plasma frequency,

$$\omega_p = \sqrt{4\pi \frac{ne^2}{m}}, \tag{3.37}$$

which is determined by the density of free charges, n, by the charge e per carrier, and by the carrier mass m. Note that n means different things in Equations (3.16) and (3.37).

Equations (2.1) - (2.12) of [128] give some very useful mathematical formulae to describe the properties of a SP wave.

Most familiar metals, with a density of free electrons on the order of $n \sim 10^{23}$ cm^{-3}, have a resonant frequency typically in the UV, in excess of $f_p > 800$ THz (free space wavelengths shorter than 0.4 μm). However, practically speaking, only some metals exhibit useful SP confinement. In most metals, at energies higher than *ca*. 1 eV (wavelengths shorter than *ca*. 1 μm) there are absorption pathways not accounted for by the Drude model, and this absorption often prevents one from exploiting the "exotic" aspects of an SP resonance. Within the theoretical framework of Section 3.1.2.2, the measured optical constants for Ag, Au, and Cu (from [129]) and for Al (from [130]) are given in Figure 3.14.

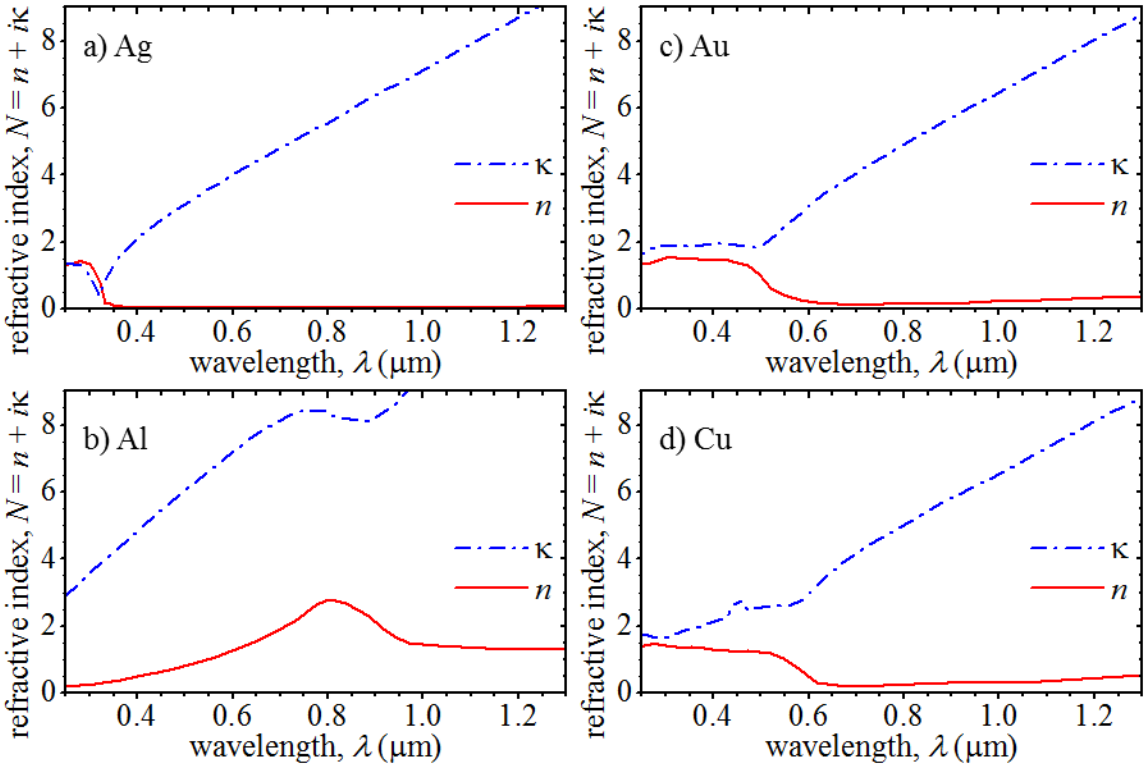

Figure 3.14: Optical constants for Ag, Al, Au, and Cu. (a), (c), and (d) are from [129], and (b) is from [130]. One can see how Ag differs from the rest. Some would say Ag is the gold standard of plasmonic metals.

Some of the useful properties of a SP wave can be identified from its dispersion relation, which, for any wave, connects a wave's frequency and wavelength. Equation (2.4) from [128] gives the dispersion relation of a SP wave traveling along a planar MI interface, and Equation (2.3) from [128] gives the length scale at which the SP is trapped onto the planar surface. I have plotted the dispersion relation for two planar metal/Al_2O_3 interfaces in Figure 3.15. The two metals I considered are Ag (panels (a-c)) and Pt (panels (d-f)) with the optical constants for Ag from [129], Pt from [131]. For the insulator, I used the Al_2O_3 optical constants from the Cauchy fit given in Equation (4.28). More discussion on the Pt and Al_2O_3 optical constants can be found in Section 4.2.2.3.

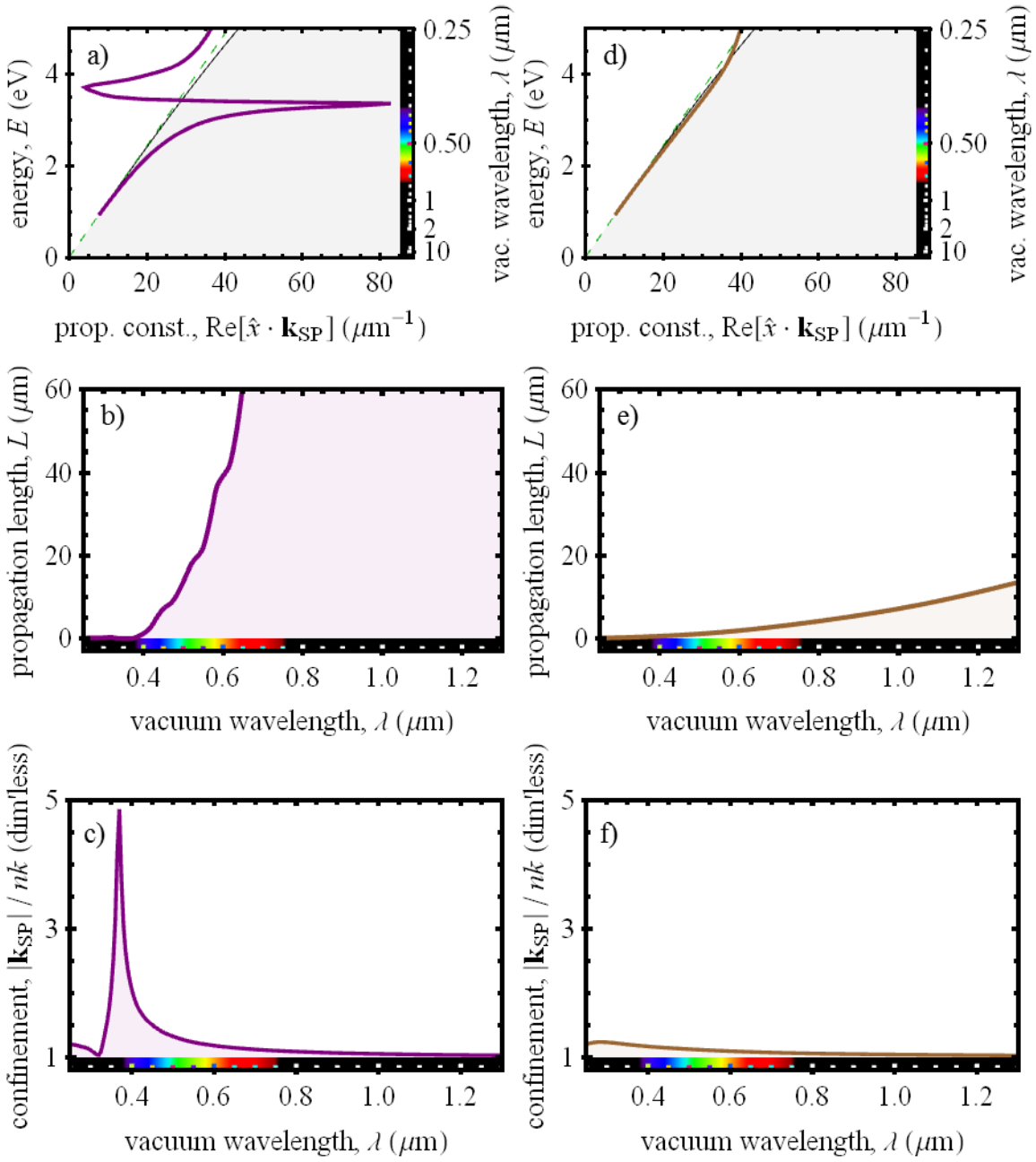

Figure 3.15: SP dispersion on a planar metal/Al_2O_3 interface. (a-c) Ag exhibits a high-Q SP resonance at $\lambda \sim 0.375$ μm. (d-f) Pt does not strongly resonate. The three rows are: dispersion curve, propagation length, and confinement factor.

Equations (2.3) and (2.4) from [128] give the SP wavevector,

$$\mathbf{k}_{SP} = k_{SP,x}\hat{x} + k_{SP,z}\hat{z}\,. \tag{3.38}$$

Note that the assumed y-component of $\mathbf{k}_{\mathrm{SP}}$ is zero, so that the SP waves, propagating along $\hat{x}$, are of infinite extent in the $\hat{y}$-direction , much like plane waves. Therefore, planar SP waves are only confined in two dimensions, along the $\hat{x}$- and $\hat{z}$-directions . The electromagnetic fields which accompany the charge oscillation in an SP wave,

$$\mathbf{E}_{\mathrm{SP}} = E_{\mathrm{SP},x}\hat{x} + E_{\mathrm{SP},z}\hat{z}\,, \tag{3.39}$$

$$\mathbf{H}_{\mathrm{SP}} = H_{\mathrm{SP},y}\hat{y} + H_{\mathrm{SP},z}\hat{z}\,, \tag{3.40}$$

are polarized transverse magnetic (TM). Some refer to the fields themselves as a "polariton", so that the oscillating charges and accompanying fields are together called a surface plasmon polariton (SPP). However, the plasmonic charge and fields are always inextricably linked, they always accompany each other. It is not as if one could ever possibly separate an SP wave clearly into charge and field parts. SP is a simpler term, so I prefer it. But I believe that SP and SPP are interchangeable terms, always describing the same plasmonic surface wave.

Figure 3.15-a) and -d) show the SP dispersion relations for planar $\mathrm{Ag}/\mathrm{Al_2O_3}$ and $\mathrm{Pt}/\mathrm{Al_2O_3}$ interfaces, plotting the wave's energy $E = \hbar\omega$ *vs.* its propagation constant $\mathrm{Re}\left(k_{\mathrm{SP},x}\right)$. There are many useful pieces of information which can be extracted from a wave's dispersion curve. For starters, the black curve which separates the shaded-white and shaded-gray areas on the left- and right-hand sides of the plots, respectively, demarcates the boundary between photonic and plasmonic behavior. Note that this boundary is itself a dispersive curve, where the tangential dashed green line is intended to approximate the long-λ optical response of $\mathrm{Al_2O_3}$. Although that green line totally neglects to account for vibrational or other low energy resonances in $\mathrm{Al_2O_3}$, which has

many features in the range $10 < \lambda < 30$ μm. The curvature in Equation (4.28) at shorter wavelengths is due to the long tail of UV absorption near $\lambda \sim 0.1$ μm. One should note that Equation (4.28), with a purely real N, one does not faithfully account for these features outside of $0.25 < \lambda < 1.3$ μm, and is technically Kramers-Kronig inconsistent.

Even though the boundary is curved, it is conventionally referred to it as the light "line". The SP dispersion curve has two branches. Below resonance, where the dispersion is entirely to the right of the light line, such that $\mathrm{Re}\left(k_{\mathrm{SP},x}\right) > n_{\mathrm{Al_2O_3}} k$, the SP wave carries more momentum than could ever be carried by a photon moving through alumina alone. $n_{\mathrm{Al_2O_3}}$ is the alumina refractive index given by Equation (4.28), and k is the vacuum wavenumber given by Equation (2.16). Therefore, SP waves on the lower branch are trapped on the surface, until they are ultimately absorbed by the metal as Ohmic loss.

Above resonance, the dispersion curve is entirely to the left of the light line, such that $\mathrm{Re}\left(k_{\mathrm{SP},x}\right) < n_{\mathrm{Al_2O_3}} k$, and the SP wave can now couple into photons moving through the bulk of either the metal or the alumina, with the former typically being very strongly absorbing in the UV. The SP waves above resonance, are not bound to the surface it as they are below resonance. Above resonance, SP waves can dissipate not only by absorption in the metal but also by escaping the surface and leaking into radiation.

So, the parts to the left and right of the light line are called "photonic" and "plasmonic", respectively. While this demarcation is useful for the above technical reasons, it is not perhaps entirely faithful in its name: all parts of the dispersion curve are plasmonic, the waves are the combined oscillation of charges and accompanying fields; so whether or not they can be separated as either "plasmonic" or "photonic" in their nature by whether or

not they are bound to the surface is unclear to me. In any case, while the two branches are connected (no gaps), the upper branch describes a plasmonic wave that is no longer bound to the surface. In principle, that upper branch is at frequencies where the metal is transparent to light. But in practice this usually isn't the case, usually the metal is absorbing. SP waves are only useful for confinement at frequencies below resonance.

Figure 3.15-b) and -e) show the SP propagation length, L, plotting $1/2\,\mathrm{Im}\left(k_{\mathrm{SP},x}\right)$ *vs.* λ. Figure 3.15-c) and -f) show the plasmonic confinement factor, which is the magnitude of the SP wavevector in ratio against the wavenumber in Al_2O_3, plotting $\left|\mathbf{k}_{\mathrm{SP}}\right|/n_{\mathrm{Al_2O_3}}k$ *vs.* λ. A confinement factor of 1 means that the SP wave has the same wavelength as light moving through alumina, and that it is trapped against the surface on a similar length scale. One can see in Figure 3.15-c) that for Ag the confinement factor on resonance, near $\lambda \sim 0.375$ μm, can be as high as 5. Note that the SP resonance depends on geometry as well, Figure 3.15 only considers a planar MI geometry. The confinement factor is never less than 1 (superluminous), and regardless how close or far one is from the SP resonance, one should note that the existence of SP waves bound to the MI interface is a topologically robust feature [125] due simply to the very existence of that interface. This means that even very far below resonance, indeed arbitrarily so, there is an SP wave trapped on the MI interface. In the long-λ limit, these are called Sommerfeld-Zenneck waves [132], [133], and while trapped on the surface, they are not confined at all to subwavelength scales. Therefore, in the long-λ limit of Figure 3.15-c) and -f), the confinement factor asymptotically approaches unity, regardless of the MI combination.

4 NANOCOAXIAL WAVEGUIDES

This Chapter is divided into 5 Sections. In Section 4.1 I cover the theoretical basis for optical confinement in nanocoaxial waveguides. Section 4.2 covers various fabrication schemes to achieve a coaxial MIM geometry. Section 4.3 summarizes some experimental results in optically interrogating these structures by polarimetric imaging and NSOM. Section 4.4 covers a finite element calculation which examines the coupling of free-space radiation at terminations of these waveguides and to study 3D taper geometries; the axisymmetry shared by LG_p^l beams and coaxial modes is used to dramatically reduce the computational burden. Finally, Section 4.5 offers some conclusions and future directions of work.

4.1 Elements of waveguide theory

Any waveguide can be treated as an extrusion of a two-dimensional cross section, with a coaxial waveguide having extruded annular layers. I will consider a coaxial MIM waveguide with a single, annular $\mathrm{Al_2O_3}$ insulator and having dimensions

$$\text{Ø}_{\mathrm{ID}} = 2a = 0.2\ \mu\mathrm{m} \qquad \text{Ø}_{\mathrm{OD}} = 2b = 0.5\ \mu\mathrm{m}, \tag{4.01}$$

where Ø_{ID} and Ø_{OD} are the inner and outer diameters, with a and b being the respective radii. The outer-to-inner aspect ratio,

$$\Phi = \frac{\text{Ø}_{\mathrm{OD}}}{\text{Ø}_{\mathrm{ID}}} = \frac{b}{a} = 2.5, \tag{4.02}$$

is a useful metric for predicting the waveguide properties. In this Section, I will highlight some key elements of waveguide theory, not rederiving already established results. The

interested reader should see any number of standard textbooks [3], [134], [135] for a comprehensive overview of waveguide theory, and in particular the 2nd Chapters of [136] and [137]. Most of the work here will be merely to cast those previously published results into the mathematical language I've been using in Chapters 2 and 3.

The aim of this Section is to write down the modal solutions for the fields of the two lowest-order modes in a coaxial waveguide. Regardless of the diameters $Ø_{ID}$ and $Ø_{OD}$, and even regardless of the frequency or materials, the lowest energy, fundamental mode has electromagnetic fields which resemble a transverse electromagnetic (TEM) wave, and the first excited mode has fields which resemble a transverse electric (TE) wave. Higher order coaxial modes are indexed as either TE_{lp} or TM_{lp} (TM being short for "transverse magnetic"), with the integer indices l and p serving much the same function as the LG_p^l beams covered in Section 3.1.2, accounting for the ϕ- and ρ-dependencies, respectively. The TEM and TE_{11} modes are pictured schematically in Figure 4.1. These modes have monopolar $(l=0)$ and dipolar $(l=1)$ character, respectively, and will be shown to overlap well with corresponding electromagnetic LG_p^l beams.

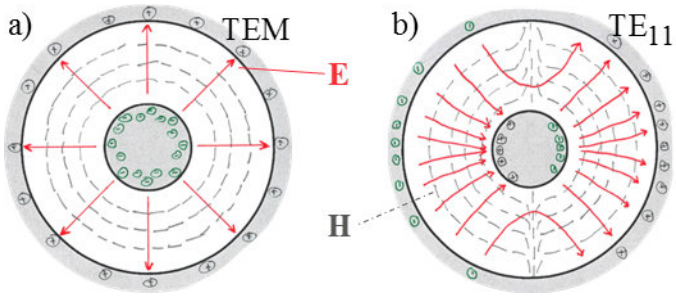

Figure 4.1: First two coaxial modes, TEM and TE_{11}. Adapted from [3].

Coaxial waveguides, bearing continuous translational and rotational symmetries, as in the cylindrical coordinates depicted in Figure 2.1, impart onto the modal fields the following ϕ- and z-dependencies , with $\mathbf{F}$ being either $\mathbf{E}$ or $\mathbf{H}$, as in Section 3.1.2.2, and omitting the harmonic time dependence in Equation (2.04),

$$\mathbf{F}_l \propto \left(Re^{-il\phi} + Le^{+il\phi} \right) e^{ik_z z}, \tag{4.03}$$

for a given angular order l, as in Equation (2.05). k_z is the propagation constant and has exactly the same meaning as in Equations (2.14) and (2.17). The standard theoretical approach to finding waveguide modal fields which solve the time-harmonic Maxwell's Equations (3.11)-(3.14), is to decompose them into the transverse $\mathbf{F}_\perp$ and longitudinal F_z parts. In cylindrical coordinates, and incorporating the z-dependence of Equation (4.03), the transverse/longitudinal decomposition of Maxwell's equations becomes

$$E_\rho = \frac{i}{k_\rho^2}\left(k_z \frac{\partial E_z}{\partial \rho} + \omega\mu_0 \frac{1}{\rho}\frac{\partial H_z}{\partial \phi} \right), \tag{4.04}$$

$$E_\phi = \frac{i}{k_\rho^2}\left(k_z \frac{1}{\rho}\frac{\partial E_z}{\partial \phi} - \omega\mu_0 \frac{\partial H_z}{\partial \rho} \right), \tag{4.05}$$

$$H_\rho = \frac{i}{k_\rho^2}\left(k_z \frac{\partial H_z}{\partial \rho} - \omega\varepsilon_0\varepsilon \frac{1}{\rho}\frac{\partial E_z}{\partial \phi} \right), \tag{4.06}$$

$$H_\phi = \frac{i}{k_\rho^2}\left(k_z \frac{1}{\rho}\frac{\partial H_z}{\partial \phi} + \omega\varepsilon_0\varepsilon \frac{\partial E_z}{\partial \rho} \right). \tag{4.07}$$

The duality between $\mathbf{E}$ and $\mathbf{H}$ can be seen in Equations (4.04)-(4.07) above.

4.1.1 PEC/Al_2O_3 coaxial waveguide modes

It is helpful when modeling the optical response of a metallic structure to simplify the problem and treat the metal as if it were a perfect electrical conductor (PEC). This effectively isolates the parts of the structure's response which can be attributed to its geometry alone. PEC modeling eliminates, for example, the SP waves discussed in Section 3.4, so that PEC coaxial modes have non-zero fields only within the alumina insulating annulus. For the PEC/TEM mode, there are no longitudinal components, $E_z = H_z = 0$. So, one cannot follow the standard transverse/longitudinal decomposition they normally would for higher order modes, which always have at least one non-zero F_z. Instead, one sets $l = 0$ with $R = L = 1/2$ and finds,

$$\mathbf{E}_{\mathrm{TEM}}^{\mathrm{PEC}} = E_0 \frac{a}{\rho} e^{ik_z z} \hat{\rho}\,, \tag{4.08}$$

$$\mathbf{H}_{\mathrm{TEM}}^{\mathrm{PEC}} = \frac{E_\rho}{Z_{wave}} \hat{\phi}\,. \tag{4.09}$$

E_0 is the electric field strength at the surface of the center conductor and Z_{wave} is the wave impedance of a plane wave propagating through $\mathrm{Al_2O_3}$. Z_{wave} is computed by dividing the impedance of free space $Z_0 = \sqrt{\mu_0/\varepsilon_0} = 377\ \Omega$ by alumina's refractive index, given as the Cauchy-fit $n_{\mathrm{Al_2O_3}} = n_{\mathrm{Al_2O_3}}(\lambda)$ in Equation (4.28),

$$Z_{wave} = \frac{E}{H} = \frac{Z_0}{n_{\mathrm{Al_2O_3}}}, \tag{4.10}$$

and is related to the characteristic impedance of the PEC coax operating in its TEM mode

$$Z_{\mathrm{TEM}}^{\mathrm{PEC}} = Z_{wave} \frac{\ln \Phi}{2\pi}\,. \tag{4.11}$$

For the free space wavelength $\lambda = 0.98\ \mu\text{m}$, $Z_{\text{TEM}}^{\text{PEC}} = 33.4\ \Omega$. This mode has all the same photonic properties as light traveling through Al_2O_3 alone, including the dispersion relation,

$$\omega_{\text{TEM}}^{\text{PEC}} = ck_z / n_{Al_2O_3}. \tag{4.12}$$

Equation (4.12), in concert with Equation (4.28), must be inverted to find the full dispersion relation $\omega = \omega(k_z)$. Noting the dependence of $n_{Al_2O_3}$ on ω, this means inverting a polynomial of order ω^5. The fields $\mathbf{E}_{\text{TEM}}^{\text{PEC}}$ and $\mathbf{H}_{\text{TEM}}^{\text{PEC}}$, along with the mode dispersion curve, are plotted in Figure 4.2. One could compare the field components for this mode to those of $\mathbf{E}_{\hat{\rho}\text{-donut}}$, plotted in Figure 3.6. The field components were evaluated at the free-space wavelength $\lambda = 0.98\ \mu\text{m}$, which is the black point on the blue dispersion curve. The green, dashed line shows the long-wavelength limit of $n_{Al_2O_3}$, as will be discussed later. The white- and gray-shaded areas to the left- and right-hand side of the dispersion curve have the same meaning as those in Figure 3.15.

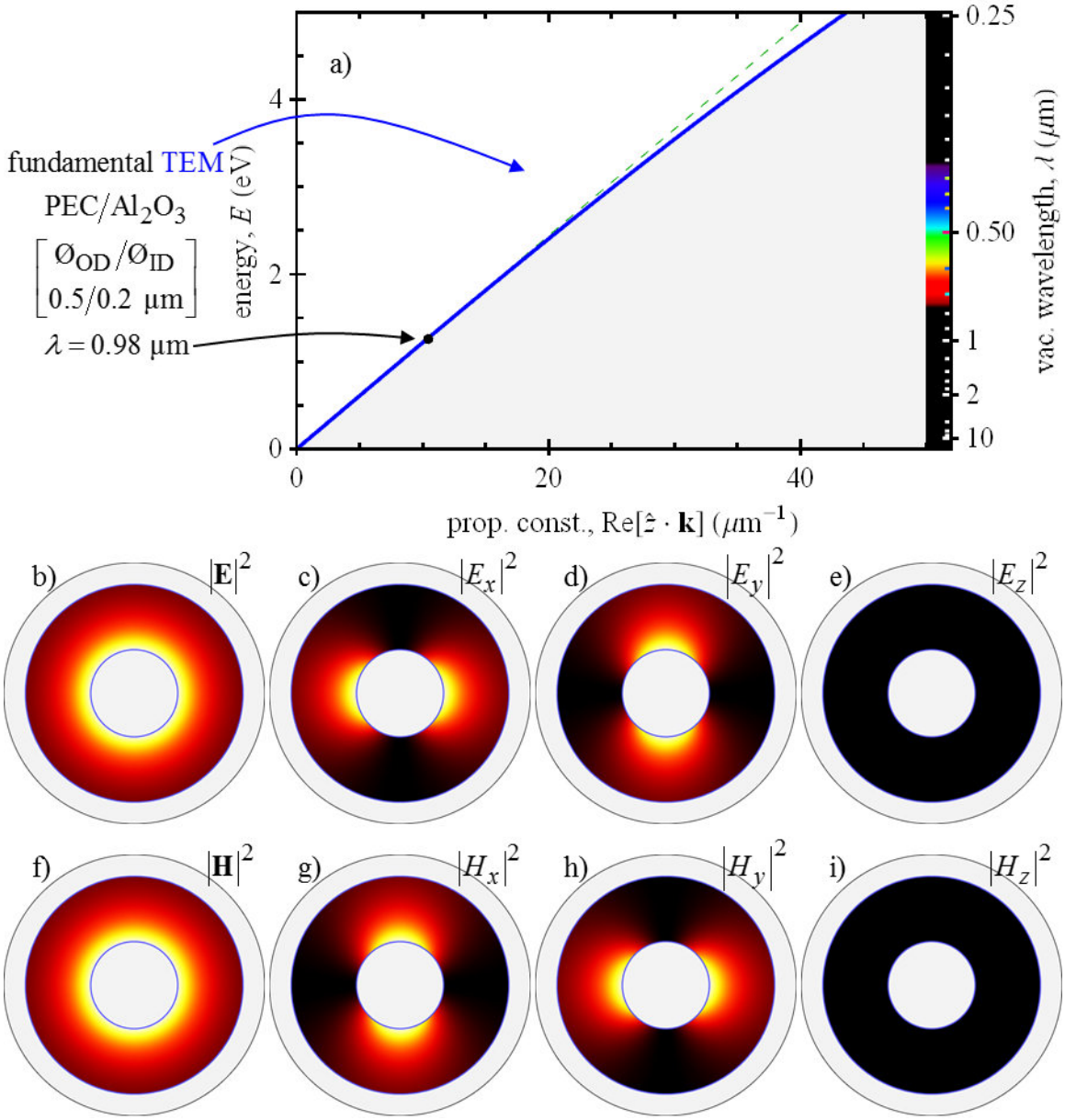

Figure 4.2: TEM mode of a $\mathrm{PEC/Al_2O_3}$ coax. (a) Dispersion curve. (b-i) field components $\mathbf{E}_{\mathrm{TEM}}^{\mathrm{PEC}}$ and $\mathbf{H}_{\mathrm{TEM}}^{\mathrm{PEC}}$. The color scale in (b-i) is the same as in the Figures from Section 3.1.2.

For the TE_{11} mode, one sets $E_z = 0$, $l = 1$, and

$$H_z = iH_0\left(Re^{-i\phi} + Le^{+i\phi}\right)\left(A\,\mathrm{J}_1\left(k_\rho\rho\right) + B\,\mathrm{Y}_1\left(k_\rho\rho\right)\right)e^{ik_z z}, \tag{4.13}$$

where $\mathrm{J}_l(x)$ and $\mathrm{Y}_l(x)$ are Bessel functions of the first and second kind, respectively, of order l, H_0 is a unit of magnetic field strength, say 1 A/μm, and the coefficients A and B are determined by enforcing the boundary conditions at the two PEC/alumina interfaces. The TE, PEC boundary conditions are

$$\begin{aligned} E_\phi\big|_a &= 0 \quad H_\rho\big|_a = 0 \\ E_\phi\big|_b &= 0 \quad H_\rho\big|_b = 0 \end{aligned}. \tag{4.14}$$

So the procedure is to plug Equation (4.13) into in Equations (4.04)-(4.07), and then find the value of k_ρ which satisfies Equations (4.14). With the three unknowns, A, B, and k_ρ, it would at first appear that the problem is overdetermined. But note that Equations (4.14) are all constraints on $\partial H_z/\partial\rho$. So there are not 4 constraints, but really only two, one at each of the radii a and b. In that case, the problem is underdetermined. One way around this is to "absorb" the coefficient B into the value of H_0 and then solve for only two unknowns: k_ρ and the ratio A/B.

Solving for k_ρ is how one finds the cutoff frequency and dispersion relation. One can think of the TEM mode has having $k_\rho = 0$. But for the TE_{11} mode, in essence, the PEC walls of the waveguide dictate that the fields must have nodes at the radii a and b. This condition is satisfied only when at least a "half wave" fits into the radial size of the annulus. That reasoning helps to make clear the textbook formula for the TE_{11} cutoff wavelength, see for example the Equation immediately following (3.159) in [3],

$$\lambda_c^{\mathrm{PEC}} \approx \pi n(a+b), \tag{4.15}$$

where n is the insulator's refractive index. So the cutoff frequency is the minimum ω which can summon enough spatial variation along ρ to put two nodes in the fields, one each at a and b. Another way to put it is that the cutoff is defined as the finite value of ω for $k_z \to 0$ in Equation (2.17). Using the recursive relation for a generalized Bessel's function $G_n(x)$,

$$G_1' = \frac{(G_0 - G_2)}{2}, \tag{4.16}$$

and applying the two conditions on E_ϕ to eliminate A and B, one gets:

$$\frac{\mathrm{J}_0(k_\rho a) - \mathrm{J}_2(k_\rho a)}{\mathrm{Y}_0(k_\rho a) - \mathrm{Y}_2(k_\rho a)} = \frac{\mathrm{J}_0(k_\rho b) - \mathrm{J}_2(k_\rho b)}{\mathrm{Y}_0(k_\rho b) - \mathrm{Y}_2(k_\rho b)}. \tag{4.17}$$

This transcendental equation can only be solved numerically. There are an infinite number of "zero crossings", or roots, to this equation, as Bessel's functions are oscillatory. Those zero crossings are enumerated by the integer index $p \geq 1$. After finding the first ($p = 1$) value of k_ρ which solves Equation (4.17), one has the dispersion relation from inverting Equation (2.17),

$$\omega_{\mathrm{TE}_{11}}^{\mathrm{PEC}} = \sqrt{\left(ck_z / n_{\mathrm{Al_2O_3}}\right)^2 - k_\rho^2}\,. \tag{4.18}$$

To find the cutoff free-space wavelength λ_c, one must then invert $k_\rho = 2\pi n_{\mathrm{Al_2O_3}}(\lambda_c)/\lambda_c$, where the refractive index $n_{\mathrm{Al_2O_3}}$ is from Equation (4.28). For the coaxial diameters given by Equations (4.01), I calculate $\lambda_c^{\mathrm{PEC}} = 1.741\ \mu\mathrm{m}$. Note that if I use the "long wavelength" or "low energy" limit of Equation (4.28), as discussed in Section 3.4, so that $n_{\mathrm{Al_2O_3}}$ takes its limiting form $n_{\mathrm{Al_2O_3}} \to n_\infty = 1.6176$ and loses its

frequency-dependence, then I calculate $\lambda_c^{\text{PEC}} = 1.738\ \mu\text{m}$. This makes intuitive sense: a slightly higher refractive index, such as one which includes the Cauchy terms, should be able to "shrink down" a slightly longer wavelength. Looking at Figure 4.14-b), one can imagine how including the Cauchy terms becomes increasingly important at shorter wavelengths (higher energies), where one expects to find the cutoff of smaller diameter waveguides. One should contrast the result from finding the root to Equation (4.17) with results from the approximate formula, Equation (4.15). In the same sequence as before, using the Cauchy terms of Equation (4.28) and then inverting Equation (4.15) results in $\lambda_c^{\text{PEC}} = 1.781\ \mu\text{m}$, and without the Cauchy terms the result is $\lambda_c^{\text{PEC}} = 1.778\ \mu\text{m}$. It's the same pattern: including the Cauchy terms lengthens the cutoff wavelength (*i.e.* lowers the frequency, or energy), however one can see that Equation (4.15) overshoots by roughly 3% for these diameters. With the cutoff value of k_ρ found, the ratio A/B is found by

$$\frac{A}{B} = -\frac{\text{Y}_0\left(k_\rho a\right) - \text{Y}_2\left(k_\rho a\right)}{\text{J}_0\left(k_\rho a\right) - \text{J}_2\left(k_\rho a\right)}. \tag{4.19}$$

For the diameters of Equations (4.01), I find $k_\rho = 5.8471\ \mu\text{m}^{-1}$ and $A/B = -4.2878$.

A TE_{11} mode can take on one of two degenerate, orthogonal polarizations. In cylindrical coordinates, this can be seen by setting either R or L equal to zero in Equation (4.13) (but not both), resulting in either a left- or right-hand circulating mode, respectively. In Cartesian coordinates, the two orthogonal polarizations are a predominantly $\hat{x}$-oriented or a predominantly $\hat{y}$-oriented mode. For a circular coax, these modes have the same cutoff. Breaking the rotational symmetry, for example by deforming the coax into ellipses [138], breaks the degeneracy by lowering the cutoff energy for one of the polarizations (*i.e.*

lengthening its cutoff wavelength). Figure 4.1-b) sketches a predominantly $\hat{x}$-oriented TE_{11} mode. Much like what was done for Equation (3.27) for an $\hat{x}$-polarized Gaussian beam, one can make the $\hat{x}$-oriented TE_{11} mode as a superposition of copropagating right- and left-handed circulating modes. Isolating the radial dependence into the dimensionless functions u and v,

$$u(\rho) = \left\{ \frac{A}{B} \mathrm{J}_1(k_\rho \rho) + \mathrm{Y}_1(k_\rho \rho) \right\}, \tag{4.20}$$

$$\begin{aligned} v(\rho) &= \frac{1}{k_\rho} \frac{du}{d\rho} \\ &= \frac{1}{2} \left\{ \frac{A}{B} \left(\mathrm{J}_0(k_\rho \rho) - \mathrm{J}_2(k_\rho \rho) \right) + \mathrm{Y}_0(k_\rho \rho) - \mathrm{Y}_2(k_\rho \rho) \right\}, \end{aligned} \tag{4.21}$$

and using dimensionless the normalization factor,

$$C = \frac{k_\rho a}{|u(a,0)|} = 0.234902\ldots, \tag{4.22}$$

the $\hat{x}$-oriented TE_{11} mode fields are:

$$\mathbf{E}^{\mathrm{PEC}}_{\hat{x}\text{-}\mathrm{TE}_{11}} = \frac{E_0}{C} \left(-\frac{u \cos\phi}{k_\rho \rho} \hat{\rho} + (v \sin\phi) \hat{\phi} \right) e^{ik_z z} \tag{4.23}$$

$$\mathbf{H}^{\mathrm{PEC}}_{\hat{x}\text{-}\mathrm{TE}_{11}} = \frac{k_z}{\omega \mu_0} \frac{E_0}{C} \left(-v \sin\phi \hat{\rho} - \frac{u \cos\phi}{k_\rho \rho} \hat{\phi} + i \frac{k_\rho}{k_z} u \sin\phi \hat{z} \right) e^{ik_z z}. \tag{4.24}$$

The factor $\omega\mu_0 / k_z$ is identified as the wave impedance, as in Equation (4.10). Note that the criterion for cutoff demands $k_z \to 0$, such that the wave impedance diverges. The fields $\mathbf{E}^{\mathrm{PEC}}_{\hat{x}\text{-}\mathrm{TE}_{11}}$ and $\mathbf{H}^{\mathrm{PEC}}_{\hat{x}\text{-}\mathrm{TE}_{11}}$ were evaluated at the free-space wavelength $\lambda = 0.98$ μm,

well above cutoff, and are plotted along with their dispersion curve in Figure 4.3. One should compare these fields to $\mathbf{E}_{\hat{x}\text{-Gaussian}}$ plotted in Figure 3.5.

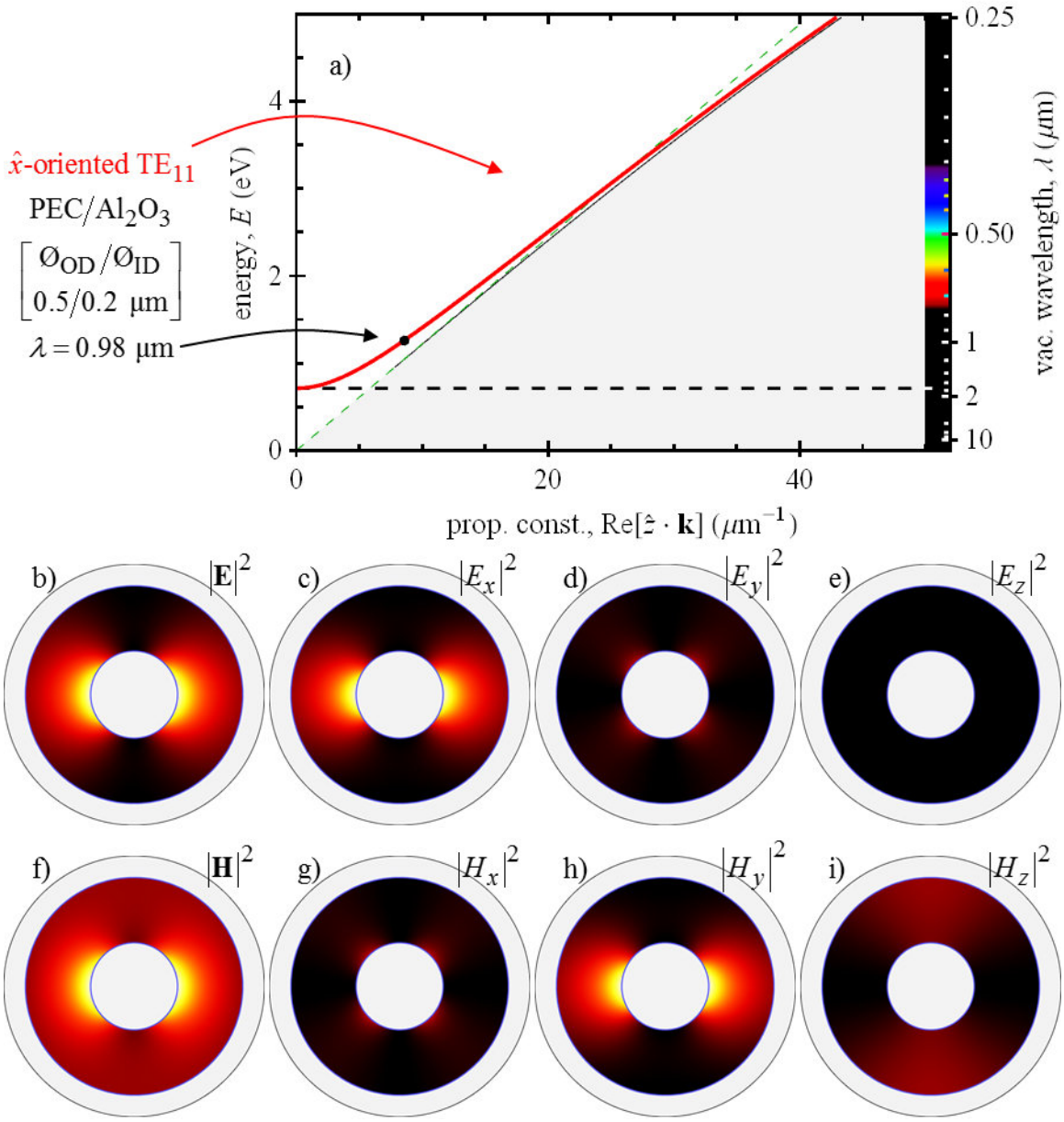

Figure 4.3: TE$_{11}$ mode of a PEC/Al$_2$O$_3$ coax. (a) Dispersion curve. (b-i) field components $\mathbf{E}^{\text{PEC}}_{\hat{x}\text{-TE}_{11}}$ and $\mathbf{H}^{\text{PEC}}_{\hat{x}\text{-TE}_{11}}$. The color scale in (b-i) is the same as in the Figures from Section 3.1.2.

Three things are worth immediate mention. First, at a glance it appears that Equations (4.23) and (4.24) do not at all account for the material response of the alumina insulator, with no explicit dependence on the refractive index given in Equation (4.28). However, the insulator's optical response is buried into $k_z = k_z(\omega)$ through Equation (2.17), so the dependence is implicit. Second, the black point in Figure 4.3 lies on the modal dispersion curve, but to the left of the light line. The light "line", for this PEC waveguide, is the blue dispersion curve in Figure 4.2, and the ratio of k_z-values at the black point to the light line at the same energy hc/λ is basically a measure of "how much of nk is required for k_ρ," with a smaller proportion required at higher energies (*i.e.* where the modal dispersion curve converges with the light light). Third, a waveguide's characteristic impedance is not unambiguously defined when operating in a higher order mode, since the measured voltage and currents depend *when* and *where* on the conductors one measures them. The voltage and current can be computed by carefully chosen path integrals. For the $\hat{x}$-oriented TE_{11} mode, there are natural paths to choose for the voltage integral [139], for example walking from $\rho = a$ to a at $\phi = 0°$. But the currents of a TE_{11} mode have a someone more complicated, frequency dependent spatial distribution: far above cutoff, the currents flow basically along $\pm\hat{z}$ and the magnetic field is dominantly $\mathbf{H}_\perp$ oscillating in phase with $\mathbf{E}_\perp$ (and with a similar spatial distribution); however approaching cutoff the current flow is principally along $\pm\hat{\phi}$ with the magnetic field dominantly H_z oscillating 90° out of phase with $\mathbf{E}_\perp$ (and with a very different spatial distribution).

Equation (4.24) for $\mathbf{H}^{\text{PEC}}_{\hat{x}\text{-TE}_{11}}$ could be compared against Equation (3.27) for the electric field of an $\hat{x}$-polarized Gaussian beam. A few common threads emerge: First, the longitudinal component oscillates out of phase with the transverse components. Second, the longitudinal component F_z is related to an angle the wave makes with the optical axis. In the case of $\mathbf{E}_{\hat{x}\text{-Gaussian}}$, this was the beam divergence angle θ_{beam}. For the TE_{11} mode, and especially considering Equation (2.14), this is the tangent of the angle the wavevector makes in the waveguide. One can think of the TE_{11} (and all higher order) guided mode as bouncing off the metallic walls (in this case by perfect reflection at the PEC/alumina interface). In contrast, the TEM mode can be thought of propagating exactly along the $\hat{z}$-direction, making no angle *w.r.t.* the waveguide axis, and never bouncing, but simply skimming off the walls. It is common to refer to θ_{bounce} as the "bounce" angle,

$$\tan\theta_{\text{bounce}} = \frac{k_\rho}{k_z}. \tag{4.25}$$

For the coaxial diameters in Equations (4.01), the free space wavelength $\lambda = 0.98$ μm corresponds to $\theta_{\text{bounce}} = 34.2°$, see Figure 4.3. Forth, and finally, in the limit that $k_z \to 0$ (i.e. at cutoff, where $\theta_{\text{bounce}} \to 90°$), the longitudinal component of H_z dominates over the transverse components $\mathbf{H}_\perp$. This is not dissimilar, in light of the $\mathbf{E}/\mathbf{H}$ duality, from the longitudinal component of $\mathbf{E}_{\hat{x}\text{-Gaussian}}$ vanishing as $\theta_{\text{beam}} \to 0°$.

4.1.2 Overlap between PEC nanocoax modes and LG beams

The TEM mode given by Equations (4.08) and (4.09) has a strong overlap with the paraxially focused, radially polarized donut beam, with an electric field given by Equation

(3.30). Similarly, the $\hat{x}$-oriented TE_{11} mode given by Equations (4.23) and (4.24) has a strong overlap with the focal fields of an $\hat{x}$-polarized Gaussian beam, with an electric field given by Equation (3.27). A similar observation has been made for the overlap of LG beams with the guided modes of a hollow cylindrical waveguide [140]. This can be readily seen by visual inspection of the field plots in Figure 4.4.

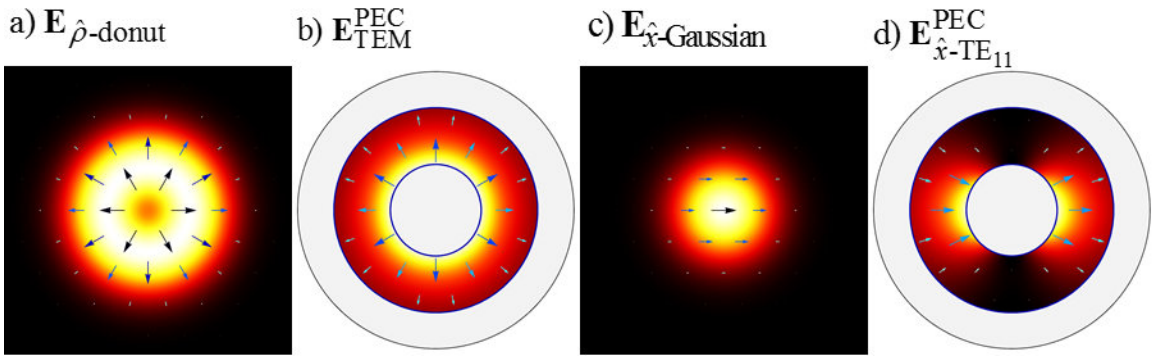

Figure 4.4: Matching LG_p^l beams to PEC coax modes. (a-b) a radially polarized donut matches the TEM mode. (c-d) An $\hat{x}$-polarized Gaussian matches an $\hat{x}$-oriented TE_{11} mode.

The coaxial diameters $Ø_{\mathrm{OD}}/Ø_{\mathrm{ID}} = 3.25/1.45$ μm in Figure 4.4 were chosen to match the beam waist, $2w_0 = 2 \cdot 0.98\ \mu\mathrm{m}/(\pi \cdot 18.1°) \approx 1.97\ \mu\mathrm{m}$, as described in Section 3.1.2.2. The overlap integral between the electric fields $\mathbf{E}_{\mathrm{beam}}$ and $\mathbf{E}_{\mathrm{mode}}$ of an LG beam and coaxial waveguide mode, respectively, was calculated by

$$M = \frac{\left|\int dA \mathbf{E}_{\mathrm{beam}}^{*} \cdot \mathbf{E}_{\mathrm{mode}}\right|^2}{\int dA \left|\mathbf{E}_{\mathrm{beam}}\right|^2 \int dA \left|\mathbf{E}_{\mathrm{mode}}\right|^2}. \tag{4.26}$$

So that $0 \le M \le 1$ measures the strength of overlap. Table 4.1 shows that "large" coaxial diameters, as those presented in Figure 4.4, can harvest a substantial fraction of the focused

beam's power. Since both $\mathbf{E}^{\text{PEC}}_{\hat{x}\text{-TE}_{11}}$ and $\mathbf{E}_{\hat{x}\text{-Gaussian}}$ have a $\cos\phi$ dependence while both $\mathbf{E}^{\text{PEC}}_{\text{TEM}}$ and $\mathbf{E}_{\hat{\rho}\text{-donut}}$ have no ϕ-dependence, it is possible to show analytically the diagonal elements in Table 4.1 are equal exactly to zero, however in light of the fact that the waveguide modes $\mathbf{E}^{\text{PEC}}_{\text{TEM}}$ and $\mathbf{E}^{\text{PEC}}_{\hat{x}\text{-TE}_{11}}$ are defined only in terms of the numeric parameters k_ρ and the ratio A/B, it is simpler to solve Equation (4.26) numerically for M than to write out the analytic results. In that sense, the diagonal entries with $M < -330$ dB could be taken as an indication of that numerical accuracy.

	$\mathbf{E}_{\hat{x}\text{-Gaussian}}$	$\mathbf{E}_{\hat{\rho}\text{-donut}}$
$\mathbf{E}^{\text{PEC}}_{\text{TEM}}$	$<10^{-35}$	61.35%
$\mathbf{E}^{\text{PEC}}_{\hat{x}\text{-TE}_{11}}$	18.25%	$<10^{-33}$

Table 4.1: LG^l_p beam to coaxial waveguide mode overlap: large coaxial diameters. The coaxial diameters $Ø_{\text{OD}}/Ø_{\text{ID}} = 3.25/1.45$ μm harvest a substantial fraction of the $2w_0 = 1.97$ μm beam's power. The table entries show values of M from numerically solving Equation (4.26).

Figure 4.4 and Table 4.1 are meant to show that appropriately-sized coaxes can harvest a substantial fraction of an LG^l_p beam's power. For completeness, since this Section deals instead with "small" coaxial diameters given by Equation (4.01), I have also computed the overlap of the paraxial beam into those "small" waveguides and summarized the results in Table 4.2.

	$\mathbf{E}_{\hat{x}\text{-Gaussian}}$	$\mathbf{E}_{\hat{\rho}\text{-donut}}$
$\mathbf{E}_{\text{TEM}}^{\text{PEC}}$	$<10^{-34}$	0.50%
$\mathbf{E}_{\hat{x}\text{-TE}_{11}}^{\text{PEC}}$	5.70%	$<10^{-35}$

Table 4.2: LG_p^l beam to coaxial waveguide mode overlap: small coaxial diameters. The coaxial diameters $Ø_{\text{OD}}/Ø_{\text{ID}} = 0.5/0.2$ μm do not harvest a substantial fraction of the $2w_0 = 1.97$ μm beam's power. The table entries show values of M from numerically solving Equation (4.26).

4.1.3 Real-metal/Al_2O_3 coaxial waveguide modes

A PEC has a complex refractive index $N_{\text{PEC}} = 0 + i\infty$. Real metals, having finite conductivity at optical frequencies, have finite refractive indices plotted variously throughout Figures 3.14, 4.14, and 4.20. Electromagnetic fields penetrate the surface of a real metal, and the PEC boundary conditions (4.14) are no longer valid. Instead, one solves for the fields in the three regions $\rho < a$, $a \le \rho < b$, and $b \le \rho$ separately, enforcing the general electromagnetic continuities as boundary conditions at the two radii $\rho = a$ and $\rho = b$. A detailed derivation of these solutions is given in the 2nd Chapters of [136] and [137]. The introduction of metallic loss into a waveguide is typically a small perturbation, and in general, for frequencies sufficiently slower than the plasma resonance frequency of the metal, the real-metal modes closely resemble their companion PEC modes. For example, plotted in Figure 4.5-b) and -e) are the first two modes of a $\text{Pt}/\text{Al}_2\text{O}_3$ coax with diameters given by Equations (4.01), and operating at the free space wavelength $\lambda = 0.98$ μm. These modes were computed using a finite element solver, and should be

juxtaposed against the companion $\mathrm{PEC}/\mathrm{Al_2O_3}$ mode profiles plotted in Figure 4.4-b) and -d).

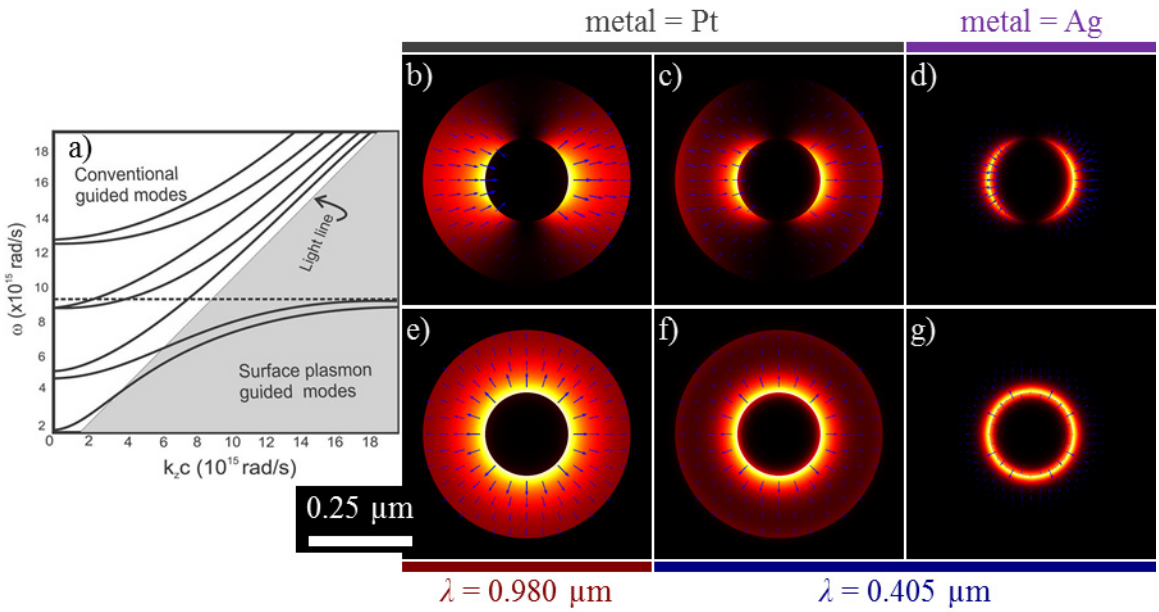

Figure 4.5: Summarizing the effects of metallic loss on nanocoaxial waveguides. (a) From [141], dispersion plots for $\text{Ø}_{\mathrm{OD}}/\text{Ø}_{\mathrm{ID}} = 0.5/0.15$ μm coax made of Ag and vacuum. Representative mode profiles in (b) through (g) for a $\text{Ø}_{\mathrm{OD}}/\text{Ø}_{\mathrm{ID}} = 0.5/0.2$ μm coax made from either $\mathrm{Pt}/\mathrm{Al_2O_3}$ or $\mathrm{Ag}/\mathrm{Al_2O_3}$ and operating at either $\lambda = 0.98$ μm or $\lambda = 0.405$ μm.

Some key characteristics emerge from the penetration of the fields into the lossy metal, here are four: First, there are no longer any purely transverse modes [142]. All modes will have both non-zero E_z and H_z. This means the TEM and $\mathrm{TE_{11}}$ modes are perturbatively morphed into TEM-*like* and $\mathrm{TE_{11}}$-*like* modes. Second, the Ohmic loss in the metallic walls introduces an imaginary component to the propagation constant k_z, and therefore a finite propagation length, $L = 1/(2\,\mathrm{Im}\,k_z)$. Third, as detailed in Section 3.4, real metals support SP waves, and depending on how close in frequency one is to the SP

resonance, real-metal coaxial modes obtain a varying degree of plasmonic character. This added plasmonic character can again be thought of as a perturbative departure from a PEC companion mode. As the frequency approaches the SP resonance, the plasmonic character of a mode increases: it becomes more tightly bound against the metal surfaces, and, as shown in Figure 4.5-a), the dispersion curve crosses the light-line such that the mode carries more momentum than ever could be carried by light propagating through Al_2O_3 alone. Fourth, and finally, since the fields penetrate into the metal, the mode occupies a physically larger cross-sectional area than when bounded by PEC walls, so real-metal coaxes have a red-shifted cutoff wavelength when compared to PEC coaxes with the same diameters [141].

As a quantitative measure of the penetration into the metal, one can use the confinement factor, Γ, which, in a similar spirit to the mode overlap integral in Equation (4.26), computes the fraction of the modal energy that lies within the insulating annulus. For a PEC waveguide, where the fields satisfy the boundary conditions (4.14), one gets automatically $\Gamma_{PEC} = 100\%$ for all modes. Table 4.3 has calculated confinement factors and propagation lengths, and optical constants for the 6 modes plotted in Figure 4.5-b) through -g). Quite generally, MIM waveguides exhibit a tradeoff between confinement and loss in the optical domain [143].

λ (μm)	refractive indices	metal/mode	panel in Figure 4.5	$\Gamma_{Al_2O_3}$ (%)	L (μm)
0.980	$N_{Al_2O_3} = 1.624$ $N_{Pt} = 3.4 + 5.7i$ $N_{Ag} = 0.04 + 7.0i$	Pt/TEM-*like*	e)	98.7	1.7
		Pt/TE_{11}-*like*	b)	98.9	1.8
		Ag/TEM-*like*	not shown	99.0	140
		Ag/TE_{11}-*like*	not shown	99.2	160
0.405	$N_{Al_2O_3} = 1.657$ $N_{Pt} = 1.7 + 2.9i$ $N_{Ag} = 0.05 + 2.2i$	Pt/TEM-*like*	f)	93.5	1.2
		Pt/TE_{11}-*like*	c)	94.1	1.1
		Ag/TEM-*like*	g)	70.6	2.2
		Ag/TE_{11}-*like*	d)	70.8	2.1

Table 4.3: Confinement and loss in real metal/Al_2O_3 nanocoaxes. For the modes plotted in Figure 4.5, and for two more not shown.

4.2 Fabrication

MIM nanocoaxes have been fabricated in a variety of ways. This section is organized as follows: first, I review some of the literature for fabrication schemes, then I describe some of my original, unpublished fabrications schemes which "didn't work", and finally, the bulk of this section is dedicated towards the ALD nanocoax, which has yielded novel optical performance.

4.2.1 Review of prior work

Deeply sub-mm coaxial cables, for example with diameters $Ø_{OD}/Ø_{ID} = 74/30$ μm [144], can be made by conventional wire drawing and extruding methods. In principle, these methods could be used to make even smaller diameter cables, for example by threading a fine wire through an insulating preform before drawing [145], however there is limited market demand so the production methods used in commercial manufacturing operations are generally not employed to make cables smaller than that. MIM microcoaxes with either

of $Ø_{OD}$ or $Ø_{ID}$ less than 10 µm are typically custom-made objects for scientific studies (*i.e.* not mass-manufactured). The core difficulty of fabricating these structures boils down to them having internal components which are totally enclosed by external components. While exterior surfaces can readily be metallized, it is generally more challenging to access an interior space by conventional microfabrication means. In this section I will describe some microfabrication approaches to making supra- and sub-µm-scale coaxes. On a high level, microfabrication methods can be divided into two overall categories [146], top-down and bottom-up. For the purposes of this thesis, I will make the distinction between those two categories based on how the coaxial geometry is achieved, so that instead of "top-down" or "bottom-up" the categories might more appropriately be called "lithographic" and "self-assembled", respectively. In the former case, any arbitrary geometry can be obtained by printing, imaging, engraving, etching, or some other patterning process. Therefore, a lithographically defined structure can have its geometry controlled independent from its material properties. In the latter case, however, the geometry is generated by the automatic organization of the constituent materials as they are added/removed/modified, so that both the geometric and material properties of the fabricated structure are determined in unison.

4.2.1.1 Top-down approaches

One way to lithographically achieve a coaxial geometry is to add materials to an axially symmetric template, such as a rod, hole, tube, pillar, or fiber. One way to add the materials is by molding. When fabricating macroscopic objects by molding, the materials are almost exclusively cast as a liquid which flows into a die, and subsequently freezes or cures solid. This very same approach has been miniaturized. Drawing inspiration from the fiber [147],

pipette [148], [149], and electrospinning [150] communities, one interesting approach is to start with a μm-scale annular insulating mold (essentially a glass tube or a hollow glass fiber), and then inject into the interior, hollow core a low melting point metal such as an In-, Ga-, Bi-, or Sn-based eutectic alloy, or even elemental Hg. This same basic approach can be used for planar integrated circuits with microfluidic channels [151], [152], and is amenable to more complex structures, such as non-planar [153] or flexible [154], [155] geometries. These low melting point metals are sufficiently conductive for electronic devices up to the RF, even if left in their liquid state [156], but these alloys are generally not useful for photonics applications due to their significant loss at optical frequencies; although one could imagine using them simply as an conductive intermediary in order to subsequently incorporate a low-loss optical metal, for example by electrochemical substitution. Some of the above works are summarized in Figure 4.6. In Figure 4.6-a), one can see that insulating sheaths can be formed around a conducting core during electrospinning. In that work [150], the electrospun sheath was a conductive electroluminescent (EL) polymer, not an insulator. But properly insulating electrospun sheaths should be compatible with their method. Their electrospun fibers were clad with an ITO outer coating to make an M-EL-M nanocoax with a molten core. Figure 4.6-b) shows that room temperature liquid metal can be injected into a flexible PDMS mold. For room temperature eutectics, this means a perfectly conforming metallic pattern even during flexure. The macroscopic device pictured was made specifically to demonstrate its flexibility, however this technique works equally well for microscopic PDMS molds. One could conceive of rendering a coaxial MIM structure by starting with an injected PDMS mold. Figure 4.6-c) shows that liquid metal can be injected into pulled micropipettes [149].

Even though the eutectic alloy was formulated to wet a clean glass surface, the metal only injected so far into the mold, stopping this case 8.2 μm short of the tip. Increasing the hydrostatic pressure during injection can further advance the metal, but only up to the mechanical yield of the capillary (30 bar). From [157], and as shown by a pair gray circles on the right-hand side of Figure 4.6-d), one promising approach is to use a through-hole multi-mode (THMM) optical fiber as the mold. The 50 μm holes on the left and right were injected while the center 62 μm hole was left empty for other purposes. While the hole sizes for the multi-mode fiber used in this case were larger than 10 μm, one can purchase single-mode holey fibers off-the-shelf with hole sizes down to ~ 1 μm. It would be interesting to see if the smaller diameter holey fibers could be injected, or perhaps electrochemically filled-in with Ag.

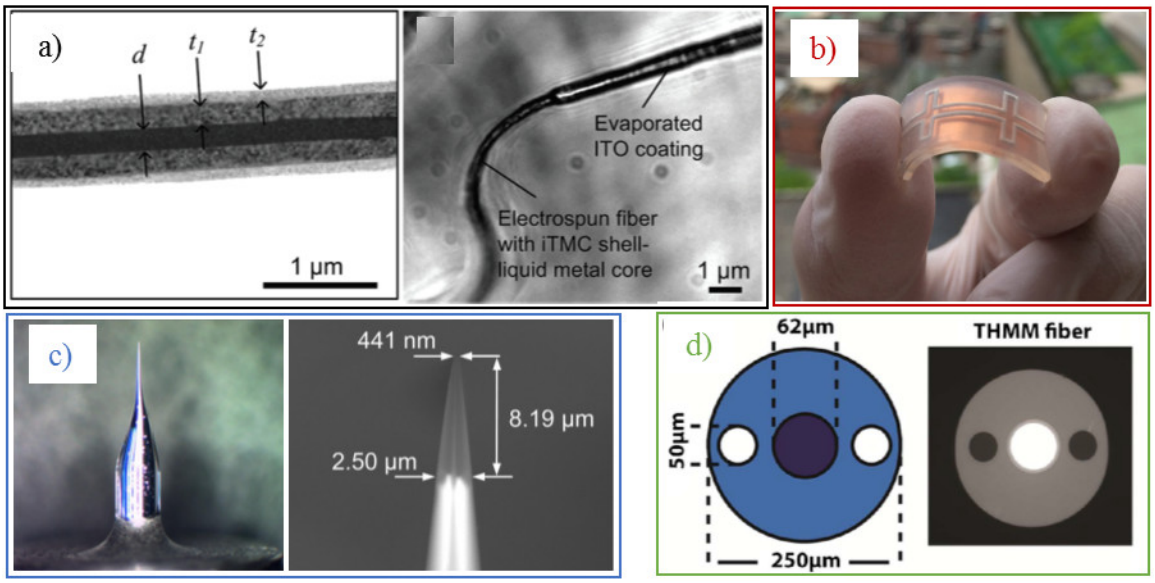

Figure 4.6: Molding µm-scale coaxial structures with molten metal. Literature review of fabrication using low-melting point metals. (a) From [150], the molten metal was extruded during electrospinning. (b) From [155], room temperature liquid metal injected into a PDMS mold. (c) From [149], a glass capillary is pulled into a micropipette/nozzle shape then molten metal is injected. (d) From [157], a polarization maintaining THMM fiber is used as the injection mold.

Materials are more conventionally added by thin film deposition and growth, where the sequential coating of metallic, insulating, and then metallic thin films results in a coaxial MIM structure. Next, I will discuss coaxial structures resulting from coating convex templates (*e.g.* rods and pillars), such that the thin films are added only to the external parts of the structure. This basic approach has been comprehensively reviewed before [158]. In that review, a broad range of application areas were discussed. In Figure 4.7 recall some of those fabrication schemes which are most pertinent to making MIM nanocoaxes for photonics applications. The templates in these approaches have been referred to as "scaffolds", however I find this term unsatisfactory since a scaffold is a *temporary* support structure. I believe that "frame" is a more appropriate term since, in all cases discussed here, the template is incorporated *permanently* into the final structure.

Although it is worth nothing that the added materials often contribute more to the final structure's mechanical integrity than the buried frame within. In many cases, the structural role of the frame is simply to seed the topology, rather than for mechanical support.

The basic scheme for this approach is illustrated in Figure 4.7-a). One can see that after the 2nd metal coating the coaxial structure is closed on the top. There are several ways to "open up" the structure [159], shown in Figure 4.7-b). Going vertically downward through the 5 rows in Figure 4.7-b), where each row pairs an illustrative schematic on the left with a corresponding scanning electron microscope (SEM) image on the right. The arrangement illustrated in Figure 4.7-a) is equivalent to the 3rd row of Figure 4.7-b). Going from the 3rd to the 4th row, one can see that the coaxial pillars are first potted in an encapsulant (such as the epoxy-based resist SU-8), as shown in gray, and then polished. If controlled correctly, the polishing action abrades away only the uppermost section of the coaxial pillar. Going from the 4th to the 5th row, one can see how the structure can be further modified, "hollowing out" the insulating annulus by selective etch, for example. Figure 4.7-e) shows a focused ion beam (FIB) cross-sectional SEM [160] from the fabrication scheme shown in Figure 4.7-b).

One major strength of this approach is that it requires only a single lithography step, in order to define the frame. Another major strength is that the transverse dimensions of the structure are controlled by the coating thicknesses. These thicknesses are very easily controlled on the deeply sub-μm or even single-nm scales. As will be discussed later in this Chapter, there are specialized coating technologies which indeed wield the ultimate precision control over a thickness, with digital atomic resolution (*i.e.* single-Å scale). In any case, film thickness precision is generally finer than even the most precise lithographic

techniques. This is demonstrated especially well in [161], as shown in Figure 4.7-c). In that work, very deeply sub-diffraction-limited confinement was demonstrated (see Equations (2.39) and (2.40)), where light with $\lambda > 1\ \mu\text{m}$ was transmitted through insulator thicknesses less than 9 nm.

For the most part, coaxes made in the manner shown in Figure 4.7 can be made only at modest overall aspect ratio (AR) defined as

$$\text{AR} = \frac{\text{length}}{\text{diameter}} = \frac{L}{Ø}. \tag{4.27}$$

This is because of limitations in lithographically defining a high-AR pillar which protrudes out of the plane. Another approach [9], one of the seminal works within the field, and as show in Figure 4.7-d), is to grow a high-AR, vertically-oriented multi-walled carbon nanotube (CNT) for use as a pillar/frame/inner metal all at once. These structures exceed $\text{AR} > 20$. While this bottom-up growth perhaps does not truly belong in this Section 4.2.1.1, one should note that it is well-established to lithographically pre-pattern the substrate before the growth [162], so that it occurs only on certain seed sites.

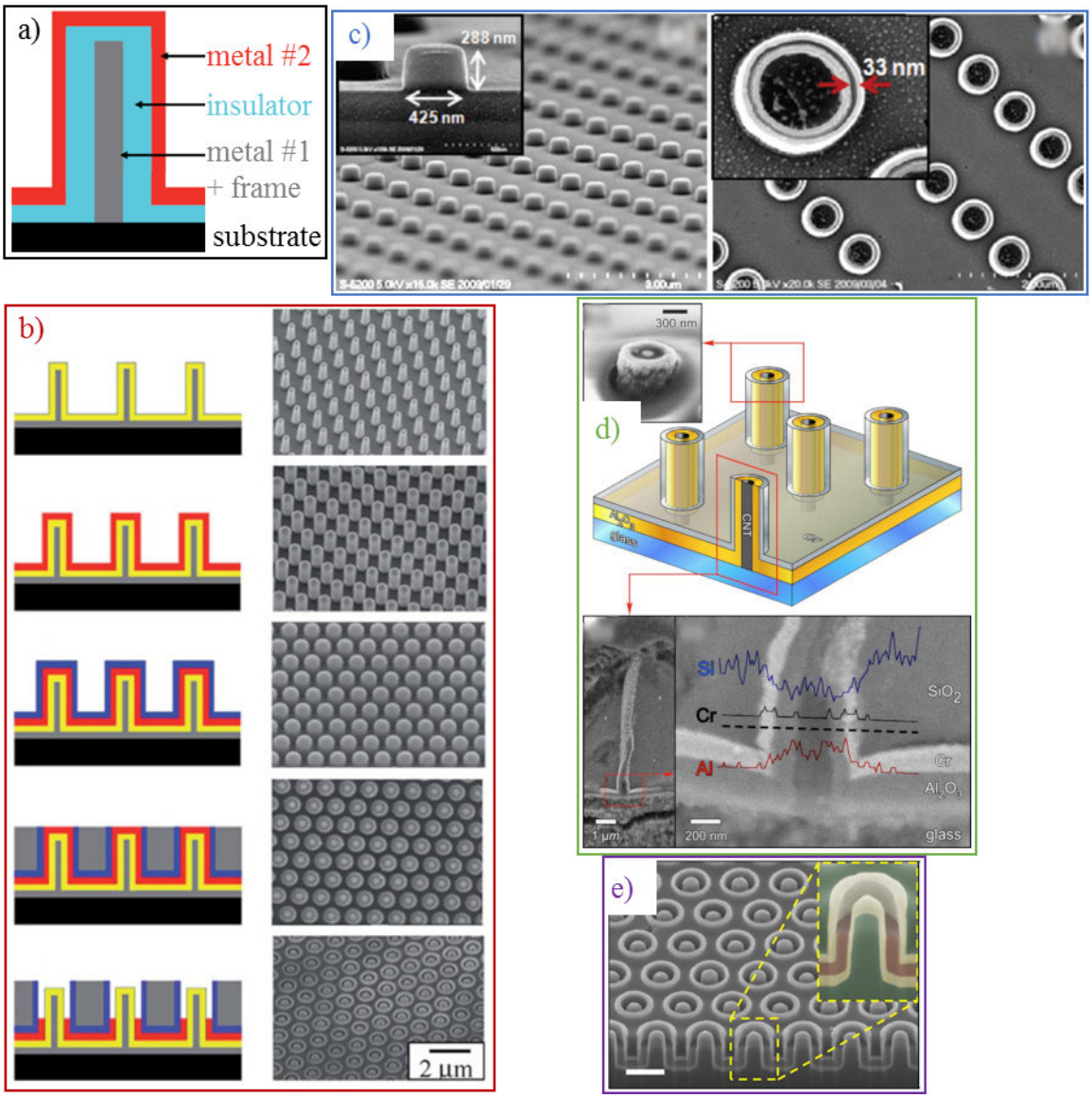

Figure 4.7: Fabricating out-of-plane, µm-scale coaxes. (a) From [158], metal and insulator layers can be coated onto a convex template, such as a rod or a pillar.(b) From [159], each of the 5 rows show a fabrication step. (c) From [161], very fine control over the transverse dimensions can be achieved. (d) From [9], the frame can be grown in a bottom-up sense to render a very high-AR pillar. (e) From [160], a FIB-cross section from fabrication scheme shown in (b).

Many prior experiments involving lithographically-defined MIM coaxes [163], [164] have generally focused on annular apertures perforating a thin film. While this is perhaps the simplest top-down coaxial fabrication scheme, the resulting coaxial MIM structure is

nearly a 2D object with $AR \sim 1$, often much less. These sub-μm apertures can readily be patterned by FIB-milling (which is the most typically encountered approach) [165], by electron beam lithography (EBL) [166], and by nanosphere lithography [167]. They can even be patterned by photolithography [168], that is even on those sub-diffraction-limited scales, with precise undercutting.

The externally clad coaxial structures just mentioned are in the vertical orientation with respect to the substrate. It is also possible to make microcoaxes which "lie flat" in the horizontal orientation, parallel to the surface of the planar substrate. This orientation grants access to much higher AR, and allows for connection and routing between neighboring integrated devices. However, this means the MIM layers cannot be prepared in the same sequential coating procedure as before. All previously reported fabrications of horizontally oriented, μm-scale coaxes have required multiple (aligned) layers of lithographic patterning. For example a monolithic coax (*i.e.* fabricated on a single substrate) can be made [169] with a series of 3 layers, as shown in Figure 4.8-a), where the height of the structure was divided into three parts: one containing the center conductor and one each above and below. The structure was fabricated and experimentally characterized, however none of the available digitized micrographs show it in any detail. This scheme necessarily has a rectangular (not circular) geometry. It is possible to make circular, horizontally oriented, split-coaxial structures by using two substrates. The authors of [170] imprint patterned the two halves of the split-coax and then bonded the aligned halves together into an assembly. Note that, even after bonding, the outer conductor is still split into two halves by the bonding membrane, which also suspends the center conductor. Schematics of these two approaches are shown in Figure 4.8.

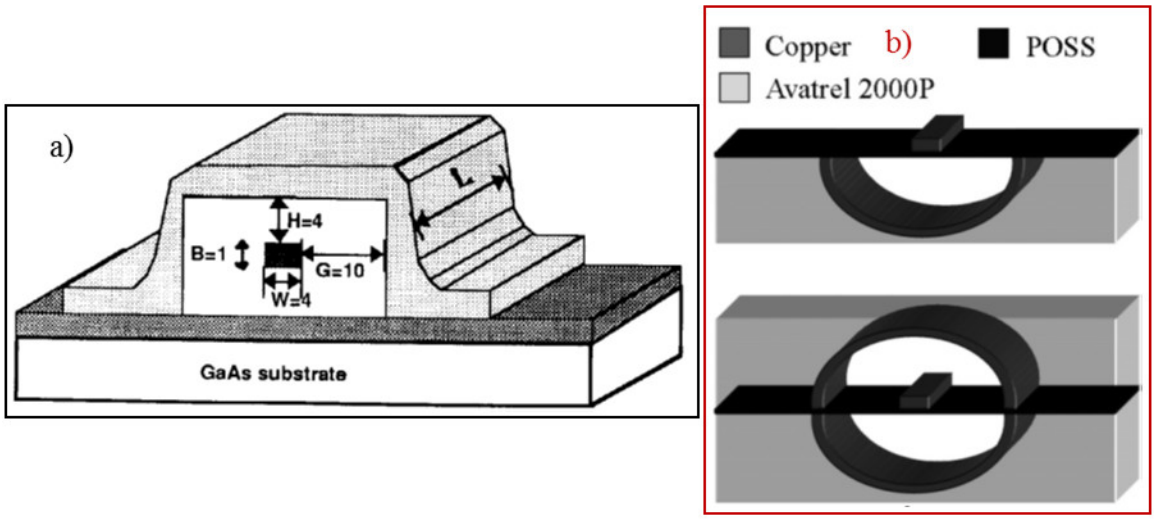

Figure 4.8: In-plane µm-scale coaxes requiring multi-layer patterning. (a) From [169], the complete structure is fabricated by 3 layers of aligned 2D exposures. (b) From [170], the authors fabricated the coaxial structure in two halves, bonding them together.

4.2.1.2 Bottom-up approaches

Self-assembled geometries are typically not arbitrary, but rather from groups of naturally emergent morphologies [171]. Coaxial structures are a commonly encountered self-assembled morphology. Furthermore, self-assembled coaxial structures are often both composed of high-quality materials (*e.g.* single crystals) and are truly nanoscopic with deeply sub-µm dimensions. The main drawback of self-assembled geometries is there is little control over the patterning and placement of these structures onto a substrate, and thus they cannot be as easily integrated into devices as with top-down structures, which affords nearly arbitrary patterning.

Single crystal silver nanowires (NW) have long been known [172] to exhibit strong nanoconfinement, mediated by guided surface plasmons guided along their axis. These Ag NW are grown in solution then cast onto a substrate for photonics experiments. The various synthesis methods [173] and photonics applications [174] have been reviewed before, and

Figure 4.9-a) shows a scheme which can grow highly 1D crystals. After seeding, the growth is terminated at the 100 facets by a sol-gel coating and self-limiting capping polymer film, leaving crystal growth to occur by reducing Ag^+ ions from solution onto at the exposed 111 facets [175]. These nanowires, while technically of pentagonal cross-section, can be modelled theoretically as axially symmetric plasmonic waveguides [176]. Shown in Figure 4.9-b) is an optical path in which the plasmon spirals around the "circumference" of the nanowire. This would be a guided mode with non-zero angular order, $l > 0$, see Equation (2.05). The nanowires can be processed further in solution before casting. For example, one can sol-gel coat a layer of SiO_2 [177], as shown in Figure 4.9-c) which are transmission electron microscope (TEM) images of this process at different points in time. The sol-gel growth rate is $R_{SiO_2} \sim 1\ \mathrm{nm/min}$. It is worth future investigation to see if the Ag/SiO_2 NW suspended in solution could then be coated electrolessly [178] with an outer metal layer to make, all in solution, a true MIM nanocoaxial waveguide before casting onto a substrate. A very similar scheme was demonstrated recently [179], where using the long-established Tollen's test Ag was deposited onto $LaMnO_3$ nanorods.

Ag NW, being made of single crystal silver and having atomically flat facets, are in some senses the optimal optical plasmonic material. As such, there is a vast body of work investigating the plasmonic properties of these structures [180], with only a handful of pertinent items retold here. First, I will discuss how the SPP can be excited. Show in Figure 4.9-d) and Figure 4.9-e) are two of the most common excitation schemes. In Figure 4.9-d), the authors of [181] illuminated one end of the NW with a tightly focused laser beam, they also showed that there is a correlation between in the incident and emitted polarizations. As it happens, this correlation is due to the spiraled nature of the guided

modes, as shown in Figure 4.9-b). The SPP wave fronts, shown as green lines in that figure, are polarized TM, and the angular order l of the guided mode is tied to the input polarization direction, α in Figure 4.9-d). In Figure 4.9-e), the authors of [182] used another popular excitation scheme, where a tapered optical fiber is mechanically positioned adjacent to the NW.

While the applications are myriad and the body of work immense, I will comment on one Ag NW based plasmonics application which, given the context of recent work conducted at Boston College, seems appropriate. Some years ago, shortly after one of the seminal works in the nanocoax field [9], it was conceived [16], [183] to make a super-resolving microscope which can extract near-field information and broadcast it into the far-field using a magnifying array of nanoscopic waveguides as an intermediary. Soon after, it was proposed that capacitively coupled sections of Ag NW could do the trick [184], and later on finite element simulation was carried out to better understand how Ag NWs could be arranged for this purpose [185]. Recently, the authors of [186], demonstrated a proof of concept experiment using two obliquely-oriented Ag NW which were FIB-milled into capacitively coupled chains. This microscope was originally named the "Nanocoaxial Converging Optical Microscope" (NCOM), where, according to the original proposal, nanocoaxes would be used in place of Ag NW, in order to eliminate crosstalk.

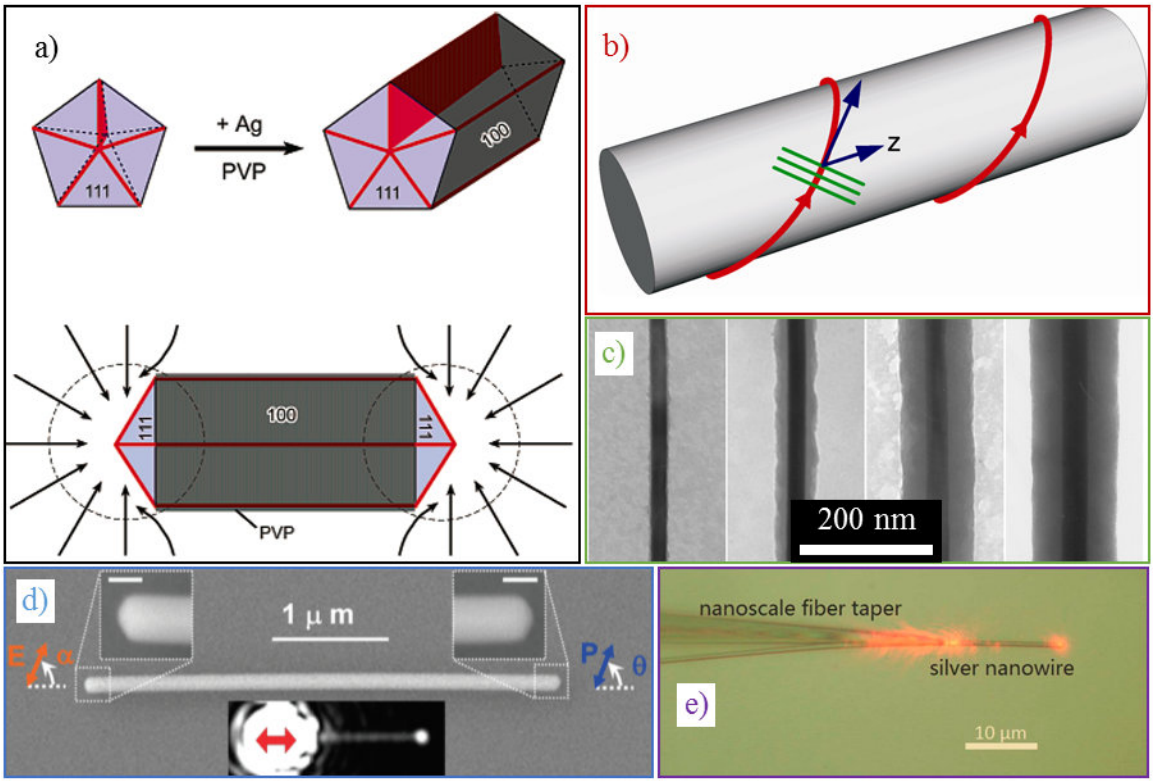

Figure 4.9: Ag nanowires as 1D plasmonic waveguides. (a) From [175], one of the synthesis methods for Ag NWs. (b) From [176], SPPs can spiral around the NW, traveling along both the circumference and the length simultaneously. (c) Adapted from [177], Ag NW can be coated with SiO_2 in solution. (d) From [181], and (e) from [182], two popular excitation methods for coupling light into guided NW SPPs.

4.2.2 Horizontal nanocoax fabrication schemes

One major limitation to the multi-layered schemes presented in Figure 4.8 is that the transverse dimensions of the coaxial structure are determined by the alignment tolerance. This tolerance is typically larger than ultimate lithographic resolution, regardless of how that lithography is performed. In some cases, such as mechanically registered photo- and imprint-mask-aligners, it can be much larger. One way to mitigate this problem is by adding the insulator cladding as a growth process instead of a lift-off or etch process,

thereby eliminating a patterning (and therefore alignment) step. In the next three sections I will describe some fabrication schemes I have developed to this effect.

4.2.2.1 By metal oxidation

One pathway for the insulator growth is to deposit the first metal and then oxidize it, provided that the resulting oxidized-metal compound is a good optical insulator and that a well-defined boundary between metal and oxidized-metal can be established. This is shown schematically in panels a-c) of Figure 4.10. In Figure 4.10-a), the only required layer of lithography is used to pattern a nanostripline by liftoff, where both the insulating and metal lines are deposited through the same mask. This metal, being reactive, can be oxidized selectively against the chemically inert ground plane, as drawn in Figure 4.10-b). Finally, as shown in Figure 4.10-c), the whole structure is "buried" with second deposition of metal, resulting in an in-plane coaxial MIM structure. Note that the second metal layer, while drawn in Figure 4.10-c) with finite lateral extent for clarity, need not be patterned.

Next, I will remark on a few material prospective combinations considering the above criteria. While Ag is the "ideal" plasmonic metal, it is noteworthy that the only oxidized-Ag compound which is easily synthesized near room temperature and which has a sufficiently high bandgap for many optical applications, $E_g \sim 1\,\mathrm{eV}$, is Ag_2S. However, Ag_2S does not fit the above requirements; Ag_2S films grown on Ag are neither continuous nor adherent, with the film crumbling off as a powdery tarnish [187]. Although recent work suggests that a high-quality Ag_2S/Ag interface can be established with pulsed electrochemistry [188]. There are perhaps several alternative "plasmonically-active" metals [189] which could fit the above criteria. Future work in this area should resolve which metal and which oxidizer (and which oxidizing method) could grow the best quality

metal/insulator interfaces. One approach is to expose a metal film to a source of oxygen (the oxidizer) in a thermal chamber (the oxidizing method). Most metals of interest can be oxidized at temperatures less than 600 °C. However, one should note that most thin metal films, even if exposed to an inert environment such as Ar, generally do not survive temperatures greater than *ca.* 300 °C. In many cases, the maximum survivable temperature can be much lower. If exposed to high temperatures, then in order to relieve any built-in stresses and to assume a lower energy state, these films often curdle into disjoint islands, losing their thin film morphology. One could achieve the same oxidation reaction at a lower temperature by using a more electronegative (or penetrative) source of oxygen than molecular O_2. For example, one could expose the film to steam, monoatomic O, or O_3 (ozone) [190]. All of these reactants (except for steam), as well as their ionized counterparts, can be generated in a plasma chamber [191]. There a few promising metal/oxide combinations which may satisfy the above criteria, including Ti/TiO_2 [192], Cu/Cu_2O [193], Cu/CuO [194], and Al/Al_2O_3 [195].

Al has a useful window of low optical loss in the blue and UV, and is the base material for a broad range of plasmonics applications [196]. Furthermore, Al can be made to establish an Al/Al_2O_3 interface by electrochemical anodization, an extensively studied and straightforward approach [197]. I employed this method for the structures presented in panels d-i) of Figure 4.10.

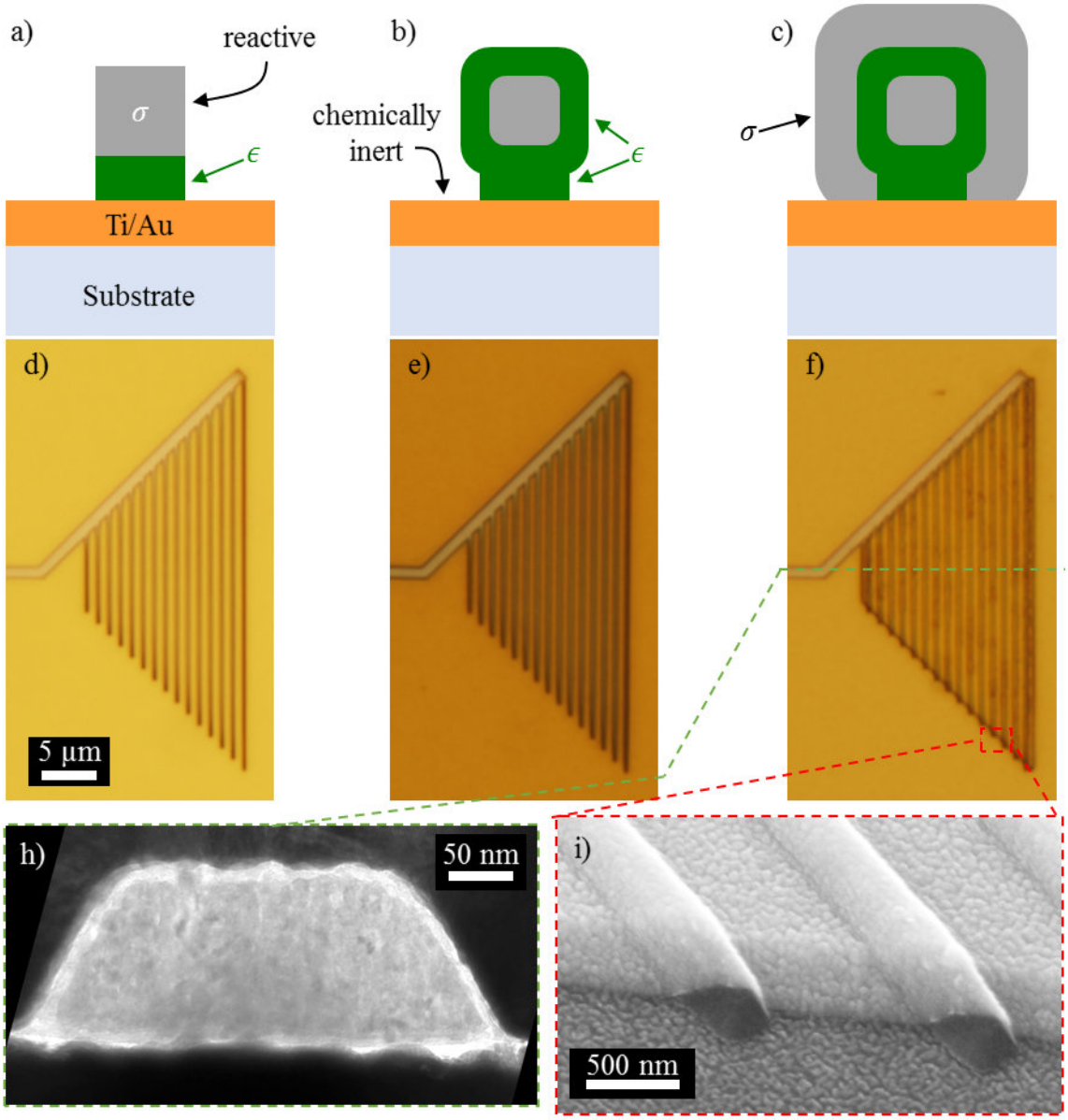

Figure 4.10: Oxidized metal nanocoax fabrication. (a-c) Illustrative schematics for a general metal/oxide process. (d-f) Photographs of the fabricated, anodized structure. (h) A TEM micrograph from a cross section lifted-out by FIB. (i) An SEM-SEI micrograph of the complete structure.

First, shown in Figure 4.10-d) the striplines were patterned EBL. A sodalime glass substrate with Ti/Au = 10/100 nm was left for 2 min on a 100 °C hotplate and then immediately (before cooling) spin-coated with a polymethylmethacrylate (PMMA, in anisole) bilayer resist. The 750/50 nm PMMA bilayer was made of molecular weight

495/950 kDa. The resist films were soft-baked (after each spin step) on a 180 °C hotplate for 90 s. A 30 kV, 75 pA electron beam exposed patterns with varying electron doses near $300\ \mu C/cm^2$. The images were developed with 60 s of stirred immersion in a solution of methyl isobutyl ketone and isopropanol (MIBK:IPA::1:3). To terminate the development, the samples were immediately swirled for 3 s in pure IPA, then immediately immersed in and subsequently rinsed by deionized water (DI). The developed samples were blown dry with a stream of N_2. Immediately before loading into the deposition chamber, the patterned samples were cleaned with a 30 s exposure to O_2-based plasma (100 SCCM O_2 flow at 270 mTorr and with 550 W of 2.45 GHz power). This "O_2 descum" plasma process is used to etch roughly 5 nm of hydrocarbon and promotes adhesion by removing residuals and exposing a clean surface. The deposition was carried out by electron beam evaporation of $SiO_2/Al = 50/150$ nm, and liftoff was performed by immersing the samples in a *vigorously stirred* 80 °C solution of Microchem's Microposit™ remover 1165 (primarily consisting of 1-methyl-2-pyrrolidinone, similar in action to N-methyl-2-pyrrolidone, NMP) for 10 minutes. The samples were rinsed with acetone, DI, then IPA and again blown dry with N_2. Finally, the samples were one more time O_2 descummed.

Figure 4.10-b) and Figure 4.11-a) show that the oxide was grown on the Al surface by anodization. Nanostriplines of varying length and width were fabricated, with $w = 300$ nm and $L = 5\text{-}30\ \mu m$. The nanostriplines were arranged in a "finger" type pattern, where the striplines are oriented in a N-S direction and connected to an "arm" electrode which is oriented in a SW-NE direction. The electrode traces-out to a macroscopic contact pad where I bonded to AWG36 Cu wire using Ag epoxy (DuPont 6838), the wire and Ag-

epoxy bond were then potted in a dollop of waterproof, non-conductive epoxy for both electrical isolation and mechanical strain-relief. The sample was immersed in a 10 mM citric acid electrolyte, and the Al was biased with 30 V DC against the 300-series stainless steel (SS) counter electrode. Under electrochemical conditions which produce a dense, pore-free oxide, the anodization process is self-limiting with the terminal film thickness depending on the DC voltage bias. Consistent with [197], I find the proportion to be $1.6\ \mathrm{nm/V}$. Figure 4.11-b) shows a current trace (blue circles) during the anodization. The Ag-epoxy also makes incidental electrical contact to the Au ground plane. As a control, I also show a current trace from an equal area unpatterned Au ground plane without any Al (red squares). Their difference, for times $t < 2\ \mathrm{min},$ is due to the oxidation of Al.

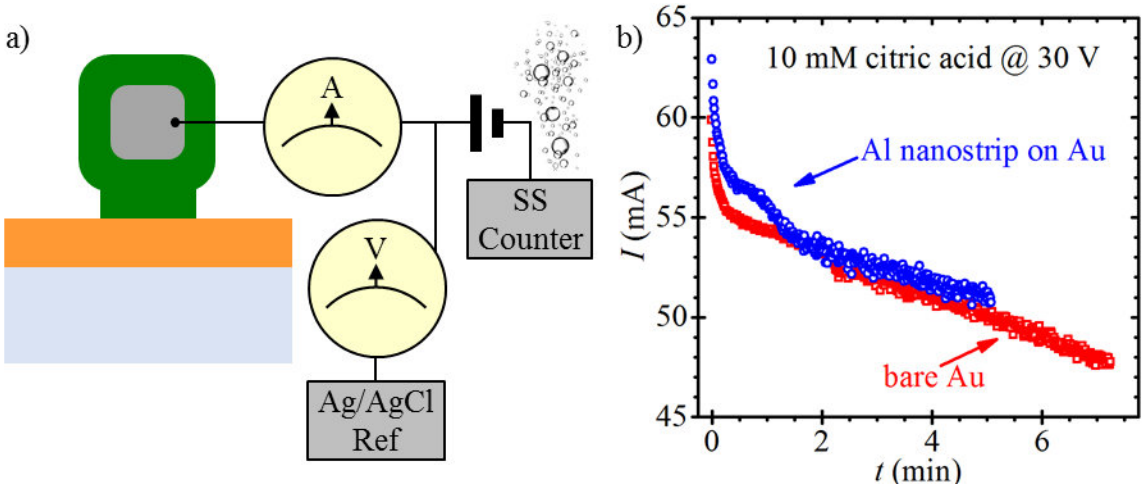

Figure 4.11: Anodized coax, electrochemical setup. (a) Schematic of the electrochemical cell and (b) a current trace during anodization.

Figure 4.10-c) and Figure 4.10-f) show that after anodizing, the second metal layer was deposited (250 nm Au in this case), encapsulating the insulator-clad nanostriplines to make a full, in-plane MIM nanocoaxes. For the sample shown in Figure 4.10, the second metal layer was patterned by lift-off with an aligned, second layer of EBL (registered

electronically against fiducials in the first layer, not shown). Going from Figure 4.10-e) to Figure 4.10-f), one can clearly see outline of the second metal layer as an isosceles trapezoid. While the second layer need not be patterned in order to achieve the desired coaxial geometry, it was patterned in this case to allow optical access on both ends, with stubs on the S-end and a stub-to-arm T-shape on the N-end. Figure 4.10-h) shows a transmission electron microscope (TEM) image of the complete structure, recorded from a cross-section excavated by FIB-milling lift-out. Figure 4.10-i) shows a perspective-view SEM of the complete structure.

In this section, I have described a fabrication scheme based on selective metal oxidation. There is a similarly-spirited form of microfabrication wherein one achieves selective electroless metal deposition by appropriately patterning surfaces with a Pt or Pd catalyst [198]. This same underlying chemistry is used to plate through holes in printed circuit boards (PCB) [199]. It would be interesting to see if, along the vein of this section and in the spirit of selective metallization, one could selectively grow an insulator on a metal surface, with appropriate surface functionalization.

4.2.2.2 Cast from a solution of Ag/SiO_2 nanowires

Section 4.2.1.2 (see especially Figure 4.9), describes how one can make a coaxial geometry by sol-gel coating a layer of SiO_2 onto single crystal Ag NW. Ag/SiO_2 NW were purchased [200] as a concentrated suspension in DI. The solution was diluted in IPA and cast onto a sodalime glass substrate with a Ti/Ag = 10/200 nm ground plane, as illustrated in Figure 4.12-a). Figure 4.12-b) shows that 50 nm of Pt was deposited by ALD, thus totally enclosing the NW to make a full MIM nanocoaxial structure. Figure 4.12-c) shows an optical micrograph (darkfield contrast) of the NW cast from the IPA solution not onto a

TEM mesh with a holey carbon film [201], with Figure 4.12-d) and Figure 4.12-e) showing TEM images of suspended Ag/SiO_2 NW before and after the deposition, respectively. The dark and bright bands in Figure 4.12-e) clearly show the individual MIM layers (with varying degrees of electron transparency). Figure 4.12-f) shows a plot of the measured NW length *vs*. "diameter" Ø for *ca*. 20 Ag/SiO_2 NW's before the Pt deposition (blue squares) and for 5 $Ag/SiO_2/Pt$ NW's after (green triangles). More details about the conformal Pt deposition are given in Section 4.2.2.3. The term "diameter" is lacking, since single crystal Ag NW's are known to have a pentagonal-faceted, not round, cross-section [202], so "diameter" really means "diameter of the circumscribed circle". Also drawn are a constant AR = 100 guide for the eye (purple line, Equation (4.27)), and a red ellipse to represent the specified dimensional range of the commercially purchased NW's.

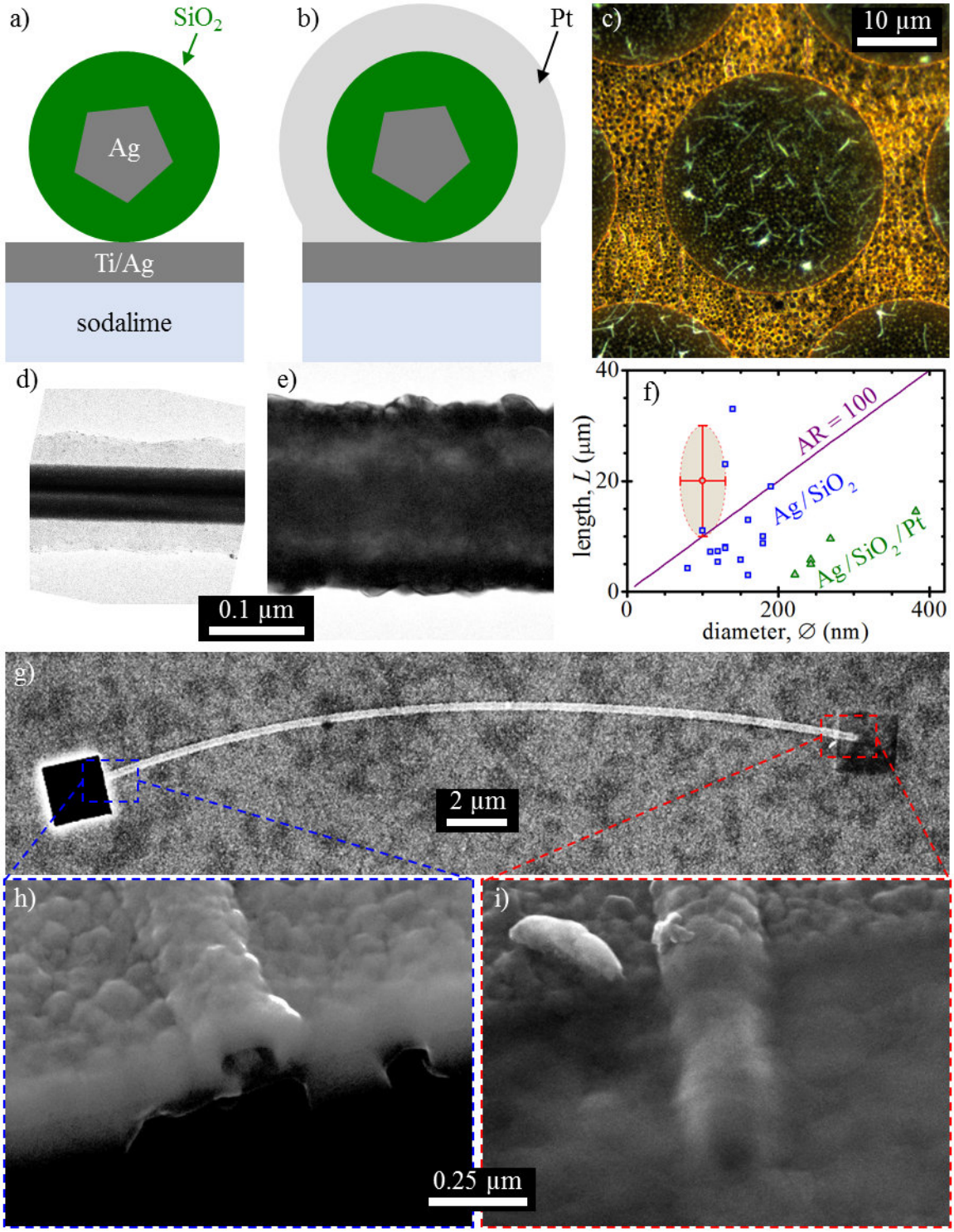

Figure 4.12: Nanocoaxial waveguides from single crystal Ag NWs. (a-b) Fabrication schematics. (c) Optical darkfield micrograph of NW's on a TEM grid. (d-e) TEM images before and after Pt deposition, respectively. (f) Measured NW dimensions. (h-i) FIB- milled nanocoax, with magnified views of the terminations.

For making useful optical devices from these in-plane nanocoaxes, one can optically "open up" the structure by FIB-milling. Figure 4.12-g) shows a $Ag/SiO_2/Pt$ NW on a sodalime glass substrate which has been FIB-milled on the two ends. On the left-hand end, outlined in blue and shown in Figure 4.12-h) is a "window" type of termination, where the milling depth reached into the glass substrate, through the Ag ground plane. This allows for backside illumination through the transparent substrate. On the right-hand end, outlined in red and shown in Figure 4.12-i) is a "stub" type of termination, where the milling was terminated after polishing away the Pt layer, exposing nominally a Ag/SiO_2 NW with only traces of the Pt left behind. The milling must be monitored in real time using either a secondary electron image (SEI) or a back-scattered electron composition (BEC) image. If one were to repeat this fabrication scheme, I would recommend a several-fold thicker ground plane, perhaps most easily obtained by electroplating.

4.2.2.3 By atomic layer deposition

The previous section considered conformal insulator growth onto the surface of a metal, and as mentioned above it is also possible, with certain chemistries, to conformally deposit metals. One way, already discussed in Section 4.2.1 is by electroless deposition from solution [178]. Another, which is leveraged extensively in this thesis, is by chemical vapor deposition (CVD), where the sample is exposed in a low-pressure chamber to a volatile precursor which chemically reacts on the sample surface and leaves behind the desired film. One specialized class of CVD is atomic layer deposition (ALD). What distinguishes ALD from other forms of CVD, is that ALD is a self-limiting, monolayer process by nature. ALD is performed in sequential cycles, where in each cycle another monolayer of material

is added. So, ALD being a digital monolayer process, one can control the deposited film thicknesses with *bona fide* sub-nm precision. Combined with its conformality, and with an appropriate geometry, one can apply this thickness control onto the transverse dimensions of their desired structure. This fabrication approach has been called atomic layer lithography [203]. Indeed, others have achieved extreme optical confinement in this way, squeezing light into less than 5 nm wide gaps [204]. Figure 4.13 shows ALD-grown, horizontal nanocoaxes fabricated by depositing sequential Pt and Al_2O_3 layers onto a Si_3N_4 nanobeam frame; the beam serves the same purpose as the pillars in Figure 4.7.

Figure 4.13-a) through -d) show the major steps of the fabrication process. First, (100)-oriented single-side polished (SSP) Si wafers with a 100 nm thick plasma-enhanced CVD (PECVD) layer of Si_3N_4 were purchased, coated with 40 nm Cr by electron beam deposition, then cut into $15\times15\ mm^2$ die. The pattern is imaged into a 100 nm 950 kDa PMMA resist, following a very similar EBL recipe to what was described in Section 4.2.2.1. The patterned PMMA, pictured in Figure 4.13-e), is used as a wet-etch mask, transferring the image into the Cr layer by room temperature immersion in a commercial Cr etchant based on ceric ammonium nitrate, $(NH_4)_2Ce(NO_3)_6$. The PMMA was exposed and developed under conditions where it acts as a positive resist, leaving behind the dark lines in areas not exposed. The line widths were varied from 100 to 300 nm. So, the targeted image features sizes in the Cr film were roughly $AR = 40/100 \sim 1$. Whenever transferring an image by isotropic etch into a layer whose thickness is comparable with the feature size, accurate etch control / timing measures must be in place, as undercutting will

eventually erase the image completely. Figure 4.13-b) shows schematically that I transferred these lines into the Cr layer then stripped the resist.

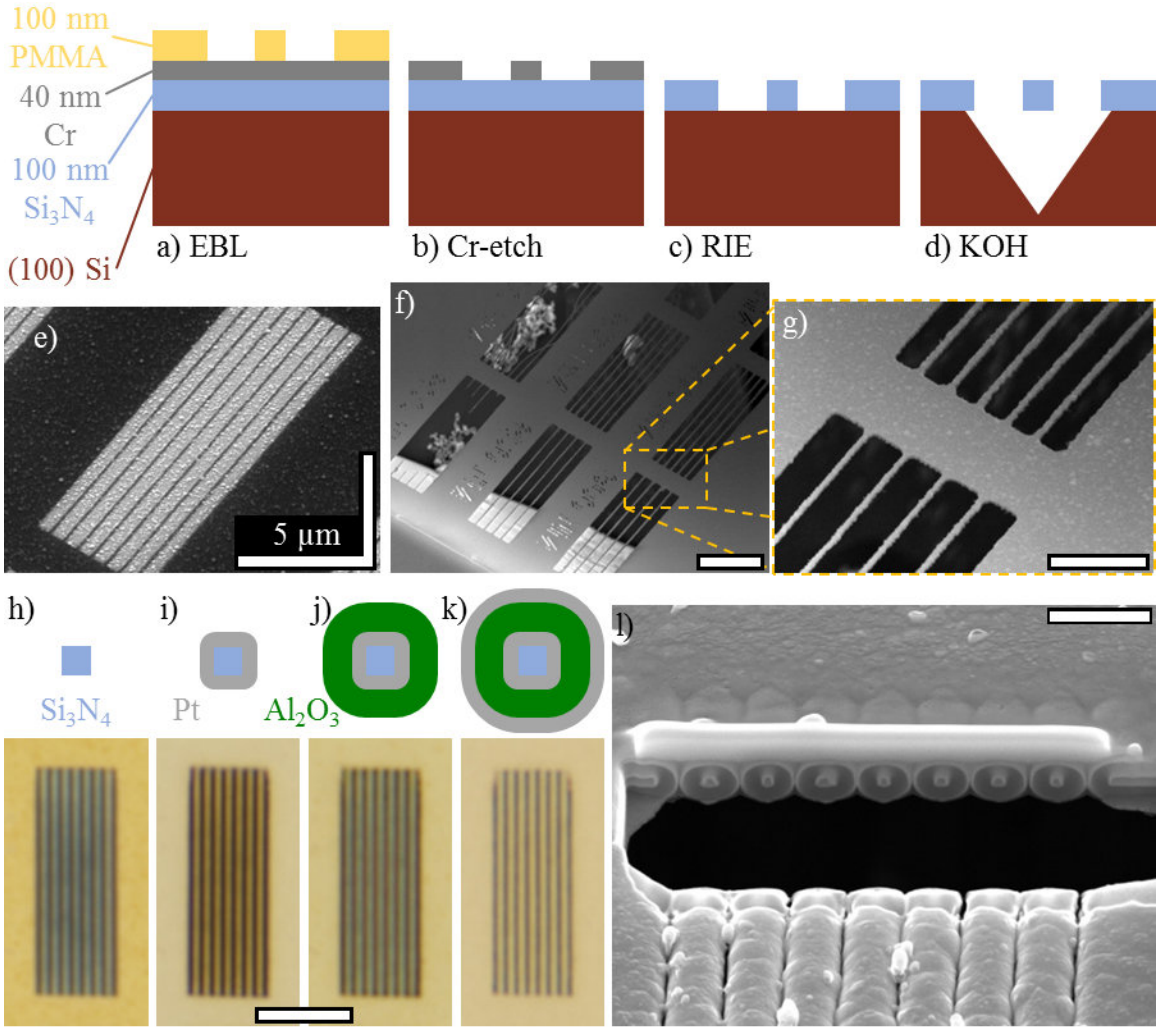

Figure 4.13: Horizontal Pt/Al_2O_3 nanocoaxes on suspended Si_3N_4 beams. (a-d) Fabrication schematics to make suspended beams, with (e) showing the PMMA etch mask, and (f) and (g) showing the suspended structure. (h-k) Fabrication schematics and corresponding optical micrographs during sequential ALD steps. (l) FIB cross-section of the complete structure. Scale bars: (e-f) 5 (g) 2 (h-k) 5 and (l) 2 µm. Note the compound scale in e), the same proportion applies to all SEM images, taken at perspective-tilts of 35°.

The function of the Cr layer was to hard-mask a reactive ion etch (RIE), shown in Figure 4.13-c), where the pattern was transferred into the Si_3N_4 using a $CHF_3 + O_2$ based, inductively-coupled plasma. The chamber pressure was fixed at 3 mTorr with flow rates of 45 and 5 SCCM, respectively for CHF_3 and O_2. The plasma is sustained by 500 W of RF power at 13.56 MHz, with the substrate biased by *ca*. 70 V DC, and cooled on the backside using flowing He at 2 Torr and 5 SCCM (in a hermetically separated space from the vacuum chamber). The substrate bias is what gives the etch its directionality. I measured an etch rate of $100\ \mathrm{nm/min}$, and stopped the etch after 120 nm of Si_3N_4 would have been consumed. ways.

With the image transferred into the Si_3N_4, the beams were suspended by anisotropically etching the (100)-oriented Si substrate in a stirred KOH solution $(30:70::\mathrm{KOH}:\mathrm{DI}\ m/m)$, heated to 80 °C and, as best as could be done with a thermally-sunk watch-glass to cover the crystallization dish, reflux-condensed. The pyramid which is hollowed out under the membrane extended to a *ca*. $100\times100\ \mu m^2$ area, undercutting the EBL fiducials (not shown) which were patterned in case the need arose to register a 2nd layer of EBL. The suspended Si_3N_4 beams, Figure 4.13-f) and -g), are therefore features within a larger suspended Si_3N_4 membrane. These membranes, with $\mathrm{AR} = 0.1/100 \sim 10^{-3}$, were surprisingly robust, surviving direct blasts from an N_2 gun pressurized to 60 PSIG, and held only a few mm away. This KOH recipe etched any exposed (100) Si facets at roughly $1\ \mu\mathrm{m/min}$.

Figure 4.13-h) through -k) show that Pt and Al_2O_3 layers were coated sequentially by thermal ALD using commercially available reactors [205], [206], with the four panels showing four pairs of schematics and optical micrographs (brightfield contrast mode, imaging exactly the same set of nanobeams) above and below, respectively. This MIM by Pt/Al_2O_3 ALD will be used again in this thesis, so here I will give some detail about those steps. First, a single cycle of Pt deposition, executed at 250 °C, is accomplished in 4 steps: 1.) Evacuate the chamber and ancillary plumbing to the roughing base pressure, *ca*. 10 mTorr. 2.) Introduce, under flow of N_2, a volatile/gaseous Pt-based precursor to the chamber by actuating a valve at the Pt source. 3.) Introduce an oxidizer, such as O_2, also within an N_2 carrier gas by actuating open and closed a valve connected to a high-purity O_2 cylinder. 4.) Purge the chamber with N_2. The Pt source is a sealed canister with liquid trimethyl(methylcyclopentadienyl)platinum(IV), $C_3H_4CH_3Pt(CH_3)_3$ (PtMe), heated to 65 °C in order to produce *ca*. 4 Torr of vapor pressure. The plumbing is heated to 115 °C to eliminate the possibility of condensation, which, because PtMe is pyrophoric, could result in a fire. The Pt-valve is opened for a 250 ms burst, and the gaseous PtMe is allowed to dwell/soak in the sample chamber for some exposure time. The pressure and exposure time combine to set the dose, with a sufficiently high dose required for monolayer formation. We find that a 250 ms burst is useful for up to 5 s of dwell time. So, for higher doses than what can be provided by a single burst, a series of consecutive burst/dwell steps can be used. The dose should be increased until the deposition rate stabilizes, and then increased no further in order to conserve the precursor. Our stable Pt deposition rate was

$R_{Pt} \sim 0.7\,\text{Å/cycle}$. Note that ALD valves must actuate with accurate timing [207]. For example, the O_2-valve is opened for only 25 ms. The chamber is left to oxidize for 1 second before being purged and pumped. During oxidation, the organic ligands are burnt off the Pt^{4+} cation. The monolayer of cations is reduced to form an elemental film, which for the ca. 50-75 nm thicknesses used in this thesis, is metallic. Each cycle takes 2-5 min depending on the parameters, so the deposition rate is on the order of $R_{Pt} \sim 1\,\text{nm/hr}$.

Al_2O_3 is also grown by thermal ALD, with essentially the same four steps as Pt, except for the following differences: 1.) The deposition temperature is not as high. We have successfully deposited Al_2O_3 films as low as 115 °C. But the standard recipe we follow is at 200 °C. 2.) The Al-based precursor is trimethylaluminum, $Al_2(CH_3)_6$ (TMA), heated to 110 °C and reaches a much higher vapor pressure (~100's Torr) at that temperature than PtMe. 3.) The oxidizer is H_2O, sourced from a 100 °C canister of DI. 4.) The pump/purge steps are basically the same. With a much higher vapor pressure, a much shorter exposure burst, 15 ms, is required to establish a useful dose of TMA than in PtMe. I measure a stable Al_2O_3 deposition rate of $R_{Al_2O_3} \sim 0.11$ Å/cycle. With each cycle taking 1-3 min, again depending on the parameters, this means $R_{Al_2O_3}$ is also of order 1 nm/hr.

Figure 4.14 shows the measured optical constants of ALD Pt and Al_2O_3. The measurements were made with a variable-angle spectroscopic ellipsometer (VASE) [208]. The VASE data were fit to extract the optical constants into the form of Equation (3.16).

Figure 4.14-a) shows the measured optical constants for Pt, with n plotted by red circles and κ by blue triangles. Also plotted are two curves as a reference from the literature: κ in a broken blue line and n in a solid red line. Note that these reference curves are fits to a 4-oscillator Drude-Lorentz model [131], based on measurements from a bulk sample [209]. Figure 4.14-b) shows the measured optical constants for Al_2O_3. Not included on this scale are the κ, which are generally all lower than 100 PPM and can be safely neglected. The real-valued n are fit to a Cauchy curve

$$n = A + \frac{B}{\lambda^2} + \frac{C}{\lambda^4}, \tag{4.28}$$

where $A = 1.6176$, $B = 6.4\times10^{-3}$ μm^2, and $C = 1.3\times10^{-5}$ μm^4. For comparison, the (ordinary) refractive index of sapphire (single-crystal α-Al_2O_3), taken from [210], is included in Figure 4.14-b).

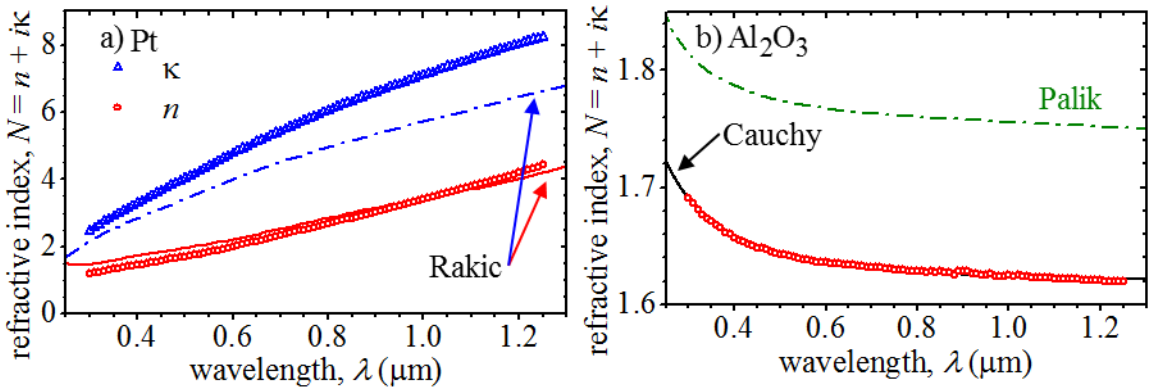

Figure 4.14: Optical constants of ALD Pt and Al_2O_3.(a) Pt and (b) Al_2O_3 refractive indices, comparing measured results from grown films against literature.

ALD alumina films are amorphous [211] and therefore optically isotropic. The temperature dependence of ALD alumina's optical constants [212] (*i.e.* the thermo-optic response) can be used to make integrated thermal phase shifters [213].

I used a 4 point probe [214] to measure the room temperature DC resistivity of the ALD Pt film, $\rho_{DC} = 16.6 \pm 0.5\ \mu\Omega \cdot cm$, which compares well with the bulk value, $\rho_{bulk} = 10.5\ \mu\Omega \cdot cm$, and with Pt films grown by plasma-enhanced ALD [215]. By clipping 4 leads onto an unpatterned thin film and dunking into liquid N_2, I find a 77 K residual resistance ratio (RRR) of only 3.4. For comparison, sputtered thin Pt films have a 77 K RRR closer to 5 [216]. This indicates the temperature-independent scattering in the ALD Pt film is quite high. It is also commensurate with the higher-than-bulk κ values measured by VASE in Figure 4.14-a).

Next, I describe some fabrication steps to gain optical access to the horizontal Pt/Al_2O_3 nanocoaxes. In Section 4.2.2.2, where Ag NW's were Pt-coated on a silvered glass substrate, optical access was gained by FIB-milling windows into the ends. However, that same approach could not work for theses suspended-nanobeams, slicing the structure all the way through would also mechanically release it. As shown in Figure 4.15-b), I fixed them with a contact adhesive [217], bonding the Pt/Al_2O_3-coated Si substrate to a sodalime glass superstrate. The 525 μm thick Si substrate was removed with an isotropic XeF_2 etch [218]. The etch exposes the sample to 4 Torr of XeF_2. The XeF_2 chemically attacks the Si, releasing SiF_4, which is pumped away under N_2 flow. The etch cycle is complete by evacuating the chamber to a 10 mTorr base pressure before exposing to the next round of XeF_2. Each cycle, taking ca. 70 s, etches 300 nm of Si, although that rate is determined by how much Si surface area is exposed in the chamber (*i.e.* the "loading" of the etch), and can vary quite a bit. At the average etch rate of $15\ \mu m/hr$, the through wafer etch takes *ca*. 35 hr.

Figure 4.15-c) shows that after the XeF_2, the nanocoaxes are shielded inside of a hollow “tent” created by Pt/Al_2O_3 deposition onto the facets of the KOH pit. Most of these pits burst during the pressure cycles of the XeF_2 etch. Probably during the first evacuation. But even the bursted tents still obscured the nanocoaxes, obstructing optical access. After the etch, I blasted the samples with 60 PSIG N_2, with the nozzle held only a few mm from the tents. The blasting opened many of the tents, with a typical result shown in Figure 4.15-d). I found that immersing the samples in an ultrasonic DI bath helped to disintegrate much of the remaining tent, shown in Figure 4.15-e) through -g). Finally, Figure 4.15-h) shows a grating structure milled into the horizontal nanocoax.

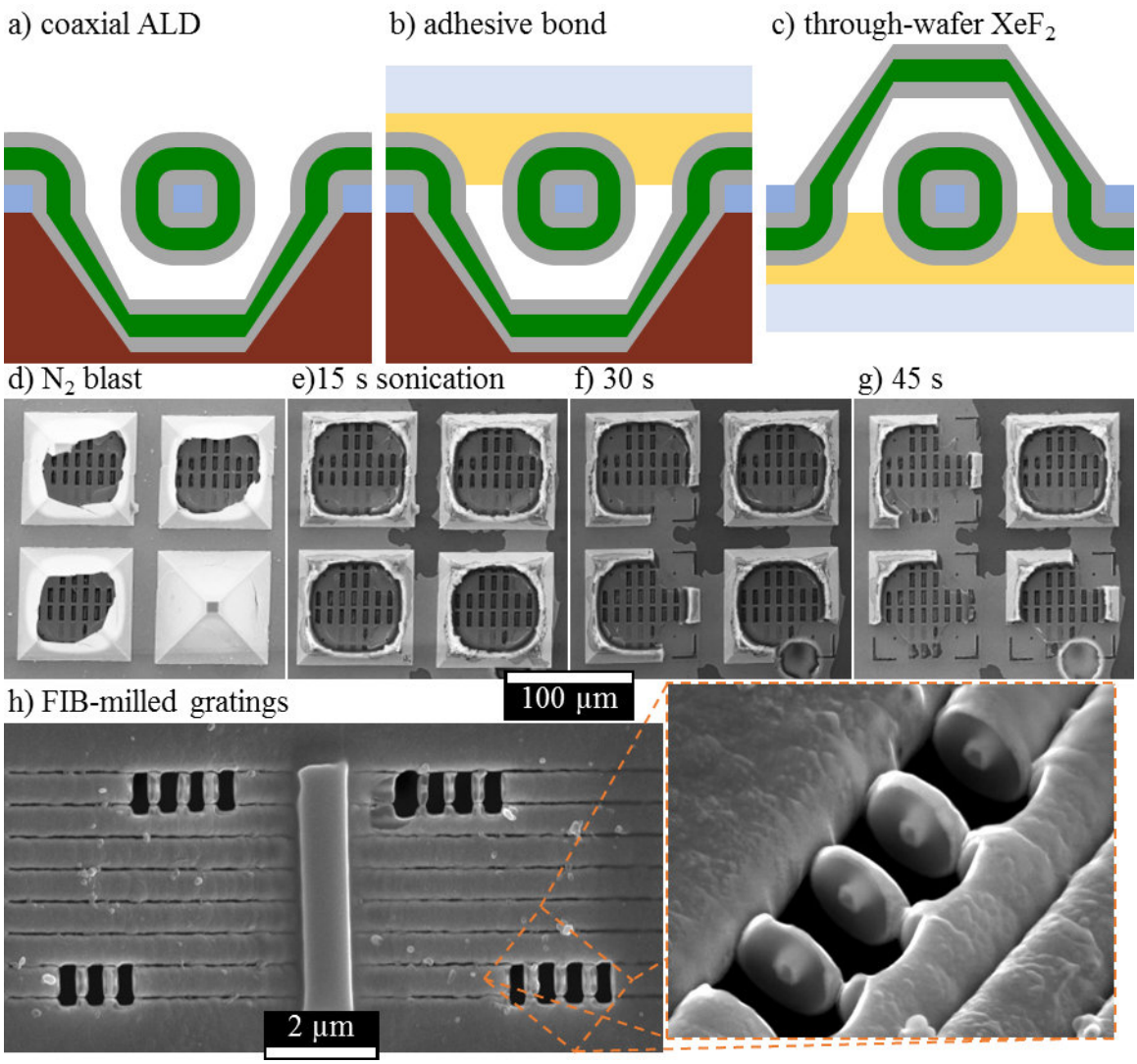

Figure 4.15: Adhesive bonding and optical access to the horizontal ALD nanocoax. (a-c) Fabrication schematics. (d-g) ALD-coating the KOH pits results in Pt/Al_2O_3 "tents" which obscure the coaxes after the through-wafer XeF_2 etch. The tents were disintegrated by sonication. (h) Gratings were FIB-milled.

4.2.3 Vertical nanocoax fabrication

Optical access to horizontally oriented nanocoaxes must be done by patterning openings into the ends (or to preemptively prevent their closure). But vertically oriented nanocoaxes, as in Figure 4.7, can be opened without needing to pattern a window, the top sides of those coaxes were opened abrasively. That facile approach (*i.e.* no patterning) requires only a

controlled abrasion rate. There is one thing that all prior vertically oriented nanocoaxes have in common: the coatings were applied to the external parts of the frame. Therefore, as the coaxial layers were coated, the diameter increased. But the conformal ALD coating discussed in Section 4.2.2.3, suggests an alternative topology for the frame. Instead of coating onto the outside of a pillar, why not coat the inside of a hole? In that case, as the coaxial layers are coated, the diameter decreases. This manner of interior-surface-coating is critically enabled by ALD. Figure 4.16 shows a summary sketch of this fabrication scheme, which is covered briefly in [219]. I made coaxial thin films by filling in a template of high aspect ratio nanoholes. Sections 4.2.3.1 through 4.2.3.4 cover each of these fabrication process steps in closer detail. Figure 4.16-a) through -h) show, in broad strokes, snapshots of different steps of the fabrication. The five hexagonal panels in Figure 4.16-i) show the fabricated MIM nanocoaxes as in panel -c), still embedded in their Si scaffold. Figure 4.16-j) shows a FIB cross-sectional image of the complete structure.

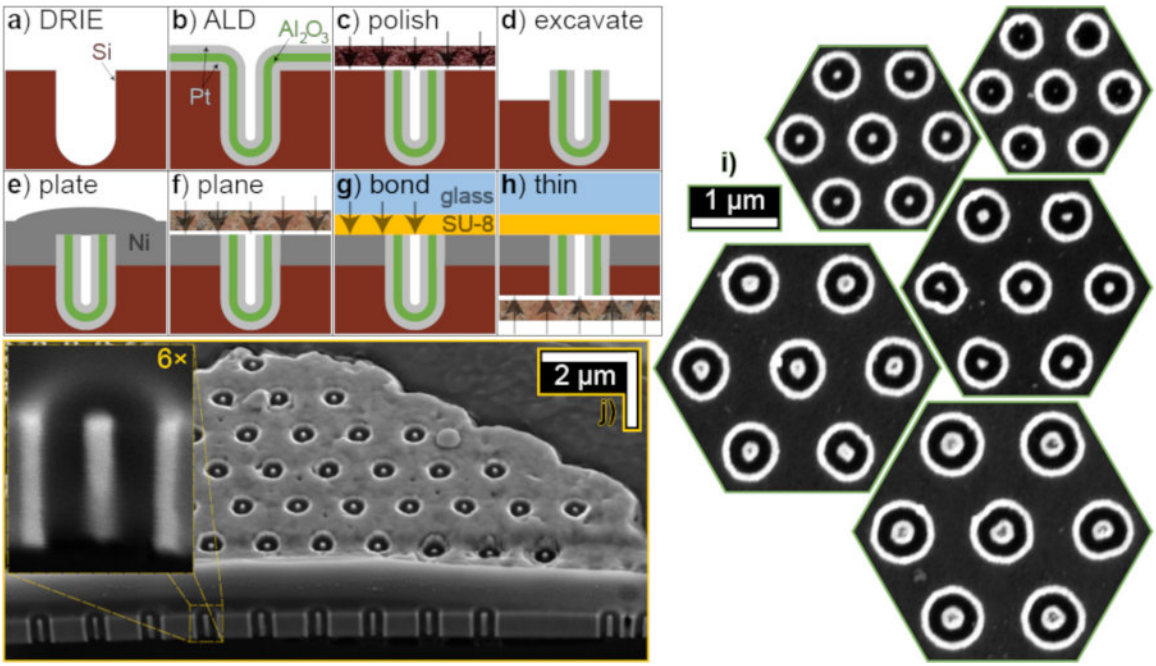

Figure 4.16: Fabrication of vertical nanocoaxes by ALD: overview. Taken with permission of the authors of [219]. (a-h) Are fabrication schematics, (i) shows the MIM nanocoaxes at step -c), and (j) shows a FIB cross-sectional image of the complete structure, backside thinned to a final thickness of 0.8 µm.

4.2.3.1 Nanohole array patterning by Bosch deep reactive ion etching

The nanohole illustrated in Figure 4.16-a), with diameter $\varnothing_{\text{hole}} \sim 0.5\ \mu\text{m}$, is generated by EBL. The samples I fabricated are not individual nanoholes, as drawn schematically for simplicity, but nanohole arrays with pitch p. Figure 4.16-a) conveys that the nanohole array pattern is transferred into a Si substrate with a Bosch deep reactive ion etch (DRIE) [220]. The etched arrays have three parameters: $\varnothing_{\text{hole}}$, p, and etch depth L. But there are a series of prerequisite fabrication steps not shown in Figure 4.16 before the Si-DRIE can be performed. Of key concern is how to mask the DRIE. The ideal mask would store an image of the pattern with high fidelity and would also have high selectivity against Si during the DRIE. While the most faithful way, in general, to transfer high fidelity images of a pattern is to use the patterned resist itself as the mask for the process, there are

problems with using the PMMA EBL resist in this case. For starters, since I am interested in $\varnothing_{\text{hole}} \sim 0.5\ \mu\text{m}$, the resist really shouldn't be much thicker than that. One could not, for example, use EBL to pattern $\varnothing_{\text{hole}} \sim 0.5\ \mu\text{m}$ into a 2 μm thick layer of PMMA. At least not easily. In my initial assessment, I found the selectivity of PMMA against Si in the Bosch etch to be around 8. This means I could etch, at maximum, a depth of roughly $L \sim 4\ \mu\text{m}$ with a PMMA mask. So, a more highly selective mask material is required. In many regards, Al would be the best candidate for a fluorinated plasma etch mask. However, I executed the Bosch DRIE on a tool at the Harvard center for nanoscale systems (CNS) which is dedicated metal-free. One cannot put Al in the chamber of that CNS tool. SiO_2, which is allowed in that chamber, has a suitably high selectivity against Si, which I found closer to 16, much in line with the literature [221]. Figure 4.17-a) through d) show some of the prerequisite fabrication steps before the DRIE.

Figure 4.17-a) shows that the nanohole array was patterned into a 250 nm thick, 950 kDa PMMA resist following an EBL recipe very similar to that of Section 4.2.2.1. The sample had a thin film stack of 1 μm of SiO_2 and 100 nm Al. The Al was deposited by e-Beam evaporation, and the SiO_2 was grown thermally. Much of the figure is dedicated towards this thermal oxide growth. Figure 4.17-h) shows an optical micrograph (darkfield contrast), using a white-balanced camera, of several nanohole arrays patterned into PMMA after development and descum, with the inset showing an SEM micrograph.

The oxide thickness, x, was measured by profilometry and normal-incidence reflectometry, which agreed to better than 5 nm. The panels in Figure 4.17-f) show normal-perspective photographs with care taken to white-balance the camera as much as possible. Figure 4.17-g) plots x *vs.* t for 4 different oxidation runs. The lower 3 were with

humidified oxygen, by sparging pure O_2 through a heated flask of DI. The upper run used different plumbing which more firmly sealed the flask. As the flask boiled and developed a head of steam, the steam was forced through insulated stainless piping into the tube furnace at *ca*. 1 bar, only 1 PSIG higher than ambient. Liquid water should never be in the tube, especially not in the heated zone. I kept all parts of the tube hot enough to prevent condensation. I further ensured the constant flow of steam through the tube by biasing the pressure gradient, pulling a slight vacuum on the exhaust by condensing it in a bucket of ice. A growth curve [146]

$$x = 0.5A\left(\sqrt{1+\frac{4B}{A^2}t}-1\right), \tag{4.29}$$

was fit to the measured thicknesses. For the steam-based growth, I found $A = 0.114\ \mu m$ and $B = 0.598\ \mu m^2/h$.

Figure 4.17-b) shows that the pattern was transferred into the Al layer using an ICP RIE tool at the CNS, where 500 W of 13.56 MHz power sustained a Cl_2+BCl_3 based plasma at 7 mTorr with each of the chlorine and boron trichloride gaseous precursors flowing at 10 SCCM. A DC bias of 300 V maintained directionality, and the sample was cooled by flowing He to maintain 20 °C (just as in Section 4.2.2). The process yielded an Al etch rate *ca*. $180\ nm/min$, but with only a modest selectivity against PMMA of 1.4. Figure 4.17-c) shows that the pattern is then transferred into the SiO_2 layer using another ICP RIE tool at the CNS, where again 500 W of 13.56 MHz power sustained a 7 mTorr $CHF_3+H_2+Ar+CF_4$ based plasma, with respective flow rates of 50, 30, 6, and 2 SCCM. With the target material this time being non-conducting (and not connected to ground in

any case), an RF bias (also at 13.56 MHz) with peak-to-peak voltage $V_{pp} \sim 900$ V was applied to assure directionality, and the sample was, as before, cooled with flowing He to maintain 20 °C. The measured SiO_2 etch rate was 110 nm/min , and I found the selectivity against Al to be greater than 12.

Figure 4.17-d) shows the nanohole pattern is finally transferred into the Si substrate by Bosch DRIE. In the Bosch process, a much higher anisotropy can be achieved than in conventional RIE by performing a directional RIE step in sequence with a PECVD isotropic passivation step. Those two steps are repeated for a number of cycles. I carried out the Bosch DRIE also on a CNS tool, where the etch step was an $SF_6+C_4F_8$ based ICP at 33 mTorr flowing at 300 and 50 SCCM, respectively, and with 2.5 kW of 13.56 MHz power to maintain the plasma. The sample, cooled on the backside by flowing He to maintain 20 °C, was biased with 18 V DC, modulated at 150 Hz. This step was terminated 1.2 s after the plasma ignited. The deposition step was a C_4F_8 based ICP at 25 mTorr flowing at 270 SCCM, and again with 2.5 kW of 13.56 MHz power to maintain the plasma. The sample is not biased for the PECVD step, which is terminated only 1.0 s after strike, and this step results in an isotropic deposition of roughly 2 nm-worth of fluorocarbon. In all the previously mentioned RIE's, after striking and establishing the plasma, typically taking 3 s, the RIE tools use feedback controllers on their various systems to keep the plasma as stable as possible. However, in Bosch DRIE, the timing of the plasma control is critical, requiring ignition, termination, and stabilization times all shorter than 1 s. The DC bias during the etch step ensures the fluorocarbon coated on the side walls is relatively untouched and therefore only normal-facing surfaces are etched. While the etch rate should

strictly be given in nm/cycle, in practice I used recipes with hundreds of cycles, and found $R \sim 1\ \mu\text{m}/\text{min}$.

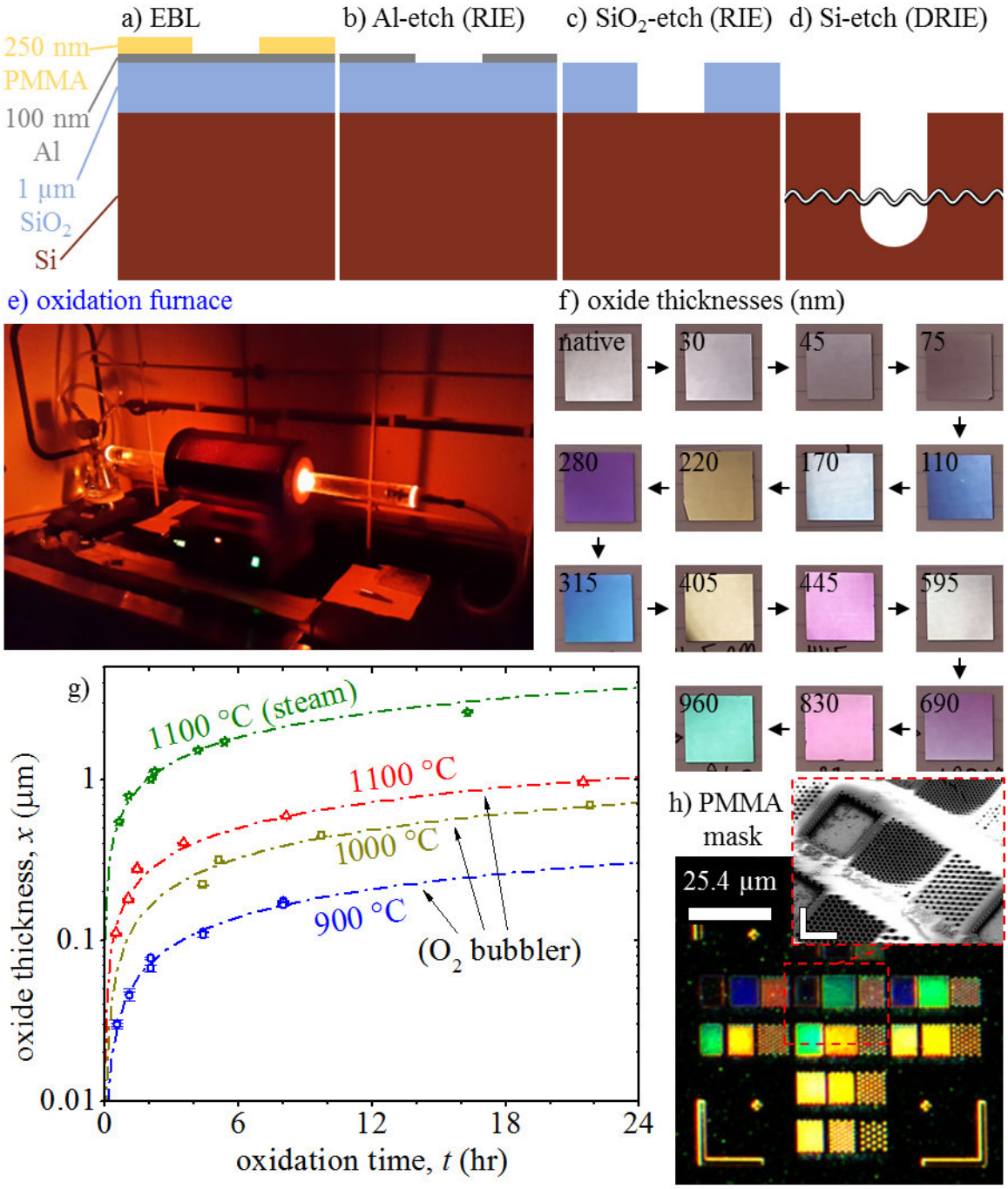

Figure 4.17: Oxide growth details. (a-d) Nanohole patterning schematics. (e) Tube furnace. (f) Array of different oxide thicknesses photographed from above. (g) Oxide growth curves. (h) Darkfield image of the PMMA resist. The RGB colors in this image faithfully portray what one sees in the ocular. The inset (compound scale bar: 5 µm) shows an SEM micrograph.

4.2.3.2 Conformal MIM coating by ALD

Figure 4.17-d) cannot properly display the full AR of the etched hole, so I use a squiggly break. I can repeatably achieve $AR \sim 20$ and fill factors of 50% (*e.g.* $L/Ø_{hole} = 10\ \mu m/0.5\ \mu m$ and hexagonally close-packed $Ø_{hole} \times p = 0.5 \times 0.68\ \mu m^2$ are typical). After the DRIE, I conformally coat the MIM layers of the coaxial structure by ALD of sequential Pt and Al_2O_3, as illustrated by Figure 4.16-b), and as discussed in detail in Section 4.2.2.3. The *conformality* of the coating is key: The films are coated radially inward from the sidewalls of the etched holes. So depending on $Ø_{hole}$ and on the sum of the film thicknesses t_{Pt} and $t_{Al_2O_3}$, the nanohole may or may not clog during the ALD steps. Because the nanohole may clog, the resulting structure can have one of four basic topologies, assuming the same t_{Pt} for the 1st and 2nd Pt layers, as sketched in Table 4.4.

topology name	**$Ø_{hole}$ range**	**resulting waveguide**
metal only	$\frac{Ø_{hole}}{2} < t_{Pt}$	wire
no core	$t_{Pt} < \frac{Ø_{hole}}{2} < t_{Pt} + t_{Al_2O_3}$	hollow cylindrical
solid core	$t_{Pt} + t_{Al_2O_3} < \frac{Ø_{hole}}{2} < 2t_{Pt} + t_{Al_2O_3}$	"conventional" coax
hollow core	$2t_{Pt} + t_{Al_2O_3} < \frac{Ø_{hole}}{2}$	coax with air-filled core

Table 4.4: Vertical nanocoax by ALD, fabrication topologies.Depending the ALD film thicknesses t_{Pt} and $t_{Al_2O_3}$, and on $Ø_{hole}$, different topologies will result.

The schematics presented in Figure 4.16-a) through -h) are for a hollow core nanocoax, *i.e.* the largest diameter hole, final row in Table 4.4. Figure 4.16-c) shows how one can access the coaxial layers after ALD by mechanical polishing on the top side, just as described in

Section 4.2.3. So, one opens the coaxial structure simply by controlling an abrasion rate, and not by lithographic patterning. This step was carried out with a vibratory polisher on an adhesive-backed felt platen, loaded with a glycerin-based slurry of 50 nm SiO_2 grit. I find that controlling the polish removal rate to less than 1 μm/h and minimizing as much as possible the total thickness removed by vibratory polishing (say to less than 15 μm, if possible) is a best practice; with careful fixturing, one can all but eliminate loss of planarity during this polishing step, removing a 150 nm Al_2O_3 film uniformly across a 15×15 mm^2 die. In Figure 4.16-e), each of the five hexagonal panels are for arrays with different $\varnothing_{hole}$ (400, 450, 500, 550, and 600 nm) after this polishing step, where the constituent film thicknesses are $t_{Pt} = 75$ nm and $t_{Al_2O_3} = 150$ nm. The coaxial diameters $\varnothing_{ID}$ and $\varnothing_{OD}$, are determined by the combination of $\varnothing_{hole}$ with these film thicknesses. Amongst the five hexagonal panels, one can clearly see the latter three topologies named in Table 4.4. After the depositing the 1st Pt layer, the coaxial outer diameter is $\varnothing_{ID} = \varnothing_{hole} - 2t_{Pt}$, then after depositing the Al_2O_3 and 2nd Pt layers the inner diameter is $\varnothing_{ID} = \varnothing_{ID} - 2t_{Al_2O_3}$.

The ALD step is the linchpin of the overall process, so I make three remarks: First, due to its conformality, ALD can make non-circular (*e.g.* square) concentric MIM waveguides. For example, some of the nanocoaxes shown in the hexagonal panels of Figure 4.16 started with out-of-round nanoholes, resulting in D-shaped layers. For the purposes of optical confinement, however, these non-circular MIM waveguides still support a totally enclosed, cuffoff-free mode [222]. Second, and this is the essence of atomic layer lithography, the transverse dimensions of the structure are controlled by the ALD

thicknesses, since the holes fill inward from the sidewalls. ALD being a digital monolayer process, one can achieve *bona fide* Å-scale control over the transverse dimensions [204]. Third, the DRIE step yields nanoholes with $\mathrm{AR} \sim 20$, but as the holes fill inward during sequential deposition cycles, the AR of the remaining void at the center of the hole diverges, and we have observed conformal Pt deposition, shown in Figure 4.18, for $\mathrm{AR} > 300$, roughly on par with other recent work [223]–[226]. One may be able to push the conformal coating to even higher AR by varying the PtMe dose during ALD, for example by changing the exposure pressure and dwell time [227]. I did not attempt to determine if the dose could have been reduced. I simply observed deposition occurred and decided to tweak the process no further, paying no mind to PtMe use.

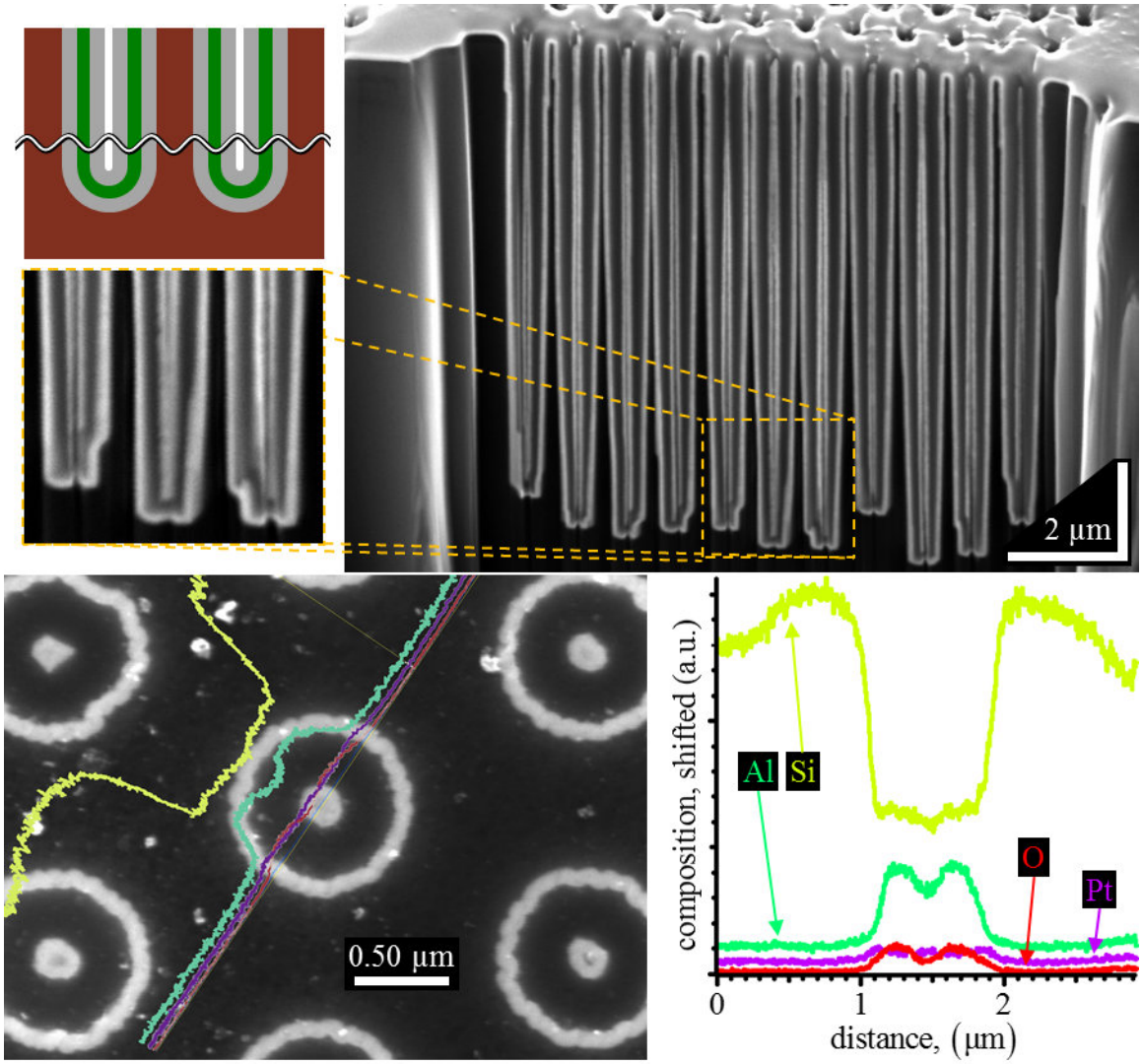

Figure 4.18: Conformal ALD into high AR nanoholes. The Pt and Al_2O_3 ALD layers coat the bottom of the hole, even as it closes to AR exceeding 300. An EDX line scan across a single nanocoax shows the material composition.

Figure 4.18 also shows an EDX line scan across a single nanocoax, with elemental compositions along this line scan plotted for Si, Al, O, and Pt. There are clearly resolved dips and peaks in the Si, Al, and O channels, but not as much in the Pt channel. The EDX were collected from a 2 nA probe current (30 kV) beam.

4.2.3.3 Excavation and electroplating

For optical interrogation, the coaxial structure in Figure 4.16-c) requires two further modifications, which I will describe in this Section and in Section 4.2.3.4. First, as shown in Figure 4.16-d), I substitute Ni for Si by "excavating" the Pt/Al_2O_3 nanocoaxes with an isotropic etch that is highly selective for Si. I used a $CF_4 + O_2$ based plasma at 420 mTorr sustained by 500 W at 2.45 GHz, with 150 and 10 SCCM flows for the gases, respectively. I measure an isotropic etch rate of $210\ nm/min$. The etch was masked with a photopatterned Shipley 1805 resist, hard baked for 5 min at 125 °C. The windows in the mask were matched to the sizes of the arrays, typically $8 \times 12\ \mu m^2$, performed with a Heidelberg µPG101 direct write system. As will be made clear in the next section, having a windowed/patterned ground plane (as opposed the whole $15 \times 15\ mm^2$ die, for example) makes the optical alignment much easier. With a local ground plane, one can focus the microscopes nearby to the array and make only a small positioning change to illuminate a single nanocoax with a tightly focused beam. The excavated coaxes, as well as the isotropic undercutting of the mask, are shown in Figure 4.19-a). The samples were descummed and coated with $Ti/Au = 5/10\ nm$ by e-Beam deposition under angled-rotation to make a conductive seed layer for electrodeposition. The top SEM micrograph in Figure 4.19-d) shows Ti/Au-coated nanocoaxes. The samples were then photopatterned with 4.5 µm thick SPR 220 photoresist with an open area $3.3\ mm^2$ using a laser-printed transparency, and then thoroughly descummed. After clamping leads, the samples were sealed up with Kapton tape so that only the $3.3\ mm^2$ is exposed to the electrolyte. Establishing a fixed electrolytic contact area is critical to process control. The rest of Figure 4.19-d) shows a

few snapshots of the electroplating process, where the voids between Pt/Al_2O_3 are filled in with Ni. The electrolyte is Transene sulfamate nickel SN-10, heated to 50 °C and stirred moderately. I plated in constant current mode, at 180/3.3 $\mu A/mm^2$ DC, Figure 4.19-e) shows the voltage trace required to sustain the constant current.

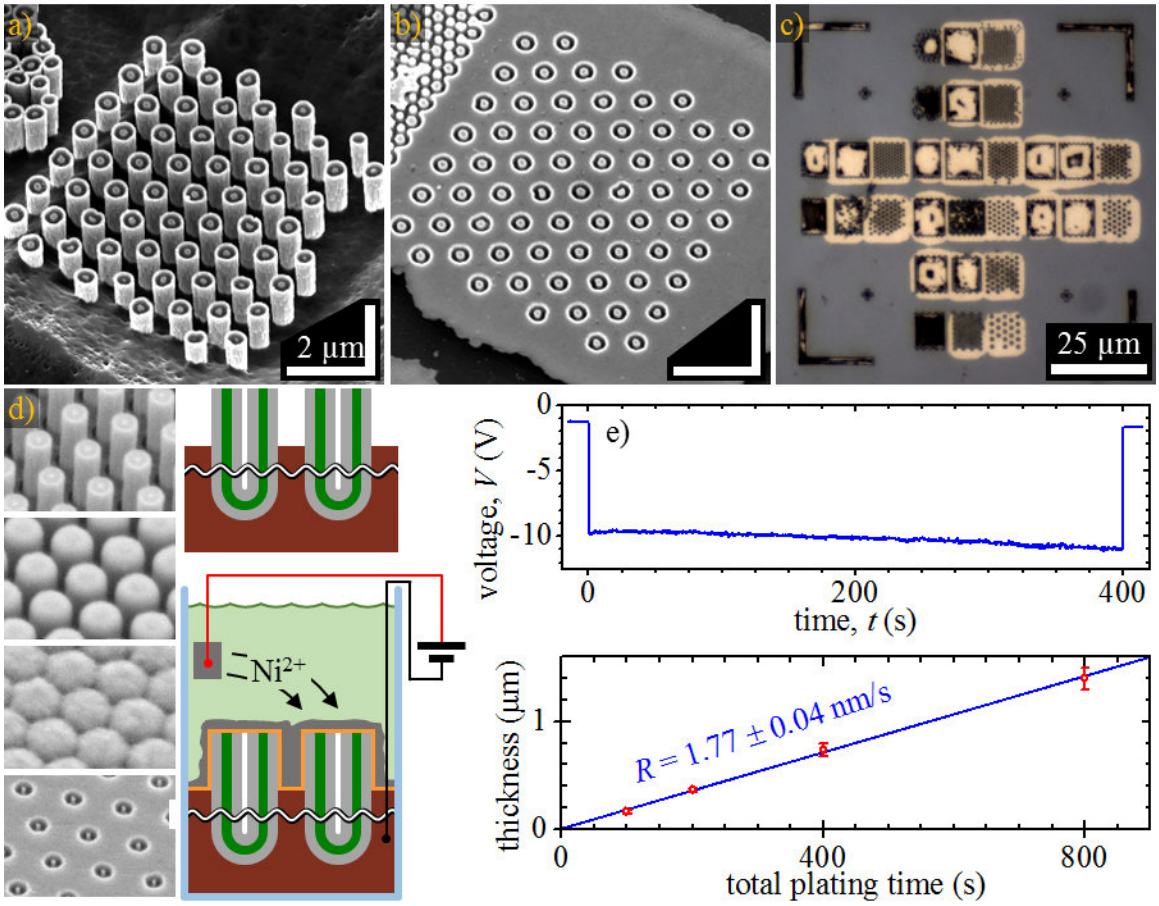

Figure 4.19: Ni-for-Si substitution by excavation and electroplating. (a) Excavation by $CF_4 + O_2$ etch. (b-c) After lapping. (d) During the plating, the Ni fills in the voids. (e) Voltage required for constant current plating and measured plating rate.

I electroplated several µm of Ni where the Si used to be, shown in Figure 4.16-e). This plating process again buries the top-side nanocoax aperture in metal, so I re-opened it with a mechanical planarization, Figure 4.16-f). Figure 4.19-b) and -c) show an SEM and optical

micrograph, respectively of the planarized structure. The planarization was performed with the home-built lapping setup described in Section 4.2.3.4. The need for planarization, as opposed to polishing, arose because I did not choose the $3.3\ \mathrm{mm}^2$ wisely. I put a single opening of that area at the center of the $15\times15\ \mathrm{mm}^2$ die. I found this gave very uneven polish rates across the die, as the plated Ni protruded by several μm, essentially putting a boss of high pressure right at the center of the die. A far better window design would distribute the electrolytic area over multiple points of contact along the perimeter of the die, thereby establishing better parallelism and uniformity in polishing pressure. Perhaps this could eliminate the need for lapping.

After planarization, the nanocoaxes perforate an optically opaque ground plane, instead of the relatively high transparency crystalline Si substrate. The Ni ground plane is mechanically refractory enough to making it easily processed by appropriate abrasives. The Ni is also plasmonically inactive, thus eliminating optical cross talk between neighboring coaxes and any enhanced/extraordinary optical transmission effects [228], and allowing one optically address an individual nanocoax. The optical constants, see Equation (3.16), for Si and Ni from [229] and [230], respectively, are plotted in Figure 4.20.

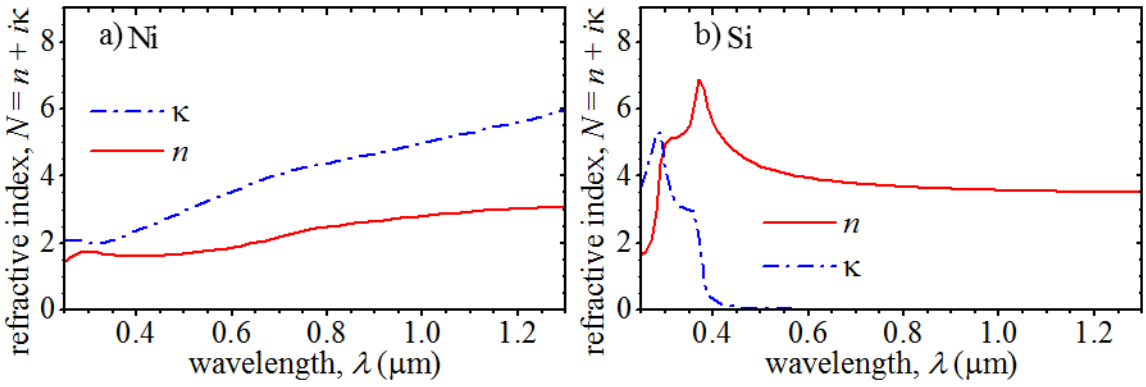

Figure 4.20: Optical constants of Ni and Si. From [229] and [230], respectively.

4.2.3.4 Wafer bonding and back-side thinning

The second change required of the coaxial structure in Figure 4.16-c) is to open up the bottom, which closes off during 1st Pt ALD see Figure 4.18. Figure 4.16-g) and -h) show that adhesive wafer bonding and back-side thinning were used to gain access. Figure 4.16-g) depicts the adhesive bonding [231], [232] of the Si substrate to an optically transparent sodalime glass superstrate using an SU-8 epoxy layer. Some details from the bonding process are shown in Figure 4.21. Glass wafers were cut into $15\times15\ \mathrm{mm}^2$ die then cleaned by piranha etch $\left(3:1::\mathrm{H_2SO_4}:\mathrm{H_2O_2}\right)$. Both the Si and glass die were treated to an $\mathrm{O_2}$ descum and left for 2 min on a 100 °C hotplate immediately before spin-coating an epoxy film (SU-8 3000), 5 µm thick. The dollop of SU-8 solution was cast on hot die, with the heat capacity of the liquid dollop used to cool the die down. Care must be used to avoid bubble formation when casting the SU-8. The edge bead which forms during spin coating, and which has deleterious effect during bonding, was mitigated by spinning at the highest possible speed, I used 8000 RPM. I measured by profilometry a 10 µm bead at the edge of the 5 µm film. The SU-8 was soft-baked on a 65 °C hotplate for 7 min. Figure 4.21-a) shows the press I used. The glass superstrate was placed edge-to-edge into contact with the Si substrate and then allowed to slowly "hinge" closed, with finger-pressure from a lint-free wipe rolling along the same direction as the hinge action afterward. After contact, the die should be firmly "wrung" together (much like Gauge blocks), with Newton's rings (optical fringes) clearly visible through the glass. A small piece of plastic transparency printing film, 100 µm thick, was placed on the bed of press with wrung die-stack laid down on top, glass-side up. The ram drives a non-rotating jaw into contact with the glass; the jaw as some freedom to articulate and auto level. The plastic film, being slightly compressible,

helps to auto-level the glass and Si together. Both the press bed and the jaw were lapped flat. I had no way to measure the pressing force, I just screwed until my knuckles turned white. The tightened press was placed in 75 °C convection oven for 1 h for the epoxy monomer films to reflow into each other. The press was cooled to ambient over 30 min before releasing the pressure, and the SU-8 was flood exposed by a Hg lamp, with $23\ \mathrm{mW/cm^2}$ measured on the I-line (365 nm) for 60 s. Immediately after exposure, the stack was again tightened in the press and left under pressure for a post-exposure, cross-linking bake of 225 °C for 1:00 h, then left to cool at room temperature under pressure for 45 min. This post exposure bake is executed well above the cross-linked SU-8 glass transition temperature [233], and is when the bonding happens.

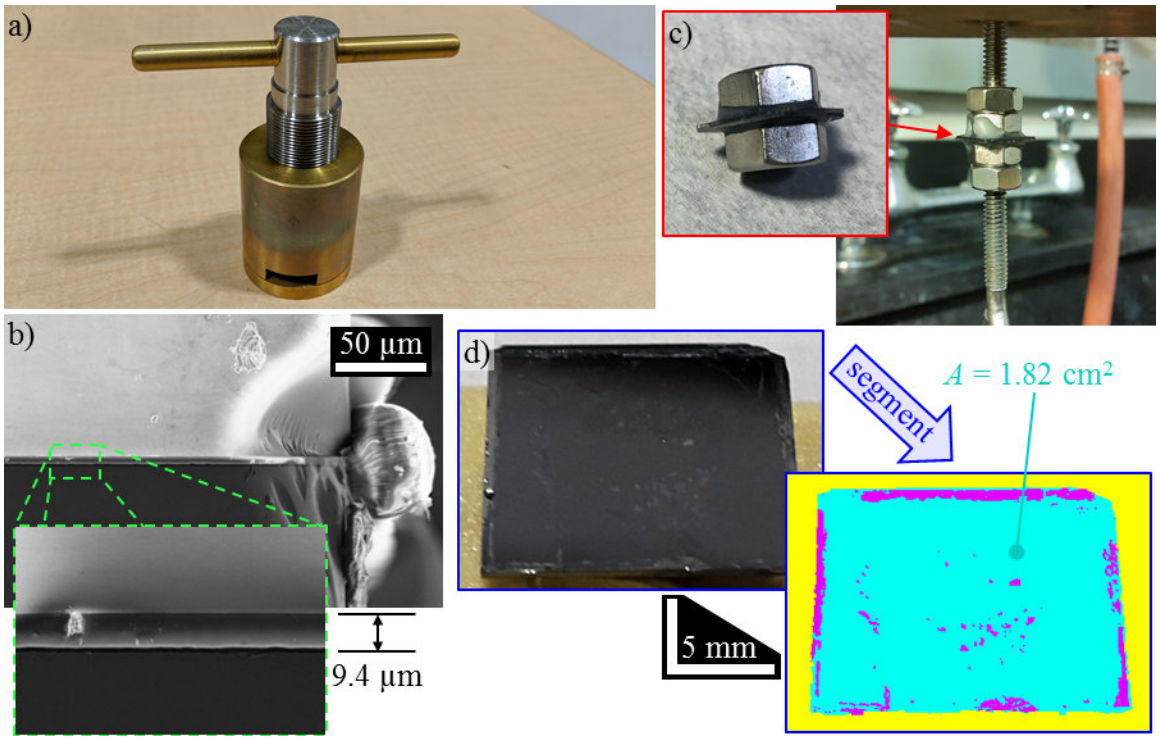

Figure 4.21: Adhesive wafer bonding. (a) Screw press. (b) SEM of the Bonding layer. (c) Apparatus for measuring the tensile strength. (d) Bonding area (cyan) measured by image segmentation after tensile failure.

Figure 4.21-b) shows a cross sectional SEM of a bonded die-stack. I cut the bonded die-stack along the diagonal with a low speed, abrasive circle saw, then ground and polished the cut for a clean cross section. The larger view shows the edge bead is pressed out during bonding. Figure 4.21-c) shows the apparatus I used for tensile strength measurement, where I hung a water jug from the bonded stack and filled with water until the stack snapped apart. I observed consistently that almost all the bond breakage was by SU-8 delaminating from the glass. By measuring the total mass suspended by the stack right before failure I could measure the bonding force. Figure 4.21-d) shows a photographed Si die with debonded SU-8 after tensile failure. I segmented the image into three parts: a background (yellow), unbonded die area (magenta) and bonded die area (cyan). By dividing the bonding force into the bonded die area, I found 3 ± 1 bar of bonding strength, and the bonding area fraction typically exceeded 95%. I believe that if contact were initiated under vacuum instead of by wringing out the air, then perhaps 100% could be achieved. The delamination from the glass could be mitigated by appropriate plasma pre-treatment [234].

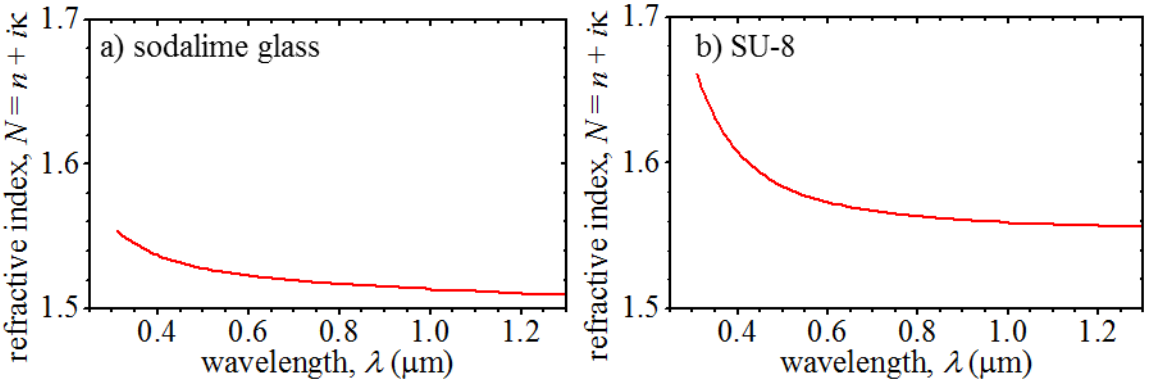

Figure 4.22: Optical constants for SU-8 and sodalime glass. From [235] and [236].

Figure 4.22 shows Cauchy fits (see Equation (4.28)) to the optical constants of sodalime glass and SU-8 3000, taken from [235] and [236], respectively. The absorption, κ, was measured in both of those works and is included in the finite element modeling presented in Section 4.4, however it is small enough (less than 0.01) to be omitted from the plot range in Figure 4.22.

I then employed a second mechanical planarization step, as shown in Figure 4.16-h). More details of this planarization are given below in Figure 4.23. Figure 4.23-a) shows an apparatus I used for hand-lapping. The brass piston, with diameter Ø1.375" slides freely through the 300-series stainless cylinder, with a 2" bore length, and +0.0005" oversized diameter. The bottom surface of the cylinder was precision ground to be perpendicular to the bore. This fixture transfers the flatness of the surface plate onto the sample and allows for backside thinning to proceed parallel to the top surface. Figure 4.23-b) shows light transmitted through thin Si, with the W filament of an incandescent lightbulb clearly visible. Figure 4.23-c) shows a measured transmittance spectrum from this sample (brown) with a multilayered thin film calculation result [237] (blue curve) for reference. Figure 4.23-d) shows the theoretical model I used to compute that result.

grit size	particle diameter (μm)	removal rate μm/min
120	125	60±10
360	40	25±5
500	30	15±5
1200	15	5±3
-	6	< 2
-	3	< 2
-	1	< 2

Table 4.5: Si abrasion rates for Al_2O_3 lapping films. Hand-lapping rates measured with a micrometer. Details in text.

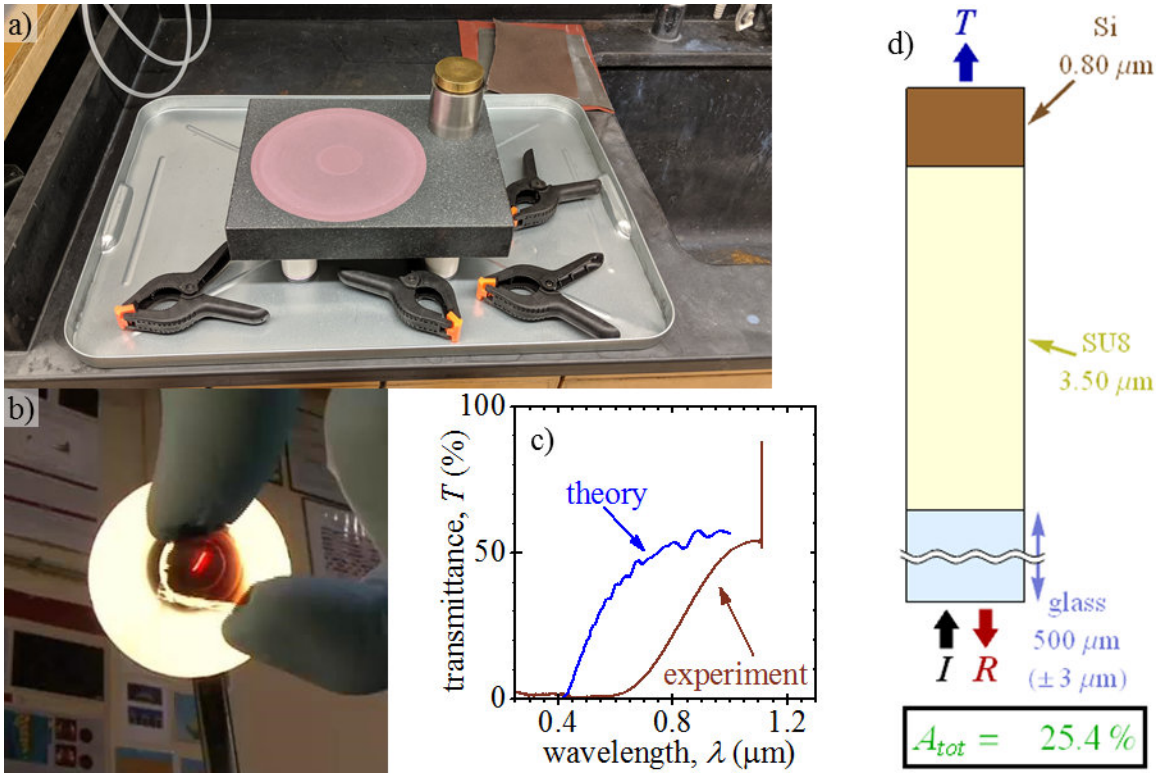

Figure 4.23: Backside thinning of Si bonded to glass. (a) Surface plate and lapping fixture. (b) Thin Si is transparent. In this white balanced photograph, the Si is roughly 1 μm. (c) Measured and calculated Si transmittance. (d) Theoretical model.

Table 4.5 give a few abrasion rates I measured on the hand lapping apparatus shown in Figure 4.23-a). The brass piston was first planarized for parallelism, then SU-8 bonded glass/Si samples were fixed to the brass piston with wax at 125 °C. The sample was pressed onto the molten wax, the brass piston was placed in a beaker with room temperature water, and a 0.1 kg weight was placed on top of the sample so that the solidified wax film measured 45±5 μm. The film was constant thickness for any given sample but varied from sample to sample. Note that the SU-8 bond may fail if exposed to temperatures greater than the glass transition temperature [233], so care must be used when selecting a pitch or wax fixative. The abrasion rate was measured by checking the thickness with micrometers, which can resolve 2.54 μm. I used ethylene glycol as a lubricant, and loaded with piston

with a 1 kg weight, so that the lapping pressure was roughly 0.4 bar. The “final approach”, for Si thicknesses less than 15 μm, should be done with vibratory polishing, as described in Section 4.2.3.2. From inspecting SEM micrographs, I find the vibratory polishing rates are typically ~ 0.8 μm/hr. Many wafer thinning and lapping recipes can be found online.

This backside thinning opens the bottoms of the nanocoaxes. With judicious. thinning the 525 μm-thick Si substrate down to a suitable thickness which is less than the etched nanohole depth planarization and final polishing recipes, one can readily control the final thickness to a precision of about 0.1 μm. Figure 4.16-j) shows a FIB cross sectional image of a finished structure with final thickness 0.8 μm. I have fabricated several samples with final thicknesses ranging from 0.8 to 5.8 μm. another one of which is pictured in Figure 4.24. After flipping the sample, the glass superstrate is relabeled as a substrate, with a thin Si layer on top.

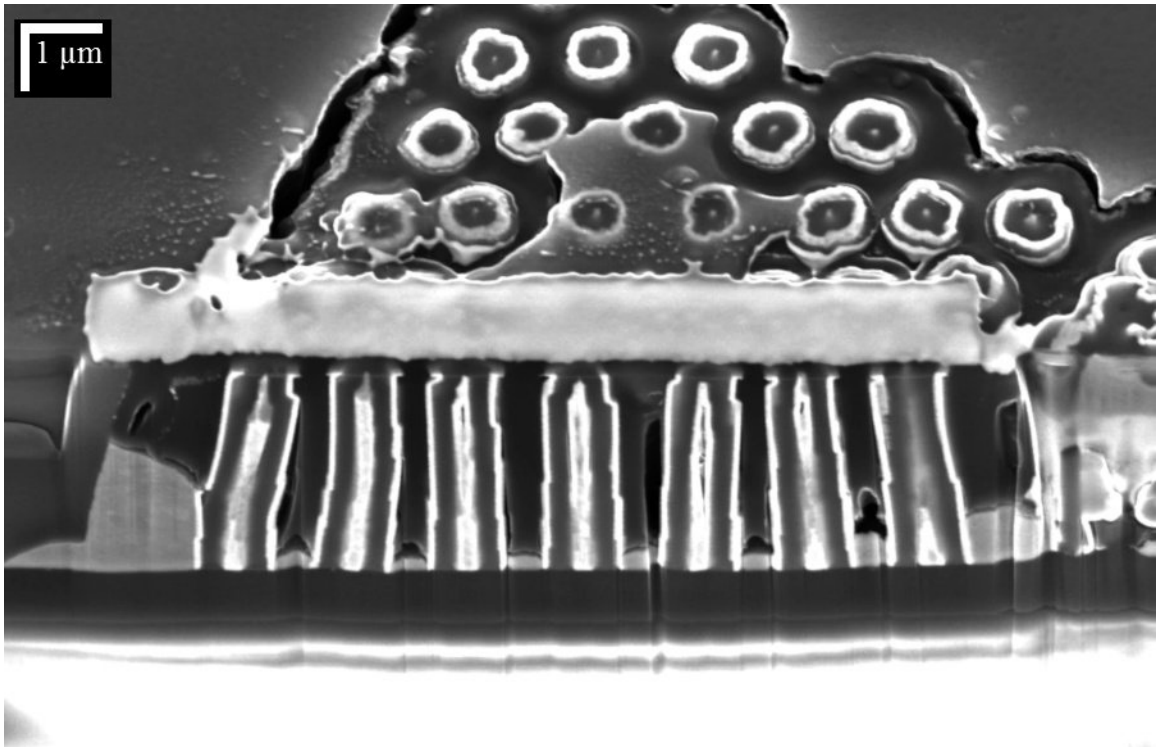

Figure 4.24: Back-side thinned nanocoaxes. The back-side thinning was terminated with 5.8 µm of Si remaining.

4.3 Optical interrogation

Since the most common sources of electromagnetic radiation are dipolar, much of the prior work involving optical excitation of nanocoaxial waveguides have been restricted in scope to dipolar guided modes, predominantly in the TE_{11}-*like* mode, but also in other dipolar modes [160]. Relatively few studies have focused specifically on coupling into the fundamental TEM-like (monopolar) mode. One scheme [238], [239] involves illuminating with TM-polarized plane waves at oblique angles of incidence, greater than 20°. Another scheme, intuitively stemming from the common cylindrical symmetry shared by a nanocoax and an LG beam, is to illuminate with a radially polarized optical vortex [114], [240], [241]. We follow the latter approach.

4.3.1 Polarimetric imaging

Figure 4.25-a) and -d) show the principle polarimetric imaging result, these data were obtained using the apparatus sketched in Figure 3.8 and discussed in Section 3.2. A heptamer of coaxes was positioned concentrically with the beam using the piezo stage. The central coax, sampling an interior annulus of bare beam shown in Figure 3.8- g), transmits a radially polarized donut which is significantly smaller than the bare beam. The peripheral 6 coaxes each transmit linearly polarized "p-orbitals" (*i.e.* with only a single hue), with the lobes of the orbital aligned to the local direction of linear polarization in the bare beam. We interpret these as direct observations of transmission by the fundamental TEM-like and the first excited TE_{11}-*like* modes, respectively. As mentioned previously, one proposed scheme for TEM-excitation is by linearly TM-polarized plane wave at oblique angles of incidence [242], larger than 20°. While a focused, radially polarized beam is TM-polarized and if strongly enough focused should contain the angular spectral content for this excitation mechanism [240], the $\mathrm{NA}_{\mathrm{beam}} = 0.31$ beam used in these experiments subtends angles of incidence only up to 12° in the glass substrate. I do not observe any multi-colored donuts on the peripheral 6 coaxes within the heptamer, only ever singly-colored p-orbitals. I conclude that, within these experimental conditions the TE_{11} coupling is the dominant means of transmission for those peripheral 6, much in line with the work of others [6].

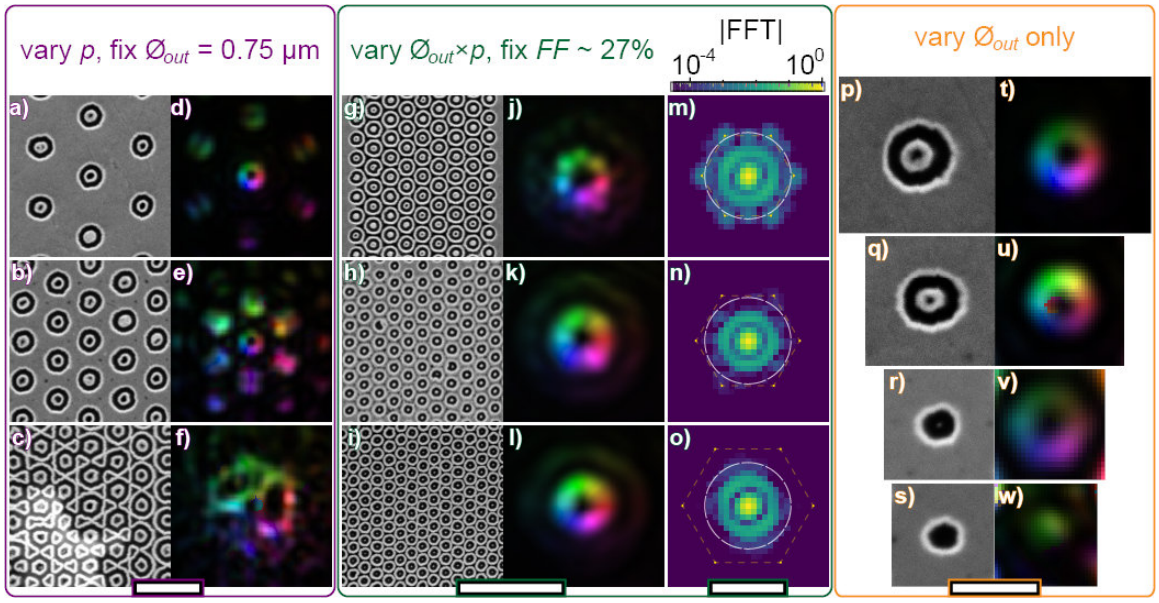

Figure 4.25: Donut transmission through nanocoaxes, polarimetric imaging. (a-f) Coalescence by arrays with fixed $Ø_{OD}$ and shrinking p. (g-o) Minimum resolved pitch for fixed $FF \sim 27\%$. FFT have been normalized against their peak. (p-w) Transmission through isolated, individual nanocoaxes. Scale bars: (a-f) 2 µm, (g-l) 5 µm, (m-o) 10 rad·µm^{-1}, (p-w) 1 µm.

Keeping the diameter $Ø_{OD}$ constant, I varied the pitch p, as shown in Figure 4.25-a) through -c). There one can see the fabrication limit of the "vertical ALD" process described in Section 4.2.3: when p approaches its lower limit, $p \to Ø_{hole}$, the insulating Al_2O_3 layer percolates. While the resulting MIM structure is a coalescence of Pt and Al_2O_3, and thus no longer an array of disjoint coaxes, it is still a multiconductor waveguide which continues to transmit light in a way that roughly preserves the polarization: one can see the central donut merging with the peripheral p-orbitals going from Figure 4.25-d) to -f). Shown in Figure 4.25-g) through -i) are SEMs of the densest arrays I fabricated, close to the percolation threshold, where the Al_2O_3 annuli subtend

about 27% of the area (*i.e.* fill factor, FF ~ 27%). In this sequence, I fixed FF and minified the array, shrinking both $Ø_{\text{hole}} \times p$. The transmitted polarimetric images, collected with a dry NA0.95 objective on the upright microscope, are shown in Figure 4.25-j) through -l). Those arrays cross the resolution limit of the microscope. For the smallest array, the transmitted donut (Figure 4.25-l)) is indecipherable from the bare beam (Figure 3.8-g)). Indeed, looking at a fast Fourier transform (FFT), plotted in Figure 4.25-m) through -o), one can see the first order diffracted peaks (yellow points) at $2\pi/p$ emerge inside the numerical aperture of the microscope (white circle). Therefore, one cannot resolve the pitch of arrays much denser than $p \square \lambda/\text{NA}$. Quite interestingly, this means the densely packed coaxes are functioning much in the same way as a phased array. The bare beam is sampled discretely on the back side by coupling into the guided modes of many individual coaxes (*e.g.* roughly 50 in Figure 4.25-i)) and, when emitted on the top side, the interference pattern broadcasted by the array resembles an apparently unaffected beam, at least within the resolution limit of the microscope. By taking the ratio of image exposure times and normalizing against FF I estimate the transmittance of these dense arrays is about 20%.

On the right-hand side of Figure 4.25, I show how the size of the transmitted donut depends on the size of the coax. As stated previously, the donut transmitted by the coax is significantly smaller than the bare beam in Figure 4.25-g). It is apparently critical for there to exist a center conductor. For example, in Figure 4.25-s) and -w), where $Ø_{\text{hole}}/2 < t_{\text{Pt}} + t_{\text{Al}_2\text{O}_3}$ (see Table 4.4), the resulting hollow cylindrical waveguide does not transmit a rainbow-colored donut. One should expect strong overlap between the donut

beam and the TM_{01}-like mode of a hollow cylindrical waveguide, provided that λ is shorter than the cutoff wavelength.

4.3.2 NSOM

The NSOM apparatus and techniques were described in Section 3.3. Figure 4.26 shows the principle near-field result from these nanocoax samples.

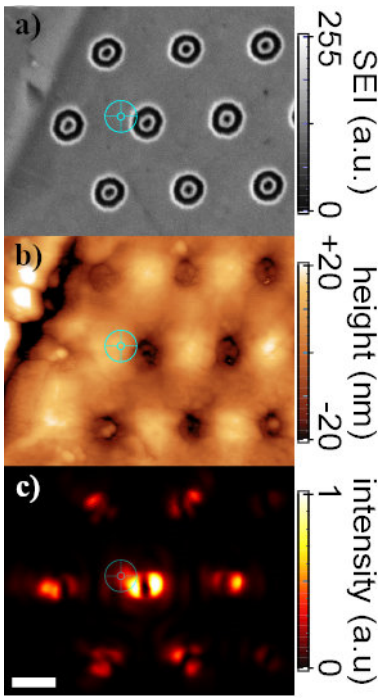

Figure 4.26: NSOM scan of donut transmission by a heptamer of nanocoaxes. The donut beam is nearly concentric with the central coax, with the suspected location of the topological singularity indicated by a cyan reticle. Scale bar: 1 µm.

The samples were aligned using the *xyz*-piezo stage shown in Figure 3.8 and in Figure 3.13. Note that this alignment requires mechanical coincidence from several objects all at once: the inverted and upright microscopes must be in focus on the top surface of the substrate, which is also the waist of the donut beam. Furthermore, the *xy*-positioning of the two microscopes and of the sample is such that the donut beam, the microscopes, and

a single nanocoaxial waveguide must all be, as close as possible, on the same optical axis. This level of alignment is actually readily obtained, adequate degrees of freedom in the optomechanics, when using a high-NA objective on the upright microscope, such as the NA0.95 and NA1.40 objectives used throughout Section 4.3.1. With a high-NA objective, one can easily resolve individual coaxes in the sparse arrays. But when using a low-NA objective, positioning an individual nanocoaxial waveguide is difficult. Mostly this is because the samples were fabricated as arrays. If the array pitch is unresolved by the upright microscope, then one just sees the collective broadcast of the phased array and has no easy way to know how the array is aligned against the beam. Compounding this, as discussed in Section 3.3, NSOM has two more limiting requirements: first, a LWD objective; second, the tip of the QTF NSOM probe must also be positioned for coincidence. Even for the sparsest arrays fabricated with $p = 2\ \mu\text{m}$, the LWD NA0.45 objective could not clearly resolve the array and the alignment for concentricity suffered.

Regardless, nearly the same information as in Figure 4.25-d) is shown in Figure 4.26-b): for coaxes not positioned concentrically, the transmission via the guided TE_{11}-*like* mode results in p-orbitals, where the lobes are directed radially away from the beam's topological singularity. If I draw lines from each of the 9 p-orbitals in Figure 4.25-b), then I conclude the beam's singularity was roughly 0.3 μm due West of the brightest coax. I have drawn a cyan reticle at this location, where the diameter of the reticle represents the circle of least confusion for the 9 lines' intersection point. Further development of an alignment procedure, which both allows space for the NSOM probe and positions an individual coax concentrically with the donut beam, is ongoing.

4.4 2D axisymmetric simulation

I used finite element analysis software [243], [244] to simulate the optical response of a nanocoax illuminated with a focused LG beam. Figure 4.27 shows an overview of the finite element model components, and Figure 4.28 shows the principle computational results. By exploiting the cylindrical symmetry, I have significantly reduced the size of the computational domain. Working within COMSOL's 2D-axisymmetric formulation allows computationally "large" volumes to be solved more quickly than in a Cartesian 3D model. For example, a model size of order $10\times10\times40\ \lambda^3$ solves several times per minute on a desktop computer. Several recent computational works have incorporated a focused LG beam into a finite element model [245]–[247].

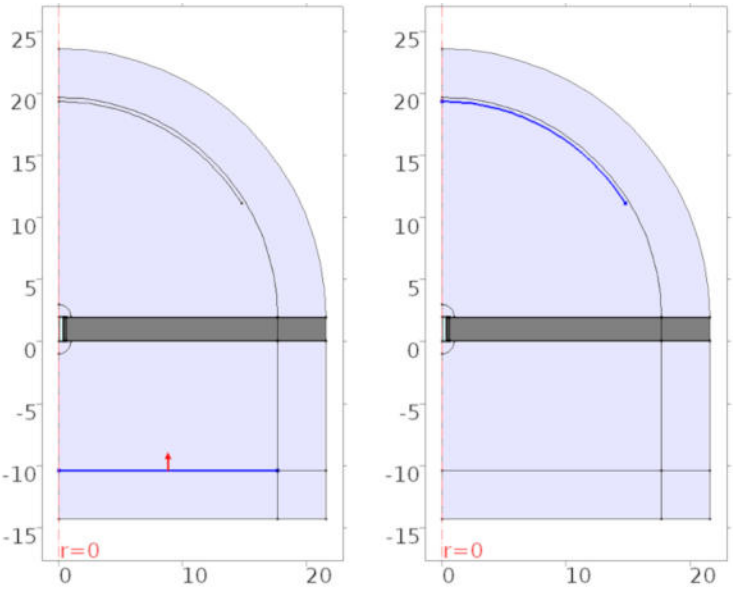

Figure 4.27: Finite element model definition. (a) Input and (b) output ports. The unit of model distance is 1 μm, with $\hat{\rho}$ and $\hat{z}$ oriented, respectively, along the horizontal and vertical axes.

Figure 4.27-a) shows the model geometry. The blue boundary on the bottom is the excitation port, where the incident LG_p^l beam is specified (with inward power flow indicated by the red arrow). The z-axis , indicated by the red $r = 0$ dashed line, is the axis of rotational symmetry. While the angular position ϕ is not a part of the 2D-axisymmetric model, and so it would appear to be only a 2D model, it is indeed a full 3D geometry, just restricted by symmetry to an assumed ϕ-dependence . Solutions are proportional to $\exp(im\phi)$, for an integer m . As discussed in the paragraph immediately preceding Equation (3.25), the overall ϕ-dependence of a paraxial electromagnetic LG_p^l beam is a sum of the spin (*i.e.* polarization) and orbital angular momentum carried by the beam,

$$m = l + \sigma_z . \tag{4.30}$$

2D-axisymmetric modeling requires one to use the circular polarization basis given in Equations (2.08) and (2.09), so either of $\sigma_z = \pm 1$. The input beam is either an $l = 0$ Gaussian as in Equation (3.27), or an $l = 1$ donut as in Equation (3.30). The model is clad with a perfectly matched layer (PML), and the gray slab in the center is a Ni ground plane which is perforated by a single, coaxial $\mathrm{Pt}/\mathrm{Al_2O_3}$ or $\mathrm{Ag}/\mathrm{Al_2O_3}$ aperture. Highlighted in blue on the top side of Figure 4.27-b) is the output "port". Although, strictly speaking, it is not a port but simply a surface to monitor power flow. Power exits the model only by absorption in the PML. The angles subtended by the input and output ports match the inverted and upright microscopes in Figure 3.8 (when using a dry objective on the top side).

The paraxially approximate formulae for the electric field in a linearly polarized Gaussian and in a radially polarized donut beam, $\mathbf{E}_{\hat{x}\text{-Gaussian}}$ and $\mathbf{E}_{\hat{\rho}\text{-donut}}$, are given in

Equations (3.27) and (3.30), respectively. The need for finite element modeling is the principle justification for using paraxially approximate formulae to model a focused LG beam, instead of a more accurate approach such as numeric integration [101]. These formulae can simply be evaluated at the input port of the model, with no need for an auxiliary computation step. This allows one to more freely adjust the model and more quickly narrow their focus onto the important physics by honing-in the model parameters appropriately.

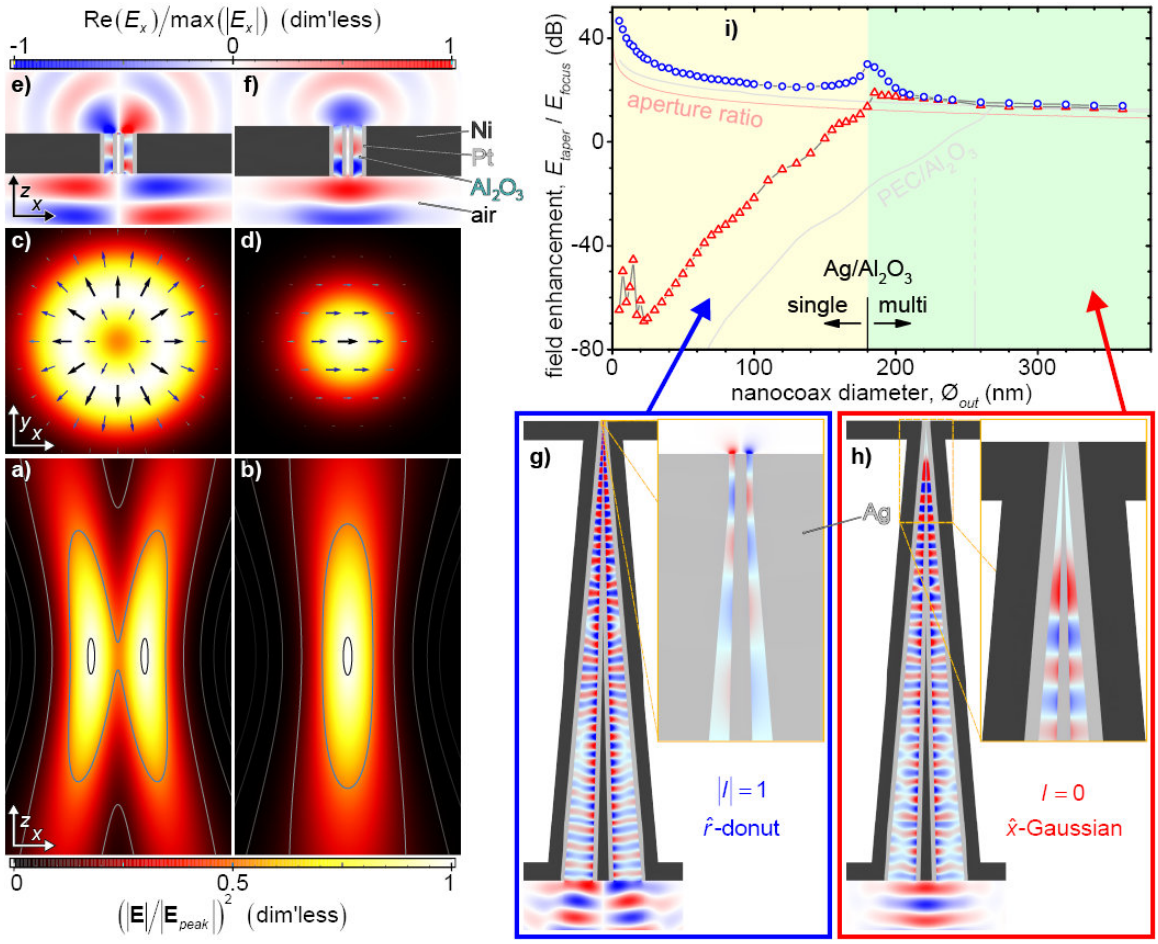

Figure 4.28: 2D-Axisymmetric simulation: overview. Taken with permission from the authors of [219]. Plots of energy density $|\mathbf{E}|^2$ in vectorial Laguerre-Gaussian beams: (a-b) longitudinal cuts in the xz-plane; and (c-d) transverse cuts at the focal xy-plane. (e-f) Straight $\mathrm{Pt}/\mathrm{Al_2O_3}$ and (g-h) adiabatically tapered $\mathrm{Ag}/\mathrm{Al_2O_3}$ coaxes transmit the LG beams as guided modes. (I) Tapered field enhancement *vs.* the coax diameter $Ø_{OD}$.

Figure 4.28-a) and -b) show longitudinal slices of the energy density $|\mathbf{E}|^2$ in the xz-plane, with contours drawn to span several decades (98, 50, 10, 1, 0.1, and 0.01% of the peak). Figure 4.28-c) and -d) show transverse slices in the xy-plane, with arrows plotting the transverse parts of the electric field, $\mathbf{E}_\perp = \left(E_x, E_y\right)$. One prominent feature of

Equations (3.27) and (3.30) are the finite longitudinal components, E_z. From Figure 4.28-a) the signature of a finite E_z is unmistakable: the finite field strength at the beam focus $(\rho,\phi,z)=(0,0,0)$, as discussed in Section 3.1.2.2, is due solely to the second term for E_z in equation (3.30) and results in all contours below roughly 50% forming a single "butterfly" shape, instead of two separate "cigar" shapes.

Figure 4.28-e) through -f) show single, hollow core $\mathrm{Pt/Al_2O_3}$ nanocoaxes perforating a Ni ground plane and transmitting an LG beam via a guided mode, with the $\hat{x}$-component of the field E_x plotted in the longitudinal xz-plane. In Figure 4.28-e), $\mathbf{E}_{\hat{\rho}\text{-donut}}$ is transmitted via the TEM-like mode, and Figure 4.28-f) shows $\mathbf{E}_{\hat{x}\text{-Gaussian}}$ transmitted via the $\mathrm{TE_{11}}$-like mode. Note that this transmission preserves the topology of the input beam. I used Pt in the experiments because it is currently the best available optical metal for conformal ALD, as described in Section 4.2.2.3. But within the parameter space that I modeled, the attenuation length for these modes ranges $10-1000$ dB/μm. If instead of Pt the coaxes are clad with Ag, the attenuation drops to a more useful $0.1-10$ dB/μm. Regardless of the material, as is the general case for all MIM guided modes, the attenuation increases as the mode gets confined to a tighter Ø_{OD}. In addition to changing the metal from Pt to Ag, I also changed the coaxial geometry from straight (as in Figure 4.28-e) and -f)) to tapered [248]–[250]. This geometry change emphasizes the main point of this thesis: a guided mode with no cutoff can be *compressed indefinitely*. shown in Figure 4.28-g) and -h) are longitudinal xz-slices of adiabatic $\mathrm{Ag/Al_2O_3}$ coaxial tapers, again plotting the

fiend component E_x. The entrance annular aperture at the bottom of the taper is enough to harvest most of the input LG beam, which couples into a guided mode and gets compressed as it propagates along the taper section, finally coupling into the nano-sized exit aperture. Additional in-coupling efficiency can be gained plasmonically [241], [251]. The insets in Figure 4.28-g) and -h) show zoomed views of the taper's exit aperture, with the TEM-like mode propagating all the way to the tip (where in this case, $Ø_{OD} = 5\ \text{nm}$), while the TE_{11}-*like* mode is reflected at some point along the taper where the constriction becomes too narrow.

The taper geometry was parameterized, and Figure 4.28-i) summarizes the results of a parametric sweep. The taper is terminated with a short straight section (where I fixed $Ø_{OD} = 2Ø_{ID}$). This straight section functions as a Fabry-Perot cavity, bounded by the exit aperture on the top-side and the impedance gradient along the taper on the bottom-side. For each of $\mathbf{E}_{\hat{x}\text{-Gaussian}}$ (red triangles) and $\mathbf{E}_{\hat{\rho}\text{-donut}}$ (blue circles), I shrunk the exit coax diameter $Ø_{OD}$ while monitoring the average field strength $\langle|\mathbf{E}_{\text{exit}}|\rangle$ at the exit aperture, that is, averaging across the radial ρ-coordinate. Keeping the taper geometry fixed, I tune the length of the straight section into resonance a find the maximal value, $\langle|\mathbf{E}_{\text{exit}}|\rangle_{max}$. The tuning of the Fabry-Perot cavity is illustrated in Figure 4.29. When a wave propagates through a lossy medium, then the more confined the wave is, the slower it moves. The confinement forces stronger and stronger interaction with the medium, which slows the wave down. The straight section at the taper's exit is where the wave is squeezed the tightest and moves the slowest, it is that part of the taper where the wave accumulates phase

at the steepest rate (at least per unit propagation length). Therefore, the optical path length a guided mode must travel as it propagates through the whole taper is more strongly dependent on the length of that straight exit section than of any other dimension of the taper. Phase matching the forward and backward propagating waves in that straight section by varying its length (*i.e.* Fabry-Perot resonance tuning) is therefore the most efficient way (at least requiring the smallest dimensional change) to maximize the field strength at the exit aperture, that is for a given taper geometry. This tuning makes for an antireflective coating on the taper's exit. As will be touched on briefly in Section 5.3, the simple linear taper geometry used in this model is not optimal. But it works well enough to demonstrate the main points of this thesis.

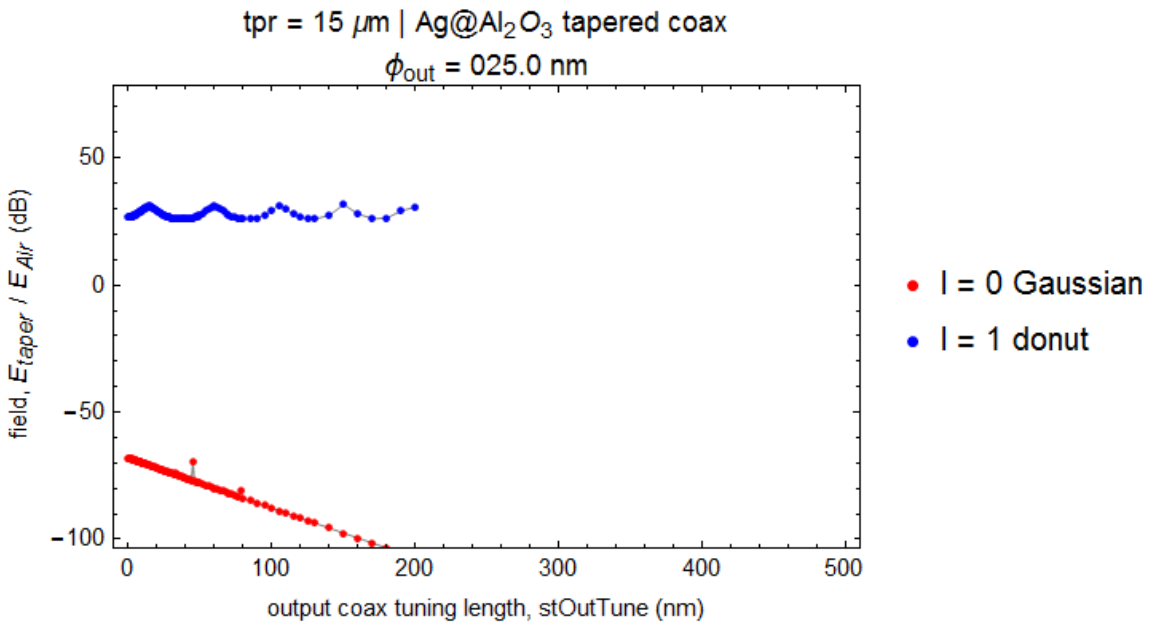

Figure 4.29: Fabry-Perot tuning of the finite element modeled taper. The taper model illustrated in Figure 4.28 is terminated by a straight section, which is tuned in length into a transmissive resonance for the Gaussian (red) and donut (blue) input LG beams.

This maximal field strength $\langle|\mathbf{E}_{\text{exit}}|\rangle_{max}$ (that is, the peak of the blue curve in Figure 4.29) is then compared to the average field strength $\langle|\mathbf{E}_{\text{annulus}}|\rangle$ of the LG beam focused in air and sampled over an annulus to represent the taper's entrance aperture. Note that the input port has a finite Fresnel number, given by Equation (2.21), typically around $N_F \sim 20$. Due to the diffraction effects discussed in Section 2.3.1, such modest values of N_F result in focal shifts [51]–[55] which compare with λ. So to counteract the focal shift effect from the finite-sized input port shown in Figure 4.27-a), I added a tuning parameter dz, a displacement, to adjust the focal point of the input fields,

$$\mathbf{E}_{\text{input}} = \mathbf{E}_{\text{input}}(\rho, z + dz). \tag{4.31}$$

To tune this parameter, I fixed the geometry of the input port and set the whole model space to air, removing all interior geometries and keeping only the PML and PEC at the perimeter of the model. I then defined an annular probe at the $z = 0$ plane, where the taper entrance aperture would have otherwise been, and monitored the area-integrated power flow through this annulus. I determined that the beam was in focus when that power flow was maximum. The field strength from the in-focus beam was averaged over the annular probe to represent the field at the entrance aperture of the taper, $\langle|\mathbf{E}_{\text{entrance}}|\rangle$. Because of the way I determined that the beam was in focus, I found different focal shifts for $\mathbf{E}_{\hat{x}\text{-Gaussian}}$ and $\mathbf{E}_{\hat{\rho}\text{-donut}}$, with LG orders $l = 0$ and $l = 1$, respectively. These are plotted in Figure 4.30. The authors of [252] have found that the focal shift should be independent of LG order, however. Further study into the focal shift at a finite port is merited. For starters, one should quantify how the focal shift depends on the port size, measured for example by N_F.

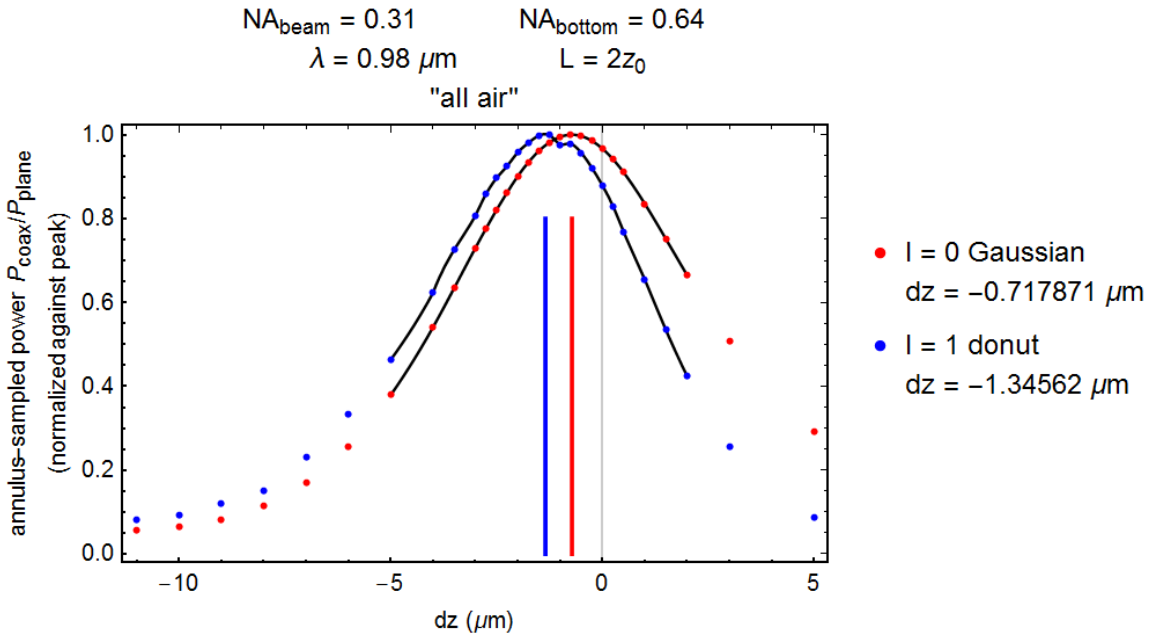

Figure 4.30: Focal shift tuning for a finite-port input beam. Due to the Fresnel number of the input port, there is a sizeable focal shift which we corrected for.

The ratio of field strengths at the taper exit aperture to entrance-sized annulus-in-air, each tuned as described above, gives the field enhancement, FE,

$$\mathrm{FE} = \frac{\left\langle \left| \mathbf{E}_{\mathrm{exit}} \right| \right\rangle_{max}}{\left\langle \left| \mathbf{E}_{\mathrm{entrance}} \right| \right\rangle}. \tag{4.32}$$

I with proper tuning, and for the smallest $Ø_{\mathrm{OD}}$, Ag-clad exit apertures that were simulated, I calculate $\mathrm{FE} > 45$ dB should be obtainable for the $l = 0$, TEM-like mode, corresponding to an intensity enhancement of 90 dB. The light at the exit aperture could be a billion times more intense than a tightly focused laser beam. Compressing the mode makes it more intense, scaling roughly in proportion to the ratio unobstructed areas at the entrance and exit apertures. When $Ø_{\mathrm{OD}} = 180$ nm in Figure 4.28-i), there is a clear bifurcation between a donut and a Gaussian input. For $Ø_{\mathrm{OD}} < 180$ nm and at $\lambda = 980$ nm, the waveguide is single mode. Note that for these single-mode waveguides, which can only operate in their

TEM-like fundamental mode, there are no Fabry-Perot resonances for the TE_{11}-like (or any higher-order) mode, since it is evanescent below cutoff. The maximum field enhancement in that case is, therefore, automatically the shortest tuning length. Replacing the Ag with a perfect electrical conductor (PEC), we find single mode behavior for a larger $Ø_{OD} < 260\ \text{nm}$, which is consistent with the textbook formula for cutoff given by Equation (4.15). The discrepancy in cutoff between PEC and a lossy metal [141] is due to the fields penetrating the metal, the larger mode size results in a redshifted cutoff. Roughly speaking, a PEC mode is exactly as large as $Ø_{OD}$, while a lossy metal mode is two penetration depths larger.

4.5 Conclusions

I have used conformal ALD to fabricate MIM coaxial waveguides with deeply sub-μm transverse dimensions and developed a novel nanofabrication process whereby backside thinning and electroplating rendered these coaxes optically addressable in a manner not previously achieved. We have used a vortex waveplate to generate a radially polarized donut beam of 980 nm light and coupled this focused beam into both the fundamental TEM-*like* mode and the first excited TE_{11}-*like* mode. While the coaxes investigated here experimentally are large enough to be multi-mode, I emphasize that atomic layer lithography boasts *bona fide* sub-nm-scale control over the transverse dimensions, and by choosing different film thicknesses one could easily fabricate much smaller single-mode waveguides [204]. This is a direction of future work.

I also presented simulation results where I studied an adiabatically tapered coaxial geometry. In Section 5.4, I propose a direction of future work is to develop fabrication

schemes for such a tapered structure. My simulation results show this taper can minify a radially polarized donut beam to length scales *arbitrarily smaller* than the free space wavelength, and indeed the resulting field enhancement in this structure diverges as the coax is minified below $Ø_{OD} \sim 40\ \text{nm}$.

5 CONCLUSIONS AND OUTLOOK

Section 1.1 says the aim of this thesis is to "to make nanostructures which confine light to smaller scales than the diffraction limit would otherwise allow." Chapter 2 defines the diffraction limit, Chapter 3 describes some tools and methods for that pursuit, and Chapter 4 covers my experimental progress towards reaching this goal. In light of that problem statement, I have compiled the polarimetric imaging and NSOM results jointly into Figure 5.1, where I plot the size of the transmitted donut (imaged by an optical microscope) *vs.* the physical size of the coaxial structure (imaged with an electron microscope).

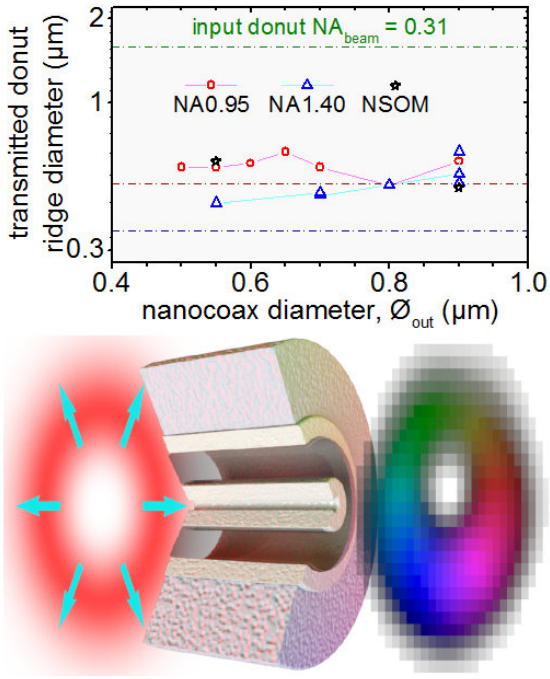

Figure 5.1: Optical confinement in the nanocoax. The nanocoax transmits a significantly smaller donut than the input beam.

I processed the V-channels of the polarimetric images (see Figure 4.25-t) to -w) and Figure 3.12-f)) using ridge detection in order to determine the transmitted donut size

as objectively as possible. Some details about ridgeline detection are given in Figure 5.2. Also plotted in Figure 5.1 are dashed lines to illustrate the resolution limits of the far-field optical systems, with, in spite of my best efforts in Chapter 2, various values of λ/NA. Although, especially in view of all of the details considered throughout Chapter 2, there is no unambiguously defined optical resolution limit which applies particularly for the circumstances of these experiments. Regardless of how the resolution limits are defined, Table 2.3, Figure 5.1, especially Figure 4.25-m) through -o), make it clear that the coaxes I have fabricated are confining light very close to the conventional diffraction limit. Regardless of which limit they are compared to, the transmitted donuts, being broadcast from nanocoaxes which sample only an interior annulus of the input beam, are nonetheless significantly smaller than the input, shown in green in Figure 5.1.

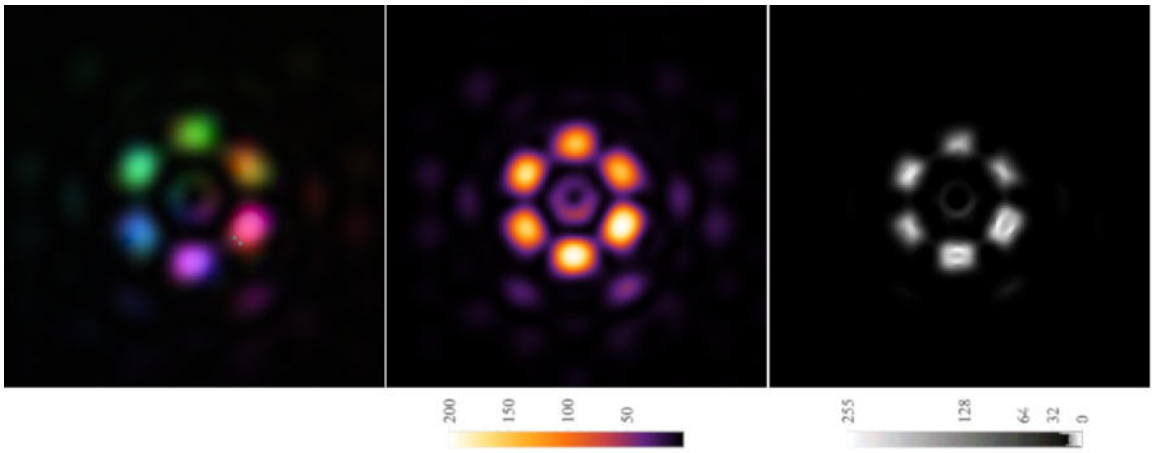

Figure 5.2: Ridgeline detection. (a) A full HSV color fusion image. (b) the V channel only. (c) Ridgeline analysis on the V-channel gives the probability local peak V-values.

The ridgeline analysis essentially applies a Laplacian filter to the image and seeks regions where the xx- and yy-curvatures have opposite signs, and also where one of them is much stronger in magnitude than the other. These are the same properties of a

mountain ridgeline, and hence the name. The transmitted donut should have a ring-like loci of maximum intensity, and the ridgeline analysis allows one to identify that ring in an objective way. For example, if one were to draw circles by hand on the ring of peak intensity from the central transmitted donut in Figure 5.2-b) and -c), it is clear that the ridgeline filtered image gives a much more narrow range of acceptable circles.

If one were to continue in this project area, here are some topics worth exploring. An over-arching goal which motivated this thesis is to make the proposed NCOM [16]. In Sections 5.1 and 5.2 I describe two potential pathways of reaching this goal which may be worth further consideration. In Sections 5.3 and 5.4 I build off of some of the work presented in this thesis and propose an alternative device morphology which would achieve the same ultimate goal: super-resolution imaging.

5.1 3D NCOM: Template-stripped pyramid

Template stripping is a way to make atomically smooth surfaces of noble metal where the roughness-free surfaces admit for longer-range SP propagation lengths [253]. Another interesting application for template stripping is the ability to mold 3D shapes out of the plane [254]–[256]. Figure 5.3 shows a template stripped Ag pyramid which has been FIB-milled into a rough version of the NCOM. The pyramidal template was generated by KOH etch into Si, with the Ag deposited by PVD afterwards. The hollow Ag pyramids were filled with epoxy and then peeled from the Si template to yield ~ 5 μm faceted pyramids protruding out from the plane. After peeling, the Ag pyramids were milled into striplines with grating couplers, as shown in Figure 5.3-a). Figure 5.3-b) shows an optical micrograph where TM-polarized 670 nm laser spot was incident from the top side and a bright spot, perhaps from an SP wave, was emitted by the end-point termination of the stripline.

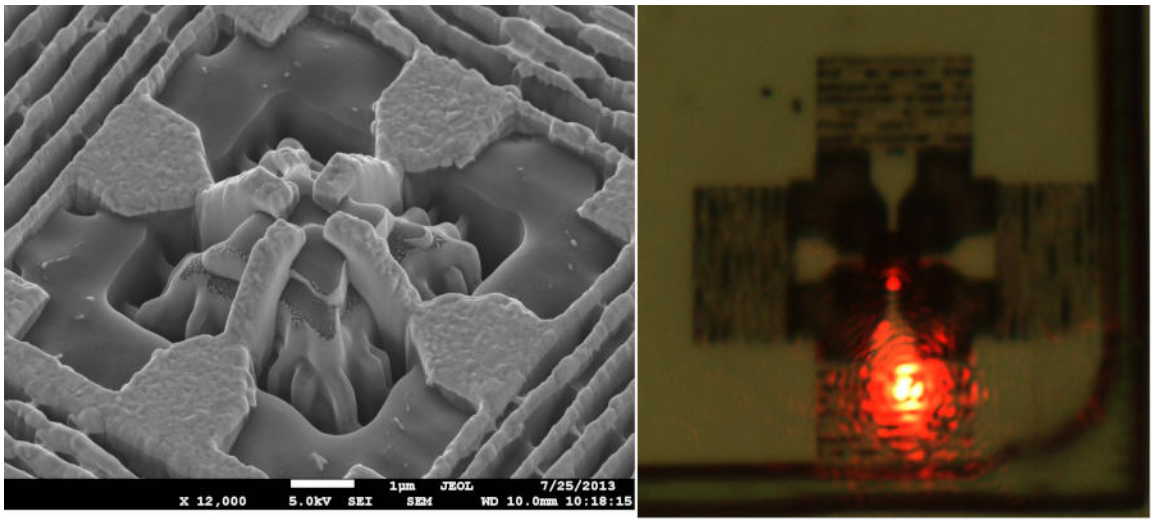

Figure 5.3: 3D NCOM from FIB-milled, template-stripped Ag on epoxy pyramids. (a) SEM of the stripped pyramid. (b) Optical micrograph showing coupling of 670 nm laser light.

5.2 2D NCOM: fanned-out Ag NW

In many respects, the Ag NW discussed in Section 4.2.1.2 are the ideal starting point for nanocoax fabrication, so long as an external metal can be coated conformally. The one drawback of using them is that they are cast from solution randomly onto a substrate and cannot be patterned/organized very easily. One way of patterning them is by adhering them to a transfer resist and then placing them down onto a substrate, much like the alignment action of a nano imprint- or photo-lithographic mask aligner [257]. When arranged into a converging array, these nanowires can form an NCOM [186], [258]. I once made such an arrangement using the Kliendiek probes on our FIB. But I never hit this sample with a laser. Especially if done on a thicker ground plane, one could repeat this corralling and then coat the external coaxial metal onto Ag/SiO_2 NW, as was done in Section 4.2.2.2. Finally, FIB-ing open some windows, that person would have a nanophotonic structure rarely investigated and worth exploration.

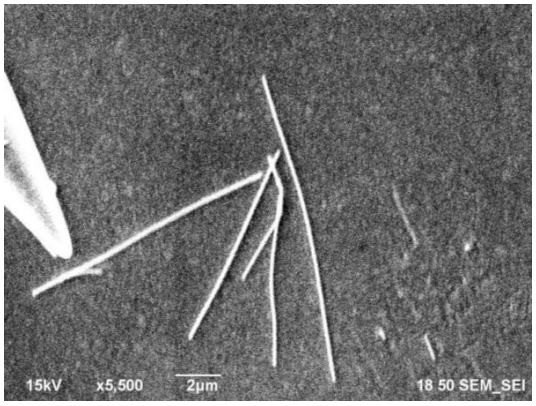

Figure 5.4: 2D NCOM by corralling Ag NW. Ag NW were arranged with a Kliendiek probe into a 2D converging array.

5.3 Revisiting Klopfenstein's taper

Some time ago, Klopfenstein put forth a theoretically optimal coaxial taper geometry, where the optimization target was to minimize the power reflected by the impedance gradient along the taper [259]. The tapered coaxial structure discussed in Section 4.4 makes no consideration of this whatsoever. It the coaxial ratio of diameters Φ (see Equation (4.02)) of that taper can be described by a pair of nested cones, where at the entrance the ratio was $\Phi = 2.24$ and at the exit the ratio was 2. The entrance ratio in my simulations was tuned a bit to maximize the in-coupled power from the $\mathrm{NA}_{\mathrm{beam}} = 0.31$ input. But very little consideration was given to the exit ratio beyond, "2 seems like a reasonable number". The authors of [141] showed, at least for the TE_{11}-*like* mode, that a ratio of 1.6 might have a better figure of merit. The authors of [19] showed a ratio of 1.25 works well for the TEM-like mode. But note both of those ratios are themselves particular to the actual value of $\varnothing_{\mathrm{OD}}$ compared to λ and furthermore on λ itself. And regardless of the ratio, my simulations still demonstrate the fundamental point, which is the potential for unlimited confinement in the TEM-*like* mode. Others have considered optimized taper geometries at

THz frequencies [260], but I believe a computational work to optimize a coaxial taper for visible frequencies is another worthwhile pursuit. One could start by linearly tapering the impedance, which in Equation (4.11) is proportionate to $\ln\Phi$, so that the actual geometry of the nested "cones" is nominally exponential.

5.4 Proposed taper fabrication scheme

Section 4.2.1.1 alluded to some recent work which may prove useful for coaxial fabrication. I believe that tapered coaxes can be made in a similar fashion to the approach of Section 4.2.3, but mixing in the "growth" idea from Section 4.2.2.1. Perhaps the biggest challenge to fabricating a tapered nanocoax lies in the varying insulator thickness. ALD, I believe, cannot be used to generate this geometry (at least not easily), since it coats a conformal, constant thickness layer. The same could be said about homogenous PVD. Figure 5.5 sketches a proposed taper fabrication scheme, wherein a varying angle of deposition unlocks that varying insulator thickness. To start, as shown in Figure 5.5-a), one would need a retrograde hole etched into Si. For simplicity, suppose that the hole is conical so that the sidewall slope is constant through, set by the retrograde angle β. If directional deposition (such as thermal or e-beam deposition) is done at a tilted angle $\theta > \beta$ (and rotating at a sufficiently "fast" ω, as drawn in Figure 5.5-b)), then the deposited film will not coat the bottom section of the conical hole, stopping somewhere along the length where the rim makes its "shadow". The key is to sweep this shadow along the length of the cone by "slowly" varying the tilt angle, $\theta = \theta(t)$, so that thin depositions (or none at all) result on the bottom of the conical hole with gradually thicker depositions at the top of the hole. A similar procedure is repeated for the insulator, shown in Figure 5.5-c). Finally, a zero-

tilt deposition of the final metal would plug-up the hole to make a solid core. Finally, the same bonding and backside thinning steps as before could be employed to get a double-open-ended, tapered MIM nanocoax.

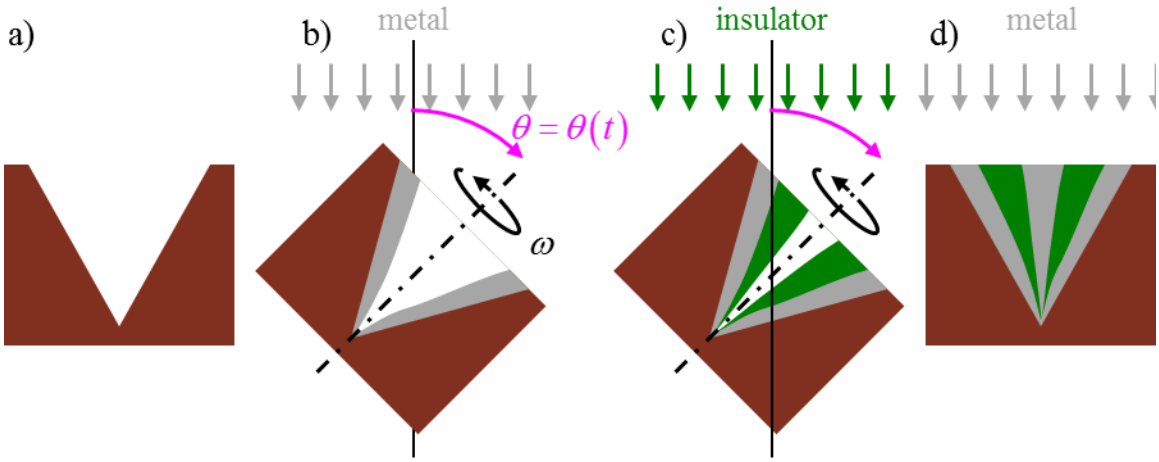

Figure 5.5: Proposed taper coaxial fabrication scheme. (a-d) Compounded angle deposition, where the "fast" rotation ω is combined with the "slowly" varying $\theta(t)$ to make a film thickness which varies along the length of a taper due to the shadowed deposition.

References

[1] Y. M. Calm, J. M. Merlo, M. J. Burns, and M. J. Naughton, "From Airy to Abbe: quantifying the effects of wide-angle focusing for scalar spherical waves," J. Opt., vol. 19, no. 10, p. 105608, (2017). https://doi.org/10.1088/2040-8986/aa8965

[2] A. Mahigir et al., "Subwavelength Plasmonic Two-Conductor Waveguides," in Wiley Encyclopedia of Electrical and Electronics Engineering, no. 7, Hoboken, NJ, USA: John Wiley & Sons, Inc., (2016), pp. 1–15. https://doi.org/10.1002/047134608X.W8292

[3] D. M. Pozar, Microwave Engineering, 4th ed. John Wiley & Sons, Inc., (2012). https://www.wiley.com/en-us/Microwave+Engineering%2C+4th+Edition-p-9780470631553

[4] W. Thomson, "LXXIV. On the electro-statical capacity of a Leyden phial and of a telegraph wire insulated in the axis of a cylindrical conducting sheath," London, Edinburgh, Dublin Philos. Mag. J. Sci., vol. 9, no. 62, pp. 531–535, (1855). https://doi.org/10.1080/14786445508641914

[5] F. I. Baida and D. Van Labeke, "Light transmission by subwavelength annular aperture arrays in metallic films," Opt. Commun., vol. 209, no. 1–3, pp. 17–22, (2002). https://doi.org/10.1016/S0030-4018(02)01690-5

[6] W. Fan, S. Zhang, B. Minhas, K. J. Malloy, and S. R. J. Brueck, "Enhanced Infrared Transmission through Subwavelength Coaxial Metallic Arrays," Phys. Rev. Lett., vol. 94, no. 3, p. 033902, (2005). https://doi.org/10.1103/PhysRevLett.94.033902

[7] J. Salvi et al., "Annular aperture arrays: study in the visible region of the electromagnetic spectrum," Opt. Lett., vol. 30, no. 13, p. 1611, (2005). https://doi.org/10.1364/ol.30.001611

[8] S. M. Orbons et al., "Optical properties of silver composite metamaterials," Phys. B Condens. Matter, vol. 394, no. 2, pp. 176–179, (2007). https://doi.org/10.1016/j.physb.2006.12.013

[9] J. Rybczynski et al., "Subwavelength waveguide for visible light," Appl. Phys. Lett., vol. 90, no. 2, p. 021104, (2007). https://doi.org/10.1063/1.2430400

[10] G. Si et al., "Annular aperture array based color filter," Appl. Phys. Lett., vol. 99, no. 3, p. 033105, (2011). https://doi.org/10.1063/1.3608147

[11] R. Rajasekharan Unnithan et al., "Plasmonic Colour Filters Based on Coaxial Holes in Aluminium," Materials (Basel)., vol. 10, no. 4, p. 383, (2017). https://doi.org/10.3390/ma10040383

[12] A. A. E. Saleh and J. A. Dionne, "Toward Efficient Optical Trapping of Sub-10-nm Particles with Coaxial Plasmonic Apertures," Nano Lett., vol. 12, no. 11, pp. 5581–5586, (2012). https://doi.org/10.1021/nl302627c

[13] S. P. Burgos, R. de Waele, A. Polman, and H. A. Atwater, "A single-layer wide-angle negative-index metamaterial at visible frequencies," Nat. Mater., vol. 9, no. 5, pp. 407–412, (2010). https://doi.org/10.1038/nmat2747

[14] Y. Liu, H. Xu, F. Stief, N. Zhitenev, and M. Yu, "Far-field superfocusing with an optical fiber based surface plasmonic lens made of nanoscale concentric annular slits," Opt. Express, vol. 19, no. 21, p. 20233, (2011). https://doi.org/10.1364/OE.19.020233

[15] M. Pu et al., "Near-field collimation of light carrying orbital angular momentum with bull's-eye-assisted plasmonic coaxial waveguides," Sci. Rep., vol. 5, no. 1, p. 12108, (2015). https://doi.org/10.1038/srep12108

[16] K. Kempa, X. Wang, Z. F. Ren, and M. J. Naughton, "Discretely guided electromagnetic effective medium," Appl. Phys. Lett., vol. 92, no. 4, pp. 2007–2009, (2008). https://doi.org/10.1063/1.2839320

[17] A. Weber-Bargioni et al., "Hyperspectral Nanoscale Imaging on Dielectric Substrates with Coaxial Optical Antenna Scan Probes.," Nano Lett., vol. 11, no. 3, pp. 1201–1207, (2011). https://doi.org.10.1021/nl104163m

[18] M. Khajavikhan et al., "Thresholdless nanoscale coaxial lasers," Nature, vol. 482, no. 7384, pp. 204–207, (2012). https://doi.org/10.1038/nature10840

[19] A. A. E. Saleh and J. A. Dionne, "Waveguides with a silver lining: Low threshold gain and giant modal gain in active cylindrical and coaxial plasmonic devices," Phys. Rev. B, vol. 85, no. 4, p. 045407, (2012). https://doi.org/10.1103/PhysRevB.85.045407

[20] M. Ibanescu, "An All-Dielectric Coaxial Waveguide," Science, vol. 289, no. 5478, pp. 415–419, (2000). https://doi.org/10.1126/science.289.5478.415

[21] G. B. Airy, "On the Diffraction of an Object-glass with Circular Aperture (scanned)," Trans. Cambridge Philos. Soc., vol. 5, no. 3, pp. 283–291, (1835). https://catalog.hathitrust.org/Record/000526741

[22] E. Abbe, "Beiträge zur Theorie des Mikroskops und der Mikroskopischen Wahrnehmung," Arch. für Mikroskopische Anat., vol. 9, no. 1, pp. 440–456, (1873). https://doi.org/10.1007/BF02956175

[23] H. E. Fripp (Ed.), "English translation of Abbe's (1873) paper," Bristol Microscopy Society. pp. 407–475, (1874). https://www.biodiversitylibrary.org/bibliography/98898#/summary

[24] Lord Rayleigh, "LVI. Investigations in optics, with special reference to the spectroscope," Philos. Mag. Ser. 5, vol. 8, no. 51, pp. 477–486, (1879). https://doi.org/10.1080/14786447908639715

[25] E. Hecht, Optics, 4th ed. San Fransisco CA: Addison Wesley, (2002). https://www.pearson.com/us/higher-education/product/Hecht-Optics-4th-Edition/9780805385663.html?

[26] B. E. A. Saleh and M. C. Teich, Fundamentals of Photonics, 2nd ed. New York: John Wiley & Sons, Inc., (2007).

[27] J. W. Goodman, Introduction to Fourier Optics, 2nd ed. New York NY: McGraw-Hill, (1996).

[28] M. Born and E. Wolf, Principles of Optics, 7th ed. Cambridge UK: Cambridge University Press, (2005). https://doi.org/10.1017/CBO9781139644181

[29] L. Novotny and B. Hecht, Principles of Nano-Optics, 2nd ed. Cambridge: Cambridge University Press, (2012). https://doi.org/10.1017/CBO9780511813535

[30] A. V. V Zayats and D. Richards, Nano-Optics and Near-Field Optical Microscopy. Boston MA: Artech House, (2009). https://us.artechhouse.com/Nano-Optics-and-Near-Field-Optical-Microscopy-P1204.aspx

[31] P. G. Kik and M. L. Brongersma, Surface Plasmon Nanophotonics. Dordrecht: Springer Netherlands, (2007). https://doi.org/10.1007/978-1-4020-4333-8_1

[32] M. Sotomayor et al., "Far-Field Optical Nanoscopy," Science, vol. 316, no. May, pp. 1153–1158, (2007). https://doi.org/10.1126/science.1137395

[33] W. E. E. Moerner, "Microscopy beyond the diffraction limit using actively controlled single molecules," J. Microsc., vol. 246, no. 3, pp. 213–220, (2012). https://doi.org/10.1111/j.1365-2818.2012.03600.x

[34] E. T. F. Rogers et al., “A super-oscillatory lens optical microscope for subwavelength imaging,” Nat. Mater., vol. 11, no. 5, pp. 432–435, (2012). https://doi.org/10.1038/nmat3280

[35] J. S. Silfies, S. A. Schwartz, and M. W. Davidson, “The diffraction barrier in optical microscopy,” Nikon Instruments, Inc., (2016). . https://www.microscopyu.com/techniques/super-resolution/the-diffraction-barrier-in-optical-microscopy

[36] K. R. Spring, T. J. Fellers, and M. W. Davidson, “Resolution and contrast in confocal microscopy,” Olympus, Inc., (2012). . http://www.olympusmicro.com/primer/techniques/confocal/resolutionintro.html

[37] J. J. Stamnes, Waves in Focal Regions. Bristol UK: Adam-Hilger, (1986).

[38] J. J. Stamnes, Selected Papers on Electromagnetic Fields in the Focal Region, vol. 168. Bellingham WA: SPIE Optical Engineering Press, (2001).

[39] K. E. Oughstun, Selected Papers on Scalar Wave Diffraction, vol. 51. Bellingham WA: SPIE Optical Engineering Press, (1992).

[40] V. Dhayalan, T. Standnes, J. J. Stamnes, and H. Heier, “Scalar and electromagnetic diffraction point-spread functions for high-NA microlenses,” Pure Appl. Opt. J. Eur. Opt. Soc. Part A, vol. 6, no. 6, pp. 603–615, (1997). https://doi.org/10.1088/0963-9659/6/6/003

[41] L. Ciocci, R. M. Echarri, and J. M. Simon, “Diffraction in high numerical aperture systems: polarization effects,” J. Opt., vol. 12, no. 1, p. 015408, (2010). https://doi.org/10.1088/2040-8978/12/1/015408

[42] A. Sobczyk, Z. Jaroszewicz, A. Kolodziejczyk, A. Kowalik, C. Prokopowicz, and M. Sypek, “Nonparaxial anamorphic diffractive lenses,” J. Opt., vol. 15, no. 2, p. 025702, (2013). https://doi.org/10.1088/2040-8978/15/2/025702

[43] N. George and W. Chi, “Extended depth of field using a logarithmic asphere,” J. Opt. A Pure Appl. Opt., vol. 5, no. 5, pp. S157–S163, (2003). https://doi.org/10.1088/1464-4258/5/5/358

[44] J. E. Kennedy, “Innovation: High-intensity focused ultrasound in the treatment of solid tumours,” Nat. Rev. Cancer, vol. 5, no. 4, pp. 321–327, (2005). https://doi.org/10.1038/nrc1591

[45] G. Kirchhoff, “Zur Theorie der Lichtstrahlen,” Ann. Phys., vol. 254, no. 4, pp. 663–695, (1883). https://doi.org/10.1002/andp.18832540409

[46] H. Osterberg and L. W. Smith, “Closed solutions of Rayleigh’s diffraction integral for axial points,” J. Opt. Soc. Am., vol. 51, no. 10, pp. 1050–1054, (1961). https://doi.org/10.1364/JOSA.51.001050

[47] J. C. Heurtley, “Scalar Rayleigh-Sommerfeld and Kirchhoff diffraction integrals: A comparison of exact evaluations for axial point,” J. Opt. Soc. Am., vol. 63, no. 8, pp. 1003–1008, (1973). https://doi.org/10.1364/JOSA.63.001003

[48] C. J. R. Sheppard and P. Török, “Focal shift and the axial optical coordinate for high-aperture systems of finite Fresnel number,” J. Opt. Soc. Am. A, vol. 20, no. 11, p. 2156, (2003). https://doi.org/10.1364/JOSAA.20.002156

[49] R. M. Aarts, J. J. M. Braat, P. Dirksen, S. van Haver, C. van Heesch, and A. J. E. M. Janssen, “Analytic expressions and approximations for the on-axis, aberration-free Rayleigh and Debye integral in the case of focusing fields on a circular aperture,” J. Eur. Opt. Soc. Rapid Publ., vol. 3, p. 08039, (2008). https://doi.org/10.2971/jeos.2008.08039

[50] J. Guo, X. Zhao, and Y. Min, "The general integral expressions for on-axis nonparaxial vectorial spherical waves diffracted at a circular aperture," Opt. Commun., vol. 282, no. 8, pp. 1511–1515, (2009). https://doi.org/10.1016/j.optcom.2008.12.062

[51] Y. Li and E. Wolf, "Focal shifts in diffracted converging spherical waves," Opt. Commun., vol. 39, no. 4, pp. 211–215, (1981). https://doi.org/10.1016/0030-4018(81)90108-5

[52] M. P. Givens, "Focal shifts in diffracted converging spherical waves," Opt. Commun., vol. 41, no. 3, pp. 145–148, (1982). https://doi.org/10.1016/0030-4018(82)90059-1

[53] C. J. R. Sheppard and P. Török, "Dependence of focal shift on Fresnel number and angular aperture," Opt. Lett., vol. 23, no. 23, p. 1803, (1998). https://doi.org/10.1364/OL.23.001803

[54] Y. Li, "Focal shifts in diffracted converging electromagnetic waves II Rayleigh theory," J. Opt. Soc. Am. A, vol. 22, no. 1, p. 77, (2005). https://doi.org/10.1364/JOSAA.22.000077

[55] Y. Li, "Predictions of Rayleigh's diffraction theory for the effect of focal shift in high-aperture systems," J. Opt. Soc. Am. A, vol. 25, no. 7, p. 1835, (2008). https://doi.org/10.1364/JOSAA.25.001835

[56] A. T. T. Friberg, T. D. D. Visser, W. Wang, and E. Wolf, "Focal shifts of converging diffracted waves of any state of spatial coherence," Opt. Commun., vol. 196, no. 1–6, pp. 1–7, (2001). https://doi.org/10.1016/S0030-4018(01)01378-5

[57] E. Collett and E. Wolf, "Symmetry properties of focused fields," Opt. Lett., vol. 5, no. 6, p. 264, (1980). https://doi.org/10.1364/OL.5.000264

[58] E. H. Linfoot and E. Wolf, "Phase Distribution near Focus in an Aberration-free Diffraction Image," Proc. Phys. Soc. Sect. B, vol. 69, no. 8, pp. 823–832, (1956). https://doi.org/10.1088/0370-1301/69/8/307

[59] J. H. Erkkila and M. E. Rogers, "Diffracted fields in the focal volume of a converging wave," J. Opt. Soc. Am., vol. 71, no. 7, pp. 904–905, (1981). https://doi.org/10.1364/JOSA.71.000904

[60] Y. Li and E. Wolf, "Three-dimensional intensity distribution near the focus in systems of different Fresnel numbers," J. Opt. Soc. Am. A, vol. 1, no. 8, p. 801, (1984). https://doi.org/10.1364/JOSAA.1.000801

[61] Y. Li, "Dependence of the focal shift on Fresnel number and f number," J. Opt. Soc. Am., vol. 72, no. 6, p. 770, (1982). https://doi.org/10.1364/JOSA.72.000770

[62] M. Leutenegger, R. Rao, R. A. Leitgeb, and T. Lasser, "Fast focus field calculations," Opt. Express, vol. 14, no. 23, pp. 11277–11291, (2006). https://doi.org/10.1364/OE.14.011277

[63] J. Lin, O. G. Rodríguez-Herrera, F. Kenny, D. Lara, and J. C. Dainty, "Fast vectorial calculation of the volumetric focused field distribution by using a three-dimensional Fourier transform," Opt. Express, vol. 20, no. 2, p. 1060, (2012). https://doi.org/10.1364/OE.20.001060

[64] M. Hillenbrand, A. Hoffmann, D. P. Kelly, and S. Sinzinger, "Fast nonparaxial scalar focal field calculations," J. Opt. Soc. Am. A, vol. 31, no. 6, pp. 1206–1214, (2014). https://doi.org/10.1364/JOSAA.31.001206

[65] G.-N. Nguyen, K. Heggarty, P. Gérard, B. Serio, and P. Meyrueis, "Computationally efficient scalar nonparaxial modeling of optical wave propagation in the far-field," Appl. Opt., vol. 53, no. 10, p. 2196, (2014). https://doi.org/10.1364/AO.53.002196

[66] Y.-H. Kim et al., "Non-uniform sampling and wide range angular spectrum method," J. Opt., vol. 16, no. 12, p. 125710, (2014). https://doi.org/10.1088/2040-8978/16/12/125710

[67] T. Kozacki, “Numerical errors of diffraction computing using plane wave spectrum decomposition,” Opt. Commun., vol. 281, no. 17, pp. 4219–4223, (2008). https://doi.org/10.1016/j.optcom.2008.05.023

[68] M. Hillenbrand, D. P. Kelly, and S. Sinzinger, “Numerical solution of nonparaxial scalar diffraction integrals for focused fields,” J. Opt. Soc. Am. A, vol. 31, no. 8, p. 1832, (2014). https://doi.org/10.1364/JOSAA.31.001832

[69] J. J. Stamnes and B. Spjelkavik, “Focusing at small angular apertures in the debye and Kirchhoff approximations,” Opt. Commun., vol. 40, no. 2, pp. 81–85, (1981). https://doi.org/10.1016/0030-4018(81)90332-1

[70] A. Egner and S. W. Hell, “Equivalence of the Huygens-Fresnel and Debye approach for the calculation of high aperture point-spread functions in the presence of refractive index mismatch,” J. Microsc., vol. 193, no. 3, pp. 244–249, (1999). https://doi.org/10.1046/j.1365-2818.1999.00462.x

[71] C. J. R. Sheppard, “Validity of the Debye approximation,” Opt. Lett., vol. 25, no. 22, pp. 1660–1662, (2000). https://doi.org/10.1364/OL.25.001660

[72] C. J. R. Sheppard, “Limitations of the paraxial Debye approximation,” Opt. Lett., vol. 38, no. 7, pp. 1074–1076, (2013). https://doi.org/10.1364/OL.38.001074

[73] S. Grill and E. H. K. Stelzer, “Method to calculate lateral and axial gain factors of optical setups with a large solid angle,” J. Opt. Soc. Am. A, vol. 16, no. 11, pp. 2658–2665, (1999). https://doi.org/10.1364/JOSAA.16.002658

[74] E. H. K. Stelzer and S. Grill, “The uncertainty principle applied to estimate focal spot dimensions,” Opt. Commun., vol. 173, no. 1–6, pp. 51–56, (2000). https://doi.org/10.1016/S0030-4018(99)00644-6

[75] G. P. Karman, M. W. Beijersbergen, A. van Duijl, D. Bouwmeester, and J. P. Woerdman, “Airy pattern reorganization and subwavelength structure in a focus,” J. Opt. Soc. Am. A, vol. 15, no. 4, p. 884, (1998). https://doi.org/10.1364/JOSAA.15.000884

[76] B. J. Lin, “The k3 coefficient in nonparaxial λ/NA scaling equations for resolution, depth of focus, and immersion lithography,” J. Micro/Nanolithography, MEMS, MOEMS, vol. 1, no. 1, p. 7, (2002). https://doi.org/10.1117/1.1445798

[77] C. J. R. Sheppard and P. Torok, “Effects of Fresnel number in focusing and imaging,” in Selected Paper From International Conference on Optics and Optoelectronics `98: Silver Jubilee Symposium of the Optical Society of India, (1999), vol. 3729, no. APRIL 1999, pp. 458–472. https://doi.org/10.1117/12.346824

[78] D. Slepian and H. O. Pollak, “Prolate Spheroidal Wave Functions, Fourier Analysis and Uncertainty - I,” Bell Syst. Tech. J., vol. 40, no. 1, pp. 43–63, (1961). https://doi.org/10.1002/j.1538-7305.1961.tb03976.x

[79] B. R. Frieden, “VIII Evaluation, Design and Extrapolation Methods for Optical Signals, Based on Use of the Prolate Functions,” in Progress in Optics, vol. 9, E. Wolf, Ed. (1971), pp. 311–407. https://doi.org/10.1016/S0079-6638(08)70049-0

[80] C. A. Mack and C.-B. Juang, “Comparison of scalar and vector modeling of image formation in photoresis,” in Optical/Laser Microlithography VIII, (1995), vol. 2440, pp. 381–394. https://doi.org/10.1117/12.209270

[81] A. V. Kildishev, A. Boltasseva, and V. M. M. Shalaev, “Planar photonics with metasurfaces,” Science, vol. 339, no. 6125, p. 1232009, (2013). https://doi.org/10.1126/science.1232009

[82] N. Yu and F. Capasso, “Flat optics with designer metasurfaces,” Nat. Mater., vol. 13, no. 2, pp. 139–150, (2014). https://doi.org/10.1038/nmat3839

[83] A. E. Siegman, Lasers. (1986). http://www.uscibooks.com/siegman.htm

[84] S. Franke-Arnold and N. Radwell, “Light Served with a Twist,” Opt. Photonics News, vol. 28, no. 6, p. 28, (2017). https://doi.org/10.1364/OPN.28.6.000028

[85] L. Allen, M. W. Beijersbergen, R. J. C. Spreeuw, and J. P. Woerdman, “Orbital angular momentum of light and the transformation of Laguerre-Gaussian laser modes,” Phys. Rev. A, vol. 45, no. 11, pp. 8185–8189, (1992). https://doi.org/10.1103/PhysRevA.45.8185

[86] S. M. Barnett et al., “On the natures of the spin and orbital parts of optical angular momentum,” J. Opt., vol. 18, no. 6, p. 064004, (2016). https://doi.org/10.1088/2040-8978/18/6/064004

[87] H. He, M. E. J. Friese, N. R. Heckenberg, and H. Rubinsztein-Dunlop, “Direct Observation of Transfer of Angular Momentum to Absorptive Particles from a Laser Beam with a Phase Singularity,” Phys. Rev. Lett., vol. 75, no. 5, pp. 826–829, (1995). https://doi.org/10.1103/PhysRevLett.75.826

[88] N. Bozinovic et al., “Terabit-Scale Orbital Angular Momentum Mode Division Multiplexing in Fibers,” Science, vol. 340, no. 6140, pp. 1545–1548, (2013). https://doi.org/10.1126/science.1237861

[89] J. Wang, “Advances in communications using optical vortices,” Photonics Res., vol. 4, no. 5, p. B14, (2016). https://doi.org/10.1364/prj.4.000b14

[90] M. Mirhosseini et al., “High-dimensional quantum cryptography with twisted light,” New J. Phys., vol. 17, no. 3, p. 033033, (2015). https://doi.org/10.1088/1367-2630/17/3/033033

[91] Y. Chen et al., “Mapping Twisted Light into and out of a Photonic Chip,” Phys. Rev. Lett., vol. 121, no. 23, p. 233602, (2018). https://doi.org/10.1103/PhysRevLett.121.233602

[92] N. M. Litchinitser, J. Sun, K. Masuda, T. Xu, K. Miyamoto, and T. Omatsu, “Shrinking optical vortex to the nanoscale,” in Optical Manipulation Conference, (2018), vol. 10712, p. 74. https://doi.org/10.1117/12.2324328

[93] S. W. Hell and J. Wichmann, “Breaking the diffraction resolution limit by stimulated emission: stimulated-emission-depletion fluorescence microscopy,” Opt. Lett., vol. 19, no. 11, p. 780, (1994). https://doi.org/10.1364/OL.19.000780

[94] J. Fischer and M. Wegener, “Three-dimensional optical laser lithography beyond the diffraction limit,” Laser Photon. Rev., vol. 7, no. 1, pp. 22–44, (2013). https://doi.org/10.1002/lpor.201100046

[95] B. Mellish, “Diagram of Gaussian beam waist parameters.” (2009). https://commons.wikimedia.org/wiki/File:GaussianBeamWaist.svg

[96] C. V. Raman and S. Bhagavantam, “Experimental Proof of the Spin of the Photon,” Nature, vol. 129, no. 3244, pp. 22–23, (1932). https://doi.org/10.1038/129022a0

[97] C. Maurer, A. Jesacher, S. Fürhapter, S. Bernet, and M. Ritsch-Marte, “Tailoring of arbitrary optical vector beams,” New J. Phys., vol. 9, no. 3, pp. 78–78, (2007). https://doi.org/10.1088/1367-2630/9/3/078

[98] J. P. Torres and L. Torner, Eds., Twisted Photons: Applications of Light with Orbital Angular Momentum. Wiley-VCH, (2011). https://www.wiley.com/en-us/Twisted+Photons%3A+Applications+of+Light+with+Orbital+Angular+Momentum-p-9783527635375

[99] A. Cerjan and C. Cerjan, "Orbital angular momentum of Laguerre–Gaussian beams beyond the paraxial approximation," J. Opt. Soc. Am. A, vol. 28, no. 11, p. 2253, (2011). https://doi.org/10.1364/JOSAA.28.002253

[100] P. P. Banerjee, G. Cook, and D. R. Evans, "A q-parameter approach to analysis of propagation, focusing, and waveguiding of radially polarized Gaussian beams," J. Opt. Soc. Am. A, vol. 26, no. 6, p. 1366, (2009). https://doi.org/10.1364/JOSAA.26.001366

[101] J. Peatross, M. Berrondo, D. Smith, and M. Ware, "Vector fields in a tight laser focus: comparison of models," Opt. Express, vol. 25, no. 13, p. 13990, (2017). https://doi.org/10.1364/OE.25.013990

[102] C. J. R. Sheppard and S. Saghafi, "Electromagnetic Gaussian beams beyond the paraxial approximation," J. Opt. Soc. Am. A, vol. 16, no. 6, p. 1381, (1999). https://doi.org/10.1364/JOSAA.16.001381

[103] V. Shvedov and W. Krolikowski, "Instantaneous field singularities in electromagnetic waves," New J. Phys., vol. 20, no. 10, p. 103034, (2018). https://doi.org/10.1088/1367-2630/aae717

[104] A. Carnicer, I. Juvells, D. Maluenda, R. Martínez-Herrero, and P. M. Mejías, "On the longitudinal component of paraxial fields," Eur. J. Phys., vol. 33, no. 5, pp. 1235–1247, (2012). https://doi.org/10.1088/0143-0807/33/5/1235

[105] M. Lax, W. H. Louisell, and W. B. McKnight, "From Maxwell to paraxial wave optics," Phys. Rev. A, vol. 11, no. 4, pp. 1365–1370, (1975). https://doi.org/10.1103/PhysRevA.11.1365

[106] H. Laabs, "Propagation of Hermite-Gaussian-beams beyond the paraxial approximation," Opt. Commun., vol. 147, no. 1–3, pp. 1–4, (1998). https://doi.org/10.1016/S0030-4018(97)00607-X

[107] W. L. Erikson and S. Singh, "Polarization properties of Maxwell-Gaussian laser beams," Phys. Rev. E, vol. 49, no. 6, pp. 5778–5786, (1994). https://doi.org/10.1103/PhysRevE.49.5778

[108] W. E. Lewis and R. Vyas, "Maxwell-Gaussian beams with cylindrical polarization," J. Opt. Soc. Am. A, vol. 31, no. 7, p. 1595, (2014). https://doi.org/10.1364/JOSAA.31.001595

[109] D. L. Andrews and M. Babiker, Eds., The Angular Momentum of Light. Cambridge University Press, (2013). https://doi.org/10.1017/CBO9780511795213

[110] H. A. Haus, Waves and Fields in Optoelectronics. Prentice Hall, (1985). https://doi.org/10.1080/716099690

[111] R. Simon, E. C. G. Sudarshan, and N. Mukunda, "Cross polarization in laser beams," Appl. Opt., vol. 26, no. 9, p. 1589, (1987). https://doi.org/10.1364/AO.26.001589

[112] J. Conry, R. Vyas, and S. Singh, "Cross-polarization of linearly polarized Hermite–Gauss laser beams," J. Opt. Soc. Am. A, vol. 29, no. 4, p. 579, (2012). https://doi.org/10.1364/JOSAA.29.000579

[113] L. W. Davis and G. Patsakos, "TM and TE electromagnetic beams in free space," Opt. Lett., vol. 6, no. 1, p. 22, (1981). https://doi.org/10.1364/OL.6.000022

[114] P. Banzer, J. Kindler, S. Quabis, U. Peschel, and G. Leuchs, "Extraordinary transmission through a single coaxial aperture in a thin metal film," Opt. Express, vol. 18, no. 10, p. 10896, (2010). https://doi.org/10.1364/OE.18.010896

[115] Thorlabs Inc., "Zero-Order Vortex Half-Wave Retarders." (2019). https://www.thorlabs.com/newgrouppage9.cfm?objectgroup_id=9098

[116] R. A. Chipman, "Polarimetry," in Handbook of Optics, vol. 1, 3rd ed., M. Bass, Ed. McGraw-Hill, (2010), pp. 15.1-46. https://www.mhprofessional.com/9780071498890-usa-handbook-of-optics-third-edition-volume-i-geometrical-and-physical-optics-polarized-light-components-and-instrumentsset-group

[117] J. S. Tyo, E. N. Pugh, and N. Engheta, "Colorimetric representations for use with polarization-difference imaging of objects in scattering media," J. Opt. Soc. Am. A, vol. 15, no. 2, p. 367, (1998). https://doi.org/10.1364/JOSAA.15.000367

[118] A. W. Kruse, A. S. Alenin, and J. S. Tyo, "Review of visualization methods for passive polarization imaging," Opt. Eng., vol. 58, no. 08, p. 1, (2019). https://doi.org/10.1117/1.OE.58.8.082414

[119] J. Scott Tyo, B. M. Ratliff, and A. S. Alenin, "Adapting the HSV polarization-color mapping for regions with low irradiance and high polarization," Opt. Lett., vol. 41, no. 20, p. 4759, (2016). https://doi.org/10.1364/OL.41.004759

[120] J. Craven-Jones, M. W. Kudenov, M. G. Stapelbroek, and E. L. Dereniak, "Infrared hyperspectral imaging polarimeter using birefringent prisms," Appl. Opt., vol. 50, no. 8, p. 1170, (2011). https://doi.org/10.1364/AO.50.001170

[121] M. Axer et al., "A novel approach to the human connectome: Ultra-high resolution mapping of fiber tracts in the brain," Neuroimage, vol. 54, no. 2, pp. 1091–1101, (2011). https://doi.org/10.1016/j.neuroimage.2010.08.075

[122] S. Aïnouz, J. Zallat, A. de Martino, and C. Collet, "Physical interpretation of polarization-encoded images by color preview," Opt. Express, vol. 14, no. 13, p. 5916, (2006). htts://doi.org/10.1364/OE.14.005916

[123] E. J. Galvez, B. L. Rojec, V. Kumar, and N. K. Viswanathan, "Generation of isolated asymmetric umbilics in light's polarization," Phys. Rev. A, vol. 89, no. 3, p. 031801, (2014). https://doi.org/10.1103/PhysRevA.89.031801

[124] B. Khajavi and E. J. Galvez, "Preparation of Poincaré beams with a same-path polarization/spatial-mode interferometer," Opt. Eng., vol. 54, no. 11, p. 111305, (2015). https://doi.org/10.1117/1.OE.54.11.111305

[125] Y. Wang, E. W. Plummer, and K. Kempa, "Foundations of Plasmonics," Adv. Phys., vol. 60, no. 5, pp. 799–898, (2011). https://doi.org/10.1080/00018732.2011.621320

[126] M. Fox, Optical Properties of Solids, 2nd ed. Oxford University Press, (2010). https://global.oup.com/academic/product/9780199573370

[127] W. L. Barnes, A. Dereux, and T. W. Ebbesen, "Surface plasmon subwavelength optics," Nature, vol. 424, no. 6950, pp. 824–830, (2003). https://doi.org/10.1038/nature01937

[128] H. Raether, Surface Plasmons on Smooth and Rough Surfaces and on Gratings, vol. 111. Berlin, Heidelberg: Springer Berlin Heidelberg, (1988). https://doi.org/10.1007/BFb0048317

[129] P. B. Johnson and R. W. Christy, "Optical Constants of the Noble Metals," Phys. Rev. B, vol. 6, no. 12, pp. 4370–4379, (1972). https://doi.org/10.1103/PhysRevB.6.4370

[130] A. D. Rakić, "Algorithm for the determination of intrinsic optical constants of metal films: application to aluminum," Appl. Opt., vol. 34, no. 22, p. 4755, (1995). https://doi.org/10.1364/ao.34.004755

[131] A. D. Rakić, A. B. Djurišić, J. M. Elazar, and M. L. Majewski, "Optical properties of metallic films for vertical-cavity optoelectronic devices," Appl. Opt., vol. 37, no. 22, p. 5271, (1998). https://doi.org/10.1364/AO.37.005271

[132] J. Zenneck, “Über die Fortpflanzung ebener elektromagnetischer Wellen längs einer ebenen Leiterfläche und ihre Beziehung zur drahtlosen Telegraphie,” Ann. Phys., vol. 328, no. 10, pp. 846–866, (1907). https://doi.org/10.1002/andp.19073281003

[133] A. Sommerfeld, “Über die Ausbreitung der Wellen in der drahtlosen Telegraphie,” Ann. Phys., vol. 333, no. 4, pp. 665–736, (1909). https://doi.org/10.1002/andp.19093330402

[134] N. Marcuvitz, Waveguide Handbook. McGraw-Hill, (1986). https://doi.org/10.1049/PBEW021E

[135] S. Ramo, J. R. Whinnery, and T. Van Duzar, Fields and Waves in Communication Electronics, 3rd ed. John Wiley & Sons, Inc., (1994). https://www.wiley.com/en-us/Fields+and+Waves+in+Communication+Electronics%2C+3rd+Edition-p-9780471585510

[136] Y. Peng, Simulations of Optical Effects in Nanostructures. (2011). https://hdl.handle.net/2345/2930

[137] A. A. E. Saleh, “Molding Light with Coaxial Plasmonic Geometries: Toward Subwavelength Active Plasmonic Waveguides and Direct Optical Manipulation of Nanoscale Specimens,” Stanford, (2015). https://purl.stanford.edu/yx147dn9333

[138] O. Kozina, I. Nefedov, L. Melnikov, and A. Karilainen, “Plasmonic Coaxial Waveguides with Complex Shapes of Cross-Sections,” Materials (Basel)., vol. 4, no. 1, pp. 104–116, (2010). https://doi.org/10.3390/ma4010104

[139] J. G. Davis and A. A. P. Gibson, “Higher order mode impedances and cut-off frequencies of overmoded coaxial waveguides,” Int. J. Electron., vol. 93, no. 5, pp. 335–346, (2006). https://doi.org/10.1080/00207210500429077

[140] J. Kindler (née Müller), P. Banzer, S. Quabis, U. Peschel, and G. Leuchs, “Waveguide properties of single subwavelength holes demonstrated with radially and azimuthally polarized light,” Appl. Phys. B, vol. 89, no. 4, pp. 517–520, (2007). https://doi.org/10.1007/s00340-007-2874-5

[141] F. I. Baida, A. Belkhir, D. Van Labeke, and O. Lamrous, “Subwavelength metallic coaxial waveguides in the optical range: Role of the plasmonic modes,” Phys. Rev. B, vol. 74, no. 20, p. 205419, (2006). https://doi.org/10.1103/PhysRevB.74.205419

[142] Y. Peng, X. Wang, and K. Kempa, “TEM-like optical mode of a coaxial nanowaveguide,” Opt. Express, vol. 16, no. 3, p. 1758, (2008). https://doi.org/10.1364/OE.16.001758

[143] R. F. Oulton, G. Bartal, D. F. P. Pile, and X. Zhang, “Confinement and propagation characteristics of subwavelength plasmonic modes,” New J. Phys., vol. 10, no. 10, p. 105018, (2008). https://doi.org/10.1088/1367-2630/10/10/105018

[144] Alpha Wire Co., “Alpha Essentials Micro Coaxial Cable.” (2019). http://www.alphawire.com/en/Products/Cable/Alpha-Essentials/Coaxial-Cable/9450

[145] M. Hopkins, M. K. Morakinyo, S. Rananavare, A. La Rosa, and J. L. Freeouf, “Coaxial tips for infrared NSOM,” 2011 11th IEEE Int. Conf. Nanotechnol., pp. 531–534, (2011). https://doi.org/10.1109/NANO.2011.6144482

[146] R. C. Jaeger, Introduction to Microelectronic Fabrication, 2nd ed. Pretince Hall, (2002). https://www.pearson.ch/HigherEducation/Pearson/EAN/9780201444940/Introduction-to-Microelectronic-Fabrication

[147] S. Etcheverry, L. F. Araujo, I. C. S. Carvalho, W. Margulis, and J. Fontana, “Digital electric field induced switching of plasmonic nanorods using an electro-optic fluid fiber,” Appl. Phys. Lett., vol. 111, no. 22, p. 221108, (2017). https://doi.org/10.1063/1.5001702

[148] A. Oesterle, Pipette Cookbook, Rev F. Sutter Instrument Co., (2018). https://www.sutter.com/PDFs/pipette_cookbook.pdf

[149] M. Tajmar and F. Plesescu, "Towards liquid metal ion source chips: Indium liquid metal ion source with glass microcapillaries," Appl. Phys. Lett., vol. 102, no. 2, p. 023115, (2013). https://doi.org/10.1063/1.4781442

[150] H. Yang, C. R. Lightner, and L. Dong, "Light-Emitting Coaxial Nanofibers," ACS Nano, vol. 6, no. 1, pp. 622–628, (2012). https://doi.org/10.1021/nn204055t

[151] M. D. Dickey, R. C. Chiechi, R. J. Larsen, E. A. Weiss, D. A. Weitz, and G. M. Whitesides, "Eutectic Gallium-Indium (EGaIn): A Liquid Metal Alloy for the Formation of Stable Structures in Microchannels at Room Temperature," Adv. Funct. Mater., vol. 18, no. 7, pp. 1097–1104, (2008). https://doi.org/10.1002/adfm.200701216

[152] B. L. Cumby, G. J. Hayes, M. D. Dickey, R. S. Justice, C. E. Tabor, and J. C. Heikenfeld, "Reconfigurable liquid metal circuits by Laplace pressure shaping," Appl. Phys. Lett., vol. 101, no. 17, p. 174102, (2012). https://doi.org/10.1063/1.4764020

[153] Z. Jiang, Q. Liang, Z. Li, P. Lv, T. Chen, and D. Li, "Experimental Demonstration of a 3D-Printed Arched Metasurface Carpet Cloak," Adv. Opt. Mater., vol. 1900475, p. 1900475, (2019). https://doi.org/10.1002/adom.201900475

[154] P. Liu et al., "Tunable meta-atom using liquid metal embedded in stretchable polymer," J. Appl. Phys., vol. 118, no. 1, p. 014504, (2015). https://doi.org/10.1063/1.4926417

[155] K. Ling, K. Kim, and S. Lim, "Flexible liquid metal-filled metamaterial absorber on polydimethylsiloxane (PDMS)," Opt. Express, vol. 23, no. 16, p. 21375, (2015). https://doi.org/10.1364/OE.23.021375

[156] J. Wang, S. Liu, Z. V. Vardeny, and A. Nahata, "Liquid metal-based plasmonics," Opt. Express, vol. 20, no. 3, p. 2346, (2012). https://doi.org/10.1364/OE.20.002346

[157] S. Etcheverry et al., "Microsecond switching of plasmonic nanorods in an all-fiber optofluidic component," Optica, vol. 4, no. 8, p. 864, (2017). https://doi.org/10.1364/optica.4.000864

[158] B. Rizal, J. M. Merlo, M. J. Burns, T. C. Chiles, and M. J. Naughton, "Nanocoaxes for optical and electronic devices," Analyst, vol. 140, no. 1, pp. 39–58, (2015). https://doi.org/10.1039/C4AN01447B

[159] B. Rizal et al., "Imprint-Templated Nanocoax Array Architecture: Fabrication and Utilization," in Nano-Optics for Enhancing Light-Matter Interactions on a Molecular Scale, B. Di Bartolo and J. Collins, Eds. Dordrecht: Springer Netherlands, (2013), pp. 359–370. https://doi.org/10.1007/978-94-007-5313-6

[160] J. M. Merlo, F. Ye, B. Rizal, M. J. Burns, and M. J. Naughton, "Near-field observation of light propagation in nanocoax waveguides," Opt. Express, vol. 22, no. 12, p. 14148, (2014). https://doi.org/10.1364/OE.22.014148

[161] W. Kubo and S. Fujikawa, "Au double nanopillars with nanogap for plasmonic sensor," Nano Lett., vol. 11, no. 1, pp. 8–15, (2011). https://doi.org/10.1021/nl100787b

[162] S. Fan, "Self-Oriented Regular Arrays of Carbon Nanotubes and Their Field Emission Properties," Science, vol. 283, no. 5401, pp. 512–514, (1999). https://doi.org/10.1126/science.283.5401.512

[163] Y. Poujet, J. Salvi, and F. I. Baida, "90% Extraordinary optical transmission in the visible range through annular aperture metallic arrays," Opt. Lett., vol. 32, no. 20, p. 2942, (2007). https://doi.org/10.1364/OL.32.002942

[164] R. de Waele, S. P. Burgos, A. Polman, and H. A. Atwater, "Plasmon Dispersion in Coaxial Waveguides from Single-Cavity Optical Transmission Measurements," Nano Lett., vol. 9, no. 8, pp. 2832–2837, (2009). https://doi.org/10.1021/nl900597z

[165] M. Melli et al., "Reaching the Theoretical Resonance Quality Factor Limit in Coaxial Plasmonic Nanoresonators Fabricated by Helium Ion Lithography," Nano Lett., vol. 13, no. 6, pp. 2687–2691, (2013). https://doi.org/10.1021/nl400844a

[166] M. A. van de Haar and A. Polman, "Fabrication process of a coaxial plasmonic metamaterial," Opt. Mater. Express, vol. 6, no. 3, p. 884, (2016). https://doi.org/10.1364/ome.6.000884

[167] H. Ni, M. Wang, T. Shen, and J. Zhou, "Self-Assembled Large-Area Annular Cavity Arrays with Tunable Cylindrical Surface Plasmons for Sensing," ACS Nano, vol. 9, no. 2, pp. 1913–1925, (2015). https://doi.org/10.1021/nn506834r

[168] W. Fan, S. Zhang, K. J. Malloy, and S. R. J. Brueck, "Enhanced mid-infrared transmission through nanoscale metallic coaxial-aperture arrays," Opt. Express, vol. 13, no. 12, pp. 4406–4413, (2005). https://doi.org/10.1364/OPEX.13.004406

[169] J. A. Bishop, M. M. Hashemi, K. Kiziloglu, L. Larson, N. Dagli, and U. Mishra, "Monolithic coaxial transmission lines for mm-wave ICs," in IEEE/Cornell Conference on Advanced Concepts in High Speed Semiconductor Devices and Circuits, (1991), pp. 252–260. https://doi.org/10.1109/CORNEL.1991.169993

[170] V. Rajarathinam, N. Fritz, S. A. B. Allen, and P. A. Kohl, "Imprint lithography enabling ultra-low loss coaxial interconnects," Microelectron. Eng., vol. 88, no. 3, pp. 240–246, (2011). https://doi.org/10.1016/j.mee.2010.10.040

[171] G. M. Whitesides, "Self-Assembly at All Scales," Science, vol. 295, no. 5564, pp. 2418–2421, (2002). https://doi.org/10.1126/science.1070821

[172] H. Ditlbacher et al., "Silver nanowires as surface plasmon resonators," Phys. Rev. Lett., vol. 95, no. 25, pp. 1–4, (2005). https://doi.org/10.1103/PhysRevLett.95.257403

[173] J. Chen, B. J. Wiley, and Y. Xia, "One-dimensional nanostructures of metals: Large-scale synthesis and some potential applications," Langmuir, vol. 23, no. 8, pp. 4120–4129, (2007). https://doi.org/10.1021/la063193y

[174] H. Wei and H. Xu, "Nanowire-based plasmonic waveguides and devices for integrated nanophotonic circuits," Nanophotonics, vol. 1, no. 2, pp. 155–169, (2012). https://doi.org/10.1515/nanoph-2012-0012

[175] Y. Sun, B. Mayers, T. Herricks, and Y. Xia, "Polyol Synthesis of Uniform Silver Nanowires: A Plausible Growth Mechanism and the Supporting Evidence - Nano Letters (ACS Publications)," Nano Lett., vol. 3, no. 7, pp. 955–960, (2003). https://doi.org/10.1021/nl034312m

[176] M. A. Schmidt and P. S. Russell, "Long-range spiralling surface plasmon modes on metallic nanowires," Opt. Express, vol. 16, no. 18, p. 13617, (2008). https://doi.org/10.1364/OE.16.013617

[177] Y. Yin, Y. Lu, Y. Sun, and Y. Xia, "Silver Nanowires Can Be Directly Coated with Amorphous Silica to Generate Well-Controlled Coaxial Nanocables of Silver/Silica," Nano Lett., vol. 2, no. 4, pp. 427–430, (2002). https://doi.org/10.1021/nl025508+

[178] A. Lahiri, G. Pulletikurthi, and F. Endres, "A Review on the Electroless Deposition of Functional Materials in Ionic Liquids for Batteries and Catalysis," Front. Chem., vol. 7, no. February, pp. 1–13, (2019). https://doi.org/10.3389/fchem.2019.00085

[179] J. Hu, Y. Liu, J. Men, L. Zhang, and H. Huang, "Ag modified LaMnO 3 nanorods-reduced graphene oxide composite applied in the photocatalytic discoloration of direct green," Solid State Sci., vol. 61, pp. 239–245, (2016). https://doi.org/10.1016/j.solidstatesciences.2016.10.008

[180] M. Rycenga et al., "Controlling the Synthesis and Assembly of Silver Nanostructures for Plasmonic Applications," Chem. Rev., vol. 111, no. 6, pp. 3669–3712, (2011). https://doi.org/10.1021/cr100275d

[181] Z. Li, K. Bao, Y. Fang, Y. Huang, P. Nordlander, and H. Xu, "Correlation between incident and emission polarization in nanowire surface plasmon waveguides," Nano Lett., vol. 10, no. 5, pp. 1831–1835, (2010). https://doi.org/10.1021/nl100528c

[182] Y. Ma, X. Li, H. Yu, L. Tong, Y. Gu, and Q. Gong, "Direct measurement of propagation losses in silver nanowires.," Opt. Lett., vol. 35, no. 8, pp. 1160–1162, (2010). https://doi.org/10.1364/OL.35.001160

[183] M. J. Naughton, K. Kempa, and Z. Ren, "Nanoscale Optical Microscope," US 7,623,746 B2(2009). http://patft1.uspto.gov/netacgi/nph-Parser?patentnumber=7623746

[184] S. Kawata, A. Ono, and P. Verma, "Subwavelength colour imaging with a metallic nanolens," Nat. Photonics, vol. 2, no. 7, pp. 438–442, (2008). https://doi.org/10.1038/nphoton.2008.103

[185] A. H. Rose et al., "Nanoscope based on nanowaveguides," Opt. Express, vol. 22, no. 5, p. 5228, (2014). https://doi.org/10.1364/OE.22.005228

[186] Y. Ohashi, B. Ranjan, Y. Saito, T. Umakoshi, and P. Verma, "Tapered arrangement of metallic nanorod chains for magnified plasmonic nanoimaging," Sci. Rep., vol. 9, no. 1, p. 2656, (2019). https://doi.org/10.1038/s41598-019-39624-1

[187] A. N. Rodríguez, M. T. S. Nair, and P. K. Nair, "Structural, optical and electrical properties of chemically deposited silver sulfide thin films," Semicond. Sci. Technol., vol. 20, no. 6, pp. 576–585, (2005). https://doi.org/10.1088/0268-1242/20/6/017

[188] D. A. Robinson and H. S. White, "Electrochemical Synthesis of Individual Core@Shell and Hollow Ag/Ag 2 S Nanoparticles," Nano Lett., vol. 19, no. 8, pp. 5612–5619, (2019). https://doi.org/10.1021/acs.nanolett.9b02144

[189] J. B. Khurgin and A. Boltasseva, "Reflecting upon the losses in plasmonics and metamaterials," MRS Bull., vol. 37, no. 8, pp. 768–779, (2012). https://doi.org/10.1557/mrs.2012.173

[190] I. Popova, V. Zhukov, and J. . Yates, "Comparative study of Al(111) oxidation with O3 and O2," Surf. Sci., vol. 518, no. 1–2, pp. 39–48, (2002). https://doi.org/10.1016/S0039-6028(02)02064-2

[191] N. R. Anderson and G. L. Snider, "Growth of Alumina From Aluminum Films Using Oxygen Plasma," Notre Dame, (2004). https://curate.nd.edu/show/mp48sb41j75

[192] C. Ting, S. Chen, and D.-M. Liu, "Structural evolution and optical properties of TiO2 thin films prepared by thermal oxidation of sputtered Ti films," J. Appl. Phys., vol. 88, no. 8, p. 4628, (2000). https://doi.org/10.1063/1.1309039

[193] G. H. Chan, J. Zhao, E. M. Hicks, G. C. Schatz, and R. P. Van Duyne, "Plasmonic Properties of Copper Nanoparticles Fabricated by Nanosphere Lithography," Nano Lett., vol. 7, no. 7, pp. 1947–1952, (2007). https://doi.org/10.1021/nl070648a

[194] M. R. Johan, M. S. M. Suan, N. L. Hawari, and H. A. Ching, "Annealing effects on the properties of copper oxide thin films prepared by chemical deposition," Int. J. Electrochem. Sci., vol. 6, pp. 6094–6104, (2005). http://www.electrochemsci.org/papers/vol6/6126094.pdf

[195] L. P. H. Jeurgens, W. G. Sloof, F. D. Tichelaar, and E. J. Mittemeijer, "Growth kinetics and mechanisms of aluminum-oxide films formed by thermal oxidation of aluminum," J. Appl. Phys., vol. 92, no. 3, pp. 1649–1656, (2002). https://doi.org/10.1063/1.1491591

[196] M. W. Knight, N. S. King, L. Liu, H. O. Everitt, P. Nordlander, and N. J. Halas, "Aluminum for Plasmonics," ACS Nano, vol. 8, no. 1, pp. 834–840, (2014). https://doi.org/10.1021/nn405495q

[197] M. Kaltenbrunner, P. Stadler, R. Schwödiauer, A. W. Hassel, N. S. Sariciftci, and S. Bauer, "Anodized Aluminum Oxide Thin Films for Room-Temperature-Processed, Flexible, Low-Voltage Organic Non-Volatile Memory Elements with Excellent Charge Retention," Adv. Mater., vol. 23, no. 42, pp. 4892–4896, (2011). https://doi.org/10.1002/adma.201103189

[198] R. A. Farrer et al., "Selective Functionalization of 3-D Polymer Microstructures," J. Am. Chem. Soc., vol. 128, no. 6, pp. 1796–1797, (2006). https://doi.org/10.1021/ja0583620

[199] E. K. Yung, "Fundamental Study of Acid Copper Through-Hole Electroplating Process," J. Electrochem. Soc., vol. 136, no. 3, p. 756, (1989). https://doi.org/10.1149/1.2096738

[200] Nanocomposix Inc., "Silica Coated Silver Nanowires." (2013). https://nanocomposix.com

[201] Ted Pella Inc., "PELCO Grids." (2019). https://www.tedpella.com/grids_html/Pelco-TEM-Grids.htm

[202] A. Graff, D. Wagner, H. Ditlbacher, and U. Kreibig, "Silver nanowires," Eur. Phys. J. D, vol. 34, no. 1–3, pp. 263–269, (2005). https://doi.org/10.1140/epjd/e2005-00108-7

[203] X. Chen et al., "Atomic layer lithography of wafer-scale nanogap arrays for extreme confinement of electromagnetic waves," Nat. Commun., vol. 4, no. 1, p. 2361, (2013). https://doi.org/10.1038/ncomms3361

[204] D. Yoo et al., "High-Throughput Fabrication of Resonant Metamaterials with Ultrasmall Coaxial Apertures via Atomic Layer Lithography," Nano Lett., vol. 16, no. 3, pp. 2040–2046, (2016). https://doi.org/10.1021/acs.nanolett.6b00024

[205] Veeco Instruments Inc. / Cambridge Nanotech, "Savannah - Thermal ALD Systems." (2019). http://www.cambridgenanotechald.com/products/Savannah-ald-system.shtml

[206] Arradiance LLC, "GEMStar Benchtop Atomic Layer Deposition Systems." (2019). https://www.arradiance.com/gemstar/gemstar.html

[207] Swagelok Inc., "ALD Valves." (2019). https://www.swagelok.com/en/catalog/Valves/Diaphragm-Sealed/Atomic-Layer-Deposition-Valves

[208] J. A. Woollam Co. Inc., "Variable Angle Spectroscopic Ellipsometers." (2019). https://www.jawoollam.com/products/vase-ellipsomete

[209] J. H. Weaver, "Optical properties of Rh, Pd, Ir, and Pt," Phys. Rev. B, vol. 11, no. 4, pp. 1416–1425, (1975). https://doi.org/10.1103/PhysRevB.11.1416

[210] W. J. Tropf and M. E. Thomas, "Aluminum Oxide (Al2O3) Revisited," in Handbook of Optical Constants of Solids, 3rd ed., E. D. Palik, Ed. Elsevier Inc., (1998), pp. 653–682. https://www.sciencedirect.com/book/9780125444156

[211] M. D. Groner, F. H. Fabreguette, J. W. Elam, and S. M. George, "Low-Temperature Al 2 O 3 Atomic Layer Deposition," Chem. Mater., vol. 16, no. 4, pp. 639–645, (2004). https://doi.org/10.1021/cm0304546

[212] D. C. Harris et al., "Refractive index of infrared-transparent polycrystalline alumina," Opt. Eng., vol. 56, no. 7, p. 077103, (2017). https://doi.org/10.1117/1.OE.56.7.077103

[213] G. N. West et al., “Low-loss integrated photonics for the blue and ultraviolet regime,” APL Photonics, vol. 4, no. 2, p. 026101, (2019). https://doi.org/10.1063/1.5052502

[214] Jandel Engineering Ltd., “Four Point Probe Systems.” (2019). http://www.jandel.co.uk/index.html

[215] H. J. K. Kim et al., “Electrical Properties of Ultrathin Platinum Films by Plasma-Enhanced Atomic Layer Deposition,” ACS Appl. Mater. Interfaces, vol. 11, no. 9, pp. 9594–9599, (2019). https://doi.org/10.1021/acsami.8b21054

[216] D. A. Dimitrov, B. M. Terzijska, V. Guevezov, and V. T. Kovachev, “Thin film platinum resistance thermometer for measurements in high magnetic fields,” Cryogenics (Guildf)., vol. 30, no. 4, pp. 348–350, (1990). https://doi.org/10.1016/0011-2275(90)90314-3

[217] Gorilla Glue Co., “Gorilla Super Glue.” (2019). https://www.gorillatough.com/product/gorilla-super-glue/

[218] D. Xu, B. Xiong, G. Wu, Y. Wang, X. Sun, and Y. Wang, “Isotropic Silicon Etching With XeF2 Gas for Wafer-Level Micromachining Applications,” J. Microelectromechanical Syst., vol. 21, no. 6, pp. 1436–1444, (2012). https://doi.org/10.1109/JMEMS.2012.2209403

[219] Y. M. Calm and M. J. Naughton, “Optical confinement in the nanocoax: coupling to the fundamental TEM-like mode,” Manuscript in Preparation. (2019).

[220] L. A. Woldering, R. Willem Tjerkstra, H. V. Jansen, I. D. Setija, and W. L. Vos, “Periodic arrays of deep nanopores made in silicon with reactive ion etching and deep UV lithography,” Nanotechnology, vol. 19, no. 14, p. 145304, (2008). https://doi.org/10.1088/0957-4484/19/14/145304

[221] K. R. Williams, K. Gupta, and M. Wasilik, “Etch rates for micromachining processing-part II,” J. Microelectromechanical Syst., vol. 12, no. 6, pp. 761–778, (2003). https://doi.org/10.1109/JMEMS.2003.820936

[222] W. Shin, W. Cai, P. B. Catrysse, G. Veronis, M. L. Brongersma, and S. Fan, “Broadband Sharp 90-degree Bends and T-Splitters in Plasmonic Coaxial Waveguides,” Nano Lett., vol. 13, no. 10, pp. 4753–4758, (2013). https://doi.org/10.1021/nl402335x

[223] L. K. Tan, A. S. M. Chong, X. S. E. Tang, and H. Gao, “Combining Atomic Layer Deposition with a Template-Assisted Approach To Fabricate Size-Reduced Nanowire Arrays on Substrates and Their Electrochemical Characterization,” J. Phys. Chem. C, vol. 111, no. 13, pp. 4964–4968, (2007). https://doi.org/10.1021/jp066841v

[224] P. Banerjee, I. Perez, L. Henn-Lecordier, S. B. Lee, and G. W. Rubloff, “Nanotubular metal–insulator–metal capacitor arrays for energy storage,” Nat. Nanotechnol., vol. 4, no. 5, pp. 292–296, (2009). https://doi.org/10.1038/nnano.2009.37

[225] G. Pardon, H. K. Gatty, G. Stemme, W. Van Der Wijngaart, and N. Roxhed, “Pt–Al2O3 dual layer atomic layer deposition coating in high aspect ratio nanopores,” Nanotechnology, vol. 24, no. 1, p. 015602, (2013). https://doi.org/10.1088/0957-4484/24/1/015602

[226] R. He et al., “Integration of gigahertz-bandwidth semiconductor devices inside microstructured optical fibres,” Nat. Photonics, vol. 6, no. 3, pp. 174–179, (2012). https://doi.org/10.1038/nphoton.2011.352

[227] A. Vaish et al., “Enhancing the platinum atomic layer deposition infiltration depth inside anodic alumina nanoporous membrane,” J. Vac. Sci. Technol. A Vacuum, Surfaces, Film., vol. 33, no. 1, p. 01A148, (2015). https://doi.org/10.1116/1.4904398

[228] S. M. Orbons et al., “Dual resonance mechanisms facilitating enhanced optical transmission in coaxial waveguide arrays,” Opt. Lett., vol. 33, no. 8, p. 821, (2008). https://doi.org/10.1364/OL.33.000821

[229] D. W. Lynch and W. R. Hunter, "Comments on the Optical Constants of Metals and an Introduction to the Data for Several Metals," in Handbook of Optical Constants of Solids, 1st ed., E. D. Palik, Ed. (1985), pp. 275–367. https://www.sciencedirect.com/book/9780080547213

[230] M. A. Green, "Self-consistent optical parameters of intrinsic silicon at 300K including temperature coefficients," Sol. Energy Mater. Sol. Cells, vol. 92, no. 11, pp. 1305–1310, (2008). https://doi.org/10.1016/j.solmat.2008.06.009

[231] F. Niklaus, G. Stemme, J. Q. Lu, and R. J. Gutmann, "Adhesive wafer bonding," J. Appl. Phys., vol. 99, no. 3, p. 031101, (2006). https://doi.org/10.1063/1.2168512

[232] R. S. Lima et al., "Sacrificial adhesive bonding: a powerful method for fabrication of glass microchips," Sci. Rep., vol. 5, no. 1, p. 13276, (2015). https://doi.org/10.1038/srep13276

[233] S. G. Serra et al., "A simple bonding process of SU-8 to glass to seal a microfluidic device," in 4M2007 Conference on Multi-Material Micro Manufacture, (2007). http://www.4m-net.org/KnowledgeBase/papers/PID367308

[234] C. Yang and Y. J. Yuan, "Investigation on the mechanism of nitrogen plasma modified PDMS bonding with SU-8," Appl. Surf. Sci., vol. 364, pp. 815–821, (2016). https://doi.org/10.1016/j.apsusc.2015.12.153

[235] M. Rubin, "Optical properties of soda lime silica glasses," Sol. Energy Mater., vol. 12, no. 4, pp. 275–288, (1985). https://doi.org/10.1016/0165-1633(85)90052-8

[236] Microchem Inc., "SU-8 3000 Permanent Epoxy." (2019). http://www.microchem.com/Prod-SU83000.htm

[237] S. J. Orfanidis, Electromagnetic Waves and Antennas. (2016). http://www.ece.rutgers.edu/~orfanidi/ewa/

[238] F. I. Baida et al., "Enhanced optical transmission by light coaxing: Mechanism of the TEM-mode excitation," Micron, vol. 41, no. 7, pp. 742–745, (2010). https://doi.org/10.1016/j.micron.2010.06.009

[239] A. Ndao et al., "Resonant optical transmission through sub-wavelength annular apertures caused by a plasmonic transverse electromagnetic (TEM) mode," J. Opt., vol. 16, no. 12, p. 125009, (2014). https://doi.org/10.1088/2040-8978/16/12/125009

[240] A. Roberts, "Beam transmission through hole arrays," Opt. Express, vol. 18, no. 3, p. 2528, (2010). https://doi.org/10.1364/OE.18.002528

[241] G. M. Lerman, A. Yanai, and U. Levy, "Demonstration of Nanofocusing by the use of Plasmonic Lens Illuminated with Radially Polarized Light," Nano Lett., vol. 9, no. 5, pp. 2139–2143, (2009). https://doi.org/10.1021/nl900694r

[242] A. Ndao, A. Belkhir, R. Salut, and F. I. Baida, "Slanted annular aperture arrays as enhanced-transmission metamaterials: Excitation of the plasmonic transverse electromagnetic guided mode," Appl. Phys. Lett., vol. 103, no. 21, p. 211901, (2013). https://doi.org/10.1063/1.4832227

[243] COMSOL Inc., "Platform Product: COMSOL MULTIPHYSICS®." (2019). https://www.comsol.com/comsol-multiphysics

[244] R. W. Pryor, Multiphysics Modeling Using COMSOL 5 and MATLAB. Mercury Learning and Information, (2016). http://www.merclearning.com/titles/Multiphysics_Modeling_Using_COMSOL_5_and_MATLAB.html

[245] K. Sakai, K. Nomura, T. Yamamoto, and K. Sasaki, "Excitation of Multipole Plasmons by Optical Vortex Beams," Sci. Rep., vol. 5, no. 1, p. 8431, (2015). https://doi.org/10.1038/srep08431

[246] W. Shang, F. Xiao, W. Zhu, L. Han, T. Mei, and J. Zhao, "Characterizing localized surface plasmon resonances using focused radially polarized beam," Appl. Opt., vol. 58, no. 21, p. 5812, (2019). https://doi.org/10.1364/AO.58.005812

[247] W. Chen and Q. Zhan, "Numerical study of an apertureless near field scanning optical microscope probe under radial polarization illumination," Opt. Express, vol. 15, no. 7, p. 4106, (2007). https://doi.org/10.1364/OE.15.004106

[248] H. Choo et al., "Nanofocusing in a metal–insulator–metal gap plasmon waveguide with a three-dimensional linear taper," Nat. Photonics, vol. 6, no. 12, pp. 838–844, (2012). https://doi.org/10.1038/nphoton.2012.277

[249] M. Schnell et al., "Nanofocusing of mid-infrared energy with tapered transmission lines," Nat. Photonics, vol. 5, no. 5, pp. 283–287, (2011). https://doi.org/10.1038/nphoton.2011.33

[250] J. Xu et al., "Field-enhanced nanofocusing of radially polarized light by a tapered hybrid plasmonic waveguide with periodic grooves," Appl. Opt., vol. 58, no. 3, p. 588, (2019). https://doi.org/10.1364/AO.58.000588

[251] A. A. E. Saleh, S. Sheikhoelislami, S. Gastelum, and J. A. Dionne, "Grating-flanked plasmonic coaxial apertures for efficient fiber optical tweezers," Opt. Express, vol. 24, no. 18, p. 20593, (2016). https://doi.org/10.1364/OE.24.020593

[252] Z.-C. Ren, S.-X. Qian, C. Tu, Y. Li, and H.-T. Wang, "Focal shift in tightly focused Laguerre–Gaussian beams," Opt. Commun., vol. 334, pp. 156–159, (2015). https://doi.org/10.1016/j.optcom.2014.08.036

[253] P. Nagpal, N. C. Lindquist, S.-H. Oh, and D. J. Norris, "Ultrasmooth Patterned Metals for Plasmonics and Metamaterials," Science, vol. 325, no. 5940, pp. 594–597, (2009). https://doi.org/10.1126/science.1174655

[254] N. C. Lindquist, P. Nagpal, A. Lesuffleur, D. J. Norris, and S.-H. Oh, "Three-Dimensional Plasmonic Nanofocusing," Nano Lett., vol. 10, no. 4, pp. 1369–1373, (2010). https://doi.org/10.1021/nl904294u

[255] N. C. Lindquist, T. W. Johnson, P. Nagpal, D. J. Norris, and S.-H. Oh, "Plasmonic nanofocusing with a metallic pyramid and an integrated C-shaped aperture," Sci. Rep., vol. 3, no. 1, p. 1857, (2013). https://doi.org/10.1038/srep01857

[256] T. W. Johnson et al., "Highly Reproducible Near-Field Optical Imaging with Sub-20-nm Resolution Based on Template-Stripped Gold Pyramids," ACS Nano, vol. 6, no. 10, pp. 9168–9174, (2012). https://doi.org/10.1021/nn303496g

[257] Z. Fang, L. Fan, C. Lin, D. Zhang, A. J. Meixner, and X. Zhu, "Plasmonic coupling of bow tie antennas with Ag nanowire," Nano Lett., vol. 11, no. 4, pp. 1676–1680, (2011). https://doi.org/10.1021/nl200179y

[258] A. W. Sanders, D. A. Routenberg, B. J. Wiley, Y. Xia, E. R. Dufresne, and M. A. Reed, "Observation of Plasmon Propagation, Redirection, and Fan-Out in Silver Nanowires," Nano Lett., vol. 6, no. 8, pp. 1822–1826, (2006). https://doi.org/10.1021/nl052471v

[259] R. Klopfenstein, "A Transmission Line Taper of Improved Design," Proc. IRE, vol. 44, no. 1, pp. 31–35, (1956). https://doi.org/10.1109/JRPROC.1956.274847

[260] A. Rusina, M. Durach, K. A. Nelson, and M. I. Stockman, “Nanoconcentration of terahertz radiation in plasmonic waveguides,” Opt. Express, vol. 16, no. 23, p. 18576, (2008). https://doi.org/10.1364/OE.16.018576